



# Contribution de l'émission acoustique pour la gestion et la sécurité des batteries Li-ion

Nina Encheva Kircheva

## ► To cite this version:

Nina Encheva Kircheva. Contribution de l'émission acoustique pour la gestion et la sécurité des batteries Li-ion. Autre. Université de Grenoble, 2013. Français. NNT : 2013GRENI014 . tel-00960011

**HAL Id: tel-00960011**

**<https://theses.hal.science/tel-00960011>**

Submitted on 17 Mar 2014

**HAL** is a multi-disciplinary open access archive for the deposit and dissemination of scientific research documents, whether they are published or not. The documents may come from teaching and research institutions in France or abroad, or from public or private research centers.

L'archive ouverte pluridisciplinaire **HAL**, est destinée au dépôt et à la diffusion de documents scientifiques de niveau recherche, publiés ou non, émanant des établissements d'enseignement et de recherche français ou étrangers, des laboratoires publics ou privés.



## THÈSE

Pour obtenir le grade de

## DOCTEUR DE L'UNIVERSITÉ DE GRENOBLE

Spécialité : **Mécanique des Fluides, Procèdes, Energétique**

Arrêté ministériel : 7 août 2006

Présentée par

**« Nina KIRCHEVA (née ENCHEVA) »**

Thèse dirigée par «**Pierre-Xavier THIVEL** » et  
codirigée par « **Sylvie GENIES** »

préparée au sein du **Laboratoire CEA/DRT/LITEN/DTS/LSE,**  
**INP-Grenoble/LEPMI/GP2E**  
dans l'**École Doctorale : IMEP2**

# Contribution de l'Emission Acoustique pour la gestion et la sécurité des batteries Li-ion

Thèse soutenue publiquement le « **16.01.2013** »,  
devant le jury composé de :

**M, Ricardo, NOGUEIRA**

Professeur des Universités Grenoble-INP, Président

**Mme, Laure, MONCONDUIT**

D.R. CNRS-Université Montpellier, Rapporteur

**M, Thierry, BROUSSE**

Professeur des Universités, Polytech Nantes, Rapporteur

**M, Hassane, IDRISI**

Maître de Conférences-HDR, INSA de Lyon, Membre

**Mme, Sylvie, GENIES**

Docteur Chef de projet, CEA/LITEN, Co-encadrante

**M, Pierre-Xavier, THIVEL**

Maître de Conférences-HDR, Université Joseph Fourier, Directeur de thèse

**M, Jean-François, COUSSEAU**

Docteur Directeur Technique et Industriel PROLLION, Membre invité





*To my daughter!*

*Мило мое слънчице, благодаря ти за търпението!*

*“Success is never final. Failure is never fatal.*

*It is courage that counts.”*

***Winston Churchill***

---



## Acknowledgements

I would like to thank firstly to Dr. Sylvie GENIES and Professor Pierre-Xavier THIVEL for their support and patience during the past three years. Their confidence in me helped much to overcome the challenges that I faced during my research.

Sincerely thanks to Dr. Sothun HING for his support and help in the solution of problems of various nature, as well as for the final corrections of the manuscript.

I am sincerely grateful to Professor Laure MONCONDUIT and Professor Thierry BROUSSE for the time spends to review this manuscript.

Sincerely thanks to Dr. Florence LAMBERT for provided technical support in DEHT and the idea to use coin cell design of the tested batteries. I am also grateful to her and Marion PERRIN to believe in my ambitions to continue my carrier in the electrochemistry.

I would like to thank to Djamel MOURZAGH, Audrey AUGUSTIN-CONSTANTIN and Anaïs D’AFFROUX from DEHT for their invaluable help in the preparation of the electrodes and the cells. I am grateful to Claude CHABROL for the support of the XRD characterization in the electrodes.

Sincerely thanks to Dr. Benoit LEGROS for his help in solution of the problems concerning the Acoustic Emission techniques.

I would like to thank to Baptiste JAMMET, for the valuable professional advices and technical and logistics help.

Acknowledgments to Mélanie ALIAS and David BRUN-BUISSON for their pioneer work in Acoustic Emission started in LITEN. Mélanie was my first teacher in the preparation of the Li-ion batteries, thanks for the experience.

Sincerely Thanks to Fathia KAROUI for the advices about the manuscript preparation.

Sincerely thanks to Angel who scarifies several weekends of gaming to correct the English language in this manuscript. Ачо, не е важно какво чувстваш към някого, по-важно е какво правиш за него, а ти правиш и невъзможното за мен! Благодаря ти!

The financial support of this thesis by Fond Carnot is gratefully acknowledged!

Last but not at least I would like to thank to all my colleagues from LSE (INES) and GP2E (LEPMI) for the interesting and useful time spent together!

---

## Résumé

L'objectif de cette thèse est de démontrer que l'Émission Acoustique (AE) est une technique appropriée pour devenir un outil de diagnostic de l'état de charge, de santé et de sécurité pour les batteries lithium-ion. Ces questions sont actuellement des points clés important pour l'amélioration des performances et des durées de vie de la technologie. La structure de ce document est organisée en deux principaux chapitres expérimentaux, l'un consacré à des éléments lithium-ion constitués de composés d'intercalation et l'autre d'alliages de lithium. Dans le premier cas, les résultats présentés concernent le suivi par AE de la formation de la SEI et de la première intercalation des ions lithium dans la structure du graphite pour des éléments C/LiFePO<sub>4</sub>. Les événements AE provenant de plusieurs sources ont été identifiés et correspondent à la formation de gaz (bulles) et à des phénomènes de craquelures (ouvertures du bord des plans de graphène quand la SEI est formée et l'écartement quand les stades d'insertion du graphite-lithium sont finis). De plus, une étude par spectroscopie d'impédance a été menée durant un vieillissement calendaire en température sur des éléments formés à différents régimes de courant.

Dans le second cas, le mécanisme d'insertion/extraction du lithium dans des éléments LiAl/MnO<sub>2</sub> a été étudié en associant plusieurs techniques incluant des techniques électrochimiques et acoustiques ainsi que des analyses *post-mortem* pour évaluer les mécanismes de dégradation. Lors du cyclage, les événements acoustiques sont plus intenses lors du processus de décharge et ils peuvent être attribués principalement à la formation de l'alliage avec la transformation de phase de  $\alpha$ -LiAl en  $\beta$ -LiAl accompagnée d'une expansion volumique importante.

L'émission acoustique peut ainsi offrir une nouvelle approche pour gérer le fonctionnement des technologies lithium-ion basées non plus seulement sur des paramètres électrochimiques classiques mais aussi sur des paramètres acoustiques. Des nouveaux d'états de santé et de sécurité peuvent ainsi être envisagés.

**Mots clé :** *Li-ion batterie, Emission Acoustique, Film de passivation, Lithium Intercalation, Vieillissement, BMS, Etat du Santé, Etat de Formation.*

---

## Abstract

The aim of this thesis is to demonstrate that the Acoustic Emission (AE) is an appropriate technique for diagnostics of for state of charge, state of health and state of safety for lithium-ion batteries. The availability and optimization of the latter issues are key points for both performance and durability improvements of this technology.

The frame of this document is organized in two main result chapters focused on AE study of two different Li-ion technologies. The beginning of the thesis is focused on the monitoring of the SEI formation by AE and the first lithium ion intercalation inside the graphite structure for C/LiFePO<sub>4</sub> cells. AE events coming from different sources have been analyzed and identified. It was found that they correspond to gas emission (bubbles) and cracking phenomena (opening on the edge of the graphene plane when the SEI is formed and spacing when lithium graphite insertion stages are completed). Further, a study of the calendar aging process supported by electrochemical impedance spectroscopy linked the aging rate with the mechanism of the SEI formation characterized by AE monitoring.

The second part of the thesis studied of lithium ion insertion/extraction in LiAl/MnO<sub>2</sub> cells combining a variety of techniques including electrochemical characterization, AE monitoring and *post-mortem* analysis in order to evaluate the degradation mechanisms. It was found that during the cycling, the acoustic events are much more intensive during the discharge process and they can be attributed mainly to the alloy were the phase transformation from  $\alpha$ -LiAl to  $\beta$ -LiAl and a huge volume expansion occurs.

It was found that battery operation under abusive conditions (overcharge, overdischarge) can be detected by AE providing new rates for battery safety management.

**Key words:** *Li-ion battery, Acoustic Emission, Solid Electrolyte Interface, SEI formation, Lithium Intercalation, Aging, BMS, State of Health, State of Formation.*

---

## Introduction

Today, it has become increasingly important to have ready access to energy in different forms and for various applications. Rechargeable batteries are therefore becoming immensely important by virtue of their ability to store electricity and make energy portable. One of the most promising rechargeable systems is the Li-ion technology because it can fulfill many of the demands made within the areas of portable electronics and EV/HEV's. It is superior in many aspects to the more traditional nickel-cadmium (NiCd) and nickel-metal hydride (NiMH) batteries. The first chapter of this manuscript will discuss the reasons of this superiority, related principally to its high specific energy and power. However, these batteries still have serious drawbacks. Effects of prolonged cycling (repeated charge and discharge) or prolonged storage push them away from their theoretical and initially excellent performance. These effects are typically capacity loss, poor cyclability, during the cycling and the open circuit stays as well as a power fade due to increase of the battery resistance. Many of the problems can be related for one part to surface phenomena occurring on the negative and positive electrodes and for another part to structural modifications (expansion-contraction, crystal disorder). Moreover, its high specific energies force to improve the safety level in operating. Consequently reliable indicators have to be developed and improved to inform properly the users about the states of charge and health of the battery. A lot of studies are oriented towards these objectives and this work is made in the same framework.

Our approach is original by comparing to the other studies in the sense that a non-conventional technique has been used. We propose to couple an acoustic sensor to Li-ion cells in order to detect in a passive way the sounds emitted by the cell during the electrochemical formation process and further during the operating processes. The main goal of this thesis is hence to demonstrate that the acoustic emission technique could contribute to the Li-ion cells all along its life.

Considering this objective, we have characterized two different technologies of lithium-ion cells: firstly a technology including  $\text{LiFePO}_4$  as positive electrode and Graphite as negative electrode which was home-made to be able to study the formation process, secondly a commercial technology including a lithium-alloy (LiAl) as negative electrode.

---

The manuscript is organized in four chapters:

Chapter I: Lithium-ion Technologies and applications.

Chapter II: Experimental.

Chapter III: Contribution of the Acoustic Emission to the study of the behavior of Graphite/LiFePO<sub>4</sub> cells

Chapter IV: Evolution of Acoustic Emission as a tool for aging characterization of LiAl/MnO<sub>2</sub> cells.

Chapter I propose a short overview of the lithium-ion technologies and the applications where they are already present (portable applications), shortly present (transportation application) or more distantly present (storage for renewable energies). We have also defined the main electrochemical parameters used to define an accumulator.

Chapter II describes the acoustic emission activity monitoring technique which is well adapted to characterize the structural and electrochemical phenomena occurring within the cells when formed cycled in a suitable voltage range or out of this voltage range. The other techniques used are also presented in this chapter.

The chapters III and IV give the main results obtained during the period of the thesis. Both chapters are organized similarly with a first part dedicated to a bibliography study on the active materials. This bibliography study would facilitate the explanation and correlate between electrochemical and mechanical phenomena occurring within these materials and detected acoustic activity. Further the results obtained under normal and abusive conditions are presented.

The AE techniques can bring new insights to the Li-ion technology in similar way which has been done on NiMH batteries and fuel cells. It can further clarify the understanding of the electrochemical phenomena taking place from the cell manufacturing till the end of its operating. Hence we hope to be able to find new solutions to the problems that remain to solve or prevent.

---

## **Contents**

<b>Acknowledgements</b>	2
<b>Résumé</b>	3
<b>Abstract</b>	4
<b>Introduction</b>	5
 <b>Chapter I</b>	 12
<b>I.1. Introduction</b>	14
<b>I.2. Applications</b>	18
I.2.1. Portable applications	18
I.2.2. Stationary applications	19
I.2.3. Electrical Transport Applications	20
<b>I.3. Performance and limitations of the Li-ion batteries</b>	22
<b>I.4. Positive electrode materials for Li-ion batteries</b>	25
<b>I.5. Negative electrode materials for Li-ion batteries</b>	28
I.5.1 Lithium metal	28
I.5.2. Graphite materials	29
I.5.3. $\text{Li}_4\text{Ti}_5\text{O}_{12}$	31
I.5.4. Metallic alloys – direct reaction	32
<b>I.6. Separators</b>	33
<b>I.7. Electrolytes</b>	34
I.7.1. Liquid electrolyte	34
I.7.2. Polymer electrolyte	35
I.7.3. Ionic liquids	36
<b>I.8. Collector</b>	36
<b>I.9. Summary of the function of the internal components of a cell</b>	37
<b>I.10. Behavior of Li-ion cell under abusive conditions</b>	38
<b>I.11. Battery Management System</b>	41
I.11.1. Voltage control	42
I.11.2. Current control	42
I.11.3. State of Charge estimation and monitoring	42

---

---

I.11.4. State of Health	44
I.11.5. Thermal management	44
I.11.6. Integration of Acoustic emission detection in the Battery Management System	45
<b>I.12. Conclusion</b>	46
<b>References</b>	47
 <b>Chapter II</b>	 50
<b>II.2. Electrochemical circuit</b>	52
<b>II.3. Electrochemical diagnostic tools</b>	53
II.3.1. Galvano - potentiostatic charge or discharge	54
II.3.2. Cycling voltammetry	56
II.3.3. Electrochemical impedance spectroscopy	57
II.3.4. Electrochemical equipment	59
<b>II.4. Post mortem analyses</b>	59
II.4.1. X-ray diffraction technique	59
II.4.2. Scanning Electron microscopy	60
<b>II.5. Acoustic emission technique</b>	61
II.5.2. Principle and history of acoustic emission	61
II.5.3. Acoustic emission testing equipment	63
II.5.3.1. Acoustic emission sensors	64
II.5.3.2. Acoustic emission preamplifier	65
II.5.3.3. Acoustic emission filter	66
II.5.3.4. Acoustic emission software	66
II.5.4. Acoustic emission acquisition parameters	67
II.5.5. Characteristic parameters of the acoustic emission wave form	68
II.5.6. Acoustic emission data treatment	70
II.5.6.1. Spectral analysis	70
II.5.6.2. Multiparametric analysis	71
II.5.6.3. Advanced analysis	73
<b>II.6. Conclusion</b>	75
<b>References</b>	76

---

---

<b>Chapter III</b>	77
<b>Summary</b>	80
<b>Résumé</b>	80
<b>III.1. Introduction</b>	81
<b>III.2. Choice of positive and negative materials</b>	81
III.2.1. Lithium iron phosphate	81
III.2.1.1. Structure	81
III.2.1.2. Lithium intercalation	82
III.2.1.3. Type of used active materials	84
III.2.2. Graphite	86
III.2.2.1. Structure	86
III.2.2.2. Intercalation process	87
III.2.2.3. Type of used graphite: meso carbon micro beads (MCMB)	89
<b>III.3. Description of the formation process</b>	91
III.3.1. Formation of the SEI on Lithium	91
III.3.2. Formation of the SEI on Graphite	92
III.3.3. Techniques used to characterize the passivation film	94
III.3.3.1. Electrochemical techniques	94
III.3.3.2. Physicochemical characterization techniques	96
III.3.4. Ageing phenomena	97
III.3.4.1. Overview	99
<b>III.4. Cell construction and material preparation</b>	101
III.4.1. Fabrication of the negative electrode	101
III.4.2. Fabrication of the positive electrode	102
<b>III.5. Experimental study and analysis of the formation process</b>	103
III.5.1. Tests of Li/Li cells	103
III.5.2. Formation of Li/MCMB	103
III.5.2.1. Introduction	103
III.5.2.2. Results presentation and preliminary analysis	104
III.5.2.2. Acoustic emission activity during formation of SEI	107
III.5.2.3 Acoustic emission activity during the lithium intercalation	114

---



---

III.5.3. Formation Li/LiFePO <sub>4</sub>	117
III.5.4. Formation MCMB/ LiFePO <sub>4</sub> cells	120
III.5.4.1. Formation MCMB/ LiFePO <sub>4</sub> type I	120
III.5.4.2. Formation MCMB/ LiFePO <sub>4</sub> type II	125
III.5.4.3. Spectral analysis of the Acoustic Emission data	129
<b>III.6. Calendar aging of the MCMB/LiFePO<sub>4</sub> –type II</b>	<b>132</b>
<b>III.7. Experimental study on the MCMB/ LiFePO<sub>4</sub> under abusive conditions</b>	<b>137</b>
III.7.1. Overcharge Tests	138
III.7.2. Overdischarge and External short-circuit tests	140
<b>III.8. Conclusions</b>	<b>141</b>
<b>References</b>	<b>142</b>
 <b>Chapter IV</b>	 <b>145</b>
<b>Résumé</b>	<b>147</b>
<b>Summary</b>	<b>147</b>
<b>IV.1. Introduction</b>	<b>148</b>
<b>IV.2. Electrochemical reactions</b>	<b>148</b>
IV.2.1. Lithium alloys as negative electrode in Li-ion batteries	148
IV.2.2. Manganese oxides as positive electrode in Li-ion batteries	153
IV.2.3. Degradation phenomena	155
IV.2.3.1. Degradation phenomena in lithium alloys used as negative electrodes	155
IV.2.3.2. Degradation phenomena in manganese oxide as positive electrode	156
<b>IV.3. Acoustic emission dedicated to the study of these types of materials</b>	<b>156</b>
IV.3.1. Study of the lithium intercalation in different metal alloys by Acoustic Emission monitoring	156
IV.3.2. Acoustic Emission monitoring during the lithium intercalation in manganese oxides	157
<b>IV.4. Evaluation of the Acoustic Emission Technique as a suitable tool for ageing characterization of commercial LiAl/MnO<sub>2</sub></b>	<b>158</b>
IV.4.1. Details about cell construction	159
IV.4.2. Experimental set-up	160
IV.4.3. Initial characterization	162
IV.4.4. Cycling voltammetry	163

---

IV.4.5. Ageing tests_____	167
<b>IV.5. Study under abusive conditions.</b> _____	177
IV.5.1. Overcharge Process_____	177
IV.5.2. Overdischarge Process _____	179
<b>IV.6. Conclusions</b> _____	182
<b>References</b> _____	183
<b>General Conclusion</b> _____	185
<b>Glossary</b> _____	188
<b>Appendix 1: Valorization of results from the thesis</b> _____	191

---

---

---

## **Chapter I**

### **Lithium-ion Technologies and Applications**

<b>Chapter I</b>	12
Lithium-ion Technologies and Applications	12
<b>I.1. Introduction</b>	14
<b>I.2. Applications</b>	17
I.2.1. Portable applications	17
I.2.2. Stationary applications	19
I.2.3. Electrical Transport Applications	19
<b>I.3. Performance and limitations of the Li-ion batteries</b>	22
<b>I.4. Positive electrode materials for Li-ion batteries</b>	25
<b>I.5. Negative electrode materials for Li-ion batteries</b>	28
I.5.1 Lithium metal	28
I.5.2. Graphite materials	29
I.5.3. $\text{Li}_4\text{Ti}_5\text{O}_{12}$	31
I.5.4. Metallic alloys – direct reaction	32
<b>I.6. Separators</b>	33
<b>I.7. Electrolytes</b>	34
I.7.1. Liquid electrolyte	34
I.7.2. Polymer electrolyte	35
I.7.3. Ionic liquids	36
<b>I.8. Collector</b>	36
<b>I.9. Summary of the function of the internal components of a cell</b>	37
<b>I.10. Behavior of Li-ion cell under abusive conditions</b>	38
<b>I.11. Battery Management System</b>	41
I.11.1. Voltage control	42
I.11.2. Current control	42
I.11.3. State of Charge estimation and monitoring	42
I.11.4. State of Health	44
I.11.5. Thermal management	44
I.11.6. Integration of Acoustic emission detection in the Battery Management System	45
<b>I.12. Conclusion</b>	46
<b>References</b>	47

## I.1. Introduction

The challenge of the modern society is jointly to search new suitable sources of energy and to reduce our energy needs. Indeed the present energy economy based on fossil fuels brings several serious problems. The first and most important is the depletion of the fossil resources by consequence of the continuous and increasing demands for oil, gas and coal. The second general problem is the production of CO<sub>2</sub> emissions, dramatically increasing during the last 30 years. The need for clean renewable and efficient energy production grows as a consequence. Wind, solar and tidal powers are examples for renewable but irregular energy sources that require storage media to supply energy at the peak of demand and to consume it when necessary. Electrochemical systems such as batteries can efficiently store and deliver energy on demand in stand-alone power plants, as well as provide power quality and load leveling of electrical grid. The efficiency of batteries is essentially related to their content in energy efficiency and lifetime [1, 2]. The main types of rechargeable batteries system currently available in the market are presented in Figure 1. Although the sealed Lead Acid technology has a low cost, security advantage and high availability but has limited cycle life and a low specific energy. This type of batteries is mainly used to store energy produced by stand-alone systems and to provide emergency power to a load when the input power source, typically mains power, fails (Uninterruptible Power Source (UPS) or battery backup). Because these both applications are not constrained by footprint, specific energies are not major selection criteria, allowing the use of Lead-acid batteries. The Nickel-Metal Hydride batteries (NiMH) are the other group of electrochemical energy storage technology, used mainly for portable applications (wireless tools) and hybrid electric vehicles. This technology belongs to the group the alkaline nickel batteries. They share the same positive electrode (nickel oxyhydroxide, NiOOH in charged state) but can have different negative electrodes: cadmium, zinc, hydrogen, metal hydride or iron. Nickel-Cadmium batteries (NiCd) have fair specific energy and high discharge rate capability but they are not environmentally friendly (cadmium is high toxic). The NiMH technology provides higher specific energy and absence of toxic components, but the high cost of the rare earth elements which are the important components for negative electrode (for example LaNi<sub>5</sub>) and high self-discharge rate are important drawback.

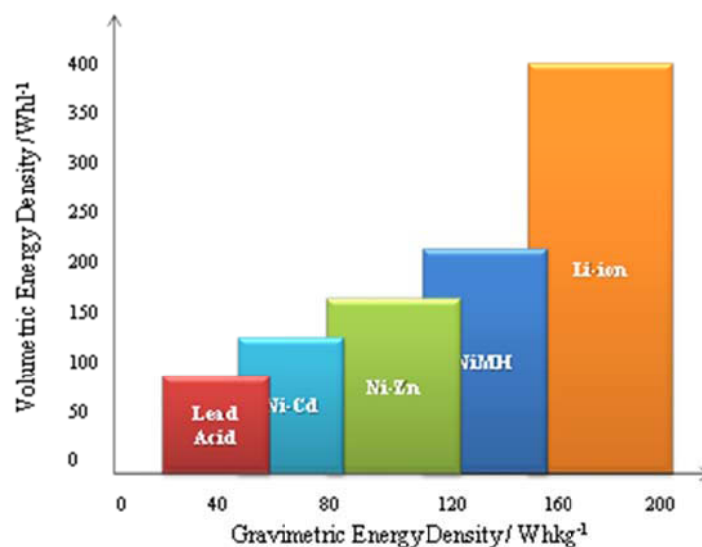






Figure 1: Comparison of varied electrical storage technologies.



The lithium-based technologies offer the highest energy density and very and long cycle life; they have been developing since the past few decades. These batteries have an important role as electrochemical storage systems in portable and autonomous devices, hybrid and electrical vehicles, and in longer term in the renewable energy systems. Some, problems of various natures like: explosion, hazard capacity fade etc., still limit the large scale use of this technology overcharge intolerance.

The electric performance characteristics several batteries types are listed in Table 1 . Note that the power density is strongly dependent from the test conditions and the specificities of the batteries according to the aimed application; it is thus difficult to give a unique value for one technology. It is extremely difficult to give a unique value for the cycling performances due to the fact that the cycling conditions (temperature, Depth of Discharge (DOD), voltage threshold) can affect the number of cycles delivered by the cell before losing 20% of the nominal capacity. The advantage of Li-ion batteries versus other technologies is obvious higher working voltage (around 3.7V or 3.2V according to the electrochemical couples used), high energy density, longer cycle life time, less self-discharge rate etc.

Table 1: Characteristics of various battery technologies [1].

System	Voltage (V)	Specific Energy (Wh.kg <sup>-1</sup> )	Energy density (Wh.L <sup>-1</sup> )	Power density (W.kg <sup>-1</sup> )	Energy cost (€.kWh <sup>-1</sup> )	Advantages	Disadvantage
Sealed lead-Acid							
Global	2	30-40	60-75	/	50-150	Cheaper, widely available	Heavy, limited cycle life
PV (AGM) 12XP73 (Energys) 	2.1 x 6 cells in series = 12V	33 (120h)		213 (CCA)	100		Cycling*: 500 cycles (flat plates), 1500 cycles (tubular plates) for 50%<SoC<100%
Cycling (Gel) HZY-EV12-26 (Haze) 		40 (20h)		90 (25°C, 5min)	120		
Ni-Cd							
Global	1.2	20-60	20-150	/	250-400	Reliable, good low temperature behavior, any charge retention after prolonged discharge	Heavily toxic material, memory effect, High cell self-discharge rate
VRE AA700 (Saft) 	1.2	45 (C/5)	125 (C/5)	>2000 (59C pulse 0.3s up to 0.65Vpc)	/	/	Selfdischarge**: 5%/ month (20°C) 13%/ month (40°C)
Sunica Plus (Saft) 	1.2 x 5 cells in series = 6V	16 (C/5)	24 (C/5)	/	/	Cycling*: 3000 cycles (C/5, 50% DOD, 20°C)	Selfdischarge**: 3% / month (20°C) 4%/ month (40°C)
Ni-MH							
Global	1.2	50-80	90-300	/	300-700	High energy density, environmental friendly	Higher internal resistance, self-discharge
VH AA1700 (Saft)	1.2	78 (C/5)	265 (C/5)	461 (6C pulse >1s up to 0.6Vpc)	/		Cycling : 450 cycles (C/5 discharge, C charge, 20°C, 100% DOD)



							
NHP Module (Saft) 	1.2 x 10 cells in series = 12V	50 (C/5)	90 (C/5)	520 (C/3) 1000 (20C pulse 2s up to 0.8Vpc)	/		Application VH: cycling : 60 000 cycles (C/3, 20% DOD, 20°C)
<b>Li-ion with Li(Ni,Co,Al)O<sub>2</sub>– based positive electrode</b>							
Global	3.6	100-160	160-315	/	800-2000	High specific energy, low self-discharge, voltage profile = f(SOC)	Expensive, requires safety electronics,
MP176065HD  (Saft)	3.6	100	160	/	1900	Self-discharge 0,8% /month (20°C, 100% SOC)	Cycling*: 500 cycles (C/3, 100% DOD)
VL45E (Saft) 	3.6	149	313	664 (30s DOD 50%)	/	Self-discharge 1,6%/ month (20°C, 100% SOC)	Cycling*: DST Cycling : 3250 cycles (80% DOD)
<b>Li-ion with LiFePO<sub>4</sub>– based positive electrode</b>							
Global	3.2	80-120	170-220	/	700-1400	Safe, voltage profile with a plateau between 20%<SOC<90 %	Expensive, requires safety electronics,
ANR26650M1 (A123Systems ) 	3.2	105	217	2250 (10s 50% SOC)	1360		Cycling*: 1000 cycles (5C discharge, 1C charge, 100%DOD)

\* to 80% of initial capacity , 70% for Sunica Plu, 85% for ANR26650M1

\*\* Self-discharge for 100% DOD

## I.2. Applications

### I.2.1. Portable applications

The recent advance in battery technologies can be connected with the growing market of the portable electronic applications. Developments of laptops, mobile phones etc... increased the needs of batteries with higher energy density and longer life. Li-ion batteries

have taken advantages of these portable markets because of its lightweight and good overall performance. Figure 2 shows the repartition in term of applications of the Li-ion sales in the word.

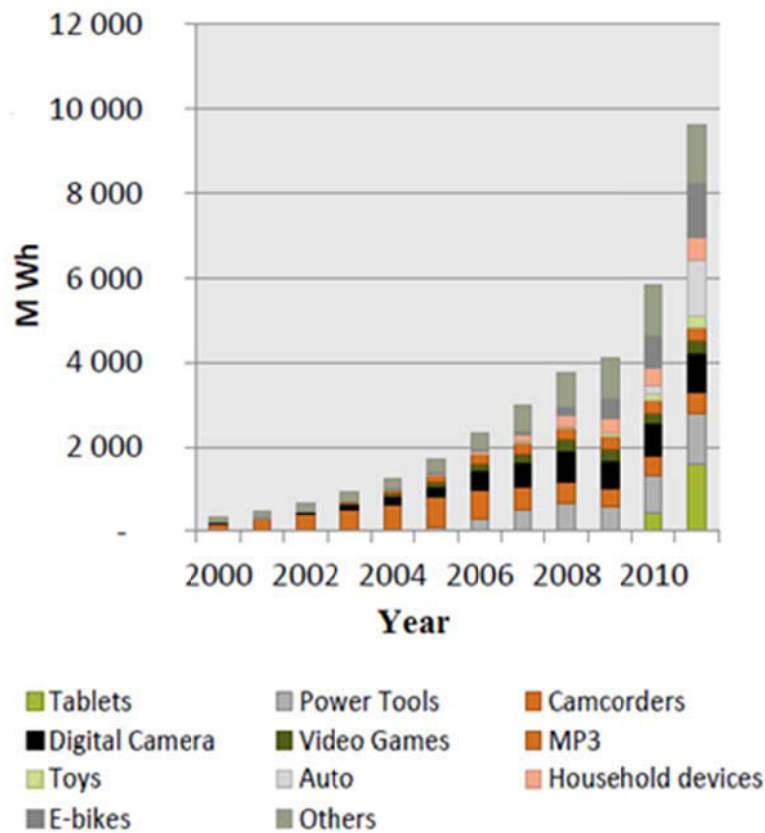


Figure 2: Li-ion Battery sales, M Wh, Worldwide, 2000-2011[3].

The construction of the cell, the pack assembly and the chemistry determines the energy density, the price and the functions. Portable applications typically use “cylindrical”, “prismatic” (inside metallic casing or pouch bag) and “button” or “coin” cells. Several Li-ion technologies have been used in the past up to now, with various types of electrochemical couples. Several years ago lithium batteries with lithium metal negative electrode and different positive electrode:  $\text{Li-TiS}_2$ ,  $\text{Li-NbSe}_2$ ,  $\text{LiMnO}_2$  etc... were used. Due to crucial failures of the lithium electrode (dendrite formation, short cycle life of 100-200 cycles, instability and safety problems), new negative electrode based on carbonaceous materials has been introduced, thus the performances have been improved, leading to longer cycle life and avoiding safety problems connected with dendrite formation keeping the energy density high due to and high operating voltages (between 3.2-3.8V per cell). For example one Li-ion cell can replace three NiCd or NiMH cells in series. Strict control of charge and discharge is

required for safety and long cycle life. Most applications use “smart charger” chips to control the operation of the battery and to predict remaining capacity [4, 5].

### I.2.2. Stationary applications

Li-ion batteries recently attract the interest such as power sources for stationary storage systems: solar, wind storage systems, telecommunication satellites etc... They are very promising energy sources with their high specific energy and long cycle life compared with other battery technologies (Lead-Acid, NiCd, and NiMH). The operation of the Li-ion batteries in high power applications can be limited by the heat generated during the charge and the discharge, due to the Joule effect. This heat has to be dissipated efficiently to prevent thermal runaway. This problem can be solved by thermal management, depending on the power/energy ratio required by the application. The heat generation rate due to the internal resistance can be also minimised by choosing appropriate electrodes and cell design [6]. Electrode materials with low charge transfer resistance of the lithium intercalation and extraction class result in Li-ion cells with lower heat generation during the cycling. For example, combination of  $\text{LiFePO}_4$  positive electrode material and  $\text{Li}_4\text{Ti}_5\text{O}_{12}$  negative electrode materials leads to lower internal heat generation because both electrode materials bear minimum structural change during Li insertion/extraction.

### I.2.3. Electrical Transport Applications

A storage system for transport applications requires high energy density, long cycle life, safety, reliability; the cost and weight are also very important. Figure 3 illustrates the performance requirements for vehicle applications against the specific energy and specific power of the previously described storage technologies. It is obvious that the Li-ion batteries have suitable performances (high energy density, high power density, high discharge rate) for all three applications: HEV (Hybrid Electrical Vehicle), PHEV (Plug-In Electrical Vehicle) and EV (Electric Vehicle) [7].

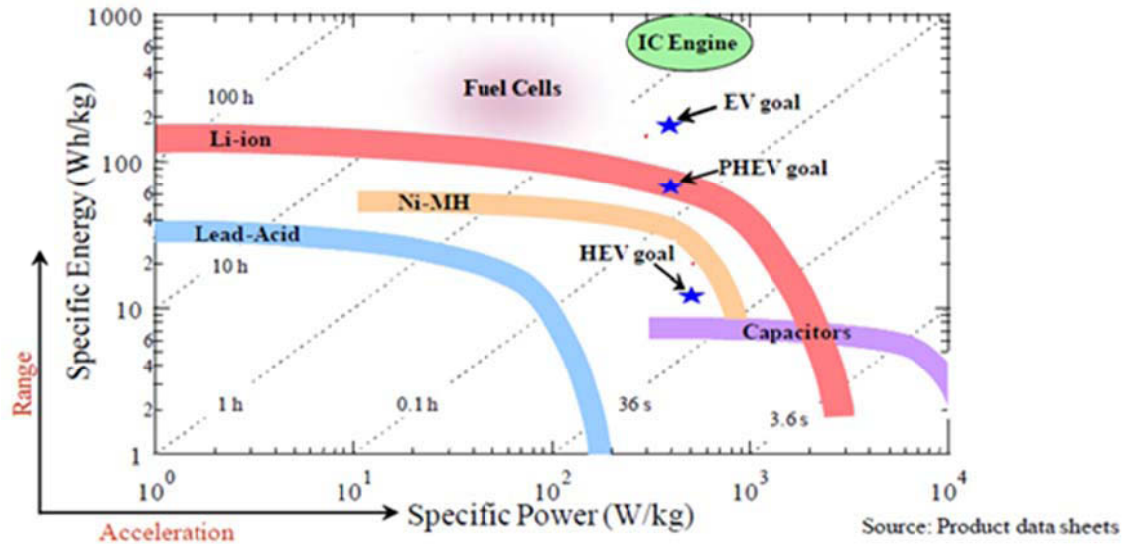


Figure 3: Ragone plot of various electrochemical energy storage and conversion devices and requirements of transport application [7].

HEV, PHEV and EV are differentiated because the requirements in term of specific energy are not the same. Indeed, HEV is based on concept to combining two or more different power sources in a vehicle. The goal is it to make the cars more environmentally friendly by reducing gas emissions. The first power sources (Internal Combustion (IC) engine) provides the main propulsion, the second power source (rechargeable battery) is only used when an additional power boost is needed (during vehicle acceleration) as well as during the regeneration. The battery should provide power on demand, normally in few seconds, and has to be able to be charged at high power rate. The battery operates in a limited domain of state of charge, around 70% allowing the use of NiMH batteries (or possibly NiZn). Due to the weak depth of discharge, their life time is guaranteed. The functioning of PEHV is between that of HEV and EV. In such vehicle, hybrid controller keeps SOC of the battery within 40-80%. Today, small electrical vehicles (fork-lift truck for industry, golf car, and kart for leisure) have still powered by flooded or sealed lead-acid batteries. These two technologies suffer from low energy density, this leads to manufacture vehicles with limited autonomy and speed. For individual electric car transport the Li-ion batteries seems to be unquestionable due to the required specific energy. Li-ion batteries have energy density three to seven times higher, which allows the construction of electrical vehicle with acceptable performances in term of range, speed and acceleration.

The Table 2 gives the respective performances of 200L and 250kg of battery pack according to the storage technology. The interest of the Li-ion is so easily comprehensible.

*Table 2: Comparison of different technologies of batteries used for EV [5].*

Technology	Pb acid	Ni-Cd	Ni-MH	Li-ion
Vehicle curb weight	1200 kg			
Battery volume	200 L			
Battery weight	250 kg			
Energy density	33 Wh/kg	45 Wh/kg	70 Wh/kg	120 Wh/kg
Onboard energy	6,4 kWh	8,8 kWh	13,0 kWh	23,4 kWh
Calculated range 120 Wh/ton/kg	53 km	73 km	114 km	195 km
Volumetric energy (module)	75 Wh/L	80 Wh/L	160 Wh/L	190 Wh/L
Power density (module)	75 W/kg	120 W/kg	170 W/kg	370 W/kg
Battery Power	15 kW	24 kW	33 kW	72 kW

Today the cost of Li-ion batteries it is one of the most important issues for vehicle application. The high cost is mainly attributed to the materials; positive electrode material represents 40-50% of the overall battery cost, and negative about 20-30%. To reduce the price it is necessary to use cost-effective electrode materials: new cheaper materials are developed in that sense. The other technical challenge is to maintain good power performances even in extremely low temperature conditions (during winter). The main limiting factors are the low mobility of  $\text{Li}^+$  in the organic electrolytes and low diffusion rate inside the active materials. These problems can be solved by specific cell construction (by increasing electrode surface, by making the electrodes thinner, by reducing the ionic pathway in the electrolyte) and by choice of selected solvents and electrolytes. The last main issue of the Li-ion batteries for transport applications is the safety. The overcharge/overdischarge protection requires hardware for monitoring of the voltage of each group of cells in parallel to avoid any overcharge/overdischarge situation.

### I.3. Performance and limitations of the Li-ion batteries

Li-ion batteries are cells which employ lithium compounds as positive and negative materials. Under normal operating, any lithium is present in metallic state. During battery in cycling, lithium ionic state ( $\text{Li}^+$ ) is exchanged between the positive and negative electrodes, and the electrolyte. Because the lithium ions rock back and forth between the positive and negative insertion electrodes as the cell is charged and discharged, in the past Li-ion batteries were named “rocking-chair” batteries [8-11].

In a very general way, the electrochemical chain can be written as:

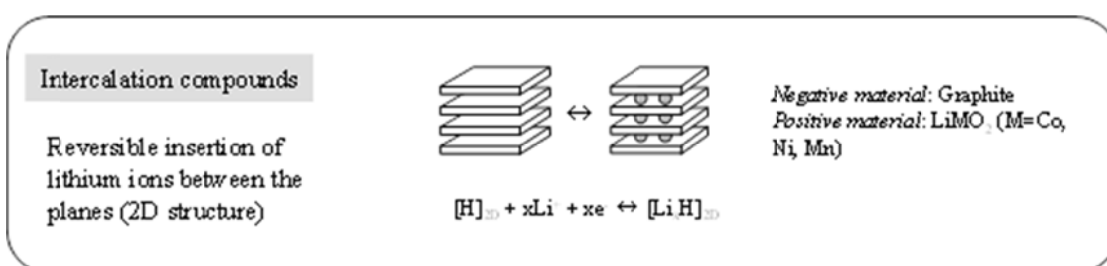


with:  $\text{M}_\text{P}$ : positive material, operating at high potential from +3 to +5V vs.  $\text{Li}^+/\text{Li}$

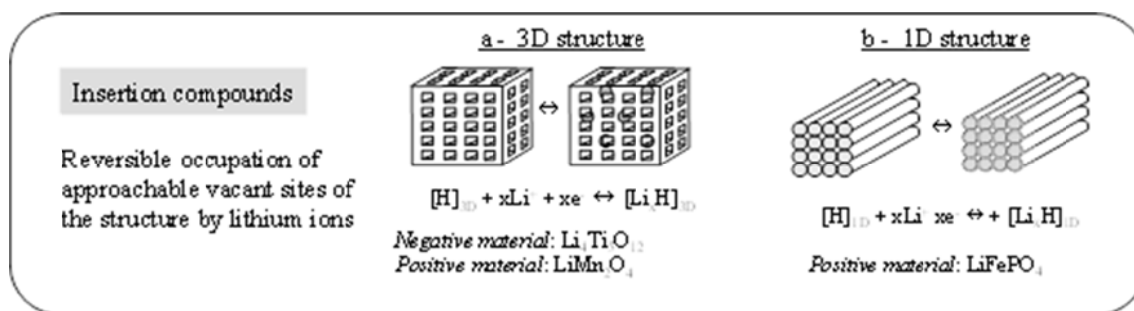
$\text{M}_\text{N}$ : negative material, operating at low potential below + 2 vs.  $\text{Li}^+/\text{Li}$

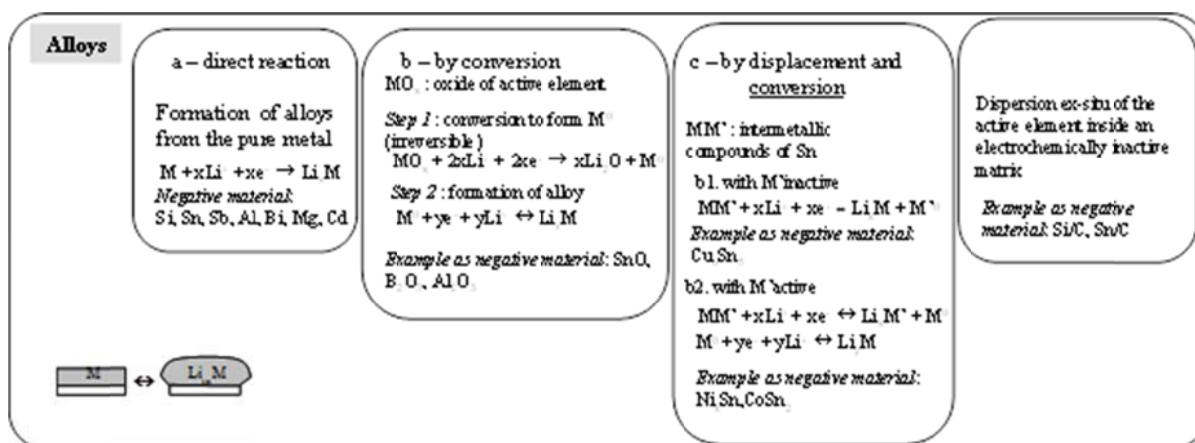
The nature, composition and structure of the lithium compounds employed as active materials are various and can be ranged according to the type of reactions taking place to incorporate the lithium ion:

- Intercalation compounds in according with UPAC in which the reversible insertion of lithium ions is made between the planes or the layers of a 2D structure: graphite,  $\text{LiMO}_2$  (with  $\text{M} = \text{Co}, \text{Ni}, \text{Mn}$ ), according to Rahner [12] and Winter [13]. The drawing below illustrates this type of reaction.



- Insertion compounds in which occurs the reversible occupation by lithium ions of approachable vacant sites of the 3D structure ( $\text{LiMn}_2\text{O}_4$ ,  $\text{Li}_4\text{Ti}_5\text{O}_{12}$ ) or 1D structure ( $\text{LiFePO}_4$ ) as schematized [12, 13].





Whatever is the nature of materials and the type of reaction involved, electrode materials should satisfy a number of requirements, as high free energy of reaction with lithium, incorporation of large quantities of lithium, reversible incorporation of lithium, high lithium ion diffusivity, good electronic conductivity, insolubility in the electrolyte, preparation from inexpensive reagents, low cost synthesis.

The intercalation compounds fill most of its requirements (except large number of lithium incorporation) and today they are the most used compounds. During the charge/discharge process, lithium ions are inserted or extracted from interstitial space between atomic layers or crystalline spaces within the active materials. The active insertion materials in the Li-ion cells operate thus by reversible incorporation of lithium without a significant structural change to the host, guarantying a long cycling life time. That's why they are largely present inside the commercial cells sold in the world contrary to the other types of materials, and also because conversion type materials are more recent. They are still an object of research in order to improve their life time performance, which typically suffers from the cyclic volume expansion that most of them undergo during the reaction with the lithium ions.

The Figure 4 gives the domains of the electrode potential of the materials of electrodes versus the metallic lithium electrode and their respective specific capacity, compared to the lithium which has a theoretical capacity at  $3800 \text{ mAh.g}^{-1}$ , and the most negative electrode potential.



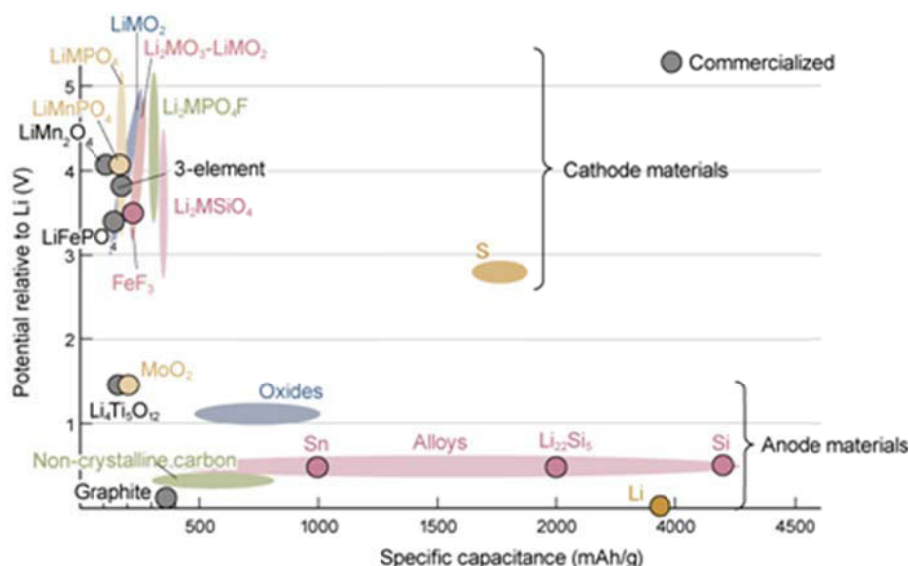


Figure 4: Potentials of negative and positive electrode materials ( $M$  corresponds to transition metals Fe, Co, Ni, Mn) [21].

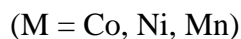
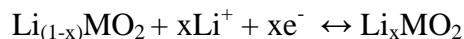
#### I.4. Positive electrode materials for Li-ion batteries

Lithiated layered oxides of transition metals  $\text{Li}_{(1-x)}\text{MO}_2$  (with  $M$  representing one or several metals such as Co, Ni, Mn...) possibly doped with aluminium or manganese, spinel of manganese like  $\text{Li}_{(1-x)}\text{Mn}_2\text{O}_4$  (LMO for lithium manganese oxide) or lithiated iron phosphate  $\text{Li}_{(1-x)}\text{FePO}_4$  (LFP : lithium “fer” phosphate) are generally used as positive material. These materials present a crystallized structure host in mono, bi or three-dimensional diffusion paths into which lithium can be inserted [22, 23].

Historically the first used, and still largely used material is  $\text{Li}_{(1-x)}\text{CoO}_2$  because it has a stable crystalline structure. However this stability is obtained only if the rate of insertion of lithium  $x$  is not higher than  $x=0.5$  ( $\text{Li}_{0.5}\text{CoO}_2$ ). In other terms, in case of overcharge, if more than half of lithium is de-inserted, an irreversible structural modification occurs, making impossible the insertion of lithium during the subsequent discharge: the battery is damaged. This structural modification consists of a collapse of the layered structure with a decrease of the inter-plane distance which does not offer sufficient space to insert lithium. Emission of oxygen occurs jointly. It is the reason for which the charge voltage threshold has to be well controlled at 4.1-4.2V vs.  $\text{Li}^+/\text{Li}$  because above this voltage, the coefficient of lithium de-insertion “ $x$ ” exceeds the limiting value of 0.5. This material has, a theoretical specific capacity, of about 160 mAh/g for  $0.5 > x > 1$  [24]. Regrettably, the cobalt is quite expensive, due to its limited worldwide reserves and its strategic character. It is also toxic element. Furthermore, completely charged and especially if overcharged ( $x \geq 0.5$ ) it becomes unstable at

high temperature, releasing oxygen. The released oxygen reacts with the electrolytic organic solvents with important risks of inflammation or explosion.

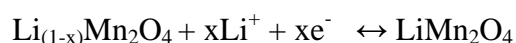
The general electrochemical reaction for these electrodes is:



More recently partial, Co substitution in  $\text{LiCoO}_2$  by Ni, Mn, and Al allowed to compensate the high cost of Co (nickel is another expensive material but less what the cobalt) and the relatively weak thermal stability of  $\text{LiCoO}_2$  [25]. Materials like  $\text{Li}(\text{Ni}_x\text{Co}_y\text{Mn}_z)\text{O}_2$ , named Nickel-Manganese-Cobalt (NMC for the compound  $\text{LiNi}_{1/3}\text{Mn}_{1/3}\text{Co}_{1/3}\text{O}_2$ ) or  $\text{Li}(\text{Ni}_x\text{Co}_y\text{Al}_z)\text{O}_2$ , named Nickel-Cobalt-Aluminium (NCA for the compound  $\text{LiNi}_{0.8}\text{Co}_{0.15}\text{Al}_{0.05}\text{O}_2$ ) were thus developed, with a moderate cost, high specific capacity and a good thermal tolerance. For example, SAFT uses often  $\text{LiNi}_{0.8}\text{Co}_{0.15}\text{Al}_{0.05}\text{O}_2$  for its industrial batteries [22, 26].

In parallel, spinels of the manganese oxide  $\text{Li}_{(1-x)}\text{Mn}_2\text{O}_4$  was developed, where lithium can be de-inserted in a range of voltages between 3 and 4.2V vs.  $\text{Li}^+/\text{Li}$  for a theoretical capacity of 148 mAh/g, comparable to that of  $\text{LiCoO}_2$ .  $\text{Li}_{(1-x)}\text{Mn}_2\text{O}_4$  offers the advantage of a moderate cost and a "low toxicity". Moreover recycling methods are well known because the manganese oxide is also used in the alkaline cells. Nevertheless it was not used for a long time because of its inferior performances in cycling at high temperature (55°C), because of the phenomenon of manganese dissolution. Research allowed solving these inconveniences by a double partial substitution of manganese by aluminium and oxygen by fluorine, coupled with a passivation of the surface. The temperature behaviour of this compound was considerably improved but the manufacturing is more complicated, penalizing the cost [27, 28].

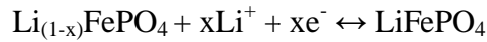
The general electrochemical reaction for this electrode is:



Recently a new alternative of the lithiated metal oxides was introduced commercially. The new positive electrode is constituted by phosphates of transition metals, and more particularly lithiated iron phosphate  $\text{Li}_{(1-x)}\text{FePO}_4$ . Its crystalline structure is isomorphic of that of olivine  $\text{LiMgFeSiO}_4$  and allows the reversible insertion of lithium. For this type of compounds, the

process of synthesis and the surface treatment (coating) have a strong influence on the delivered capacity. Their weak conductivity requires the synthesizing of nano-powders (particles from 20 to 50 nm) with carbon deposits on surface. They are very attractive materials because in spite of a nominal voltage lower than that of the other materials (3,2 - 3,3V against 3,6V vs. graphite for the lithiated cobalt oxide) they are less dangerous in case of abuse conditions [29, 30]. Furthermore, these materials are much less toxic.

The general electrochemical reaction for this electrode is:



The table below gives the theoretical and practical mass capacities of the most current positive materials.

*Table 3: Positive materials [10, 31].*

Material	Theoretical mass capacity (mAh/g)	Practical mass capacity (mAh/g)	Cost
LiCoO <sub>2</sub>	274	150	High
LiNiO <sub>2</sub>	275	220	Intermediate
LiMn <sub>2</sub> O <sub>4</sub>	148	120	Low
LiCo <sub>0,2</sub> Ni <sub>0,8</sub> O <sub>2</sub>	247	180	Intermediate
LiFePO <sub>4</sub>	170	160	Low

The Figure 5 shows the three types of crystalline structures able to host reversible lithium ions. The structures are drawn by binding the atoms to form plans and so to visualize easier the available spaces, the cavities, in which lithium ion is positioned.

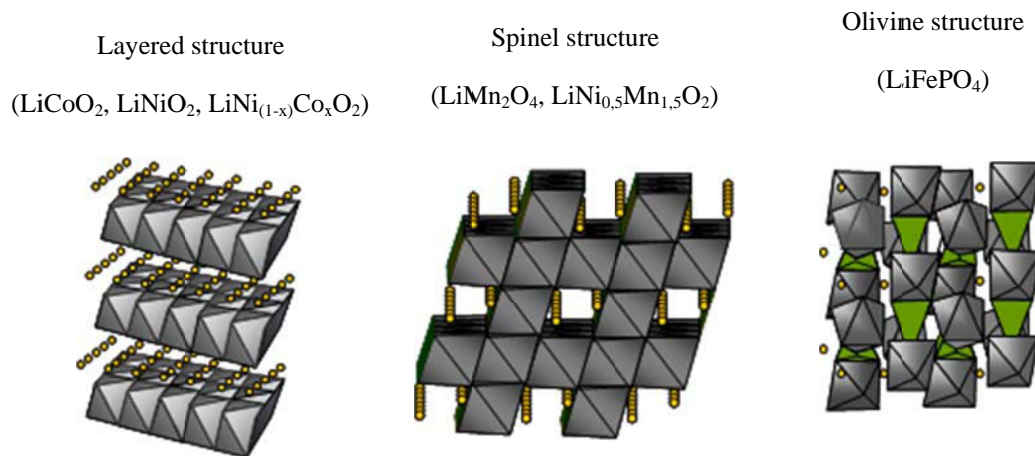


*Figure 5: Type of crystalline structure of insertion materials [23, 26, 27].*

As already explained, these materials present a minimum variation of volume of the crystalline structure when lithiated: the variation of volume can be calculated by taking into account the variation of the crystal lattice parameters: 6.5 % in the case of  $\text{Li}_x\text{FePO}_4$ , 3.8 % in the case of  $\text{Li}_x\text{Ni}_{1/3}\text{Co}_{1/3}\text{Mn}_{1/3}\text{O}_2$  (Table 4) [32]. That guaranties a long cycling life time because the mechanical stress is low.

*Table 4: Volume variation of crystal (a) NMC, (b) LFP.*

(a)  $\text{Li}_x\text{Ni}_{1/3}\text{Co}_{1/3}\text{Mn}_{1/3}\text{O}_2$  (NMC)

	a (Å)	c (Å)	volume (Å <sup>3</sup> )	Volume variation (%)
No Lithiated (x=0)	2.832	13.938	96.8	3.779
Lithiated (x=1)	2.858	14.223	100.6	

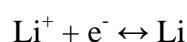
(b)  $\text{Li}_x\text{FePO}_4$  (LFP)

	a (Å)	b (Å)	c (Å)	volume (Å <sup>3</sup> )	Volume variation (%)
No Lithiated (x=0)	5.792	9.821	4.788	272.4	6.5
Lithiated (x=1)	6.008	10.334	4.683	291.3	

## I.5. Negative electrode materials for Li-ion batteries

### I.5.1. Lithium metal

The electrochemical couple  $\text{Li}^+/\text{Li}$  has a standard potential of - 3.04 V vs. SHE what makes it the most negative anode in the nature.



This potential allows reaching in association with a judiciously chosen cathode voltages of cell superior to 3.5 V. However, an important problem appears on the lithium electrode during the recharge process: the electrode deposition of the lithium doesn't result in the formation of a uniform and compact layer, but in the growth of dendrites (Figure 6).

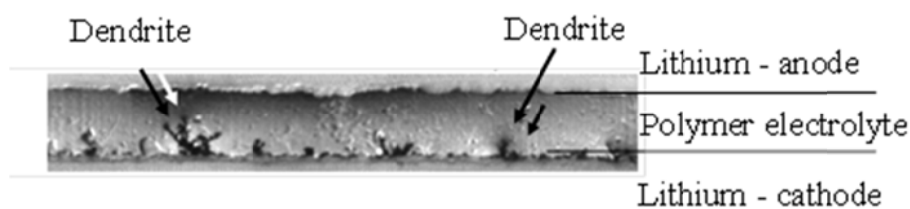


Figure 6: Observation of a dendrite [33].

This phenomenon leads to two fatal consequences:

- At first, the dendritic lithium has a stronger tendency to react with the electrolyte.
- Then, these dendrites grow through the separator and create micro short-circuits. By contacting the cathode, this has the effect to produce heat which can sometimes entail an explosion of the cell.

### I.5.2. Graphite materials

These safety issues and cycling stability of the lithium metal electrodes caused the development of Li-ion cells by using lithium intercalation materials at negative electrode. The choice of the suitable negative material has to obey certain criteria: it has to accept a large number lithium-ion and to have a redox potential as low as possible. Carbons answer one of these criteria and more particularly graphite by the virtue of its low and flat working voltage profile between 0.210 and 0.010 V vs.  $\text{Li}^+/\text{Li}$ . However, its capability is to accept only 1 atom of  $\text{Li}^+$  for 6 atoms of carbon. Its theoretical capacity is consequently limited to 370 mAh/g for  $\text{LiC}_6$ .

The structure of the graphite allows a high reversibility because it is constituted by planes of graphene spaced out by 0.335 nm, which during the insertion of the lithium, increases slightly to a value of 0.370 nm for  $\text{LiC}_6$ . This space remains low enough so that the layered structure of graphite is well preserved. The structure of  $\text{LiC}_6$  is presented below:

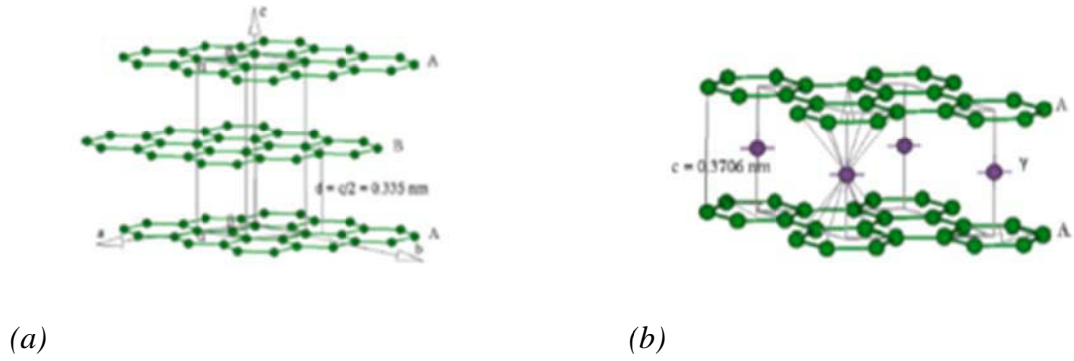
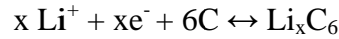


Figure 7 : Crystalline structure of graphite (a) not lithiated (b) lithiated [35].

In fact, the quantity of lithium intercalation depends on the crystallinity of the microstructure (graphitic and non-graphitic), and the micromorphology of the carbonaceous material [34, 35]. A lot of efforts are concentrated on the development of carbon materials with "high capacity". These materials are rather synthesized in low temperatures, from 500°C to 1000°C [36].

Due to electrochemical reduction of the carbon host, lithium ions from the electrolyte penetrate into the carbon and form a lithium/carbon intercalation compound,  $\text{Li}_x\text{C}_6$ . The general electrochemical reaction for this electrode is:



For lithium and other alkali metals, it is usually accepted that an ionic compound is formed while inserting into graphite and the lithium ion do not change its oxidation degree. But the real state of lithium inside graphite is not well known yet. A recent study, of the electronic structure measurement using electron energy loss spectroscopy, showed a metallic character of lithium ion in the compound  $\text{Li}_x\text{C}_6$  [37].

Graphite's offer a good cyclability only in compatible electrolytes for which a protective surface layer can be formed during the first reduction process. Electrolyte is reduced on the surface of the carbon electrode at its operating potential range (around 0.8 and 0.2V vs.  $\text{Li}^+/\text{Li}$ ) leading to the formation of a passivation film called "Solid Electrolyte Interface". The Figure 8 schematizes the formation of this layer.



Figure 8: Mechanism of SEI formation [38].

That layer, when formed, stops the further electrolyte reaction but produce an important irreversible capacity. Despite that, the SEI plays a key role because it prevents the insertion of solvated lithium ions between the planes of the graphene which would provoke the exfoliation of particles by an excessive mechanical stress (volume expansion of the graphite) and consequently a rapid decrease of the capacity of the cell.

During the successive charge and discharge cycles, the structure of graphite is dimensionally stable enough not to damage this passivation layer. In such conditions, the volume variation can be evaluated and corresponds to 11.4% (Table 5).

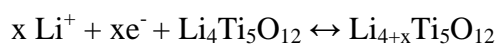
Table 5: Volume variation of graphite [39].

	a (Å)	c (Å)	volume (Å <sup>3</sup> )	Volume variation (%)
Graphite	2.460	3.350	52.670	
LiC <sub>6</sub>	2.485	3.706	59.458	11.4

### I.5.3. Li<sub>4</sub>Ti<sub>5</sub>O<sub>12</sub>

Today, the spinel of lithiated titanium oxide (Li<sub>4</sub>Ti<sub>5</sub>O<sub>12</sub>) or LTO (lithium titanate) appears as an alternative negative material towards graphite. For this material, the insertion of lithium is made in an electrochemical potential superior to the electrochemical potential of deposition of metallic lithium (1.55V vs. Li<sup>+</sup>/Li). It thus accepts high currents of charge without risk to form lithium metal in the interface, contrary in the graphite for which the potential of insertion is close to the potential of reduction of the lithium and the charge transfer reduced by the SEI [40, 41].

The general electrochemical reaction for this electrode is:



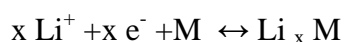
LTO, with a spinel crystalline structure, appears to be a performing material for negative electrode (high chemical and thermal stability, not toxicity, high electrochemical efficiency). Due to its high potential of lithium insertion and its three-dimensional structure, it gives good results in term of cycling (life time), safety and fast charge acceptance. Besides, the chemistry of titanium allows the realization of a whole range of morphologies (texture, size) of  $\text{Li}_4\text{Ti}_5\text{O}_{12}$ , in particular within a nanometre size, often mentioned in the literature [42]. Such modifications can allow a fast insertion / de-insertion, thus a use for power applications. The theoretical mass capacity of  $\text{Li}_4\text{Ti}_5\text{O}_{12}$  is comparable to the positive materials (175 mAh/g) but in practice is lower (67 mAh/g). This compound is however promising for the HEV due to its capability to be quickly charged. A lot of studies are dedicated to the validation of its performances on the long term. The table below gives the theoretical and practical mass capacities of the most current negative insertion materials.

*Table 6 Negative insertion materials [43]*

Material	Theoretical mass capacity (mAh/g)	Practical mass capacity (mAh/g)	Cost
Graphites	372	350	Intermediate
Cokes	372	300	Weak
$\text{Li}_4\text{Ti}_5\text{O}_{12}$	175	67	High

#### I.5.4. Metallic alloys – direct reaction

The utilization of metals and alloys as negative electrode materials is based on reversible reaction with lithium in the metal/alloy which acts as a host for the lithium in the alloy. Examples of binary alloys for rechargeable lithium batteries are:  $\text{LiAl}$ ,  $\text{Li}_{4.4}\text{Si}$ ,  $\text{Li}_{4.4}\text{Sn}$ ,  $\text{Li}_4\text{Sb}$ ,  $\text{Li}_4\text{Bi}$ ,  $\text{Li}_3\text{Cd}$ . Chemical corrosion of these electrodes is less pronounced, though not completely avoided. This is partly because the alloys are less reactive and partly because a protective surface film is formed on the electrode [44, 45]. The electrochemical reaction at these electrodes can be expressed as:





With some exceptions ( $M=Ti, Ni, Mo, Nb, Al$ ), Li alloys are formed at ambient temperature by polarizing the metal  $M$  at sufficiently negative potential in a  $Li^+$  containing electrolyte. The result is the formation of complex binary systems  $Li-M$ . The metal matrix undergoes major structural changes while alloying with lithium (Figure 9).

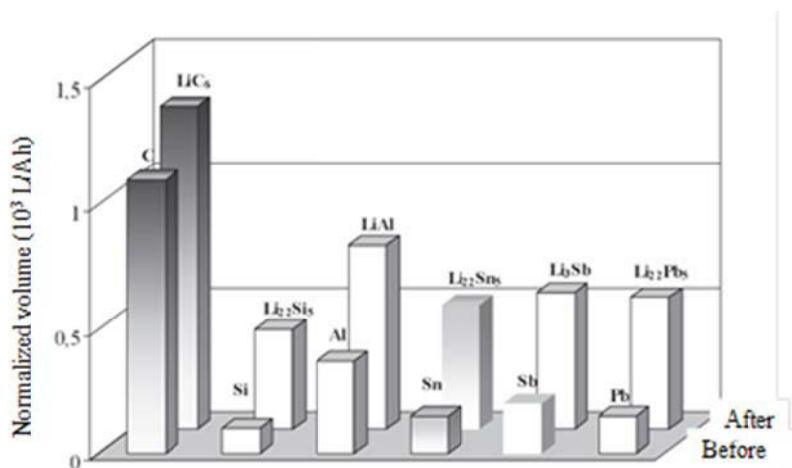


Figure 9: Volume expansion of alloys comparatively to graphite [45].

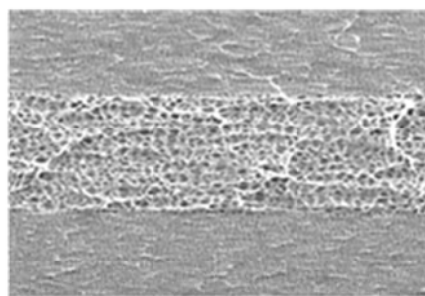
Lithium alloys  $Li_xM$  are of highly ionic character and for this reason they are usually fairly brittle. Thus the mechanical stress related to the volume changes induces a rapid decay in mechanical properties and finally a “pulverization” of the electrode appears [46, 47]. But many ways exist to buffer or limit the consequence of volume expansion. Several alloys may provide hundred cycles.

## 1.6. Separators

The membrane between both electrodes is a mono or multilayer microporous polyethylene (PP) and polypropylene (PE) sheet. It electrically isolates the electrodes. An example of a three layer separator from Celgard is shown in Figure 10. The requirements of security for large cells call for this last type of separators which leads to an effect of “shutdown”. In case of abnormal increase of temperature, polyethylene which has a low melting point, melts towards  $110^{\circ}C$ , chokes the porosity increasing considerably the resistance of the cell and acts as a “chemical circuit breaker”. The polypropylene, more stable at higher temperature, maintains the physical separation between the electrodes. Once the pores of the separator are closed, the cell does not deliver nor can receive any more electricity. The separator plays thus an important role for safety characteristics of the cell.



*Microporous separators*



*SEM image of a three layer PP/PE/PP  
Celgard separator*

*Figure 10 : Example of microporous separators [48].*

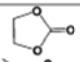
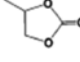
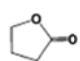
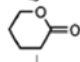
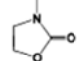
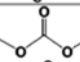
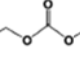
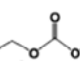
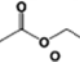
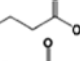
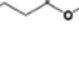
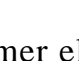
## **I.7. Electrolytes**

Four types of electrolytes have been used in Li ion batteries: liquid electrolytes, gelled or plastified electrolytes, ionic liquids and ceramic electrolytes. The last type will not be discussed due to its specific applications.

### **I.7.1. Liquid electrolyte**

Liquid electrolyte is a solution of lithium salt ( $\text{LiPF}_6$ ,  $\text{LiBF}_4$ ,  $\text{LiN}(\text{SO}_2\text{CF}_3)_2$  or  $\text{LiTFSI}$ ,  $\text{LiN}(\text{SO}_2\text{C}_2\text{F}_5)_2$  or  $\text{BETI}$ ) in a mixture of organic solvents, typically alkyl carbonates or ethers (Table 7). Today, the electrolyte present in the commercial cells is constituted by a mixture of ethylene carbonate (EC) and dimethyl carbonate (DMC) with  $\text{LiPF}_6$ . Some SEI precursors like VC (vinylene carbonate) could be added. The lithium salts have to offer stability, good safety properties and compatibility with electrode materials.  $\text{LiClO}_4$  is not used today due to the fact that perchlorates can be formed and these compounds are explosive. The most popular salt for liquid electrolyte is  $\text{LiPF}_6$ . Its solution has high conductivity and good safety properties. The salts as  $\text{BETI}$  are more stable in water than  $\text{LiPF}_6$ , offer high conductivity and do not cause aluminium corrosion. They are thus more and more used for liquid and polymer electrolytes.

Table 7: Major solvents used for non-aqueous liquid electrolyte [49].

Solvent	Structure	M. Wt	T <sub>m</sub> / °C	T <sub>b</sub> / °C	η/cP 25 °C	ε 25 °C	Dipole Moment/debye	T <sub>f</sub> / °C	d/gcm <sup>-3</sup> , 25 °C
EC		88	36.4	248	1.90, (40 °C)	89.78	4.61	160	1.321
PC		102	-48.8	242	2.53	64.92	4.81	132	1.200
BC		116	-53	240	3.2	53	4.23	97	1.199
γBL		86	-43.5	204	1.73	39	4.29	81	1.057
γVL		100	-31	208	2.0	34	4.52	110	1.17
NMO		101	15	270	2.5	78			
DMC		90	4.6	91	0.59 (20 °C)	3.107	0.76	18	1.063
DEC		118	-74.3 <sup>a</sup>	126	0.75	2.805	0.96	31	0.969
EMC		104	-53	110	0.65	2.958	0.89		1.006
EA		88	-84	77	0.45	6.02		-3	0.902
MB		102	-84	102	0.6			11	0.898
EB		116	-93	120	0.71			19	0.878

### I.7.2. Polymer electrolyte

The principle of realization of a polymer electrolyte was presented in the middle of the 1970s. It is based on the ability of a polymer to possess two main properties:

- A strong affinity towards the liquid electrolyte to assure the formation of a gelled polymer having a high ionic conductivity (interactions polymer/solvent favoured). Polymers mostly used for gel electrolyte are polyethylene oxide (PEO), polyacrylonitrile (PAN) and methyl polymethacrylate (PMMA).
- A good mechanical behaviour, allowing to the film to play at the same time the role of physical separator between both electrodes and electrolytic matrix soaked by the electrolyte (interactions polymer/polymer favoured). In that case, only some molecules of solvents fit between the macromolecular chains. These films are said "plasticized", and the principal is illustrated in Figure 11. They are constituted by fluoride polymers with vinylidene polyfluoride (PVDF) or polystyrene (PS) and mineral additives which can swell in contact with the liquid electrolyte [50].

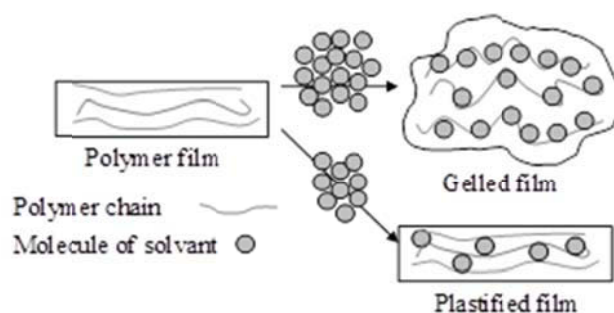


Figure 11 : Schematic representation of a gelled and plastified polymer.

### I.7.3. Ionic liquids

Because organic electrolytes present two inconveniences: low ionic conductivity (10 mS/cm) and strong flammability, new electrolytes were proposed, constituted by cations and by anions from the dissociation of organic salts. They have very low melting points, thus liquid at room temperature and have good ionic conductivities. These types of electrolytes contain cations as  $\text{EMI}^+$  (ethyl-methyl imidazolium) or  $\text{BMI}^+$  (butyl-methyl imidazolium) and anions as  $\text{BF}_4^-$  (tetrafluoroborate) or  $\text{PF}_6^-$  (hexafluorophosphate). The main advantages of these compounds are a high thermal stability, according to the electrolyte, between  $90^\circ\text{C}$  and  $400^\circ\text{C}$ , a wide window of electrochemical stability (5V) as well as ability to be gelled by polymers (polyvinylidene fluorure PVDF) and a low pressure of saturated vapour at room temperature. However, these electrolytes can be used in a Li-ion battery only if they contain a lithium salt. For that purpose, it is necessary to have lithium salt which is strongly soluble in the electrolyte. Today, these salts are expensive. The use of ionic liquids as electrolyte can be made only by the development of new and less expensive salts, produced by aqueous synthesis for example [51].

## **I.8. Collector**

Metallic foils are used as current collectors. The collector can be aluminium (which is a very good conductor) for all the positive electrodes and those with  $\text{Li}_4\text{Ti}_5\text{O}_{12}$ . They can be made of copper (which has also a very good conductivity) for graphite or silicon electrodes. Copper can be used only if the voltage is lower than 3.2V vs.  $\text{Li}^+/\text{Li}$  because copper oxidizes

over this value, also aluminium can't be used if the voltage is lower than 0.7V vs.  $\text{Li}^+/\text{Li}$  because aluminium inserts lithium below this value [52].



*Figure 12 : Copper and aluminium foil*

## I.9. Summary of the function of the internal components of a cell

The Table 8 summarizes the different components of Li-ion cell and their principal functions and failures.

*Table 8: Functions and failures of the components*

Elements	Functions	Failures
Positive collector	<ul style="list-style-type: none"> <li>• Collect the current</li> <li>• Support the positive active mass</li> </ul>	<ul style="list-style-type: none"> <li>• Corrosion</li> <li>• Loss of electronic contact</li> </ul>
Positive electrode	<ul style="list-style-type: none"> <li>• Reversibly incorporate lithium ions</li> <li>• High lithium ion diffusivity</li> <li>• Good electronic conductivity</li> </ul>	<ul style="list-style-type: none"> <li>• Capacity loss in higher temperature (thermal degradation)</li> </ul>
Separator	<ul style="list-style-type: none"> <li>• Electrically isolate positive and negative electrodes</li> <li>• Chemically inert in contact with electrolyte</li> </ul>	<ul style="list-style-type: none"> <li>• Degradation after ageing</li> <li>• Shutdown of the cell in abuse thermal condition</li> </ul>
Electrolyte	<ul style="list-style-type: none"> <li>• Transport the anions and cations</li> <li>• Decompose (solvents and salt) to form the SEI</li> </ul>	<ul style="list-style-type: none"> <li>• Loss of ionic conductivity</li> <li>• Instability in high temperature</li> </ul>
Negative electrode	<ul style="list-style-type: none"> <li>• Reversibly incorporate lithium ions</li> <li>• Must be covered by the passivation film to guarantee a good stability of the electrode during the time</li> </ul>	<ul style="list-style-type: none"> <li>• Destruction of SEI under abuse condition : reaction between electrolyte and lithiated graphite no more protected by the SEI</li> <li>• Capacity loss based of bad formation of the SEI</li> </ul>
Negative collector	<ul style="list-style-type: none"> <li>• Collect the current</li> <li>• Support the negative active mass</li> </ul>	<ul style="list-style-type: none"> <li>• Loss the electronic contact</li> </ul>

## I.10. Behavior of Li-ion cell under abusive conditions

The Li-ion batteries are rapidly growing market providing energy storage solutions for many industries like the electronics industry, reserve power systems, electrical vehicles etc... Despite the many advantages making this technology highly attractive, the relatively high safety risk, compared to the other traditional power sources as lead acid and metal hydrides batteries, limits the further faster increase of this market.

The Li-ion batteries have a different chemistry (more complex) in comparison with the other power sources; both the positive and the negative electrodes serve as host structures for charge carrying species (lithium ions). The consequences of a failure event tend to be more severe compared to the other rechargeable chemistries for two reasons. First, there is more energy stored in Lithium cell as compared the cells of the other chemistries, therefore more heat can be generated by the chemical reaction between the electrodes. Second, the Li-ion cells use flammable organic solvents as electrolytes rather than water-based electrolytes. If those electrolytes are released into the air, they can generate explosive atmosphere mixtures. This combination of high energy density and flammable electrolyte makes the safety issue of the Li-ion energy storage systems [53].

Commercially Li-ion battery has an operating voltage range from 1.5V up to 4.4V depending on the used material. Charging or discharging batteries with voltage exceeding the recommended voltage range can lead to safety hazards. Applying higher voltage than the rated one can initiate reaction leading to thermal runaway. The possible consequences from a thermal runaway are presented in Figure 13.

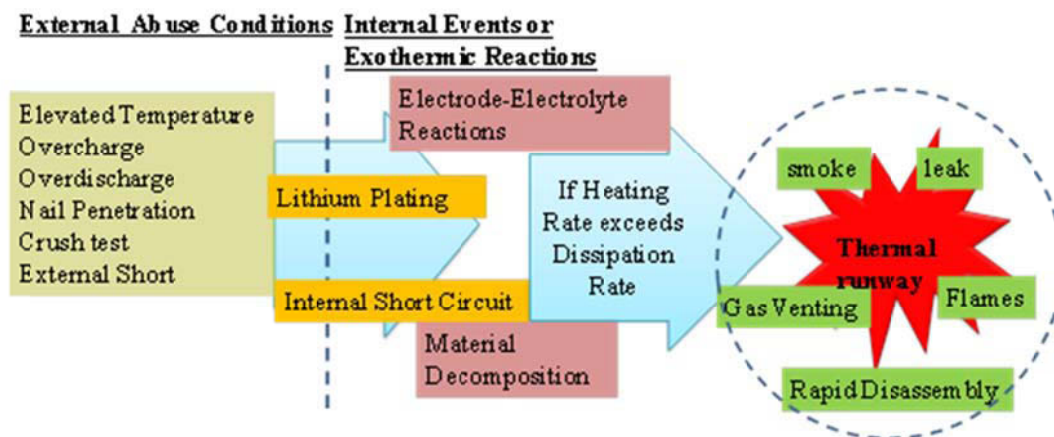


Figure 13: Possible consequences from thermal runaway [54].

Once the voltage reaches its upper limit (the cell is fully charged); the positive electrode is depleted of  $\text{Li}^+$ . If the cell is charged further the lack of  $\text{Li}^+$  in the positive electrode results in an increase of its potential and a start of processes of oxidation of the electrolyte or active materials components. The oxidation products are usually highly reactive and cause the appearance of exothermic reactions in the cell. As the cell internal temperature rises, the electrolyte starts to decompose and generate more heat. When temperature reaches approximately  $135^\circ\text{C}$  the separator pores start closing and this inhibits the movement of the ions between electrodes. The pores can be closed completely terminating the charge current, and causing the cell shut-down. However if the exothermic reaction continues the cell eventually goes to thermal runaway looped between the electrolyte, positive and negative electrode. Reactions causing thermal runaway are: SEI decomposition, reactions between positive and negative electrode material and the electrolyte. The positive electrode structure may further collapse in consequence of the complete delithiation [55, 56].

If the cell voltage drops below the lower voltage limits the negative electrodes are depleted of  $\text{Li}^+$ . If the cell continues to be discharged, the oxidation of the copper current collector starts. This process leads to the dissolution of the copper into electrolyte. As the over-discharged cell is recharged, the dissolved copper redeposit in regions of the cell capable of reducing it back to copper metal. This process can reduce the cell performance, blocking the access to the electrode material or blocking the pores of the separator. The overcharge of the negative electrode beyond the interaction limit of the graphite (for example) results in the start of the electrodeposition of metallic Li in the form of dendrites. If the Li-ion cell is overcharged frequently, dendrite growing formation may start to occur between positive and negative electrode, leading eventually to internal short circuits, or full exfoliation of the graphite negative electrode [57, 58]. Safety cannot be determined or evaluated by only one criterion or parameter at least several approaches should be applied.

Batteries and battery materials can be safety characterized and optimized by various techniques as an electrochemical characterization, thermal characterization, physical damage etc... These techniques evaluate the response of materials, electrode formulation, cell constructions and battery assembly under a variety of “of-normal” conditions that simulate abusive events such as mechanical, electrical and thermal stress. Characterization of cells provides an information on safety and abuse tolerance of a given cell chemistry. Further the battery pack have other failure mechanisms such as inter-cell shorting, inter-cell charging, and cell imbalance that can lead to overcharge or overdischarge of one cell or a group of cells [59].

### **I.10.1.1. Electric Abuse Tests**

The electric abuse characterization can be provided by controlled overcharge, overdischarge and short circuit of rechargeable batteries. The ability of the battery to tolerate overcharge depends on several parameters: battery resistance, current rate, maximum voltage and chemistry of the active materials and the electrolyte.

### **I.10.1.2. Thermal Abuse Tests**

Thermal characterization of the batteries and batteries material as materials for positive and negative electrodes, electrolytes, separators etc...are one of the important aspects of safety. During normal operation of the Li-ion batteries, chemical, electrochemical and reaction of mass transfer take place; it is known that many of these reactions are affected by the temperature, according to the scheme presented previously in Figure 13.

- The Differential Scanning Calorimetry (DSC) and Thermal-Gravimetric Analysis (TGA) are analytical techniques used to study the thermal abuse on battery materials. These techniques allow evaluating the thermal response of cell components (electrolytes, active materials, etc...) over a wide temperature range while scanning at a fixed temperature rate. The obtained information permits the identification of the components participating in the thermal activity. The DSC and TGA methods allow the quantitative measurement of the effect of the temperature at a fixed state of charge of the electrodes. DSC and TGA technique are limited to small sample size, but results about the chemical reactive studies can be effectively applied in the evolution of the temperature stability of the cell [60].
- Calorimetric technique used to study the thermal behavior of batteries is the Accelerating Rate Calorimetry (ARC). The tests in this method are run under adiabatic conditions (those conditions allows the precise control of the heat exchange between the cell and its environment). Under adiabatic condition the cell heating rate is a function of the heat generating reaction rate and the thermal heat capacity of the cell components. The cell heating starts very slowly and increases through a series of accelerating stages until a final high-over thermal runaway. Because of the adiabatic environment, the beginning of the self-heating due to the chemical reactions in the interior of the cell can be detected with high sensitivity [61].



The thermal stability can be studied by Thermal Ramp Test. In this test cell is heated with linear increase of the  $T^{\circ} \approx 5^{\circ}\text{C}/\text{min}$  from room temperature up to  $250^{\circ}\text{C}$  or until the cell fails by thermal runaway [59, 62].

#### **I.10.1.3. Mechanical Abuse Tests**

The Mechanical Abuse Tests include penetration tests, drip tests, controlled crushing and shocks. All these tests cause physical damage of the cell or pack accompaniments of the deformation, force of displacement, of the voltage before, during and after the test, internal and external temperature monitoring and chemical analysis of vented gas and smoke [59, 62, 63].

### **I.11. Battery Management System**

The basic task of Battery Management System is to ensure that optimum use is made of the energy inside the battery powering the portable product and that the risk of damage inflicted upon the battery is minimized. This is achieved by monitoring and controlling the battery's charging and discharging process. Li-ion battery has become the most widely used chargeable battery because of its advantages, such as higher voltage level, higher energy density, no memory effects and no pollution to the environment

Li-ion battery packs of multi cells in series or parallel provide a high-voltage power supply; have become more and more useful in many applications an example hybrid electric vehicle, electrical vehicle electro motors, photovoltaic systems etc. For more powerful voltage, the cell number is increased and the voltage rises as well. Battery management for battery packs composed of multi cells is quite different from single cell applications, and thus challenges arise. The information of each battery must be acquired and processed to ensure the safety operation of every single cell and improve performance of the whole battery pack. Estimation on state of charge (SOC) and monitoring the battery characteristics have always been important parts in battery management research. High performance battery management system (BMS) is able to allow the cell work in the best performance. BMS can improve the battery's performance and extent its working life through the real-time battery state monitoring and battery SOC estimation [64].

The BMS system has a function to monitor the batteries, to protect, estimate the battery state, to maximize their performance. BMS system should do the following task: prevent the voltage of any cell from exceeding a limit, by stopping the charging current for

example. This is the safety issue for all Li-ion cells. Prevent the cell for increasing temperature by stop the current directly and requesting cooling. The exceeding temperature can bring the batteries to the thermal runaway process.

Keep from drooping of cell voltage below the limit. Limited the charging and discharging current. BMS can balance the battery to maximize its capacity [65]

The BMS may provide different functions in order to control a cell, module or a complete pack.

- Charge and Discharge Voltage control;
- Control of the Charge and the Discharge Current;
- Monitoring of the SOC;
- Monitoring of the SOH;
- Monitoring of State of Function (SOF);
- Monitoring and Control of the Temperature.

#### I.11.1. Voltage control

The BMS monitors the cell voltage and controls the charge and discharge current in such a manner that this voltage remains in the recommended limits. In this way the battery overcharge or over-discharge are prevented [66].

#### I.11.2. Current control

The charge and discharge of Li-ion cells with currents higher than the recommended ones leads to rapid degradation in terms of energy storage capacity and power delivery. The higher currents increase the cell internal temperature from one hand and exert an additional stress on the active materials from the other. A main function of the BMS is to control the magnitude of the charge and discharge (if possible) current and thus providing longest possible time of battery exploitation [67].

#### I.11.3. State of Charge (SOC) estimation and monitoring

The SOC (state of charge) is the percentage ratio between residual discharge capacity ( $C_{res}$ ) and discharge capacity obtained after complete recharge ( $C_F$ , full capacity):

$$SOC_{discharge} = \frac{C_F - C_{res}}{C_F} \cdot 100$$

When a completely discharged the battery is recharged SOC is expressed by the ratio between the injected charge ( $Q_{ch}$ ) and  $C_F$ :

$$SOC_{charge} = \frac{Q_{ch}}{C_F} \cdot 100$$

Often, instead of SOC, the remaining charge in the cell is expressed by the Depth of Discharge (DOD), i.e. how much of the total available battery capacity is used during the discharge:

$$DOD = 100 - SOC$$

Using the above definitions, the State of Charge can be estimated and monitored by the so-called Ah integration or Ah balancing. In this method the current through the cell  $I(t)$ , positive during the charge and negative during the discharge, is continuously integrated and the SOC is calculated by the following formula:

$$SOC(t) = SOC_{initial} + \frac{100}{C_F} \int_0^t I(t) dt$$

In order to have precise SOC estimation in time, the BMS should be provided by an initial value  $SOC_{initial}$ . Typically such a value is available after complete recharge ( $SOC_{initial} = 100\%$ ), complete discharge ( $SOC_{initial} = 0\%$ ) or by some complementary method of SOC estimation.

Another way to estimate the State of Charge of a Li-ion cell is to use the relationship between the cell electromotive force (EMF) and the State of Charge. Usually instead of EMF one uses the cell open circuit voltage after sufficiently long period of relaxation. In the case of the Li-ion cells the different SOC values are associated with different Li intercalation compounds and corresponding phase equilibria. The latter define different electrode potentials and corresponding EMF values. In some cases like Co-based positive materials combined with hard carbon negative materials this approach provides very accurate SOC estimation due to close to linear relationship between EMF and SOC within 1500-2000mV range. In other cases like graphite / lithium iron phosphate cells this approach is not efficient due to the very “flat” OCV vs. SOC dependence in the SOC range from 10-15 to 85-90%.

More sophisticated SOC monitoring can be done using voltage/current/temperature/SOC look-up tables where SOC is derived by comparison of the actual battery voltage and current values with corresponding values of voltage, current and SOC stored in the memory of the BMS.

#### I.11.4. State of Health (SOH)

In applications relying on the energy delivery the State of Health typically is defined as the percentage ratio between the actual battery discharge capacity obtained after complete recharge ( $C_F$ ) and the battery nominal capacity ( $C_n$ ):

$$SOH = \frac{C_F}{C_n} \cdot 100$$

In this case the best and the most simple way to estimate SOH is to subject the battery to the so-called “check-up” cycle where the battery is charged and discharged one or several times at standard conditions (temperature, charge and discharge current values, open circuit stay duration etc...) using the corresponding equipment (battery or pack cycling test bench).

In applications using the battery for power delivery like engine cranking, SOH is defined using the battery internal resistance in a similar way:

$$SOH = \frac{R_{\max} - R_f}{R_{\max}} \cdot 100$$

Where  $R_F$  is the battery internal resistance after a complete recharge and  $R_{\max}$  is the maximally tolerated internal resistance of the battery. This type of SOH diagnostics is much faster and cheaper but it is relevant only on the power delivery of the battery.

The State of Health depends on many factors – number of cycles (or number of equivalent cycles), the temperature, the current of charge and discharge as well as the time and average SOC range of operation [1, 68]

#### I.11.5. Thermal management

During the battery charge and discharge certain amount of electric energy is transformed into Joule heat throughout the battery internal and charge transfer resistance. The result is an increase of the battery temperature. Additionally the battery can be subjected to heating from the nearby power electronics (chargers, invertors, convertors etc...) or to cooling in the case of outdoor applications. For most of the available Li-ion technologies the longest

cycle life is achieved in the temperature range 15-35°C. The aim of the thermal management is to keep the battery temperature as close as possible to this recommended temperature range. The battery cooling is achieved in different ways depending on the severity of the application: passive cooling using specifically engineered pack, casing design for low power applications, air fan cooling for moderate power applications or liquid cooling circuits for high power applications.

Most of the Li-ion systems exhibits relatively low temperature stability point – typically between 75 and 90°C depending on the particular technology. A main function of the thermal management (and the battery management too) is to prevent reaching this threshold. Else way in the pack the thermal runaway starts and it may lead to fire, explosion and toxic gas hazards.

#### I.11.6. Integration of Acoustic emission detection in the Battery Management System

The acoustic emission detection is carried out typically by piezo-electric sensors which can be very compact, thus suitable for integration into a Li-ion battery modules and packs. The signal provided by the acoustic emission sensors can be used by the Batter Management System in several ways:

- An acoustic emission resulting from phase transitions in the active materials during the battery cycling can be associated with changes in the battery State of Charge;
- Battery degradation phenomena like corrosion or growth of the SEI can be detected also by acoustic emission providing new ways for State of Health monitoring;
- Abnormal battery operation like overcharge and the corresponding electrolyte decomposition to gaseous products can be detected too by AE thus extending this method towards the battery State of Security monitoring.

## **I.12. Conclusion**

This chapter presents the working principal of the Li-ion batteries. Li-ion batteries are promising energy storage systems for Hybrid and Electric Vehicles. They have high energy density and long cycle life; however their safe operation is still an issue. Moreover, during the cycling, most of the materials degrade resulting in capacity fade. The reason for the capacity loss can be the active materials volume expansion during the intercalation process, the modification of the composition of the passivation film on the negative electrode, the electrochemical instability of the materials or the degradation of the positive electrode. Under some extreme conditions as overcharge or exposure to high temperature, the battery degradation can be very fast and the process is usually denoted as “thermal runaway”. Since the last phenomenon is a substantial hazard to the electric and hybrid vehicle users and the environment, it is important to develop methods and strategies for its prevention. These normal or abusive internal phenomena should be identified and detected as early as possible in order to evaluate the state of health and the state of security of the battery. The aim of this chapter is to propose innovating battery management systems (BMS).

## References

1. Bergveld H.J., Danilov D., Pop V., “*Encyclopedia of Electrochemical power Sources*”, Vol. N°1, (2009), 459-477.
2. Yang Z., H.J., Zhang J., Kinter-Meyer C.W., Lu X., “*Chemical Reviews*”, Vol. N°111 (5), (2011), 3577-3613.
3. Pillot C. in “*The worldwide battery market 2011-2015*”, Conference Batteries 2012, October 24-26, Nice France.
4. Brodd R.J., “*The Electrochemical Society Interface*”, (1999), 20-23.
5. Broussely M. in “*Lithium Batteries Science and Technology*”, (Nazri G–A, Pistoia G., Eds.), Chapter N°21, Springer (2009), 645-684.
6. Manthiram A., “*Journal of Phys. Chem. Lett.*”, 2, (2011), 176-184.
7. Srinivasan V., “*Academic Journal - AIP Conference Proceeding*”, 1044 N°1, (2008), 283.
8. Grant M.E. in “*Handbook of Batteries*”, (Linden D., Reddy T.B. Eds.), Chapter N°35, McGraw-Hill (2001), 35.1-35.94
9. Miomandre F., Sadki S., Audebert P. in “*Electrochimie Des concepts aux applications*”, (Amatore C. Eds.), Chapter N°11, DUNOD, 205-224.
10. Doublet M.-L. in “*Techniques de l'Ingénieur*”, Reference AF6612.
11. Robert J., Alzieu J. in “*Techniques de l'Ingénieur*”, Reference D3354.
12. Rahner D., Machill S., “*Solid State Ionics.*”, 86-88, (1996), 891-896.
13. Winter M., Besenhard J.O., “*Advance Materials*”, 10, (1998), 725-763.
14. <http://goldbook.iupac.org/103077.html>
15. Shukla A. K., Kumar T.P., “*Current Science*”, Vol. 94, N°3, (2008), 314-331.
16. Armand M., Tarascon J.-M., “*Nature*”, Vol. 451, N°7, (2008), 652-657.
17. Taberna P.L., Mitra S., Poizot P., “*Nature Materials*”, Vol. 5, (2006), 567-573.
18. Dudezert C., “*PhD.Thesis*”, from “L'Universite Paris Sud”, (2009), 1-42.
19. Zhang W.-J., “*Journal of Power Sources*”, 196, (2011), 877-885.
20. Besenhard J.O., Yang J., “*Journal of Power Sources*”, 68, (1997), 87-90.
21. Kariatsumari K., Kume H., Keys P., “*Nikkei Electronics Asia*”, February, (2010).
22. Whittingham M.S., “*Chem.Rev.*”, 104, (2004), 4271-4301.
23. Bazito F.C., Torresi R., “*Journal Braz. Chem. Soc.*”, Vol.17, (2006), 627-642.
24. Park B., Kim J.Y. in “*Lithium Batteries Science and Technology*”, (Nazri G–A, Pistoia G., Eds.), Chapter N°14, Springer (2009), 410-444.

25. Wu M.-S., Chiang P.-C., “*Electrochimica Acta.*”, 49, (2004), 1803-1812.
26. Ellis B.L., Lee K.T., “*Chem. Mater.*”, 22, (2010), 691-714.
27. Patil A., Patil V., “*Material Research Bulletin*”, 43, (2008), 1913-1942.
28. Li C., Zhang H.P., “*Electrochimica Acta.*”, 51, (2006), 3872-3883.
29. Padhi A.K., Nonjundaswamy K.S., Masquelier C., “*Journal of Electrochem. Soc.*”, Vol.144, N°5, (1997), 1609-1613.
30. Padhi A.K., Nonjundaswamy K.S., Goodenough J.B., “*Journal of Electrochem. Soc.*”, Vol.144, N°4, (1997), 1188-1194.
31. Tao H., Feng Z., “*Material Science Journal.*”, M2, (2011), 204-214.
32. Liu H., Wang G.X., “*Electrochemistry Communications*”, 10, (2008), 165-169.
33. Teyssot A., “*PhD.Thesis*”, from “Ecole Polytechnique Paris”, (2005), 1-42.
34. Besenhard J.O., Yang J., Winter M., “*Journal of Power Sources*”, 68, (1997), 87 – 90.
35. Ogumi Z., Inaba M. in “*Advance in Li-ion Batteries*”, (Schalkwijk W.A., Scrosati B. Eds.), Chapter N°2, Klumer Academic Publisher, (2002), 79-102.
36. Ogumi Z., Wang H. in “*Li-ion Batteries*”, (Yoshio M., Brodd R. J. Eds.), Chapter N°3, Springer, (2009), 49-73.
37. Hightower A., Ahn C.C., “*Applied Phys. Lett.*”, 77, (2000), 238.
38. Vetter J., Novak P., “*Journal of Power Sources*”, 147, (2005), 269-281.
39. Doyen-Long S., “*PhD.Thesis*”, from “L’Universite de Metz”, (1993), IV.2- IV.58.
40. Scrosati B., Garche J., “*Journal of Power Sources*”, 195, (2010), 2419-2430.
41. Karhunent T., Lahde A., “*ISRN Nanotechnology*”, Vol. 2011, (2011), 2419-2430.
42. Ferg E., Gummow J., “*Journal of Electrochemical Society*”, Vol.141, N°11(1994) L147-L150.
43. Nasar L. F., Crosnier O. in “*Lithium Batteries Science and Technology*”, (Nazri G–A, Pistoia G., Eds.), Chapter N°2, Springer (2009), 112-139.
44. Dimov N. in “*Li-ion Batteries*”, (Yoshio M., Brodd R. J. Eds.), Chapter N°11, Springer, (2009), 241-266.
45. Winter M., Besenhard J.O., “*Electrochimica Acta*”, 45, (1999), 31-50.
46. Yang J., Winter M., Besenhard J.O., “*Solid State Ionics*”, 90 (1996) 281-287
47. Dey A.N., “*Journal of Electrochemical Society*”, 118 (1971) 1547-1549.
48. Zhang Z. in “*Li-ion Batteries*”, (Yoshio M., Brodd R. J. Eds.), Chapter N°20, Springer, (2009), 367-412.
49. Xu K., “*Chemical Revs*”, Vol.104, N°10, (2004), 4303-4417.
50. Song J.Y., Wang Y.Y., “*Journal of Power Sources*”, 77, (1999), 183-197.



51. Lewandowski A., Swiderska-Mocek A., "*Journal of Power Sources*", 194, (2009), 601-609.
52. Tada H., Fukumoto Y., "*Journal of Power Sources*", 68, (1997), 301-303.
53. Arora A., Harris J., "*International Stationary Battery Conference - Battcon*", (2011), 17-1.
54. Gi-Heon K., Pesaran A., "*The 3rd International Symposium on Large Lithium Ion Battery Technology and Application*", (2007)
55. Leising R.A., Palazzo M.J., "*Journal of Power Sources*", 97-98 (2001), 681-683.
56. Wang Q., Ping P., "*Journal of Power Sources*", 208 (2012), 210-224.
57. Belov D., Yang M.-H., "*Solid State Ionics*", 179, (2008), 1816-1821
58. Onda K., Ohshima T., "*Journal of Power Sources*", 158 (2006), 535-542.
59. Unkelhaeuser T., Smallwood D., "*Electrochemical Storage System Abuse Test Procedure Manual*", (1999).
60. Richard M.N., Dahn J.R., "*Journal of Electrochemical Society*", 146, N°6, (1999), 2078-2084.
61. Mohamedi M., Ishikawa H., "*Journal of Applied Electrochemistry*", 34, (2004), 1103-1112.
62. Doughty D., Roth E.P., "*Interface*", 21, N°2, (2012), 37-47.
63. Jeevarajan J.A., Hall A.D., "*ESC Transactions*", 1(24), (2006), 1-5.
64. Xiao X., Lui X., "*Procedia Engineering*", 29, (2012), 738-743.
65. Anfea D., "*Battery Management Systems for Large Lithium Ion Battery Packs*", (2010).
66. Pop V., Bergveld H.J., "*IEEEExplore Digital Library*", 81-84.
67. Jurgen G., Jossen A., "*Measurements Science and Technology*", 16, (2005), R93-R110.
68. Chaturvedi N.A., Klein R., "*American Control Conference*", June 30-July 02, (2010), 1997-2002.

## **Chapter II**

### **Experimental part**

---

<b>Chapter II</b>	<b>50</b>
<b>Experimental part</b>	<b>50</b>
<b>II.2. Electrochemical circuit</b>	<b>52</b>
<b>II.3. Electrochemical diagnostic tools</b>	<b>54</b>
II.3.1. Galvano - potentiostatic charge or discharge	54
II.3.2. Cycling voltammetry	56
II.3.3. Electrochemical impedance spectroscopy	57
II.3.4. Electrochemical equipment	59
<b>II.4. Post mortem analyses</b>	<b>59</b>
II.4.1. X-ray diffraction technique	59
II.4.2. Scanning Electron microscopy	60
<b>II.5. Acoustic emission technique</b>	<b>61</b>
II.5.2. Principle and history of acoustic emission	61
II.5.3. Acoustic emission testing equipment	63
II.5.3.1. Acoustic emission sensors	64
II.5.3.2. Acoustic emission preamplifier	65
II.5.3.3. Acoustic emission filter	66
II.5.3.4. Acoustic emission software	66
II.5.4. Acoustic emission acquisition parameters	67
II.5.5. Characteristic parameters of the acoustic emission wave form	68
II.5.6. Acoustic emission data treatment	70
II.5.6.1. Spectral analysis	70
II.5.6.2. Multiparametric analysis	71
II.5.6.3. Advanced analysis	73
<b>II.6. Conclusion</b>	<b>75</b>
<b>References</b>	<b>76</b>

## II.1. Introduction

The purpose of this chapter is to present the different electrochemical and structural methods and instruments and the tests protocols used during this study of the electrochemical behavior of Li-ion coin cells. We also would present more deeply the acoustic emission which appears to be very innovative and promising for the study of electrochemical processes during normal and abuse operations and which have the advantage to be non-invasive and non-destructive.

## II.2. Electrochemical circuit

A secondary electrochemical cell is constituted by two electrochemical couples which convert the chemical energy into electrical energy by reversible redox reactions occurring during the charge or discharge processes. Their respective thermodynamic potentials have to be distant from one to the other in order to deliver high enough electromotive force (EMF) and thus high energy. Note that by definition, a battery is composed of two or more electrochemical cells in series, parallel or both, according to the required output voltage and capacity. In this work “battery” and “cell” terms will be used to denote the same object.

The Figure 1 presents an electrochemical cell in steady state and allows easily recognition of the redox reactions occurring on the electrodes when the cell is charged or discharged.

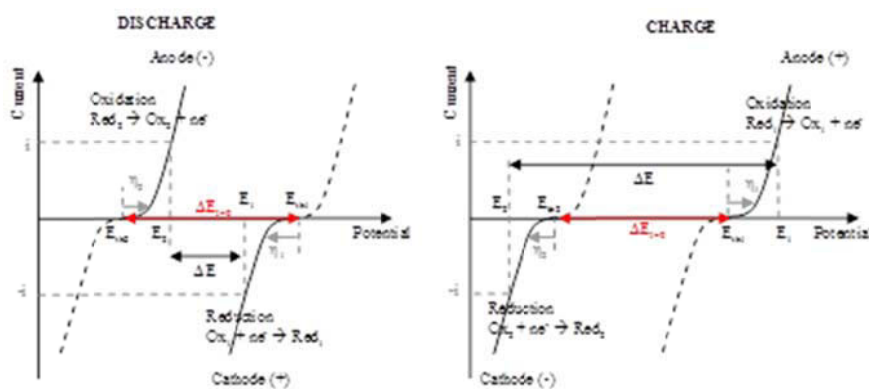


Figure 1 : Steady state representation of an electrochemical chain:  $Ox_1/Red_1$  and  $Ox_2/Red_2$  in discharge and in charge [1].

The voltage of the cell during charge or during discharge includes to the contribution of the electrochemical potential of electrodes, the overpotentials and the ohmic drops inside the electrolyte, the separator and the electrodes if they are not enough conductive.

It is possible to write considering “1” for a positive electrode:

- on discharge:

$$\Delta E = E_1 - E_2 = (E_{th1} - E_{th2}) - (\eta_1 - \eta_2) - \sum R_i I$$

- on charge:

$$\Delta E = E_1 - E_2 = (E_{th1} - E_{th2}) + (\eta_1 - \eta_2) + \sum R_i I$$

with :

- $E_{th1}, E_{th2}$  : Electrochemical thermodynamic potential of electrodes (at  $I = 0$ ),
- $\eta_1, \eta_2$  : Electrode overpotentials due to charge-transfer and/or diffusion polarization,
- $R_i$  : Internal resistance of the cell (ionic resistance of the electrolyte (within the separator and the porous electrodes), electronic resistances of the active mass, contacts, resistance etc...),
- $I$  : Electric current which is negative when discharge occurs and *vice versa*.

The Figure 2 gives the laws with which the electrochemical and kinetics parameters evolve.

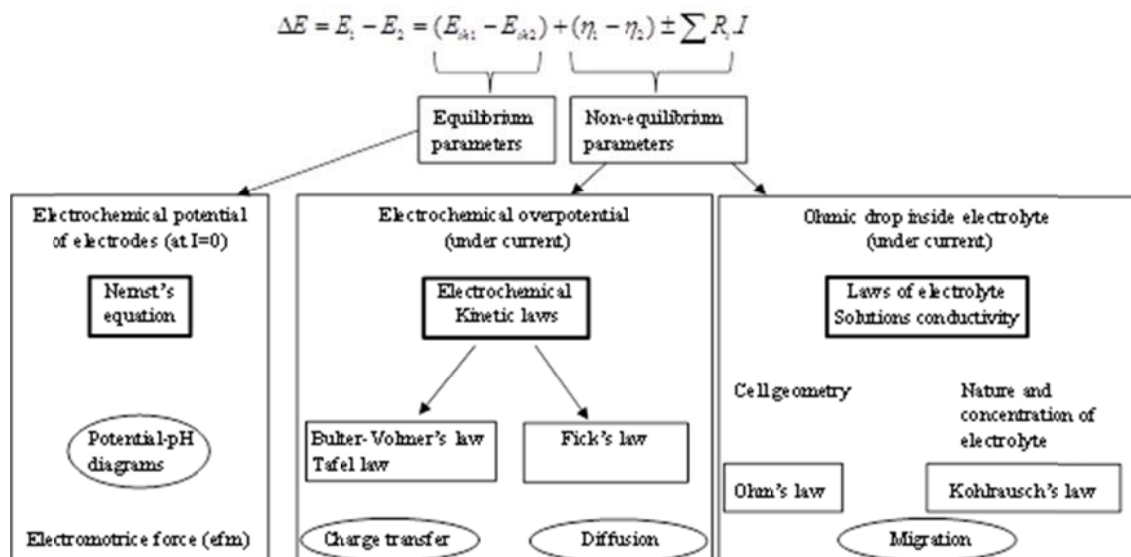


Figure 2 : Expression of the voltage on the terminals of a cell [1].

## II.3. Electrochemical diagnostic tools

The Electrochemical properties and performance of battery or of a single electrode can be characterized by a large variety of techniques. Galvano and potentiostatic charge and discharge, cycling voltammetry, and electrochemical impedance spectroscopy are typically used and will be described as follows.

### II.3.1. Galvano - potentiostatic charge or discharge

In this technique a constant current is applied to the electrode (cell) and its potential (or voltage) response with the time indicates the electrochemical processes taking place here. When the high or low voltage limit is reached the current direction is reversed (Figure 3).

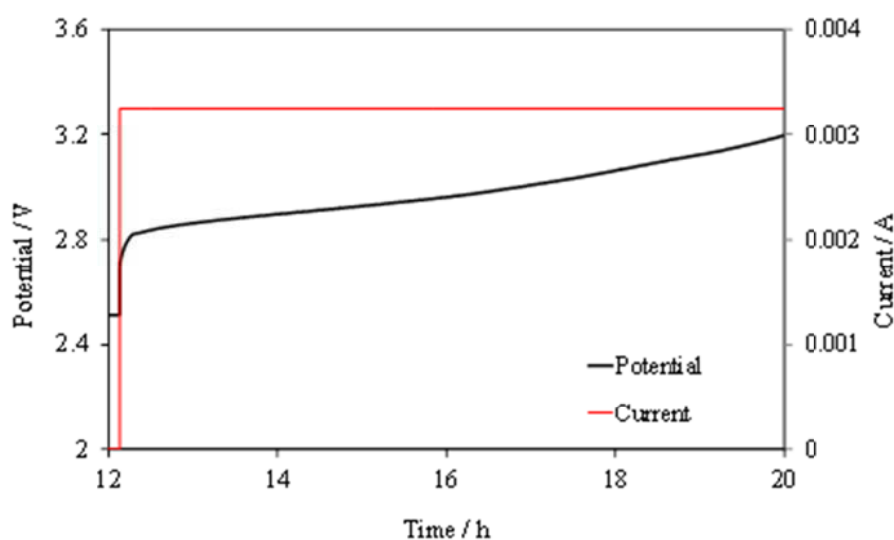


Figure 3: Typical constant current charge profile.

Galvanostatic or constant-current (CC) discharge is the standard process used to measure the electrochemical capacity of a cell. It can be performed at different current values (often denoted as “rates”). The applied current rate is calculated from the nominal capacity of the cell ( $C_{nom}$ ). The nominal capacity of the cell is defined by the electrochemical equation of the limiting electrode and the coefficient of the utilization of its active material. The following equation makes reference to the “C rate” convention which is very handy for representing the value of the applied current. A “C/t rate” means that in principle the battery will discharge fully in t hours.

Equation 1:

$$I = \frac{C_{\text{nom}}}{t}$$

The electrochemical capacity is obtained by integrating the applied current over the time:

Equation 2 :

$$C = \int_0^t I \cdot dt$$

In the case of galvanostatic ( $I = \text{constant}$ ) process, is can be rewritten as

Equation 3 :

$$C = I \cdot t$$

Capacity is expressed often in ampere-hours (Ah), where  $1\text{Ah} = 3600\text{C}$ .

Constant-current and constant-voltage (CC/CV) is a typical charge algorithm for a lithium-ion cell (Figure 4).

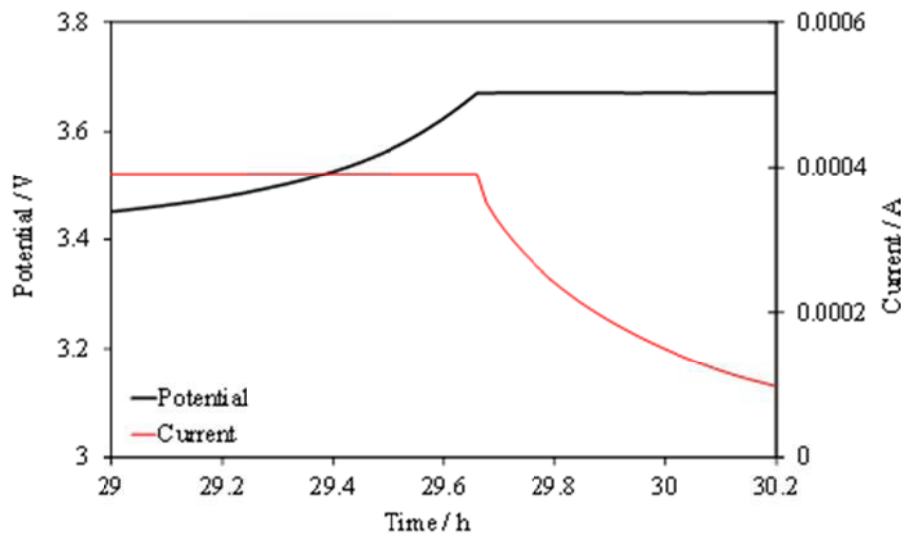


Figure 4 : Typical constant current and constant voltage charge profile.

This type of charge procedure is commonly used for charging Li-ion cells and some other accumulators which may be vulnerable to damage if the upper voltage limit is exceeded. Each technology is specified by a nominal and maximum constant current charging rate and an upper voltage limit that the cell (material, design) can tolerate without damaging. This implies that chargers for Li-ion cells must be capable of controlling both the charging current and the battery voltage. During the constant current mode, the voltage of the cell increases with various profiles depending on the nature of the electrode materials until the cell upper voltage limit is reached. After that point the charging voltage is maintained at that level,

known as the float level (constant voltage mode). During this constant voltage period, the current decreases as the charge approaches completion. Cut off occurs when a predetermined minimum current point, is reached beyond which the cell would accept a negligible quantity of electricity [2, 3, 4].

### II.3.2. Cycling voltammetry

Cyclic voltammetry (CV) is a type of potentiodynamic electrochemical measurement. Where the working electrode potential is ramped linearly versus time with a defined scan rate (V/s). When cyclic voltammetry reaches a vortex potential, the working electrode's potential ramp is inverted. This inversion can happen multiple times during a single experiment as it is illustrated in Figure 5a. In Figure 5b, the current is plotted versus the applied potential showing the typical cyclic voltammogram data presentation.

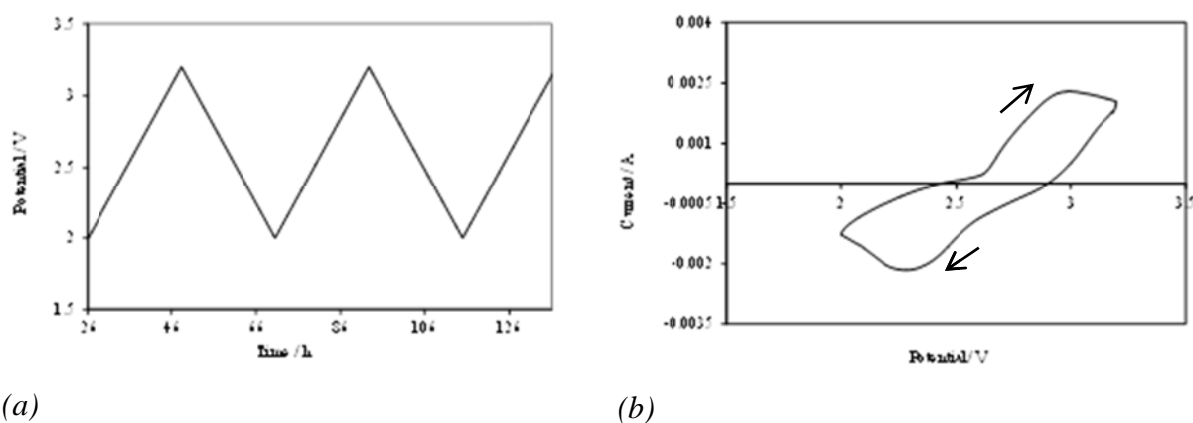


Figure 5: Waveforms of cycling voltammetry experience, (a) potential versus time (b) current versus potential.

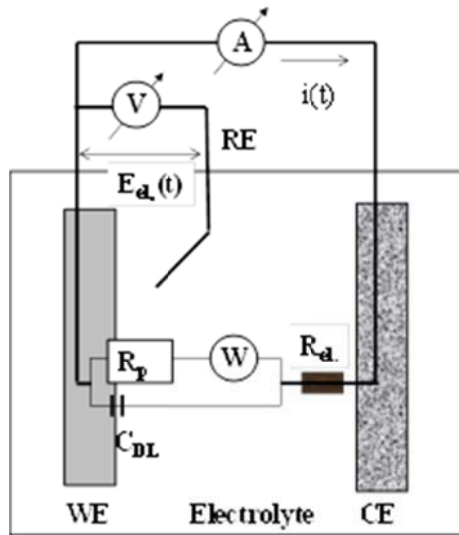
During the forward scan, the electrode potential increases and when it exceeds the value of the corresponding redox couple species in contact with the electrode, the current starts to increase. The current passes through a maximum and starts decreasing when the concentration of the active component is depleted close to the electrode surface. When the applied potential is reversed, if the redox couple is reversible, the product formed in the first oxidation reaction is reduced and a current of reverse polarity is produced. This reduction peak usually has a similar shape to the oxidation peak. As a result, information about the redox potential and electrochemical reaction rates of the redox couple is obtained. For instance if electronic transfer at the surface is fast and the current is limited by the diffusion of



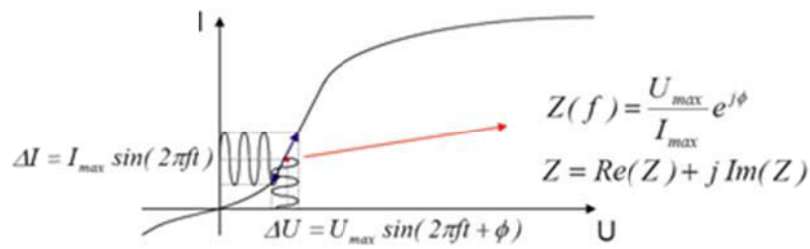
the species to the electrode surface, the current peak is proportional to the square root of the scan rate.

### II.3.3. Electrochemical impedance spectroscopy

Electrochemical impedance spectroscopy (EIS) is commonly used as a tool for in-situ characterization of the properties of the cell or the individual electrode. It allows studying diffusion processes, electrochemical redox reactions and surface related phenomena by measuring the changes in the electrical impedance of an electrode or entire cell as it is illustrated in Figure 6a.



(a)



(b)

Figure 6: Schema of an electrode immersed in an electrolyte.

The impedance measurement is based on the classical method of transfer functions (TF). The system under investigation is perturbed with a sinusoidal wave input and the

response is measured on the output. When determined in a sufficiently wide frequency range, the TF described entirely the dynamic properties of a linear system. If the system is linear, the response is also sinusoidal with the duration of the applied frequency and a different phase and amplitude. The ratio between the response and the input signal determines the complex transfer coefficient for the corresponding frequency. The frequency dependence of this coefficient defines the transfer function of the system. If the system is in a steady-state for the duration of the applied frequency, the response is also steady-state. The direct application of the classical TF method for electrochemical systems is impossible due to their non-linear behaviour. The problem is solved using the theory of Friedhol-Volterra and lies in the local application of the theory of linear system. It allows the approximation of the non-linear system with linear terms. In electrochemical systems the local analysis is implemented by measuring the Transfer Function with small amplitude of the perturbation signal either by current ( $\Delta I$ ) or by voltage ( $\Delta V$ ), taking into account only the local linear part of the response as it is illustrated in Figure 6b. The impedance of an electrode corresponding to a simple Faradic reaction can be expressed as:

$$Z = R_E + \underbrace{\frac{R_P}{1 + \omega^2 C_D^2 R_P^2}}_{Z'} - \underbrace{\frac{j\omega^2 C_D R_P^2}{1 + \omega^2 C_D^2 R_P^2}}_{Z''}$$

The impedance can be represented as its real part plotted against its imaginary part ( $Z'$  vs.  $Z''$ ), known also as Nyquist plot (Figure 7), or as a module and phase angle as a function of the frequency ( $|z| = f(\omega)$  and  $\phi = f(\omega)$ ) denoted as a Bode plot.

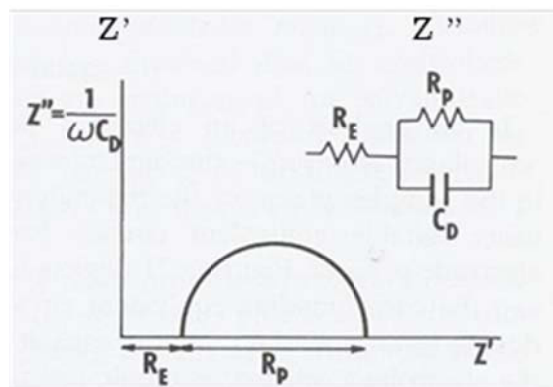


Figure 7 : Typical impedance spectra in Nyquist of an electrode.

The values of electrical circuit elements could give a significant contribution to the physical understanding of the investigated systems. Impedance elements can be divided into two basic groups: the first group are named (lumped elements): resistances  $R_E$ ,  $R_P$ , capacitance  $C_D$ , and induction  $L$  usually describing homogeneous systems. Phenomena related with inhomogeneity in the system can be described with frequency-depending elements. For example the Warburg element ( $W$ ) represents the impedance of linear semi-infinite diffusion of ionic species [5, 6].

For this work, the impedance spectra are obtained at open circuit in frequency range  $f_{\max} = 65000\text{Hz}$  and  $f_{\min} = 10\text{Hz}$  with amplitude 5 mV and spectral density of five points per decade. ZView 2 is the program used for equivalent circuit fitting. We are going to present the results in Nyquist plan.

#### II.3.4. Electrochemical equipment

The electrochemical measurements were done by using 8 channel potentiostat/galvanostat SOLARTRON 1470 connected with SOLARTRON 1250 FRA (Frequency response Analyser). The equipment is controlled by Corrware 2 software for DC experiments and Zplot 2 software for AC impedance measurements.

### **II.4. *Post mortem* analyses**

#### II.4.1. X-ray diffraction technique

X-ray diffraction (XRD) is used to characterize the structure of crystalline materials. It can be also used to determinate strain and phase composition in electrode materials, but cannot give directly information about macroscopic processes such as fracturing.

In an X-ray diffraction measurement, a crystal or a powder is mounted on a goniometer and gradually rotated while being bombarded with X-rays, producing a diffraction pattern of regularly spaced spots known as reflections. The two-dimensional images taken at different rotations are converted into a three-dimensional model of the density of electrons within the crystal using the mathematical method of Fourier transforms, combined with chemical data known for the sample.

Crystals are regular arrays of atoms, and X-rays can be considered waves of electromagnetic radiation. Atoms scatter X-ray waves, primarily through the atoms' electrons.

Just as an ocean wave striking a lighthouse produces secondary circular waves emanating from the lighthouse, so an X-ray striking an electron produces secondary spherical waves emanating from the electron. This phenomenon is known as elastic scattering, and the electron (or lighthouse) is known as the scatterer. A regular array of scatterers produces a regular array of spherical waves. Although these waves cancel one another out in most directions through destructive interference, they add constructively in a few specific directions, determined by Bragg's law:

*Equation 4:* 
$$2d \sin \theta = n\lambda$$

Here ( $d$ ) is the spacing between diffracting planes  $\theta$ , is the incident angle,  $n$  is any integer, and ( $\lambda$ ) is the wavelength of the beam. These specific directions appear as spots on the diffraction pattern called reflections. Thus, X-ray diffraction results from an electromagnetic wave (the X-ray) impinging on a regular array of scatterers (the repeating arrangement of atoms within the crystal). X-rays are used to produce the diffraction pattern because their wavelength  $\lambda$  is typically the same order of magnitude (1–100 angstroms) as the spacing  $d$  between planes in the crystal. In principle, any wave impinging on a regular array of scatterers produces diffraction. To produce significant diffraction, the spacing between the scatterers and the wavelength of the impinging wave should be similar in size.

In this work XRD is applied to characterize the positive and negative electrodes of Li-ion (LiAl/MnO<sub>2</sub>) coin cells. The XRD tests were done with BRÜKER D8 Advance (Bragg Brentano geometry) equipped with a Cu anticathode (Cu K<sub>α</sub> radiation).

#### II.4.2. Scanning Electron microscopy

A scanning electron microscope (SEM) is a type of electron microscope observing a sample by scanning it with a beam of electrons in a raster scan pattern. The electrons interact with the atoms that make up the sample producing signals that contain information about the sample's surface topography, composition, and other properties such as electrical conductivity. The types of signals produced by a SEM include secondary electrons, back-scattered electrons (BSE), characteristic X-rays, light (cathodoluminescence), specimen current and transmitted electrons. Secondary electron detectors are common in all SEMs, but it is rare that a single machine would have detectors for all possible signals. The signals result from interactions of the electron beam with atoms at or near the surface of the sample. In the most common or standard detection mode, secondary electron imaging or SEI, SEM can

produce very high-resolution images of a sample surface, revealing details less than 1 nm in size. Due to the very narrow electron beam, SEM micrographs have a large depth of field yielding a characteristic three-dimensional appearance useful for understanding the surface structure of a sample. A wide range of magnifications is possible, from about 10 times (about equivalent to that of a powerful hand-lens) to more than 500,000 times, about 250 times the magnification limit of the best light microscopes.

The SEM observations in this work were done using an electronic microscope Philips XL'30 connected with EDX analyzer (INCA, oxford instrument).

## **II.5. Acoustic emission technique**

### **II.5.2. Principle and history of acoustic emission**

Acoustic emission (AE) refers to “the class of phenomena where transient elastic waves are generated due to the rapid release of energy from localized source or sources within a material”. Each AE event is result from the elastic waves which propagate into the material yielding detectable AE signals. The latter allows the detection of active defects within materials in real time and continuous basis during the test. Thus method can be used in the industry either for process monitoring, material characterization or damage assessment. AET has become a recognized and commonly used nondestructive testing test (NDT).

The origin of the method is attributed to J. Kaiser in the 1950 years. He studied the acoustic emission phenomena during tensile tests of different metallic materials. He discovered the irreversible character of the acoustic emission during a tensile test, which now is called Kaiser's effect. In the recent years, the interest for this method grows in different scientific domains: seismology, electrochemistry, medicine etc... [7, 8, 9].

The frequency range of the acoustic emission phenomena varies from infrasonic frequencies to ultrasonic frequencies (Figure 8). However, the usual frequency range for AE study, defined by Kaiser and used today, is from 50 kHz to 1.5 MHz. At higher frequency, the acoustic emission is not intense enough in most cases and the material also absorbs a large part of the signal. The low frequency limit is primarily set by the background noise.

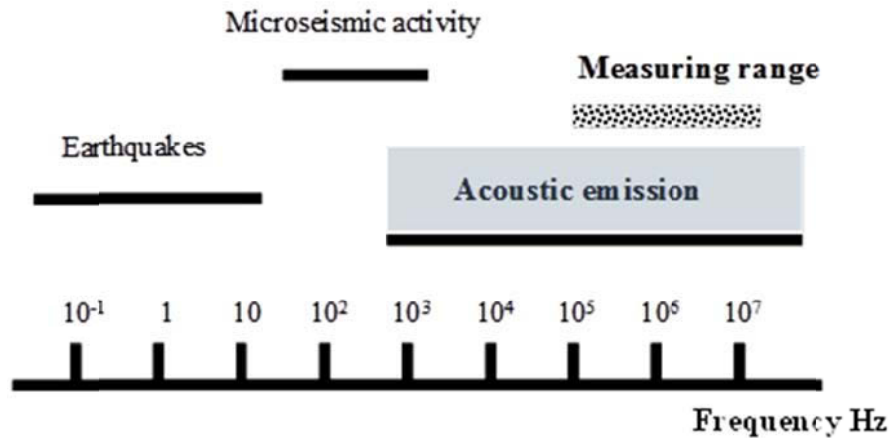


Figure 8 : Frequency range of Acoustic emission phenomena [9].

The sources of the Acoustic Emission events include different mechanisms of deformation and fracture such as earthquakes, rock burst, dislocations, bubble formation, phase transformation etc...

These sources can be classified as macroscopic, microscopic and pseudo-sources (Table 1). The term “macroscopic” refers to circumstances where a large part of the test material is contributing to the acoustic emission. “Microscopic” sources are related to individual events or microscopic mechanisms such as dislocation motion; slip formation, micro-cleavage formation. Apart of this, there are other mechanisms such as leaks, cavitation, or friction which release acoustic events and are denoted as "pseudo-sources".

Table 1: Different source of Acoustic emissions [9].

Source of Acoustic Emission			
Macro	Micro		Pseudo
Geological	Metals	Composites	Liquid-Gas
Degradation	Plastic deformation and yielding	Matrix cracking	Crack closures/rubbing
Piping	Phase transformations	Fibre-Matrix delamination	Loose particles parts
Initiation of cracks	Deformation Twinning	Fibre pull-out	Frictional rubbing
Propagation of cracks	Microcrack Initiation	Ply delamination	Slag cracking
Relative movement of structural units	Fatigue Cracking	Fibre Breakage	Cavitation
-	Stress Corrosion Cracking	Rubbing of Fractured	-

The multiple sources of the acoustic emission activity allow its utilization in applications like material characterization and damage assessment (Table 2).

*Table 2 : Acoustic emission applications [9].*

Applications			
Production Tests		Inservice Inspection	
During production	Quality control	Prequalification tests	On-line monitoring
Welding	Shop hydro tests of pressure vessels and pipes	Pressure vessels and pipes	Pressure vessels and pipes
Heat treatment	Proof testing of components	Bridges	Bridges
Tempering	-	Machines	Buildings
Firing of ceramics	-	Ropes	River dams

### II.5.3. Acoustic emission testing equipment

A system of Acoustic emission acquisition is intended to transform the micro-displacement of a surface into an electric signal available for analysis. Processing the vibration signal into an electrical signal is carried out using a piezoelectric sensor. However, this electrical signal needs to be filtered, amplified, measured and analysed by a corresponding hardware and software. The equipment for processing AE signals include sensors (transducer), preamplifiers, filters, amplifiers and signal conditioning circuit (Figure 9).

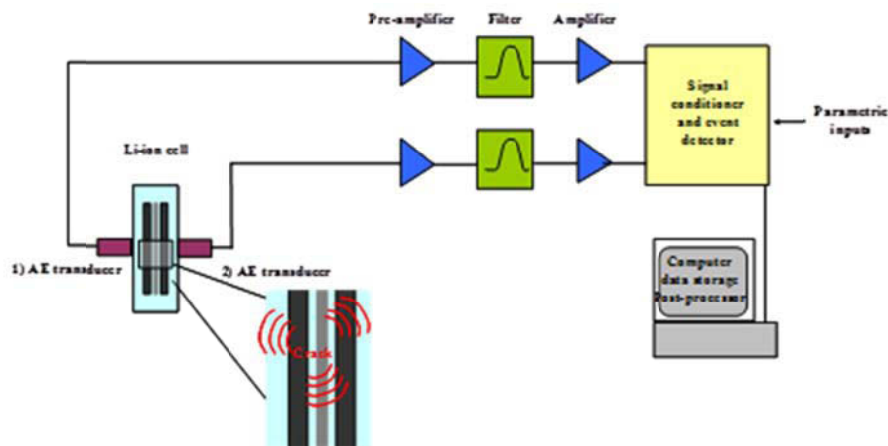


*Figure 9 : Construction of an acoustic emission test bench.*

### II.5.3.1. Acoustic emission sensors

The sensor is the heart of the AE equipment. It acts as a signal transmitting interface between the surface to be investigated and the data acquisition system. Usually, piezoelectric sensors are used in AET due to their high bandwidth, sensitivity, ruggedness and fidelity (Figure 10).

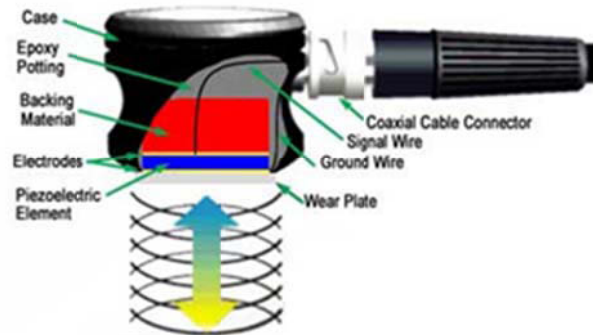


Figure 10 : Schematically presentation of piezoelectric sensor [10].

The signal, detected by the sensor, is converted into readable electric form usually as voltage over the time. For this study, Physical Acoustic Corporation's R-15 $\alpha$  sensor was selected due to its wide temperature range, high sensitivity and low frequency rejection (Table 3) [11].

Table 3 : Sensor R-15 $\alpha$  specification [12]

Sensor	Dimension/mm	Weight/g	Operating temperature /°C	Peak Sensitivity dB	Operating Frequency range (kHz)
R-15 $\alpha$	19x22	34	-65 to 175	69	50-400

An important point is the good acoustic contact between the sensor and the surface to be investigated. In this way, an acoustic couplant is used. An ideal couplant should have the following features:

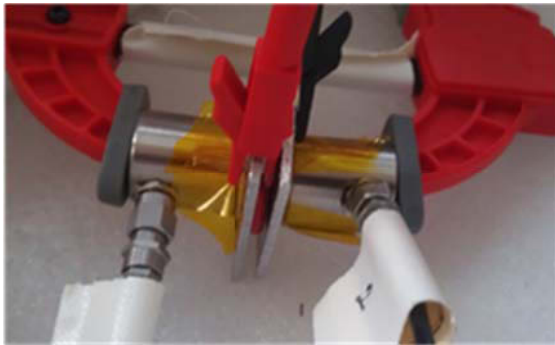
- High Wettability,
- Corrosion Resistance,
- Sufficient Viscosity,
- Easy Removal.



- Usually silicon grease is employed.

At the beginning and the end of an acoustic test, the coupling between sensor and surface should be checked using “Hsu-Nielsen” simulation signal. The "Hsu -Nielsen" coupling test consists in breaking a pencil lead (hardness 2H) using, thanks to a standardized pencil, a specific angle on the cell surface. When the pencil lead breaks there is sudden release of stress on the surface. The measured amplitude of this test must be close to 100 dB.

Two different holders were used to fix the sensor to the cell. The following figures (Figure 11) illustrate the experimental assembly. This holder permits the connection of both the electrochemical device and acoustic equipment to the cell under test. The sensors are held by clamps ensuring sufficient pressure, neither excessive nor weak. A Kapton film is used in order to isolate electrically the sensor and the surface.



(a)



(b)

Figure 11: Various holders used to keep sensor and battery together.

### II.5.3.2. Acoustic emission preamplifier

The signal, coming from the piezoelectric sensor, is weak and needs to be amplified before analysis. This role is played by the preamplifiers. The main functions of the Preamplifiers are:

- enhancing the signal level against noise,
- transmitting the signal over long signal cables,
- matching the high impedance of the sensor to the low impedance of the signal cable reducing the electrical pick-up from sensor and sensor cable.

For our study, two type's preamplifiers were used (Figure 12).



(a)



(b)

Figure 12 : The photos of the preamplifiers: a) Preamplifier 1227WT, b) Integral Preamplifier with a sensor.

The preamplifier 1227WT supplied with 20/40/60dB selectable gain switch can operate with different sensors (R-15 $\alpha$ , WD etc...) used in PCI-2 system. Integral Preamplifier sensor is a new family of low power Integral Preamplifier sensors for USB-AE Node system. These systems are smaller and compact providing good low noise performance and long cable drive distance supplied with 40dB gain, used at USB-AE system.

#### II.5.3.3. Acoustic emission filter

The filters play an important role in attenuating undesired background noise. Typically low-pass, band-pass or high-pass filters can be used. A low-pass band filter is a filter that passes low frequencies but attenuates frequencies higher than the cut off frequency. A high-pass filter works in the opposite way allowing only the frequencies higher than the cut off. The band-pass filter allows only a band of frequencies and can be considered as a combination of low-pass and high-pass filters. Typically the user of Acoustic emission techniques uses the band-pass filters ranging from 100 kHz-300k Hz. In our study, we used 100 kHz-1 MHz filter with PCI-2 equipment (study of batteries Graphite/LiFePO<sub>4</sub>) and 400 kHz-990 kHz filter with USB-AE equipment (study of LiAl/MnO<sub>2</sub> batteries). These bandwidth values are discussed in §III.5.2 and §IV.4.2.

#### II.5.3.4. Acoustic emission software

All acoustic emission tests were done using two different acquisition cards "PCI-2" and "USB-AE system". Both are controlled by AEwin software provided by "Mistras Group Inc". The AEwin software allows the AE acquisition and analysis and also includes waveform processing. The comparison between acquisition cards used in PCI-2 AE and USB-AE system is presented in (Table 4).

Table 4 : The specification of PCI-2 and USB –AE acquisition cards [11].

Specification	PCI-2 AE system	USB-AE system
Number channels	4	3
Frequency response	1kHz – 3MHz	1kHz – 1MHz
High pass Filters	3, 20, 100, 200 kHz	1, 20, 400 kHz
Low pass Filters	100, 200, 400, 1000, 2000, 3000 kHz	200, 300, 400, 500, 990, 1000 kHz
Minimum threshold	22 dB <sub>AE</sub> with sensor R15 (preamplifier 2/4/6)	22 dB <sub>AE</sub> with sensor R15 (preamplifier 4)
Maximum signal amplitude	100 dB <sub>AE</sub>	100 dB <sub>AE</sub>
Sample rate	100, 200, 500 kS.s <sup>-1</sup> 1, 2, 5, 10, 20, 40 MS.s <sup>-1</sup>	500 kS.s <sup>-1</sup> 1,5,10 MS.s <sup>-1</sup>

#### II.5.4. Acoustic emission acquisition parameters

There are two types of acoustic emission activity: the burst emission and the continuous emission, presented in Figure 13.

Burst emission is discrete type of signals with very short duration ranging from few microseconds to few milliseconds. This type of AE activity is characteristic for crack growth.

Continuous emission signal appears if the acoustic emission impulses are emitted close to one another or if the burst rate is very high then the signals occur very close.

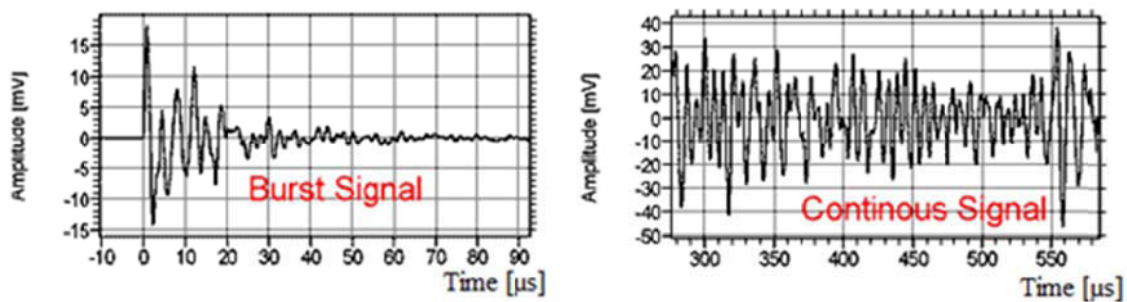


Figure 13: Typical AE signal [8, 13].

In ordering to insure correct indication of the acoustic emission signal it is important to precise the used parameters of acquisition: preamplifier gain, filters, sample rate as well as

parameters like, PDT, HDT, HLT and pre-trigger. Precise definitions of the value of those parameters give us the possibility to attribute the onset and end of the acoustic emission event.

- The “*Sample Rate*” is the rate at which data acquisition card samples waveforms on a per second basis. A sample rate of 1 MSPS (Mega Samples per Second) means that one waveform sample is taken in every  $\mu\text{s}$ .
- The “*Peak Definition Time*” (PDT) allows defining the peak of the maximum amplitude of the signal. It corresponds to the maximal authorized period of time in  $[\mu\text{s}]$  between the detection of the first threshold and the moment of the peak signal is detected. A well-defined PDT range allows avoiding the acquisition of signals with small amplitudes and fast propagation preceding the main event.
- The function “*Hit Definition Time*” (HDT) enables the system to determine the end of the event (denoted as a hit), to close the measurement process and store the measured data. The HDT must be long enough in order to record the signal fade.
- The function of the “*Hit Lockout Time*” (HLT) is to avoid the measurement of reflected waves and late-arriving parts of the AE signal (echo). The HLT is the duration of the period after the “event” when no data are recorded.
- The “*Pre-trigger*” time is the duration of the waiting period before the start of the recording of the signal corresponding to the main event.

The adjustment of these parameters is made using the “Hsu-Nielsen” test. A set of acquisition parameters for our adjustment test is shown in Table 5.

*Table 5 : Principal acquisition parameters chosen to follow test of the Li-ion batteries.*

Acquisition parameters AE equipment	HDT $\mu\text{s}$	PDT $\mu\text{s}$	HLT $\mu\text{s}$	Pre-trigger $\mu\text{s}$	Sample-Rate $\text{MS.s}^{-1}$	Threshold dB
PCI-2	200	100	200	25	5	26
USB	200	100	200	50	5	26

#### II.5.5. Characteristic parameters of the acoustic emission wave form

The activity of an Acoustic Emission source is typically denoted as an event. Each acoustic event (hit) could be classified regarding different components of its wave-form: maximal Amplitude (dB), Duration ( $\mu\text{s}$ ), Rise time( $\mu\text{s}$ ), Absolute Energy (aJ), Ring down count (RDC), Peak Amplitude (kHz), Energy and Signal level (RMS voltage). The AE wave form schema is presented in Figure 14.

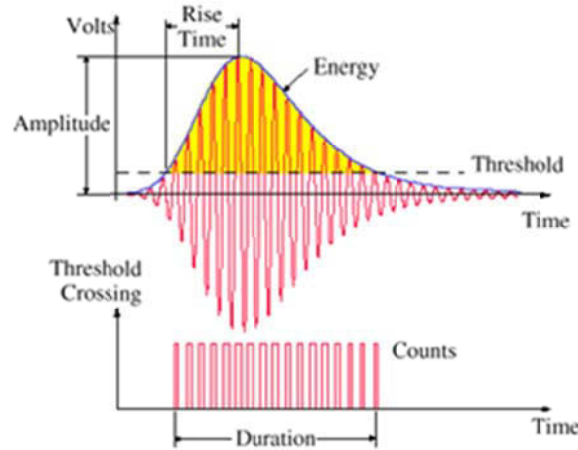


Figure 14 : Schematic presentation of the parameters of one acoustic emission wave [14].

- “Threshold” (dB) value corresponds to the level of the signal value, under which there is no acoustic events detection [15, 16].
- “Hit” is recorded when the signal exceeds the threshold.
- “Counts” are the registered peak signals which exceed the threshold. The Counts depend strongly on the employed band-pass filter and threshold. Sometimes the counts between the triggering time over the threshold and the peak amplitude are referred as “Count to Peak”.
- “Duration” ( $\mu\text{s}$ ) is the time between the first and the last threshold crossing. It depends on the sources magnitude and the noise filtering.
- “Rise time” ( $\mu\text{s}$ ) refers to the time required for the signal to reach its peak amplitude. It is accounted from the first threshold crossing and the moment of the Peak amplitude. It is related to the sources time function, and used to classify the type of fracture or eliminate noise signals.
- “Amplitude” (dB) is the peak voltage of the signal waveform. It is related to the source events.
- “Absolute Energy” ( $\text{aJ}=10^{-18} \text{ J}$ ) is the energy of the signal.
- “Frequency Centroid” (kHz) is the sum of the magnitude-weighted frequency values divided by the sum of the magnitudes.

- “*Average frequency*” (kHz) is calculated as the ratio “counts”/”duration”. It is used to evaluate the events with the same frequency but from different sources.
- “*Peak frequency*” (kHz) is defined as the point in the power spectrum at which the peak magnitude is observed.

#### II.5.6. Acoustic emission data treatment

The final goal of the AE monitoring is to correlate the acoustic activity to the real phenomena happening within the material. Detectable signal from AE experiment can be defined as a detectable transmitted energy which carries information. It can be a time-dependent variation of some characteristic of the physical phenomenon used to convey information. The signal contains information not only for frequency domain but for sources nature. This information can be extracted with few different methods of data treatment. In generally there are three basic methods: spectral analysis, multi-parametric analysis, and advanced data mining (pattern recognition, unsupervised and supervised cluster analysis and neural networks).

##### **II.5.6.1. Spectral analysis**

The data treatment of the Acoustic Emission signal can be done using a spectral analysis based on numerical Fourier transformation. The Fourier transformation is used to characterize a signal by its frequency spectrum that represents the signal of an acoustic emission and the calculated Fourier transform (Figure 15)

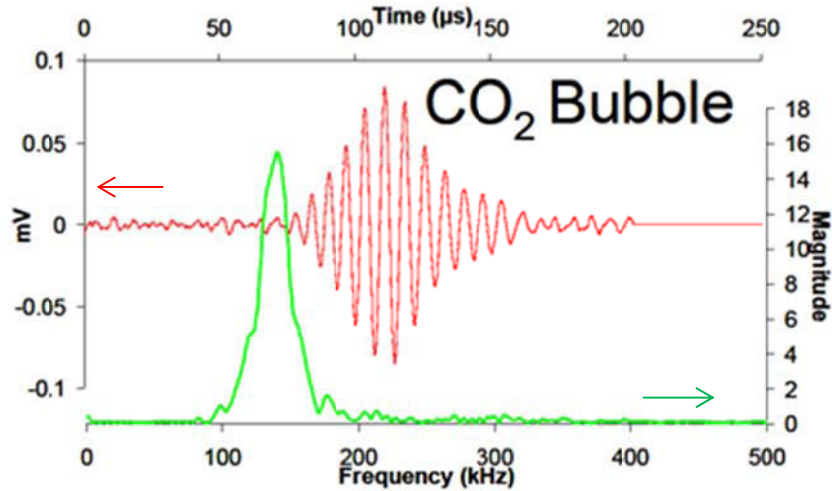


Figure 15: Acoustic Emission signal wave form and frequency spectrum density. Comparison of waveform and FFT observed for bubbling of carbonated beverage [17].

The frequency domain could be correlated with the mechanisms of the phenomena taking place within the material: for example it is found that cracking is between 250 kHz and 400 kHz, and gas formation between 50 kHz and 250 kHz etc... [17, 18].

#### II.5.6.2. Multiparametric analysis

The multi parametric analysis is the most commonly used method for AE signal data extraction and analysis. The first step of this approach is the time-dependent analysis [11, 18]. The temporal analysis is done by plotting one of the acoustic emission parameters as a function of the time: cumulated number of events, frequency, energy... As example, Figure 16 shows the variation of the amplitude and the number of hits with time during a test.

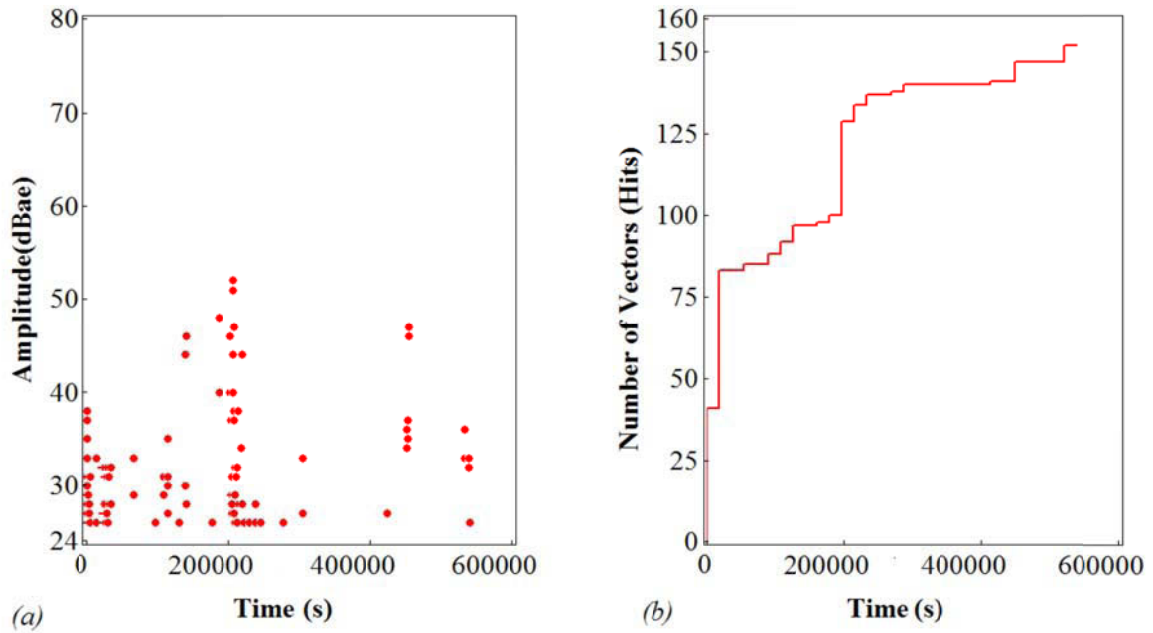


Figure 16 : a) Amplitude of AE signal as a function of time and b) Number Hits as a function of time.

The second step of the data evolution is the parametric analysis. The purpose of this approach is to find and show a correlation between several different parameters. The observation of this correlation and comparison with the electrochemical experiment (in our case galvanostatic cycling or cycling voltamperometry) gives the possibility to identify several physical and electrochemical phenomena.

In the Acoustic Emission technique, as well as in several other domains, the user can use a correlation diagram in order to obtain information on the acoustic activity and on the generated phenomena. Figure 17 represents a correlation diagram of the counts as a function of Amplitude. This diagram is usually employed in the treatment of AE signal. The idea of this approach is that all signal corresponding to the electromagnetic or mechanic perturbation will get into zone 1 and 3 of the correlation diagram. Another possibility is to plot in logarithm scale the Absolute Energy versus Duration.



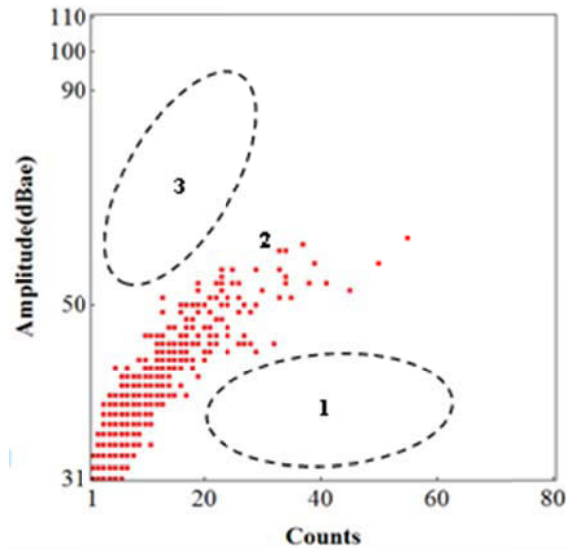


Figure 17: Correlation graph represent the counts as a function of the Amplitude.

### II.5.6.3. Advanced analysis

The identification and the classification of the physical phenomena causing AE often require an advanced analysis. The Advanced analysis uses several statistic techniques: principal components analysis, clustering, neural network etc... In this section, the essence of Pattern Recognition Analysis (PRA) and unsupervised clustering method “k-means” are presented.

#### II.5.6.3.a) Pattern Recognition Analysis

The Pattern Recognition Analysis (PRA) is a technique which determines classes of similar AE signals. PRA is numerical process giving a possibility to group a data set of “N” patterns to a limited number of “C” sub-groups, called classes. The numbers of classes and their characteristics have been determinate by the PRA methodology.

The pattern vector which describes each signal must be composed of features enabling discrimination between the different sources of AE signals. Each vector is represented in a multidimensional space baring as many dimensions as the number of considered AE parameters. Each AE parameter is initially considered as an independent variable. Then the two correlation descriptors are merged in one and a new cluster is formed, followed by the updating of the correlation matrix. The merging process continues until all descriptions are placed in the same group. The results are presented in dendograms (Hierarchical Tree), showing the merging sequence at each correlation level (Figure 18) [18, 20].

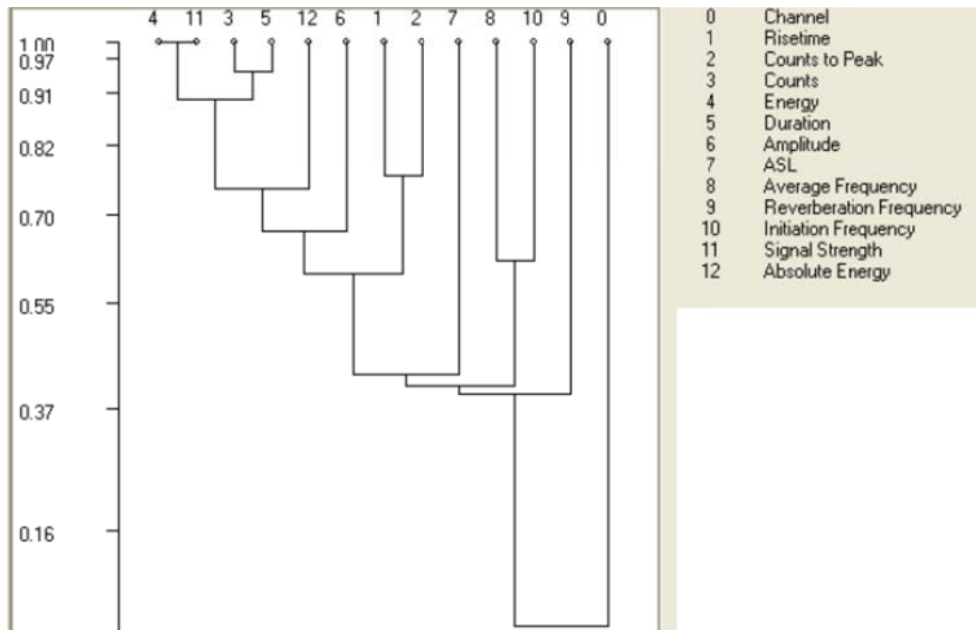


Figure 18: Dendrogram (Hierarchical Tree) determinate by PRA methodology.

The Pattern Recognition Analysis (PRA) is applied on the selected AE parameters as risetime, counts to peak, duration, absolute energy, frequency centroid etc... Furthermore, all features are normalized to a range from -1 to 1 in order to avoid biasing. The original data are projected on a set of orthogonal axes where maximum variance is achieved.

The techniques known as a principal component analysis, allow calculating the “degree of fit” when a subset of the transformed space is used [15, 17, 19].

#### II.5.6.3.b) K-Means unsupervised cluster analysis

The cluster analysis classifies a set of observations into several undefined group based on a combination of properties. The idea of the cluster analysis is to find a system organizing events into groups, where events of the same group share common properties. This concept is applied to the AE signal [20].

K-means clustering is a method of cluster analysis which aims to portion “N” observation into “K” clusters in which each observation belongs to the cluster with the nearest mean value. Each point is then assigned to the closest centroid, and each collection of points assigned to a centroid is a defined as cluster. The numbers of created clusters correspond to the number of observed physical (electrochemical, chemical, mechanical) phenomena.

## II.6. Conclusion

The experimental methods described above were used to study more precisely two types of batteries: Graphite /LiFePO<sub>4</sub> and LiAl/MnO<sub>2</sub>. In particular the behaviour of Graphite /LiFePO<sub>4</sub> cells during formation process and aging test was studied by coupling AE technique and electrochemical methods (CC/CV, CVA and EIS measurements). Further, the aging of LiAl/MnO<sub>2</sub> cells was evaluated by using AE technique, electrochemical methods and *post mortem* analysis.

## References

1. Catonné J.-C. in "*Techniques de l'Ingénieur* ", Reference K800.
2. Miomandre F., Sadki S., Audebert P., Méallet-Renault R., "*Electrochimie des concepts aux applications*", Dunod, Paris, 2005.
3. Linden D. in "*Hand book of batteries*", (Linden D., Reddy T.B. Eds.), Chapter N°1, McGraw-Hill, (2002), 1.3-1.17.
4. Pavlov D. in "*Power Sources for Electrical vehicles*", (Rand D.J. and McNicol B.D., Eds.), Chapter 4, Elsevier, (1984), 111.
5. Vladikova D., "*a,b,c Impedance training course* ", EU project Portable and Emergency Energy Sources POEMES – Centre of Excellence, E-School "<http://www.bas.bg/cleps/poemes/eschool.htm>
6. Vladikova D., "*Advanced Techniques for Energy Sources Investigation and Testing*", Proceeding of the International Workshop, 4-9 September, Sofia Bulgaria, (2004).
7. Hellier C.J in "*Handbook of Nondestructive Evaluation*", (Hellier C.J, Eds.), Chapter N°10, McGraw-Hill, (2000), 10.1-10.39.
8. Shiotami T. in "*Acoustic Emission Testing, Basics for Research-Applications in Civil Engineering*", (Grosse C.U., Ohtsu M., Eds.), Springer (2008).
9. Kalyanasundaram P., Mukhopadhyay C.K. in "*Practical Acoustic Emission*", (Raj B., Venkatraman B., Eds.), Alpha Science International Ltd., (2002).
10. <http://www.ndt-ed.org>
11. Mistras Group, "*PCI-2 Based AE system User's Manual*", (Physical Acoustic Corporation, Eds), (2007).
12. <http://www.mistrasgroup.com>
13. <http://www.ndt.net>
14. Huang M., Jiang L., "*JOM-Nondestructive Evalution*", Vol.50, N°11, (1998).
15. Boinet M., "*PhD. Thesis*", from "L'Institute Polytechnique de Grenoble", (2004), 38-54.
16. Legros B., "*PhD. Thesis*", from "L'Institute Polytechnique de Grenoble", (2010), 72-78.
17. Rhodes K, "*PhD. Thesis*", from "The University of Tennessee", (2011), 28-40.
18. Etienneble A., Idrissi H., "*Journal of Power Sources*", 195, (2011), 5168-5173.
19. Mistras Group, "*Noesis User's Manual*", (Physical Acoustic Corporation, Eds), (2007).
20. Tan P.-N., Steibach M., Kumar V., in "*Introduction in Data Mining*", (Tan P.-N., Steibach M., Kumar V., Eds), Chapter N°8, Errata, (2007), 490-568.

---

---

**Chapter III**  
**Contribution of the Acoustic Emission to the study of the  
behaviour of Graphite/LiFePO<sub>4</sub> cells**

<b>Chapter III</b>	77
Contribution of the Acoustic Emission to the study of the behaviour of Graphite/LiFePO <sub>4</sub> cells	77
<b>Summary</b>	80
<b>Résumé</b>	80
<b>III.1. Introduction</b>	81
<b>III.2. Choice of positive and negative materials</b>	81
III.2.1. Lithium iron phosphate	81
III.2.1.1. Structure	81
III.2.1.2. Lithium intercalation	82
III.2.1.3. Type of used active materials	84
III.2.2. Graphite	86
III.2.2.1. Structure	86
III.2.2.2. Intercalation process	87
III.2.2.3. Type of used graphite: meso carbon micro beads (MCMB)	89
<b>III.3. Description of the formation process</b>	91
III.3.1. Formation of the SEI on Lithium	91
III.3.2. Formation of the SEI on Graphite	92
III.3.3. Techniques used to characterize the passivation film	94
III.3.3.1. Electrochemical techniques	94
III.3.3.2. Physicochemical characterization techniques	96
III.3.4. Ageing phenomena	97
III.3.4.1. Overview	99
<b>III.4. Cell construction and material preparation</b>	101
III.4.1. Fabrication of the negative electrode	101
III.4.2. Fabrication of the positive electrode	102
<b>III.5. Experimental study and analysis of the formation process</b>	103
III.5.1. Tests of Li/Li cells	103
III.5.2. Formation of Li/MCMB	103
III.5.2.1. Introduction	103
III.5.2.2. Results presentation and preliminary analysis	104
III.5.2.2. Acoustic emission activity during formation of SEI	107
III.5.2.3 Acoustic emission activity during the lithium intercalation	114
III.5.3. Formation Li/LiFePO <sub>4</sub>	117
III.5.4. Formation MCMB/ LiFePO <sub>4</sub> cells	120
III.5.4.1. Formation MCMB/ LiFePO <sub>4</sub> type I	120
III.5.4.2. Formation MCMB/ LiFePO <sub>4</sub> type II	125
III.5.4.3. Spectral analysis of the Acoustic Emission data	129

<b>III.6. Calendar aging of the MCMB/LiFePO<sub>4</sub> –type II</b>	<b>132</b>
<b>III.7. Experimental study on the MCMB/ LiFePO<sub>4</sub> under abusive conditions</b>	<b>138</b>
III.7.1. Overcharge Tests	139
III.7.2. Overdischarge and External short-circuit tests	140
<b>III.8. Conclusions</b>	<b>141</b>
<b>References</b>	<b>142</b>



## Summary

*The Li-ion batteries with  $\text{LiFePO}_4$  material are important class of rechargeable batteries with high specific power and good energy density constituted by inexpensive and nontoxic material. During the first formation cycle of the battery MCMB/ $\text{LiFePO}_4$  and during ageing, several important phenomena appear. Considering the battery cycle life, the most important phenomenon is the formation of the passivation film on the surface of the graphite particles of the negative active material and the subsequent lithium intercalation between the graphene layers. The second phenomenon is the lithium intercalation/deintercalation and phase change inside lithium iron phosphate and the third is to the study of the degradation of the positive and the negative materials during the calendar ageing. The objective of this chapter is to evaluate the potential of the Acoustic Emission (AE) technique as a non-destructive method for monitoring and study of the electrochemical phenomena during the formation and the ageing of the Li-ion cells with the above-mentioned chemistry. The origins of the Acoustic Emission activity in the studied Li-ion cells are in the appearance of spontaneously generated transient elastic waves due to the stress in the active materials accumulated during the electrochemical processes taking place there. This method is able to detect such phenomena even at very fine level.*

## Résumé

*Les batteries Li-ion à base de  $\text{LiFePO}_4$  (matériaux peu coûteux et non toxique) représente une classe importante de batteries rechargeables avec une puissance spécifique et une densité énergétique élevées. Au cours de la formation et du vieillissement des batteries MCMB/LFP plusieurs phénomènes importants apparaissent. Le phénomène le plus important est la formation de la couche de passivation sur la surface des particules de graphite et la première intercalation du lithium à l'intérieur des plans de carbone lors du premier cycle dit de formation. Le deuxième phénomène est constitué par l'intercalation et la désintercalation du lithium ainsi que le changement de phase de l'électrode LFP lors des phases de cyclage. Le troisième est la dégradation de la matière active positive et/ou négative durant la vie de la batterie. L'objectif de ce chapitre est d'évaluer le potentiel de la technique de l'émission acoustique (AE) comme méthode non destructive pour le suivi et l'étude des phénomènes électrochimiques au cours de la formation et du vieillissement des batteries Li-ion. L'activité acoustique dans les cellules Li-ion est due à l'apparition d'ondes élastiques transitoires*

*spontanément générées par les contraintes accumulées dans les matériaux actifs au cours de son utilisation. Cette méthode est capable de détecter ces phénomènes, même à un niveau très faible. En particulier, il a été montré que l'émission acoustique apparaît lors de la formation du film de passivation lors du premier cycle d'utilisation de la batterie.*

### **III.1. Introduction**

The aim of this chapter is to present Acoustic Emission (AE) results obtained during the electrochemical formation process of cell comprised of graphite and lithium iron phosphate electrodes. For that, we have progressed step by step by studying individually each electrode faced to lithium metal electrode counter/reference before assembling them inside complete cells. AE events coming from different sources could be thus more clearly identified. We expect to detect a large number of acoustic emission events during the film formation at the graphite surface due to the gas emission and particle cracking phenomena which are known to occur (lithium insertion and co-solvent reduction before intercalation). In parallel, the own AE signature of  $\text{LiFePO}_4$  electrode will be determined in order to detect when lithium is extracted and inserted back in structure. We hope to demonstrate that AE can become a method for survey and management of the formation process.

### **III.2. Choice of positive and negative materials**

#### III.2.1. Lithium iron phosphate

##### **III.2.1.1. Structure**

The olivine structure of  $\text{LiFePO}_4$  belongs to the family of super ionic conductors called *Nasicon*, known as fast ionic conductors and used as solid electrolytes in electrochemical cells. The inventors of those electrodes materials are Padhi and Goodenough, who are discovering electrochemical properties of the olivine phase [1, 2]. The crystal structure of  $\text{LiFePO}_4$  is constituted by hexagonal close-packed lattice of oxygen with one dimensional channel (Figure 1). The structure is drawn by binding atoms to form plans, allowing visualizing polyhedrons and the available spaces between them. The cavities are the spaces in which the lithium ions (the smallest spheres) are placed. The red tetrahedra represent  $[\text{PO}_4]$ , and the blue octahedra are  $[\text{FeO}_6]$  (Fe or P is in the center of the polyhedron). The atypical feature of this structure is the presence of common edge between each  $\text{PO}_4$  tetrahedron and each  $\text{FeO}_6$  octahedron, by sharing

oxygen atom in every summit of polyhedrons. The strong covalency of P-O bond and O-O distance are fixed and almost invariant. In such phospho-olivine structure, this edge-sharing induces strong distortions at the local scale that spread in all the crystallite.

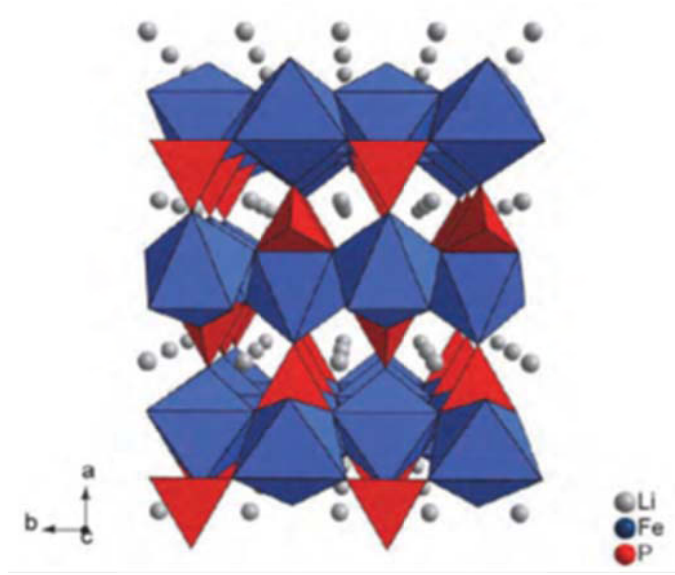


Figure 1: Insertion structure of  $\text{LiFePO}_4$ . [3]

The material is thus constituted by two-dimensional (2D) sheets, parallel to the (bc) plane; these sheets are connected along the (a) direction to make the 3D skeleton. Lithium is inserted in 1D channel [3, 4].

### III.2.1.2. Lithium intercalation

The olivine structure leads to reduce of the structural flexibility and produces structural constraints during the lithium intercalation and deintercalation. During lithium deintercalation,  $\text{Fe}^{2+}$  ions are oxidized to  $\text{Fe}^{3+}$  with change into  $\text{FeO}_6$  octahedra (change into Fe-O covalent bonds and O-O distance) leading to distortion. The distortion between the two 3D frameworks induces a change in the O-O distance corresponding to the edge between  $\text{FeO}_6$  octahedra and  $\text{PO}_4$  tetrahedon. The differences in both structures ( $\text{FeO}_6$ ,  $\text{PO}_4$ ) are substantial and it is very difficult to introduce a significant amount of  $\text{Fe}^{3+}$  ions in  $\text{LiFePO}_4$  and equal amount of  $\text{Fe}^{2+}$  ions into  $\text{FePO}_4$ . Consequently, there is the existence of two phases  $\text{LiFePO}_4$  and  $\text{FePO}_4$  [4, 6, 7, 8].

The diffusion process of lithium ion inside the 1D structure is linked to the energy barrier that the lithium ion has to overcome in order to move from one unit structural to the next one, either along the *b* direction (0.55eV), or *c* direction (2.89eV). Thus the lithium ions

move along the path requiring minimum energy, i.e. the  $b$  axis [5, 9]. However, even today, the diffusion process of the Li ions inside  $\text{LiFePO}_4$  structure is still a subject of debate.

Figure 2 presents the charge/discharge process of  $\text{Li}_x\text{FePO}_4/\text{FePO}_4$  expressed by the following equation:



The continuous presence of the two phases and  $\text{FePO}_4$  and  $\text{LiFePO}_4$  leads a flat profile of the potential vs. the insertion rate curve [8].

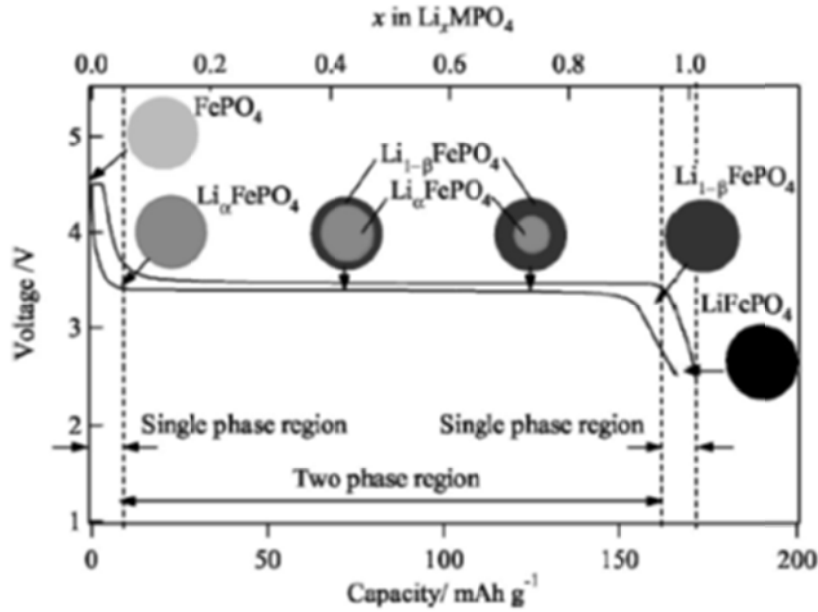


Figure 2: Schematic illustration of the charge/discharge voltage curve measured at  $C/20h$  current rate of  $\text{LiFePO}_4$  vs. lithium cell [8].

There are three theoretical models describing the mechanism of insertion/extraction of lithium ions in  $\text{LiFePO}_4$  structure. The first one is denoted as “shrinking-core” or “shrinking-shell” model and is proposed by Padhi and Goodenough [2]. According to these models the insertion of lithium into  $\text{FePO}_4$  is reversible: lithium is transported from the surface to the interior of the particles through the solid lattice as schematized in Figure 3a. The crystal structure of the material provide small free volume for  $\text{Li}^+$  movement (diffusion-limited process) allowing the electrode cycling only at low current density at room temperature, leading to the capacity loss otherwise [8, 10].

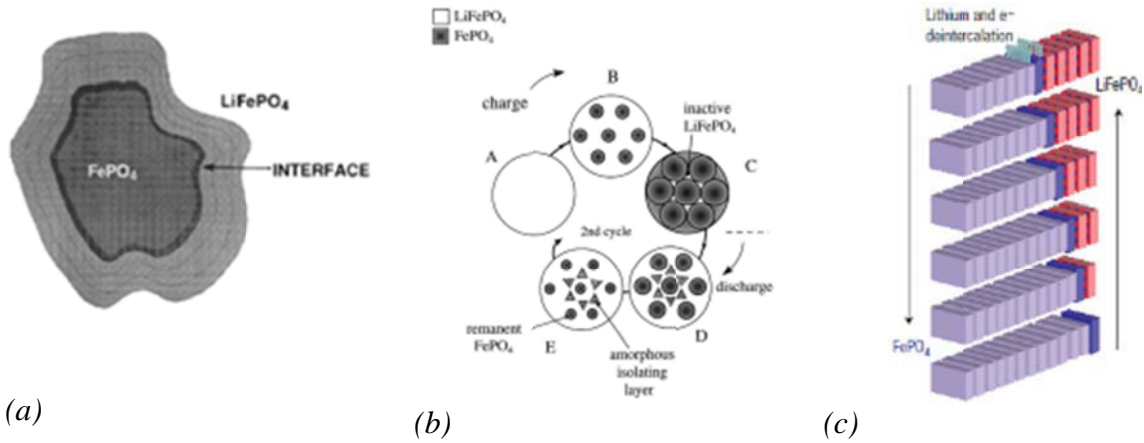


Figure 3: Schematic representation of the different models of lithiation/delithiation of the  $\text{LiFePO}_4$ : (a) represent the shrinking-core model, (b) mosaic model and (c) domino-cascade model [4, 11, 12, 13, 14].

The second model is named “mosaic model” and presumes that the insertion /extraction of lithium starts at different nucleation sites (Figure 3b) [11]. The third model is the “domino-cascade” model. This model suggests to a fast lithiation/delithiation of each particle which will be totally charged or totally discharged (Figure 3) [4]. This model is based on the fact that the rate capability of  $\text{LiFePO}_4$  is limited by its poor electronic conductivity and by low rate of  $\text{Li}^+$  transports. The improvement of the  $\text{LiFePO}_4$  electrode performance can be achieved combining several approaches like decrease of its particle size bellow  $1\mu\text{m}$ , application of carbon coating of the particles surface and doping with different metal ions ( Mg, Nb...) in order to increase the interesting electric conductivity of the material [12, 13, 14].

### III.2.1.3. Type of used active materials

The LFP grade used in this study is supplied by Pulead Technology Industry Co (China). Figure 4 and Figure 5 shows SEM and TEM images of the used positive active material.

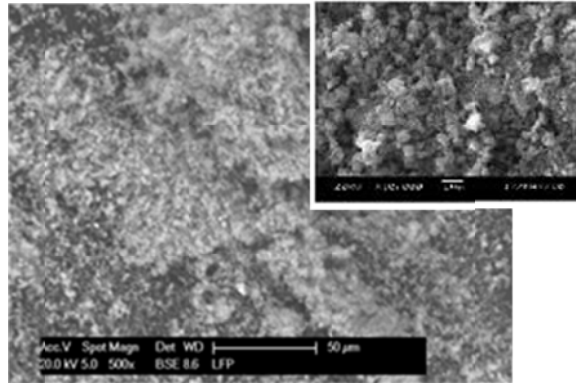


Figure 4: SEM image of LFP powder (x 500) (label: SEM image presented on the website of the manufacturer - <http://www.pulead.com.cn>) [15].

The particles are coated by a thin carbon surface layer (thickness = 5nm) as shown in the TEM images.

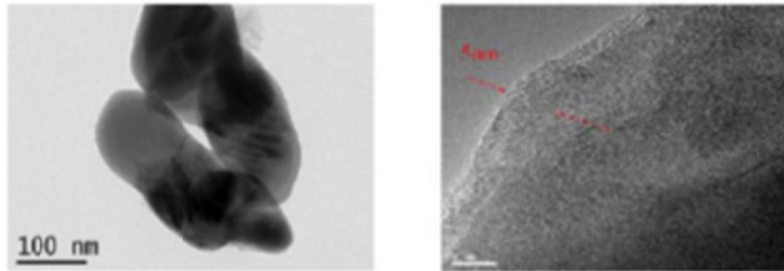


Figure 5: TEM image of LFP-Pulead coated with carbon [15].

Table 1 present the Pulead's data sheet of the used material. It can be seen that 50% of particles have a size of 1.0-1.5 nm. The powder contains also 2% of carbon.

Table 1: Physical parameters of LFP powder (Pulead)

Physical parameters		Sep.	Standard
Particle size ( $D_x = x\%$ of particle size)	$D_{10} (\mu\text{m})$	$\leq 0.4$	0.5
	$D_{50} (\mu\text{m})$	1.0-1.5	1.3
	$D_{90} (\mu\text{m})$	$\leq 6.0$	4.3
Tap density ( $\text{g}/\text{cm}^3$ )		$\geq 1.2$	1.3
Specific surface area (BET) ( $\text{m}^2/\text{g}$ )		10.0-16.0	13.7
Moisture content (%)		$\leq 0.2$	0.13
Carbon content (%)		1.6-2.2	1.9

The Figure 6 gives the X-ray diffractogram of the LFP powder. The corresponding lattice parameters for  $\text{LiFePO}_4$  phase are:  $a=10.3197\text{\AA}$ ,  $b = 6.0046\text{\AA}$  and  $c=4.6930\text{\AA}$ .

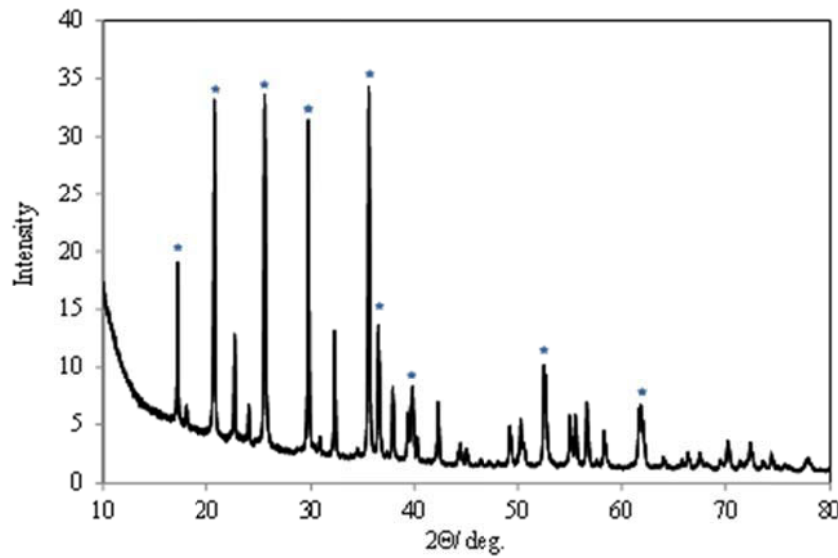


Figure 6: X-ray diffractogram of LFP powder, ★  $\text{LiFePO}_4$ , the rest of the peaks correspond to the  $\text{FePO}_4$ .

### III.2.2. Graphite

#### III.2.2.1. Structure

The carbonaceous materials can be very different in terms of crystallinity, microstructure and micromorphology. The mechanism of lithium intercalation depends on all these characteristics. The carbons can be divided in several groups depending on their properties: the diamond and the graphite are crystalline phases, while materials like the glassy carbon and the carbon black are non-crystalline solids. Electric conductivity is provided simultaneously by graphitic and non graphitic structural units [16, 17, 18]. The Figure 7 gives few examples of carbonaceous materials tested as negative electrodes in Li-ion batteries.

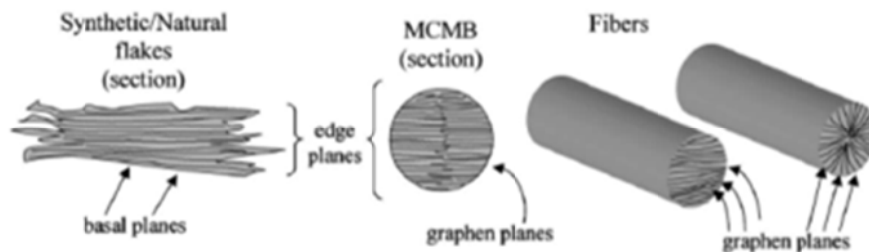


Figure 7: Schematic presentations of various type carbons [17, 18].

Inside the graphitic family, various micromorphologies can be found as a flake (natural graphite), beads (MCMB), as well as fibers which can be chopped or milled. They offer high

specific capacities close to the theoretical value 372 mAh/g (for  $x=1$  in Equation 2), and irreversible capacity (about 15%) and good cycleability (depending on the choice of the most suitable electrolytic mixture).



Lithium ions can be intercalated in most kinds of carbon, the obtained lithiated carbon has electrochemical potential close to the one of the metallic lithium.

### III.2.2.2. Intercalation process

The graphite intercalation compounds (GIC) with lithium ( $\text{LiC}_6$ ) are shown in Figure 8a. Li intercalates between the graphite planes taking a position in the middle of a hexagon, surrounded with 6 hexagons, leading to the  $\text{LiC}_6$  stoichiometry (Figure 8b). The space between the graphene planes increase slightly, from 0.335 nm to 0.370 nm (+10.3%) when the lithium is intercalated [19].

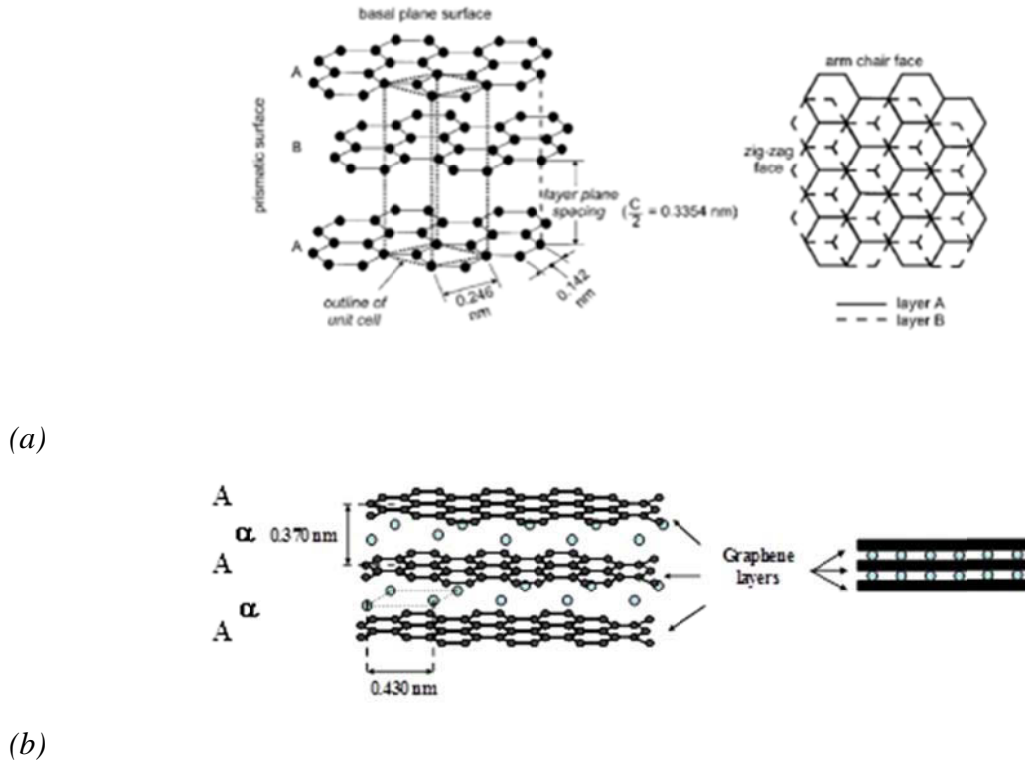


Figure 8: (a) Schema of the crystal structure of the graphite, showing the AB layer stacking sequence and the unit cell, (b) Lithium intercalation inside the carbon matrix [19].



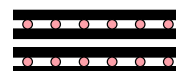
The lithium intercalation into graphite, firstly observed about fifty years ago, is made in stepwise mode to form several intercalation phases. The stage during which the corresponding phase is formed, is denoted with Roman numerals:

*Stage I:* each graphene plane is separated by an intercalated layer:



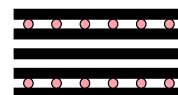
A maximum lithium content of one Li guest atom per six carbon host atoms can be reached for highly crystalline graphitic carbons ( $n = 6$  in  $\text{LiC}_n$  or  $x = 1$  in  $\text{Li}_x\text{C}_6$  or Stage I). The intercalation reaction occurs only at prismatic surfaces (arm-chair and zigzag faces). The intercalation through the basal planes is possible only at defect sites.

*Stage II:* two graphene planes are separated by an intercalated layer:



The stage II corresponds to intercalation compound  $\text{Li}_{0.5}\text{C}_6$ . It is commonly accepted that stage II is presented between the compositions of  $x = 0.25$  and 1.

*Stage III:* three graphene planes are separated by an intercalated layer:



On the basis of XRD measurements, stage III  $\text{Li}_{0.222}\text{C}_6$  and stage IV  $\text{Li}_{0.166}\text{C}_6$  compounds can be observed between about  $x = 0.1$  and 0.25 depending on the degree of graphitization. Higher intercalation stages with lithium are difficult for crystallographic identification.

In the latter case less  $x < 0.1$ , the lithium is positioned randomly in between every graphene layer, with an interlayer spacing very close to the one of graphite.

Staging phenomena as well as the degree of intercalation can be easily observed during electrochemical reduction of carbons in  $\text{Li}^+$  containing electrolytes at low current rate. Figure 9 shows a schematic potential/composition curve for the constant current reduction of graphite to  $\text{LiC}_6$  corresponding to a lithium storage capacity of 372 mAh/g with respect to the graphite mass in correlation with the above discussed processes.

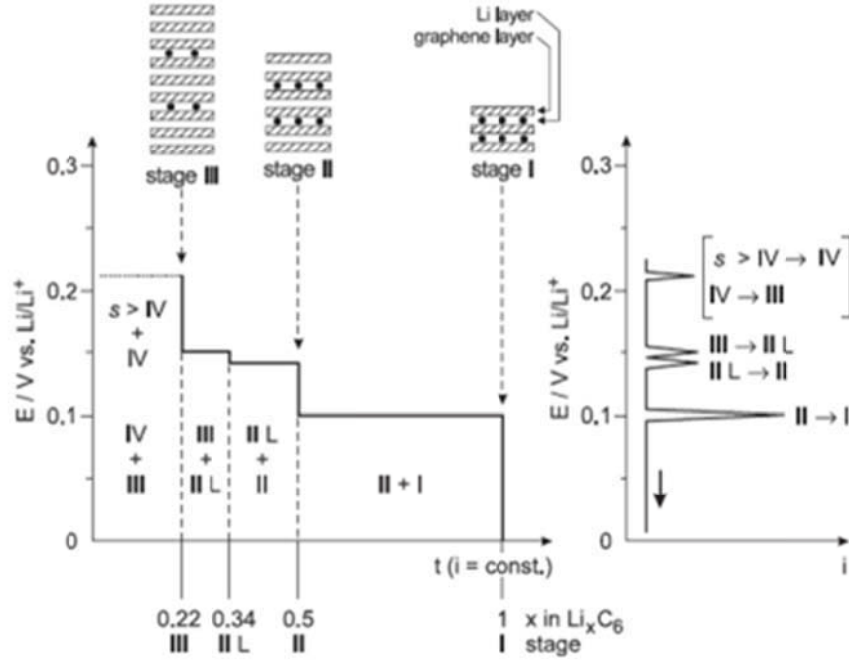


Figure 9: Stage formation during electrochemical intercalation of lithium into graphite. Left: schematic galvanostatic potential transient. Right: schematic voltammetric curve [20].

Under galvanostatic control, the potential plateaus indicate two-phase regions (Figure 9) [20, 21]. Under potentiodynamic control (LPSV) these phase transients appear like current peaks. The current peaks correspond to the different stage of intercalation of the lithium ions into graphite. There are no sharp differences between the two phase regions because the packing density of  $\text{Li}_x\text{C}_6$  varies slightly and the various type of overpotential cause plateau sloping in galvanostatic measurements. The phases correspond to the stage of intercalation were identified from electrochemical curves and confirm by X-ray diffraction and Raman spectroscopy [22 - 25].

### III.2.2.3. Type of used graphite: meso carbon micro beads (MCMB)

The graphite material MCMB which was used in this study is manufactured by Osaka Gas Chemical. The material is prepared in the following way:

- Heat treatment of a pitch at 410-415°C eliminating the impurities and forming the mesospheric particles (balls of 10µm of diameter),
- Dissolution of the pitch which did not react in toluene,
- Recapture of the balls and heat treatment at 900°C.

The MCMB powder was been characterized by SEM and XRD technique, the results from both tests are present in Figure 10 and Table 2.

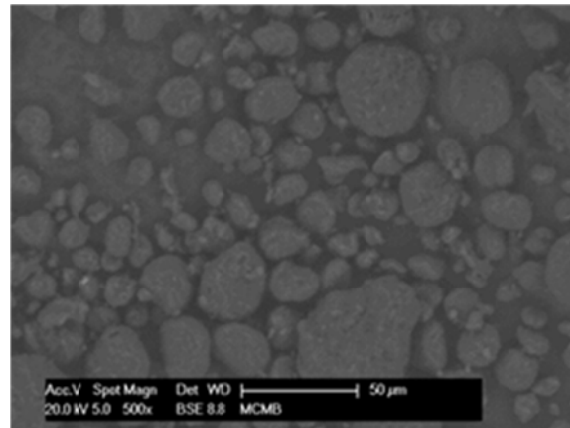


Figure 10: SEM image of MCMB powder ( $\times 500$ ).

The MCMB powder is constituted by beads of  $25\mu\text{m}$  (50% of particles). Its BET surface is  $2\text{ m}^2/\text{g}$ .

Table 2: Physical parameters of MCMB powder

Physical parameters	Average
Particle size $D_{50}$ ( $\mu\text{m}$ )	25
Specific surface area (BET) ( $\text{m}^2/\text{g}$ )	2

Figure 11 presents the diffraction patterns for MCMB negative electrode material. The calculated lattice parameters for graphite hexagonal phase are:  $a=2.465\text{ \AA}$  and  $c = 6.736\text{ \AA}$ .

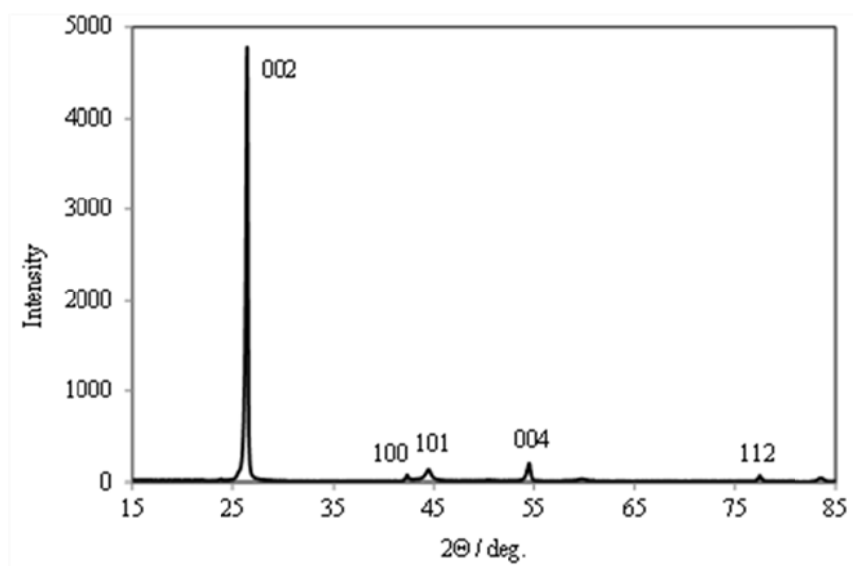


Figure 11: XRD patterns of MCMB powder.

### III.3. Description of the formation process

Solid Electrolyte Interphase or SEI is the layer formed at the contact between the electrolyte and the lithium metal or the lithiated graphite. It consists of insoluble and partially soluble reduction products of electrolyte components. This layer acts as an interface between the graphite/metal electrodes and the electrolyte, and has similar properties of a solid electrolyte with high electronic resistance. SEI determines the stability, power capability, and morphology of lithium deposits, or intercalation compounds as well as the calendar and cycling life time of the batteries [26].

#### III.3.1. Formation of the SEI on Lithium

This paragraph will present briefly the formation of SEI on the surface of the metallic lithium because the latter is presented in the electrochemical cells used to study the individual formation of the negative and the positive electrodes.

In the non-aqueous electrolytes (liquid, solid, polymer) typically used in the Li-ion batteries a film formed from the products of the electrolyte decomposition covers spontaneously the lithium surface (Figure 12).

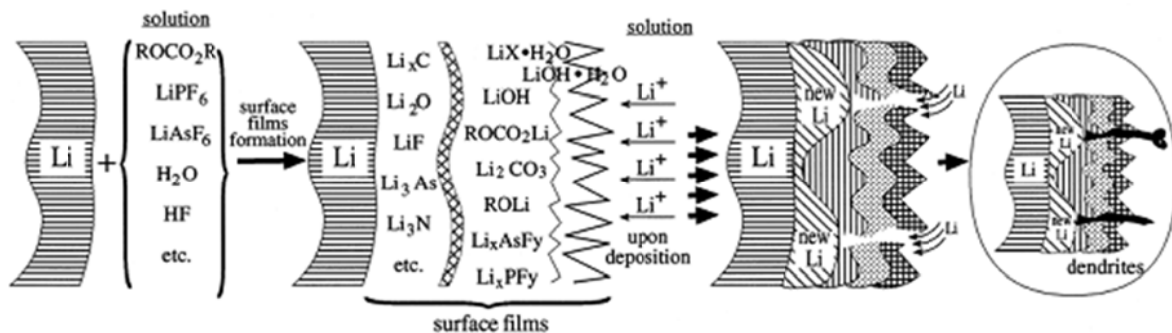


Figure 12: Schematically presentation of film formed on metallic lithium in organic electrolytes [27].

The film protects the surface of the metal from further corrosion. The same type of film is formed on the surface of the alloys rich in lithium (as LiAl alloys discussed in Chapter IV).

The composition and morphology of SEI layer on the metallic lithium depends on the used electrolytes. Generally the film contains a) thick, porous, permeable phase composed of organometallic products (ROCO<sub>2</sub>Li, ROLi) and b) thin, compact, impermeable phases composed by inorganic decomposition products (Li<sub>2</sub>CO<sub>3</sub>, LiOH, LiF ect...). The formed

interphase is a mosaic-type polyhetero microphases media. This micro-heterogeneous surface film leads to dissimilar current distribution and heterogeneous electrochemical properties [27]. Hence when metal is deposited selectively at a certain site, it is exposed to solution species that react immediately, consuming continuously the solvent and the salt. Due to the non-homogenous structure of SEI, dendritic deposition is possible to appear on the metal surface (Figure 12), with the associated safety risks already discussed in §I.10.

### III.3.2. Formation of the SEI on Graphite

In the same way as for lithium metal, SEI film is mainly formed on the graphite during the first charge (formation step). The choice of the solvent and the mixture of them have crucial role to guarantee the good performances of cells. At a commercial level, liquid electrolytes are essentially composed by a mixture of alkyl carbonates: EC (ethylene carbonate), PC (propylene carbonate), DMC (dimethyl carbonate), DEC (diethyl carbonate), EMC (ethyl methyl carbonate) at different volume ratio depending the manufacturers. But a variety of electrolyte solutions, including ethers (THF and glyme), esters (butyrolactone and methyl formate) are also possible and tested at a laboratory level. Alkyl carbonates and particularly ethylene carbonate (EC) have been chosen because of their ability to form stable carbonaceous compounds during their first electrochemical reduction on carbon electrodes [19, 28, 29, 30]. Moreover, electrolyte additives as vinylene carbonate (VC) is used in order to stabilize the SEI and to allow the decrease of the irreversible capacity lost during first initial charge [47]. These solid decomposition products create a protective film preventing the later intercalation of solvated lithium ions. It protects also the lithiated graphite from further reaction with the electrolyte. Thanks to this film, electronically insulating and ionically conducting, a reversible insertion/extraction of dissolves lithium ions is possible, with a low increase of the graphene interlayer distance, leading to preserve the graphitic structure on time. The latter is thus dimensionally enough stable to not damage the SEI. The Figure 13 gives a schematic model of the SEI formation [26, 31].

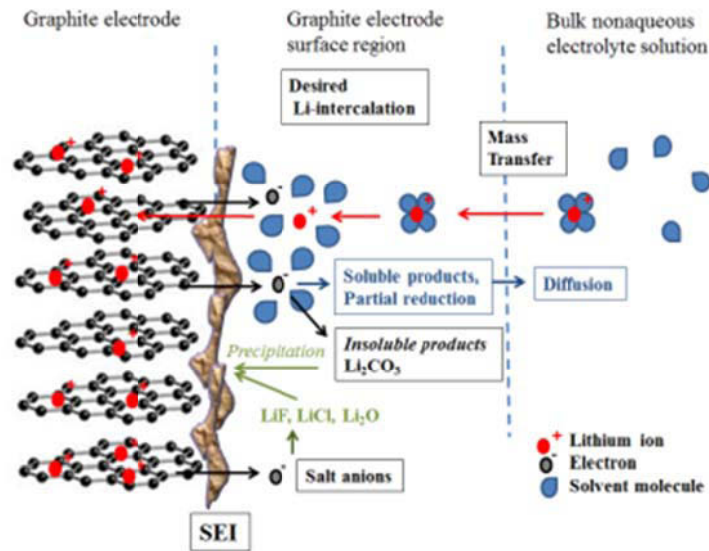


Figure 13: Schematic model of the SEI formation [26, 31].

It is commonly accepted today that the film is composed by an organic part ( $\text{CH}_2\text{-OCO}_2\text{Li}$ )<sub>2</sub>, polymeric part ( $\text{CH}_2\text{-CH}_2$ )<sub>n</sub> and by an inorganic part due to the lithium salt decomposition (for instance, if the salt used is  $\text{LiPF}_6$ :  $\text{LiF}$ ). It is important to note that this decomposition comes along with emission of gas (for instance  $\text{C}_2\text{H}_4$  by reduction of EC). The Figure 14 describes the decomposition reactions for ethylene carbonate electrolyte [16].

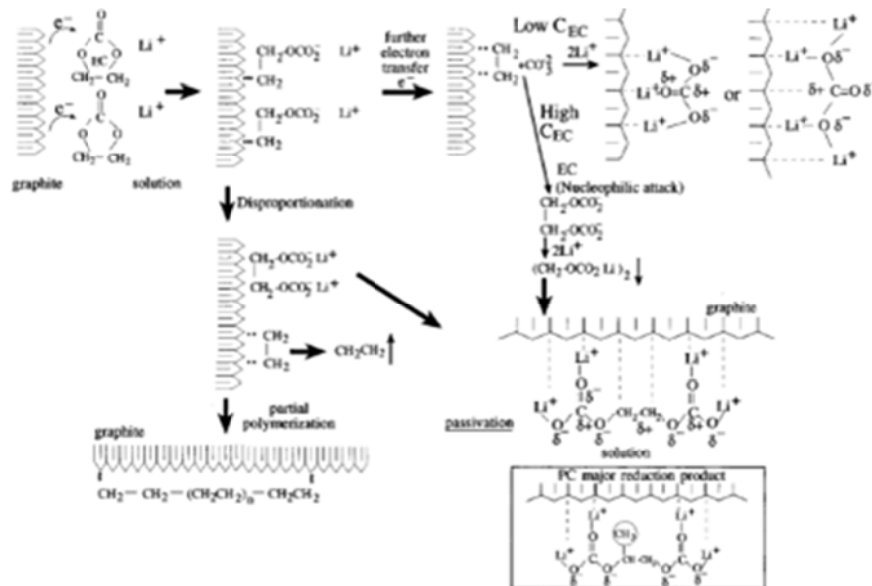


Figure 14: Various reduction patterns of EC on graphite and the possible product distribution (expected major PC reduction product given for a comparison) [16].

### III.3.3. Techniques used to characterize the passivation film

#### III.3.3.1. Electrochemical techniques

##### III.3.3.1. a) Galvanostatic test

During the electrochemical reduction of graphite, the electrolyte decomposition occurs at a higher potential than the insertion of lithium in graphite (about 0.8V vs.  $\text{Li}^+/\text{Li}$ ). This phenomenon can be observed electrochemically at galvanostatic conditions from the potential transient corresponding to the first insertion of lithium inside graphite structure. It is based on the fact that the amount of electricity involved significantly exceeds the theoretical specific capacity of 372 mAh/g. The subsequent process recovers only ~ 80-95 % of this amount of electricity consumed. In the second and subsequent cycles the charge recovery is close to 100% (Figure 15). The excess charge consumed in the first cycle is generally attributed to irreversible reactions related to (a) reduction of impurities like  $\text{H}_2\text{O}$  and  $\text{O}_2$  present on the surface of the graphite and (b) to the passivation film formation on (lithiated) graphite due to the applied strongly negative potential on the graphite (and other carbon anodes) electrode during the lithium intercalation proceeds.

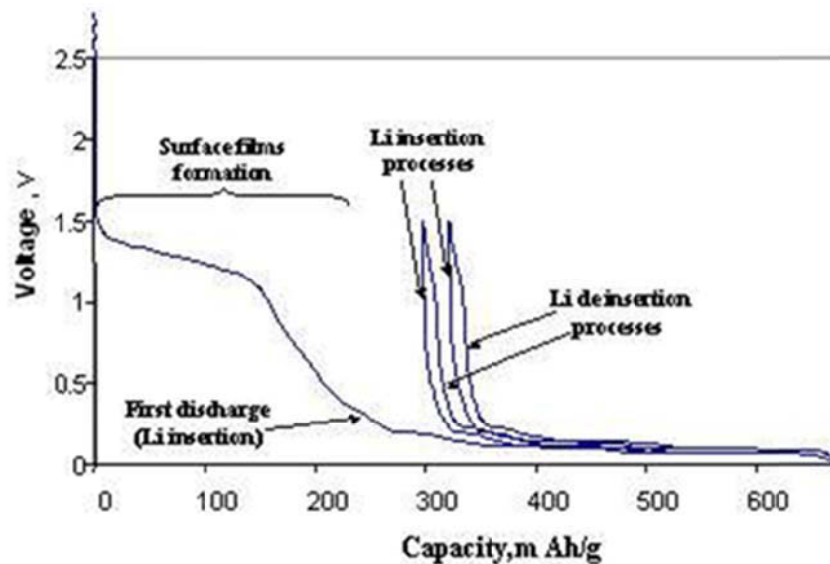


Figure 15: Typical voltage transient (time is transformed to capacity in mAh/g) of a composite graphite electrode comprised of synthetic flakes in EC-DMC  $\text{LiPF}_6$  1M (lithium as counter electrode) during the first and the few next cycles at C/10 [32].

The nature of the film and the amount of the decomposed electrolyte also depend on the composition of the electrolyte. Ethylene carbonate based organic electrolytes in combination

with other linear carbonate solvents are systematically presented because they tend to form a compact SEI layer [19, 28, 29, 30]. For instance, the electrolyte containing EC-DEC-LiPF<sub>6</sub> shows less electrolyte decomposition, suggesting that systems containing cyclic ethylene carbonate may provide a safer operation for the lithium batteries. The potential of graphite electrodes subjected to formation process in electrolytes which used different combination of solvents, are presented in Figure 16. The observed modifications in voltage profile lead to change in the amount of the irreversible capacity.

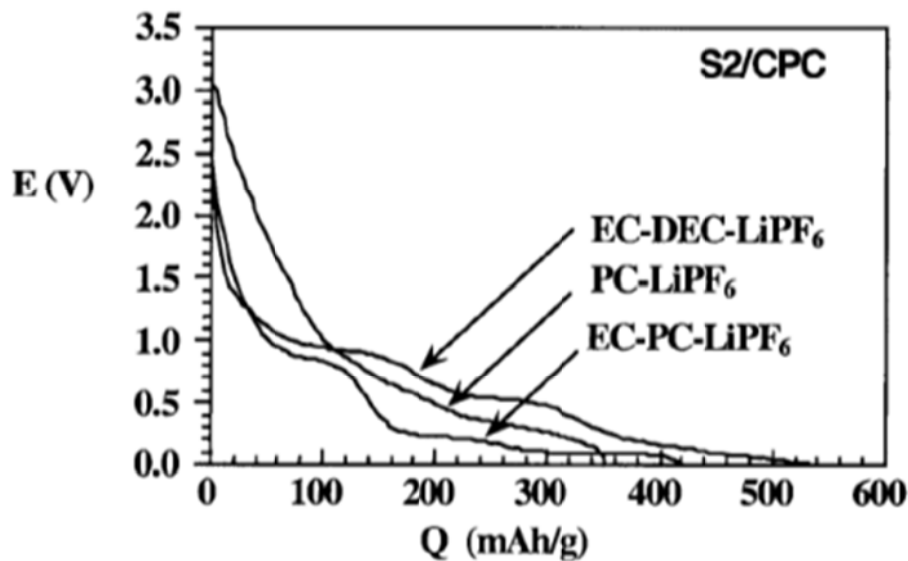


Figure 16: Voltage profile of graphite electrode in different electrolytes [33].

#### III.3.3.1. b) Electrochemical impedance spectroscopy

Electrochemical impedance spectroscopy, or EIS, is commonly used technique to study the electrochemical properties of electrodes and has been largely employed to characterize the process of lithiation of graphite electrodes. The impedance characteristics during cycling provide very useful information on the stabilization mechanisms of Li-graphite electrodes [34, 35]. The Li intercalation in the graphite is a serial multistep process in which Li ions have to pass through the surface films that cover the electrodes, after which the insertion into the carbon is accompanied by charge transfer in the solid state. Figure 17 represents typical EIS spectra of Li/Graphite cells. The large semicircle (high – medium frequencies) belongs to the resistance of Li<sup>+</sup> transport across the surface film coupled with the film capacitance. At low frequencies, the spectrum includes loops corresponding to electrochemical reaction of the intercalation containing the charge transfer resistance of the process and the double layer



capacitance of the interface between the adjacent phases in the graphite particle. The lower frequency part of the spectra is related to the diffusion-limited processes in the system.

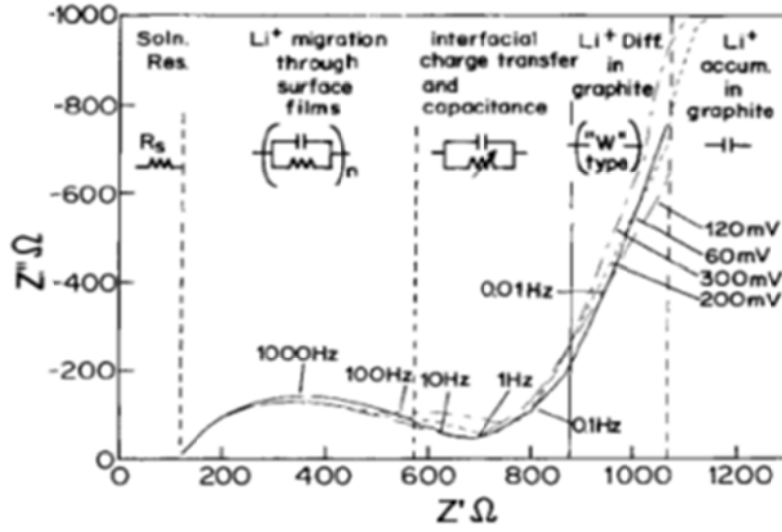


Figure 17 : Impedance spectra of ultrathin electrode at different potentials. The electrode was lithiated - delithiated several times before the measurements in order to stabilize the SEI (electrolyte DMC 1:3 / LiAsF<sub>6</sub> 1M solution) [16].

### III.3.3.2. Physicochemical characterization techniques

Various techniques have been successfully used to characterize SEI: a) techniques providing specific identification of surface species (FTIR, XPS, SEM, TEM), b) techniques which allow *in situ* analysis electrode characterization (Raman spectroscopy, XRD, STM, AFM, EQCM, dilatometry). Some of them can be performed *in-situ* thanks to special experimental set-ups. Acoustic emission technique can be ranked inside this last category [21].

In this bibliographic part, we present only the SEI observation by TEM because it allows to visualise SEI and to determine its thickness [36, 37].

The Figure 18 presents TEM image, of the surface of a carbon black after one cycle in EC/Li. This carbon was chosen because its particle size with dimension 500 and 1000 Å is easily observed by TEM and because its surface border is well defined. A smooth film which covers the carbon particles is observed, corresponding to the passivation film. Its thickness is measured at 1.9 nm.

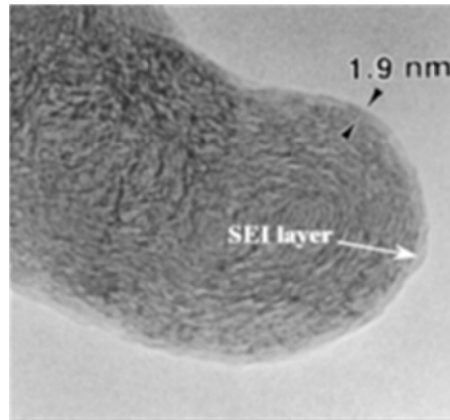


Figure 18 : TEM micrograph of carbon black particle after one cycle in EC/LiClO<sub>4</sub> [37].

#### III.3.4. Ageing phenomena

The degradation phenomena at the positive and the negative electrodes occur in different ways. It is difficult to propose universal cell ageing mechanism because each cell has its own chemistry and because many ageing effects are influenced by the nature of the cell compounds components like active material, electrode design, capacity ratio between the electrodes, electrolyte composition, possible impurities (H<sub>2</sub>O, metallic cations...) etc. The ageing and the corresponding capacity loss can be related to the following phenomena:

- Mechanical changes : particle fractures, formation of gas bubbles,
- Modification or growth of the solid electrolyte interface and lithium plating,
- Structural modification : lattice changes in the crystalline structure of the active materials,
- Parasite reactions: degradation of the possible additives, local corrosion.

Figure 19 summarizes schematically the different mechanisms which lead to the degradation in the Li-ion cell [38].

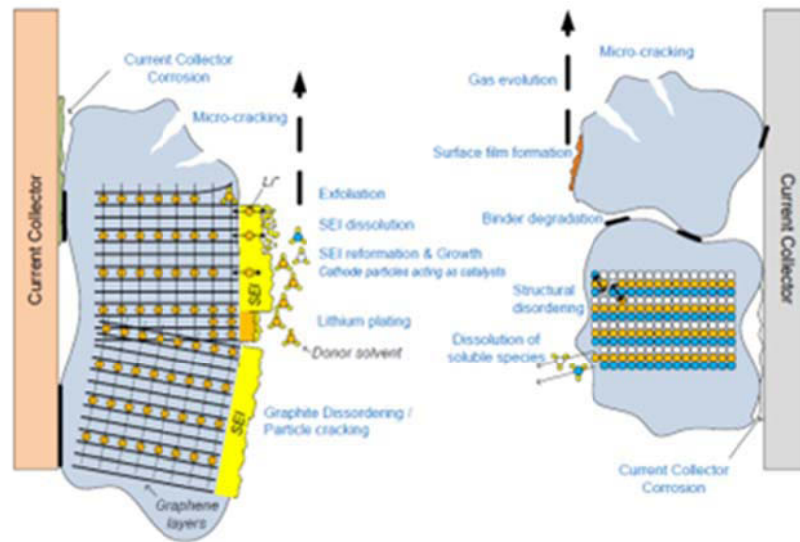


Figure 19: Main aging mechanisms occurring at Li-ion electrodes [38].

According to Figure 19, the main ageing mechanisms for negative and positive electrodes are:

For graphite negative materials:

- Shift during the lithium uptake providing mechanical stress leading to cracking and practical damage,
- Micro-fractures in the passivation film,
- Lithium plating: the electrodeposition of metallic lithium at graphite negative electrode if is recharged at low temperatures ( $T < 1-2^{\circ}$ ) with high current density,
- Contamination: traces of contaminant elements in the electrolyte introduced during the manufacturing process or by electro-dissolution from the positive electrode,
- Corrosion: during overdischarge the graphite electrode polarisation may become more positive than that of the  $\text{Cu}/\text{Cu}^{+}$  or  $\text{Cu}/\text{Cu}^{2+}$  electrodes and the copper current collector may start to corrode,
- Migration of species from one electrode to the other: typically the metal ions dissolved from the positive active materials (phosphates, oxides etc...), are electrodeposited on surface of the negative electrode.

The changes in positive active material which leads to the capacity fading are:

- Degradation of conducting agents, and the binder and corrosion of the current collector,
- Oxidation of the electrolyte components and surface film formation,

- Chemical decompositions, and dissolution of the positive active material.

The process of insertion and extraction of the lithium ions leads to a cyclic change of the molar volume of the materials, which induce mechanical stress, strain and cause the appearance of micro-crackings. The degradation phenomena can be slowed down or accelerated by the profile of the battery cycling and sizing. The latter defines the applied voltage and current density limits, operating temperature and open circuit duration periods.

The quality of the materials (especially the impurities level) and cell design (Amp-hour equivalent ratio negative / positive active material) can also contribute to the degradation rate.

The temperature is a major factor of degradation and change (morphology and composition) of electrodes and their interfaces. The elevated temperature facilitates the kinetics of the lithium insertion/deinsertion process into/from host lattice [39]. However the increasing of the ambient temperature leads to acceleration of electrolyte degradation and corresponding growth of SEI of the negative electrode. The SEI itself can degrade faster at higher temperatures. It has been proposed that at elevated temperature metastable organic SEI compound's like lithium alkyl carbonate are converted into more stable inorganic products (lithium salt like lithium carbonate, lithium fluoride etc.) [40]. Low temperatures leads to slower lithium ion diffusion in the host structures and reduced lithium ion mobility in the electrolyte.

#### III.3.4.1. Overview

The Table 3 provides an overview of the causes and effects of the ageing and mentions which parameters enhance or reduce these effects [19].

Table 3: Lithium-ion negative materials, aging-causes, effects and influence [36, 41, 42].

Cause	Effect	Leads to	Reduced by	Enhanced by
Electrolyte decomposition	Loss of lithium Impedance rise	Capacity fade Power fade	Stable SEI (additives) Cycling rate decreasing with time	High temperature High SOC (low potential)
Solvent co-intercalation, gas evolution and subsequent cracking formation in particles	Loss of active material (graphite exfoliation) Loss of lithium	Capacity fade	Stable SEI (additives) Carbon pre-treatment	Overcharge
Decrease of accessible surface area due to continuous SEI growth	Impedance rise	Power fade	Stable SEI (additives)	High temperature High SOC (low potential)
Change in porosity due to volume changes, SEI formation and growth	Impedance rise Overpotentials	Capacity fade	External pressure	High cycling rate High DoD
Decomposition of the binder	Loss of lithium Loss of mechanical stability	Capacity fade	Proper binder choice	High SOC (low potential) High temperature
Current collector corrosion	Overpotential impedance rise Inhomogeneous distribution of current and potential	Power fade Enhances other ageing mechanisms	Current collector pre treatment	Overcharge Low SOC (high potential of the negative plate)
Metallic lithium plating and subsequent electrolyte decomposition by metallic Li	Loss of lithium (loss of electrolyte) Short-circuit	Capacity fade (power fade) Fast Self-discharge	Narrow potential window	Low temperature High cycling rates Poor cell balance Geometric misfits
Degradation of positive compounds	Dissolution of metallic cations Loss of mechanical stability Loss of lithium	Capacity fade (power fade)	Narrow potential window	High temperature High cycling rates Poor cell balance Geometric misfits

### III.4. Cell construction and material preparation

In this study, home-made: Li/Li, Li/MCMB/, Li/LiFePO<sub>4</sub> and MCMB/LiFePO<sub>4</sub> cells were assembled using of stainless steel coin cells, about 20 mm in diameter and 1,6 mm in thickness. Since lithium reacts with the nitrogen and the water, the cells were prepared in a dry glove-box filled with argon. Details of the different components of the button cell design are shown in Figure 20. The electrolyte used is LP10: LiPF<sub>6</sub> (1mol/L) in PC/EC/DMC (1:1:3 weight), with 2% of VC additive (vinylene carbonate). Figure 20 shows the schematic view of cell design.

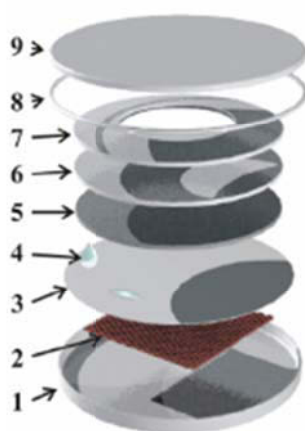


Figure 20: Schematic view of a coin cell design. **1,9** Stainless steel current collectors , **2** Positive electrode material **3** Separator Celgard 2400, Villedon, **4** Electrolyte, **5** negative electrode (diameter 16 mm), **6** Stainless steel spacer, **7** Disc spring (SS Belleville washer style spring), **8** PP ( polypropylene) gasket

#### III.4.1. Fabrication of the negative electrode

The composite electrodes used in this study were made from a copper foil coated with the active material. The active material was composed of 72 wt. % of active material (MCMB), 19.2 wt. % of graphite type SFG6, 2wt. % of carboxy methyl cellulose (CMC) and 2wt. % of nitrile butadiene rubber (NBR). The total thickness of the electrodes was 300μm. Their nominal capacity C is calculated by multiplying the global specific capacity (340mAh/g) by the quantity of graphites MCMB and SFG6. The various home-made cells are denominated by the code “NKM<sub>H</sub>\_number” for Li/MCMB cells.

The manufacturing process of the graphite electrode can be divided roughly into the seven major steps:

- Weight of the components and mixing,
- Mechanical stirring,
- Coating of the active material on current collector (copper foil, thickness 18  $\mu\text{m}$ ) with a scraper knife with dimension 300  $\mu\text{m}$  (I type electrodes) and 100  $\mu\text{m}$  (II type electrodes),
- Compression of the electrode with an equivalent force of 2T,
- Curing of the active materials at 55°C for 24 h,
- Pellet cuttings using a steel punch with diameter 14 mm,
- Heating at 80°C in vacuum overnight (Büchi oven), to remove traces of solvent and water before entering into the glove box.

#### III.4.2. Fabrication of the positive electrode

The composite electrodes used in this study were made from aluminum foil coated with the active material. The latter was composed of 90wt. % of  $\text{LiFePO}_4$ , 2wt. % of super P, 2 wt.% of additive vapor grown carbon fiber (VGCF), 6 wt.% polyvinylidene fluoride (PVDF 6020) dissolved at 1 methyl- 2 pyrrolidone (NMP). The total thickness of the electrode was 300 $\mu\text{m}$ .

Their nominal capacity C is calculated by multiplying the global specific capacity (170mAh/g) by the mass of  $\text{LiFePO}_4$ . The various home-made cells are denominated by the code “NKLH\_number” for cell Li/ $\text{LiFePO}_4$  and “NKMLC\_” for the cells MCMB/ $\text{LiFePO}_4$ .

The manufacturing process for  $\text{LiFePO}_4$  electrode can be divided roughly into the seven major processes:

- Weigh of the components and mixing,
- Mechanical stirring,
- Coating of the active material on current collector (aluminum foil, thickness 18  $\mu\text{m}$ ) using a scraper knife with dimension 400  $\mu\text{m}$ ,
- Compression of the electrode with the force 10 T,
- Curing of the active materials at 55°C for 24 h,
- Pellet cuttings using a steel punch with diameter 14 mm,
- Heating at 80°C in vacuum overnight (Büchi oven), to remove traces of solvent and water before entering into the glove box.

### **III.5. Experimental study and analysis of the formation process**

All electrochemical and acoustic testing equipment and methods were described in §II.3 and §II.5.

#### **III.5.1. Tests of Li/Li cells**

Firstly Li/Li cell was tested in order to estimate the possible AE activity during charge and discharge process of Li-metal electrodes which are further used in some cells as counter and reference electrodes.

The electrochemical cells Li/Li are cycled in CC conditions with the current rate  $I = 0.02A$  ( $13mA/cm^2$ ). No substantial activity was detected during these experiments. Thus the dissolution of Li from the Li foil or the plating of Li on the foil can be excluded as sources of AE for these conditions. This observation permits the study of acoustic events coming from MCMB/Li and LFP/Li without any interaction due to phenomena appearing in lithium foil.

#### **III.5.2. Formation of Li/MCMB**

##### **III.5.2.1. Introduction**

The formation of Li/MCMB cells was performed galvanostatically with constant current C/20h, and with cycling voltammetry at 50°C. All conditions are presented in Table 4 .



Table 4: Characteristic of the Li/MCMB cells, subjected to Acoustic Emission study.

N° cells	Nominal Capacity [mAh]	Specific Capacity [mAh/cm <sup>2</sup> ]	Formation conditions	Acoustic conditions	Irreversible Capacity loss [%]
NKMH_1	19.38	12.4	CC/CV $I_{ch/dsch} = C/20h$  <i>Charge termination</i> $U = 1 \text{ V vs. Li}^+/\text{Li}$ until $I_{ch} < C/50h$ $T = 50^\circ\text{C}$  <i>Discharge termination</i> $U < 0.1\text{V vs. Li}^+/\text{Li}$	Threshold = 25 dB Band Pass Filters from 100kHz to 1Mhz Preamplifiers gain 60dB R15 sensor	18
NKMH_2	17.68				6
NKMH_5	19.72				27
NKMH_6	18.36				22
NKMH_8	19.38				24
NKMH_14	17.34				19
NKMH_15	17.34				22
NKMH_13	18.36		CC/CV $I_{ch/dsch} = C/100h$  <i>Charge termination</i> $U = 1 \text{ V vs. Li}^+/\text{Li}$ until $I_{ch} < C/50h$ $T = 50^\circ\text{C}$  <i>Discharge termination</i> $U < 0.1\text{V vs. Li}^+/\text{Li}$		24
NKMH_12	18.36		Potentiodynamic ramp		-
NKMH_16	18.36		From 1V to 0.1V vs. $\text{Li}^+/\text{Li}$ With $4\mu\text{V/s}$ $T = 50^\circ\text{C}$		-

### III.5.2.2. Results presentation and preliminary analysis

The acoustic activity measured during electrochemical tests could be represented in different ways. For example the Figure 21 shows the acoustic activity in terms of Amplitude or Absolute Energy versus time (Figure 21a and Figure 21b). It is also possible to represented AE in cumulative form (Figure 21c and Figure 21d).

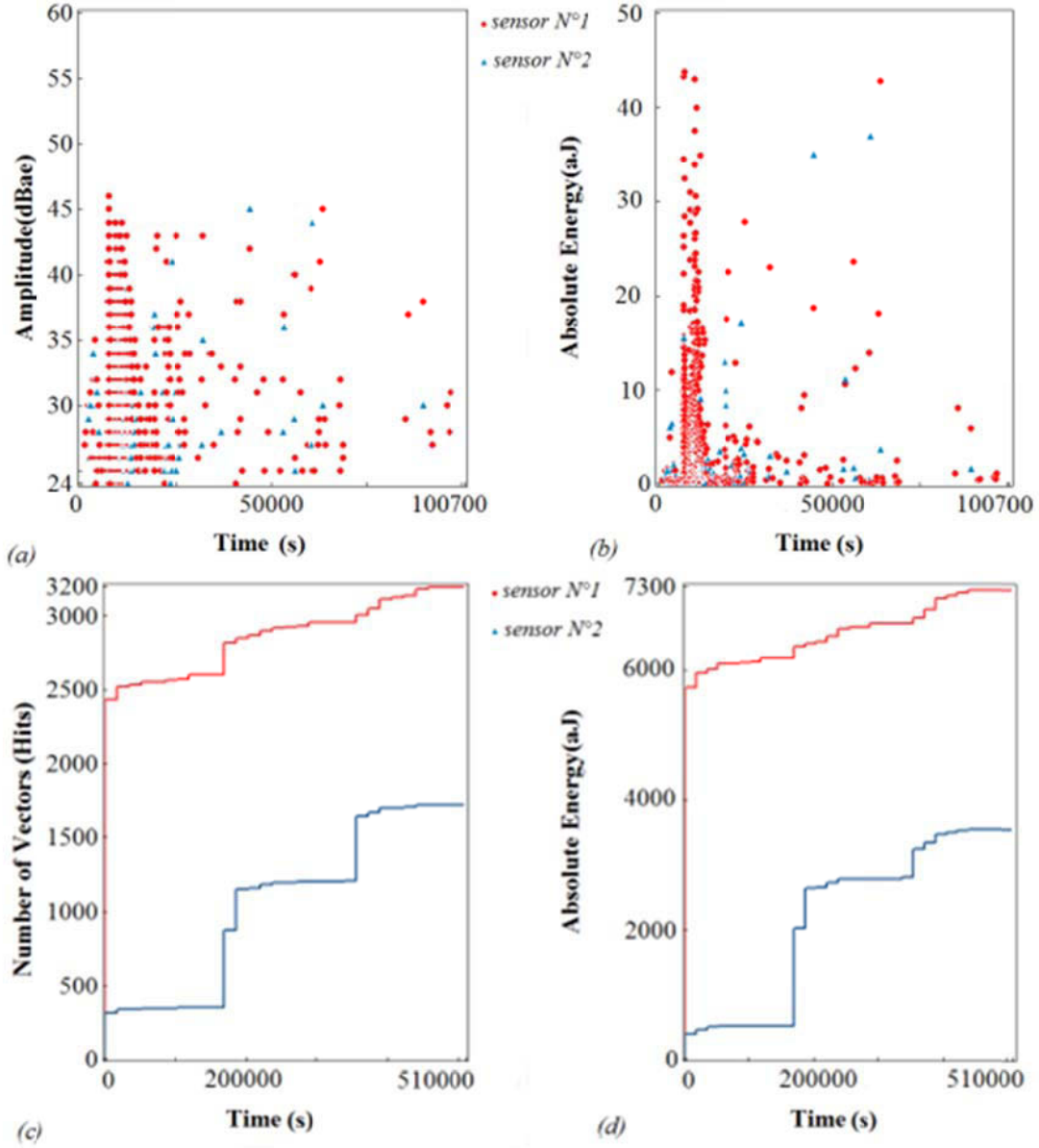


Figure 21: Typical plot from Acoustic Emission monitoring experiment: (a) Amplitude as a function of the time, (b) Absolute Energy as a function of the time, (c) cumulated hits as a function of the time and (d) Absolute Energy as a function of the time. The recording is made in the same conditions.

The AE activity on the lithium side is lower and less intensive than on the other one. In order to check if this difference is not due to the piezoelectric sensor sensibility, sensors 1 and 2 have been switched. In this second experiment, a lower acoustic activity is recorded by the sensor located on the lithium side as expected. This difference could be due to the fact that firstly the acoustic activity on the lithium/electrolyte interface is very low and secondly the acoustic signals produced at the graphite/electrolyte interface must pass through the electrolyte, the separator and the lithium foil to reach sensor 2 (as represented in Figure 22). For the other

side, the acoustic signals pass only through the graphite electrode. Moreover, because the lithium foil is a ductile metal, the acoustic signals could be strongly reduced by going through it.

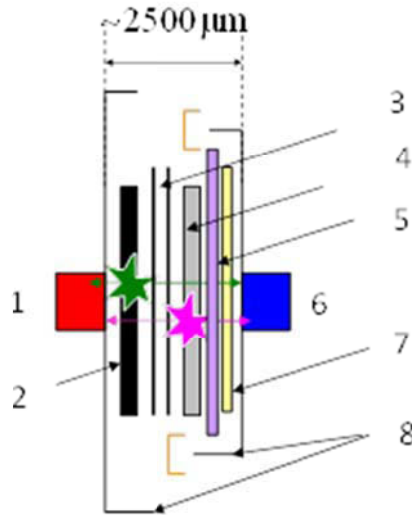


Figure 22: Schema of coin-cell: **1** - sensor 1 connected to the Graphite electrode, **2** - Graphite electrode with the current collector Cu with thickness 150  $\mu\text{m}$ , **3** - Villedon and Celgard separator, thickness 150  $\mu\text{m}$ , **4** - lithium foil (thickness 140  $\mu\text{m}$ ), **5** - disc stainless steel used as support for Li foil (thickness 500  $\mu\text{m}$ ), **6** - sensor 2 connected to the Li electrode with thickness 150  $\mu\text{m}$  (Sensor 2), **7** - spring (thickness 500  $\mu\text{m}$ ), **8** - casing and polypropylene gasket (thickness 1000  $\mu\text{m}$ ).

### III.5.2.2. Acoustic emission activity during formation of SEI

Figure 23 and Figure 24 present the AE activity in terms of cumulative hits (CH) and cumulative absolute energy (CAE) during the formation process (first graphite lithiation).

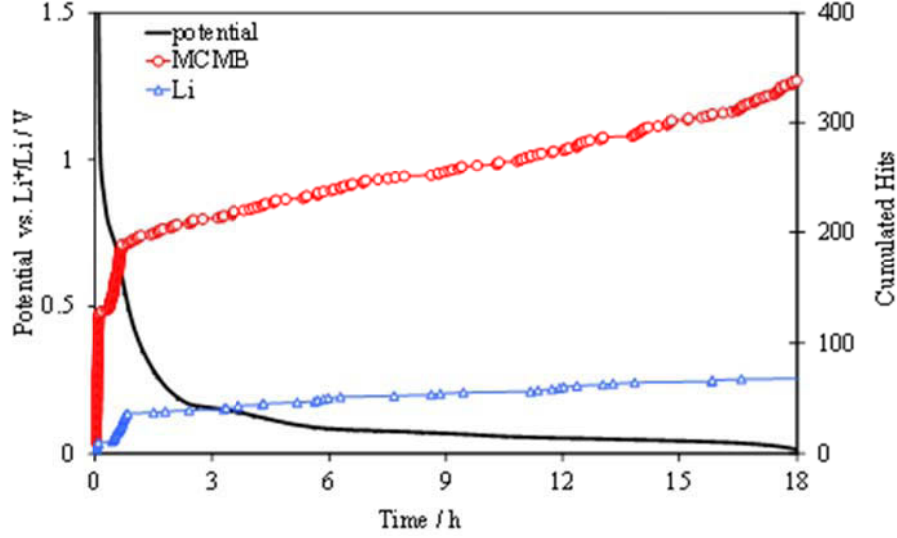


Figure 23: Evolution of the cumulated hits and the cell voltage during the formation of the Li/Graphite cell. The red curve corresponds to the evolution of hits from sensor 1 (graphite electrode) and the blue one from sensor 2 (Li foil).

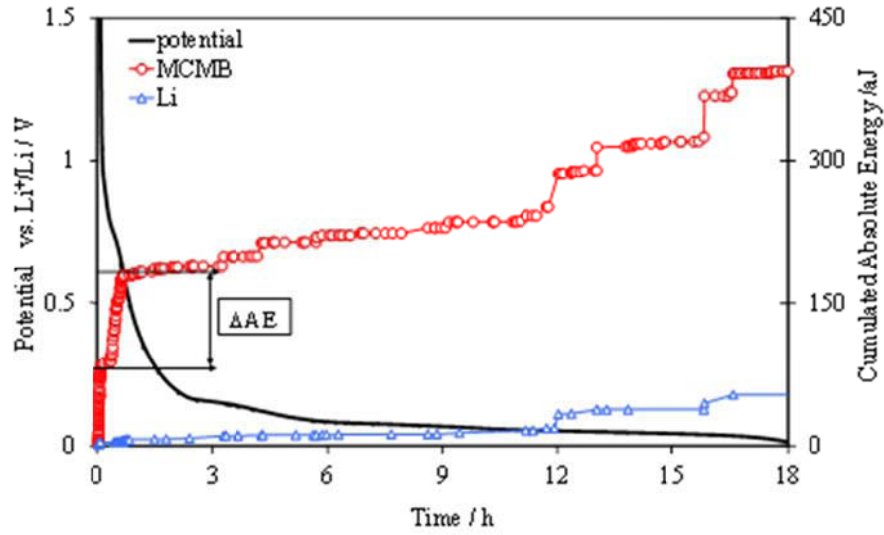


Figure 24: Evolution of the cumulated absolute energy and the cell voltage during formation of Li/Graphite cell. The red curve corresponds to the evolution of cumulated absolute energy from sensor 1 (graphite electrode) and the blue one from sensor 2 (Li foil).

On both figures, three main domains can be recognized:

- in the first minutes of the current application, a sharp increase of the acoustic activity is observed. This activity could be attributed to an initial stress on the electrochemical interfaces not yet well understood,
- secondly, another increase in acoustic activity is recorded in the first hour of formation. This acoustic activity appears in the voltage range corresponding to the onset of the passivation film formation on the graphite surface,
- finally, during the rest of the first discharge, new acoustic activity events appear, especially in terms of energy. These “jumps” coincide with the phenomenon of the lithium intercalation.

Figure 25 presents the AE data from Figure 23 in differential form, plotting the number of hits per hour vs. the time.

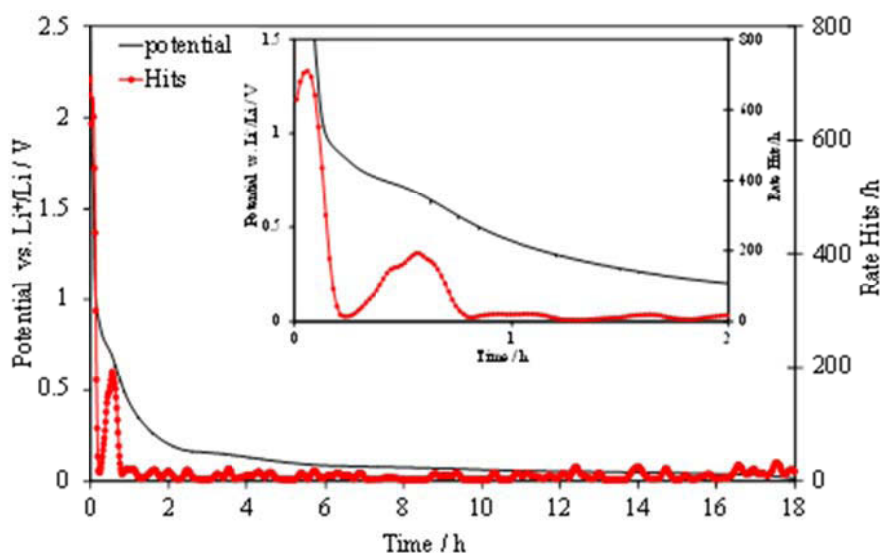


Figure 25: Evolution of the AE rate in terms of cumulated hits per hour and the cell voltage during formation of Li/MCMB. The red curve corresponds to the evolution of cumulated hits from sensor 1 (graphite electrode). Label: focus on the first two hours.

The cell potential transient shows two inflex points. The first one corresponds to the initial current application, the second one begins at potential about 0.8V vs.  $\text{Li}^+/\text{Li}$  and ends when the potential becomes lower than 0.5V vs.  $\text{Li}^+/\text{Li}$ . This activity can be correlated with the formation of SEI.

In order to study more precisely the correlation between the acoustic activity and the region where the major part of the passivation film is formed, the acoustic emission data

activity were plotted versus the potential. The comparison of the normalized AE data as a function of the potential is shown in Figure 26 for a group of Li/MCMB cells.

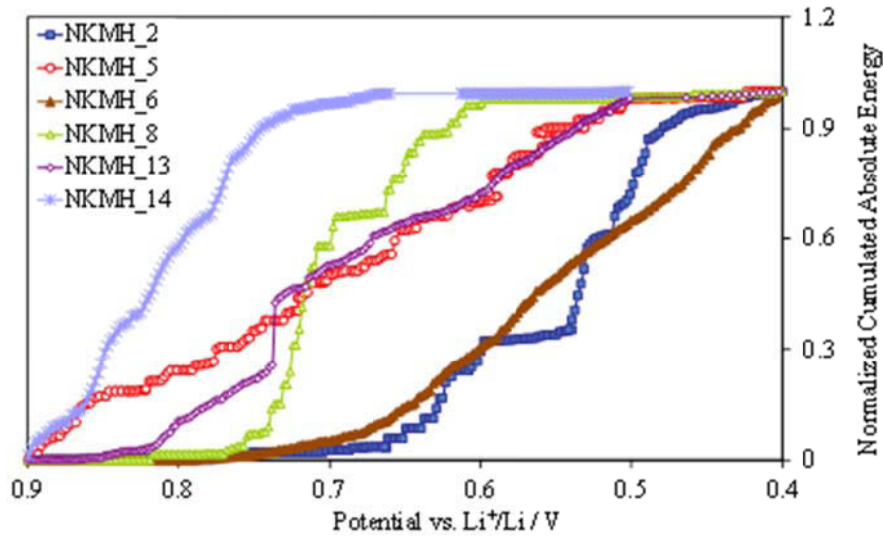


Figure 26: Normalized cumulative absolute energy versus cell potential during the formation of cells Li/MCMB (formation at C/20 except for NKMH\_13 formed at C/100).

The film formation on graphite proceeds with solid compounds deposition and gas formation related to solvents and lithium salt decomposition [20, 43]. It is known that these phenomena generate intensive AE events [44, 45]. As it can be seen, for all the batteries tested, the acoustic activity increases sharply during the first discharge for potentials below 0.9V and stops when the potential reaches 0.4V vs.  $\text{Li}^+/\text{Li}$ . Accordingly, the passivation film that appears usually between 0.8 and 0.5 vs.  $\text{Li}^+/\text{Li}$  implies acoustic events. Note that the AE vs. potential profile during the SEI formation in cell NKMH\_13, using the current is C/100h, is very similar to the other ones corresponding to cells formed with a current equal to C/20h. This result indicates that the AE is rather related to the quantity of the electricity used in the formation of SEI than the intensity of the applied current.

Thus the acoustic emission technique can:

- offers the possibility to detect more accurately the onset of the film formation,
- indicate more precisely the begin and the end of the cell formation.

The cycling voltammogram obtained from tested Li/MCMB cell is shown in Figure 27.

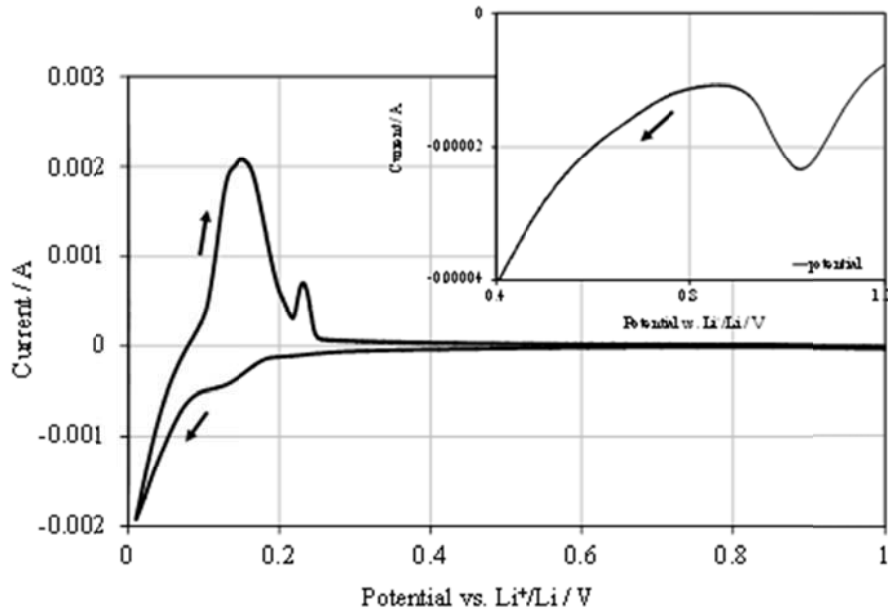


Figure 27: Cyclic voltammogram of lithium/graphite cell (NKMH\_16) in the first charge/discharge cycle with  $4\mu\text{V/s}$ . Inset: zoom on the potential region 1.2 and 0.4V.

During the first cathodic potential sweep, a small reduction peak appears at 1.0V vs.  $\text{Li}^+/\text{Li}$  (see the insert in Figure 27), which can be attributed to the reduction of the electrolyte and the corresponding formation of SEI film on graphite. The peak is shifted to 0.2V compared to the galvanostatic experiments. As the potential becomes more negative, the reduction current increases which corresponds to the insertion of lithium ions into graphite. The two mechanisms are well distinguished due to the slow voltage scan rate applied. Figure 28 presents the voltammetry data only for potentials range 0.4V-1.6V vs.  $\text{Li}^+/\text{Li}$  and the corresponding acoustic activity in terms of hits and energy respectively. The comparison of the voltammogram with the evolution of the AE activity shows that the most intensive acoustic events coincide with the peak of the current corresponding to the formation of SEI. Due to the low rate of the battery formation process, the mechanisms generating AE events are less energetic resulting in a weak acoustic emission activity.

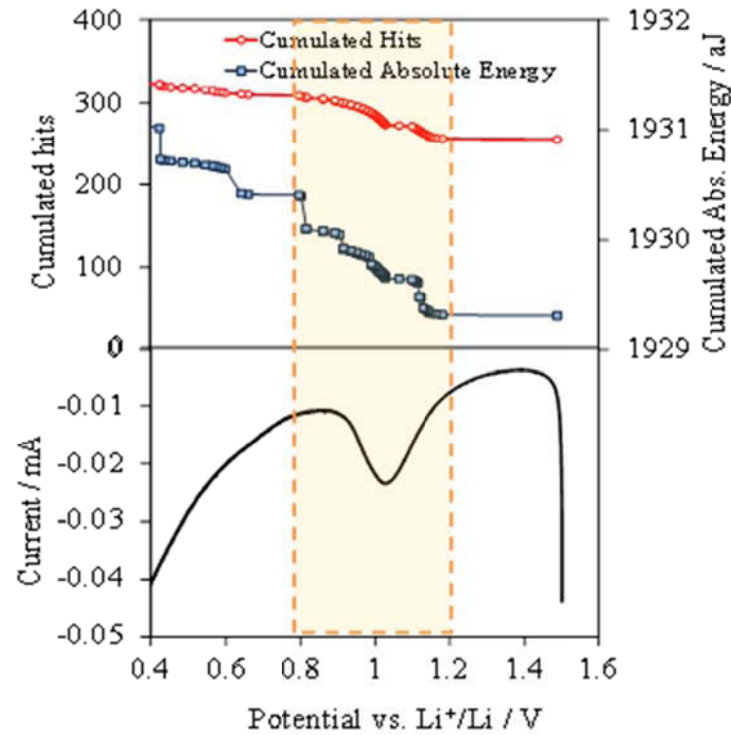


Figure 28: Evolution of the AE parameters (cumulated hits and absolute energy) and the current with the potential during the potentiodynamic formation of Li/MCMB cell (NKMH\_16) with 4  $\mu$ V/s.

Table 5 gives the change of the absolute energy  $\Delta AE$  corresponding to the duration of the formation process for the different cells.  $\Delta AE$  is measured as shown in Figure 24.

Table 5: Change of the absolute energy  $\Delta AE$  corresponding to the passivation film formation and the associated passivation film resistance.

Cell number	$\Delta AE$ (aJ)	$R_f + R_{ct}$ ( $\Omega$ )
NKMH_6	5410	104
NKMH_14	1749	40
NKMH_13	336	66
NKMH_15	234	34
NKMH_2	177	33
NKMH_8	92	-
NKMH_5	66	36
NKMH_1	15	34
NKMH_16	2	17
NKMH_12	1	17



The impedance spectra of the charged cells were measured after three charge-discharge cycles required to stabilize SEI. The obtained results are presented in Figure 29. The spectra are composed of two depressed semi-circles at high and medium frequencies and a tail with a slope close to  $45^\circ$  at low frequencies.

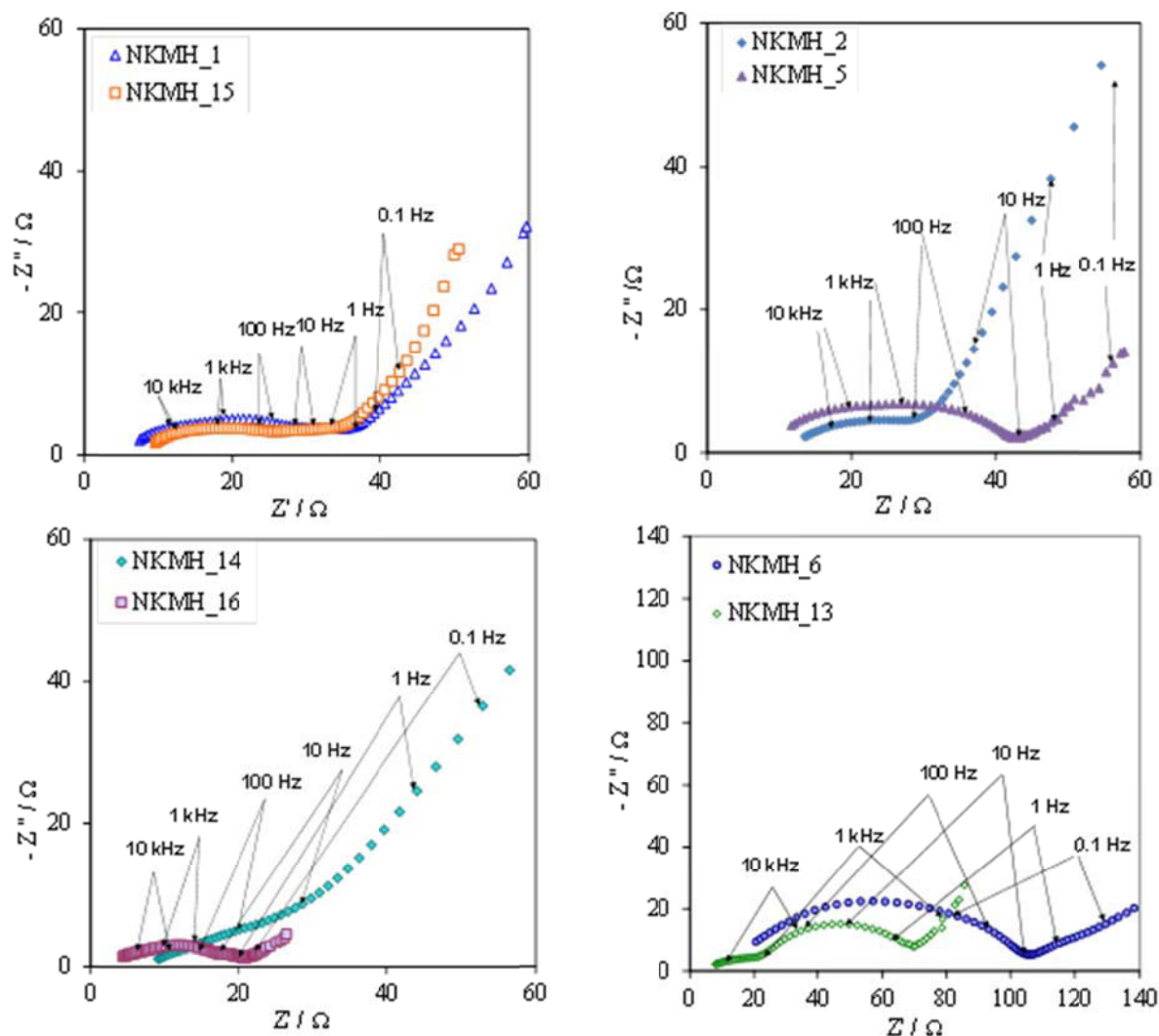


Figure 29: Electrochemical impedance spectroscopy of the different cells tested.

Figure 30 presents the equivalent circuit used in the interpretation of the impedance spectra.

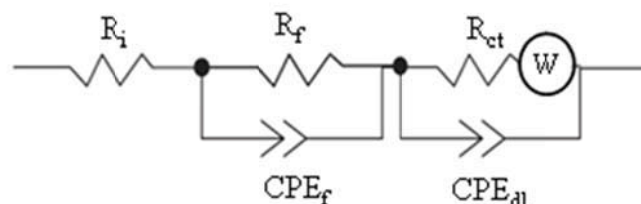


Figure 30: Equivalent circuit used in the interpretation of the impedance spectra of Li/MCMB cells.

The first time constant corresponding to the  $\text{Li}^+$  transfer across SEI can be modelled electrically by the resistance ( $R_f$ ) and the capacitance ( $\text{CPE}_f$ ) of SEI. The second time constant corresponds to the electrochemical intercalation/deintercalation of  $\text{Li}^+$  in the graphite structure and it is comprised by the charge transfer resistance ( $R_{ct}$ ) and the electric double layer capacitance ( $\text{CPE}_{dl}$ ). The straight line observed in the low frequency part of the Nyquist plots can be attributed to the  $\text{Li}^+$  in the solid state graphite matrix. The latter will not be discussed in this work since it does not contribute much directly to the battery performance in terms of energy, power and aging.

The sum of the resistances values relative to the passivation film and the charge transfer ( $R_f + R_{ct}$ ) is listed in the Table 5. The observed values are in the same order of magnitude that is typically observed for this technology using coin cells [46].

The AE energy is plotted vs. SEI and charge transfer resistance ( $R_{ct}$ ) in Figure 31. It can be seen that the high level of AE energy appears to be correlated with a highly resistive passivation film. The latter corresponds to cells with lower power delivery capabilities. Thus the acoustic emission techniques could be used as a tool for identification of well-formed cells. The obtained data are quite dispersed with cumulative AE energy of formation ranging between 15 to 5410 aJ. The lowest value ( $\Delta\text{AE} = 1 \text{ aJ}$ ) corresponding to the formation by cyclic voltammetry is not taken into account. This low value was already explained by the very low current of the process.

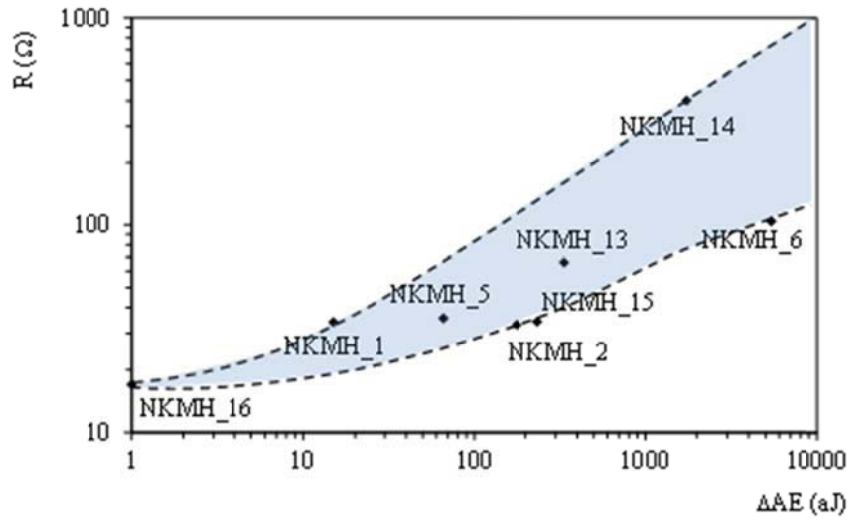


Figure 31: Correlation between acoustic emission energy variations and the passivation film and charge transfer resistance.

### III.5.2.3 Acoustic emission activity during the lithium intercalation

The second part of the cell transformation includes another important phenomenon the first intercalation of lithium ions in the graphite in the potential range between 0.2V and 0.01V vs.  $\text{Li}^+/\text{Li}$ . [47]. Figure 32 focuses on the AE activity on the voltage range corresponding to the lithium intercalation stages [48] for two cells.

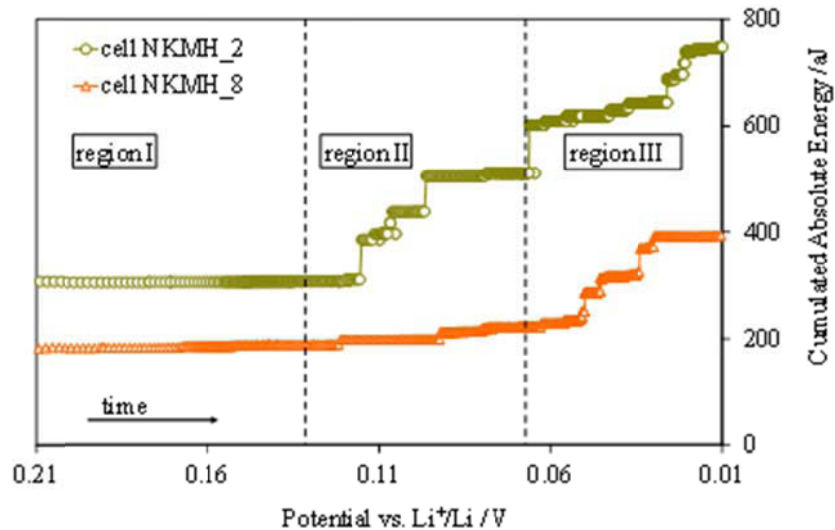
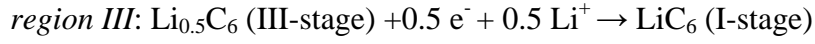
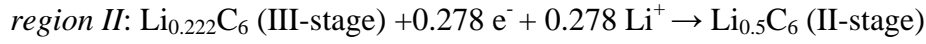
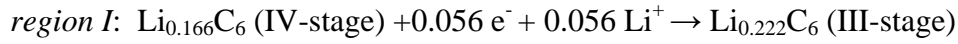


Figure 32: Cumulative absolute energy versus cell potential for two cells during the first lithium intercalation.

The  $\text{Li}^+$  intercalation in graphite proceeds according to the following reactions:



Below 0.21V vs.  $\text{Li}^+/\text{Li}$  (region I), the lithium ions are intercalated between the graphene planes forming the phase  $\text{Li}_{0.222}\text{C}_6$ . The second-stage takes place between 0.130V and 0.065V vs.  $\text{Li}^+/\text{Li}$  (region II) leading to the formation of  $\text{Li}_{0.5}\text{C}_6$ . Finally the complete intercalation is achieved from 0.065V to 0.01V vs.  $\text{Li}^+/\text{Li}$  (region III) forming  $\text{LiC}_6$  [16]. The lithium intercalation corresponds to the opening of graphene planes (moderate and not simultaneous). The increase of the interlayer distance between the graphene layers is small and an insertion plane is completed before the filling of another one leading to a stepwise formation, or so called stage formation, which is energetically favoured over a more random distribution. The diluted lithium stage above (0.130V vs.  $\text{Li}^+/\text{Li}$ ) is hardly detectable by acoustic emission ( $\text{Li}_{0.083}\text{C}_6$  down to  $\text{Li}_{0.166}\text{C}_6$ ). *Table 6* shows the overall AE energy change for the three stages of intercalation mentioned above. The AE energy measured between 0.130 and 0.01V vs.  $\text{Li}^+/\text{Li}$  can be attributed to the opening of the graphene planes during the lithium intercalation. Only the formations of the two richest lithium stages cause the appearance of enough intensive AE activity.

*Table 6: Energy change during the intercalation stages in graphite host matrix.*

Cell number	Stage of intercalation III (region I) $\Delta\text{AE}(\text{aJ})$	Stage of intercalation II (region II) $\Delta\text{AE}(\text{aJ})$	Stage of intercalation I (region III) $\Delta\text{AE}(\text{aJ})$
NKMH_6	346	522	563
NKMH_14	166	98	85
NKMH_13	67	407	3102
NKMH_5	30	42	1348
NKMH_15	13	23	94
NKMH_8	7	166	171
NKMH_2	3	202	237

The average value for the different stages are respectively 100, 240 and 920aJ. The formation of the graphite phases formation [49] requires a supply of energy to :

- Change of sequence of graphitic planes from ABAB to AAAA that is to say the sliding of the layers to align the atoms of carbons one under the others,
- Increase of the distance between grapheme plans (space of the graphitic plans, dp-p, from 0.335 nm to 0.370 nm),
- Increase the distance of the distance of the in-plane carbon-carbon (size of the distances carbon-carbon, dc-c, in the plane from 0.1420 nm to 0.1435 nm).

Figure 33 presents the detected acoustic activity during the first and the second cycle .

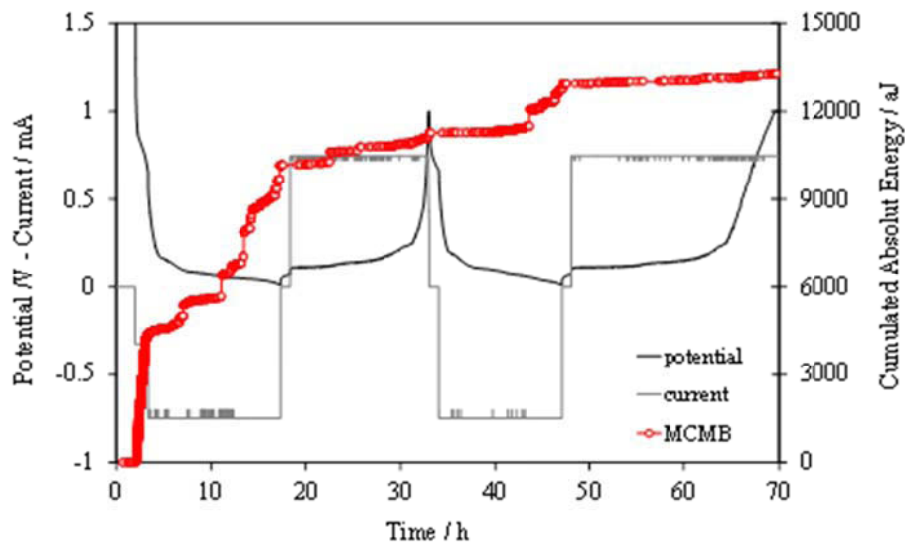


Figure 33: Cumulated absolute energy and cell potential versus time. Red curve corresponds to evolution of cumulated absolute energy.

During the second  $\text{Li}^+$  intercalation in the graphite host AE activity is detected in its end. The first and the second charge (corresponding to the  $\text{Li}^+$  extraction from the previously lithiated graphite) proceeds without significant acoustic activity. This fact confirms that the acoustic activity during the first discharge is well due to the film formation. The absence of notable AE activity during the Li deintercalation can be related to the fact that kinetics of this process is much faster i.e. the inverse process is much easier.

### III.5.3 Formation Li/LiFePO<sub>4</sub>

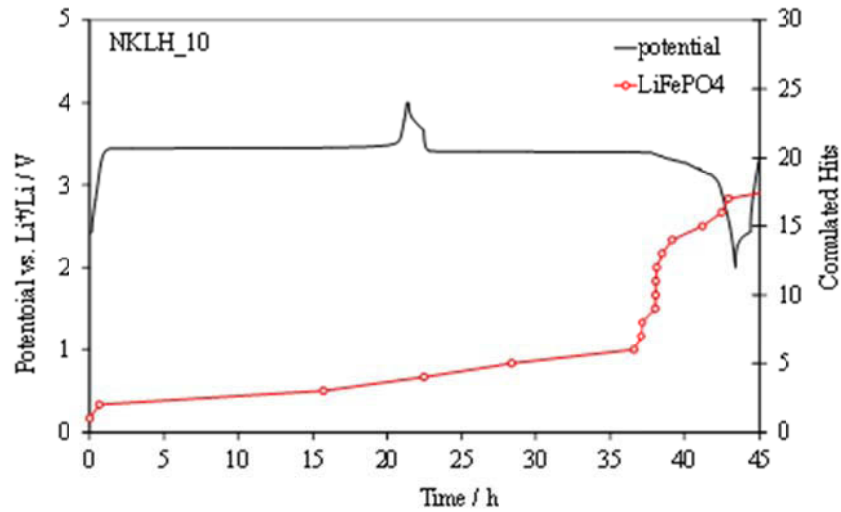
The formation of the cells Li // electrolyte // LiFePO<sub>4</sub> was performed at constant current equal to C/20h between 2V and 4V vs. Li<sup>+</sup>/Li at 50°C. The conditions of the formation process are presented in Table 7.

Table 7: Characteristics of the Li/LiFePO<sub>4</sub> cells.

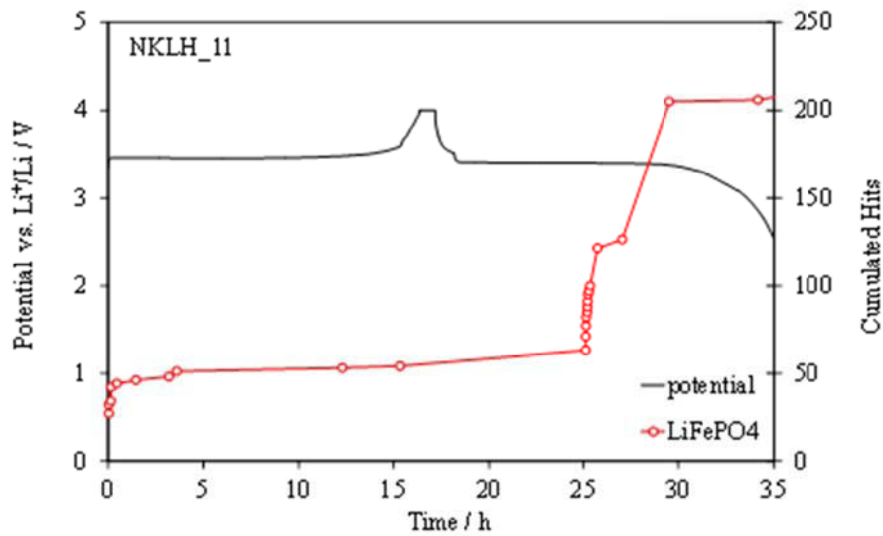
N° cells	Nominal Capacity [mAh]	Specific Capacity [mAh/cm <sup>2</sup> ]	Formation conditions	Acoustic conditions	Active material utilization [%]
NKLH_1	4.11	2.7	CC/CV $I_{ch/dsch} = C/20h$  <i>Charge termination</i> $U = 4 \text{ V vs. Li}^+/\text{Li}$ until $I_{ch} < C/50h$ $T = 50^\circ\text{C}$  <i>Discharge termination</i> $U < 2 \text{ V vs. Li}^+/\text{Li}$	Threshold = 25 dB Band Pass Filters 100kHz - 1Mhz Preamplifiers gain 60dB	89
NKLH_2	4.12				89
NKLH_3	4.11				87
NKLH_4	4.04				88
NKLH_5	4.07				89
NKLH_6	4.04				89
NKLH_7	4.15				86
NKLH_8	4.18				88
NKLH_9	4.11				93
NKLH_10	3.92				88
NKLH_11	4.08				93
NKLH_12	4.06				87

The cells were equipped with a pair of AE sensors coupled with silicon grease on the both sides of the coin-cells. The acoustic emission sensors are the same as the ones used during the experiments on Li/ MCMB cells.

Figure 34 represents the AE activity in terms of cumulated hits (CH) recorded by both sensors: one connected to LiFePO<sub>4</sub> side and the second attached to Li side during the cell formation.



(a)



(b)

Figure 34: Evolution of cumulative hits and cell voltage during the formation of  $\text{Li}/\text{LiFePO}_4$ , (a) cell N° NKLH\_10 and (b) N°NKLH\_11.

The acoustic activity detected by the sensor attached to the negative electrode terminal (Li foil) is lower than the one obtained by the sensor attached to the positive electrode terminal ( $\text{LiFePO}_4$ ). This difference could be related to the fact that the lithium is a ductile metal, and the acoustic signals are strongly dampened by going through it. The same effect was observed at the cells  $\text{Li}/\text{MCMB}$ . Compared to graphite, the structure of the  $\text{LiFePO}_4$  permits easier lithium ion transport (insertion/deinsertion) along the  $b$  axis by requiring minimum energy [5, 9].

Two main domains can be observed during the first cycle (Figure 34):

- In the moment of the current application: a weak increase in acoustic activity is observed for both sensors. The same initial stress was observed during the formation of Li/MCMB cells,
- In the middle of the first discharge: a burst of acoustic activity is observed, with higher intensity at the sensor attached to  $\text{LiFePO}_4$ . This activity could be related to the lithium insertion inside the host structure.

According to the “domino-cascade” model [4, 6],  $\text{Li}^+$  extraction occurs by a progressive emptying of the lithium channels (oriented along the  $b$  axis), perpendicular to the  $ac$ -plane in which the particles are laid (Figure 35). The insertion of the  $\text{Li}^+$  ions starts into the channels that are closer to the  $\text{LiFePO}_4$  phase. The kinetics of lithiation is slower than for delithiation [4, 6, 10]. The latter means that the lithiation process will be considered “noisier” than the delithiation.

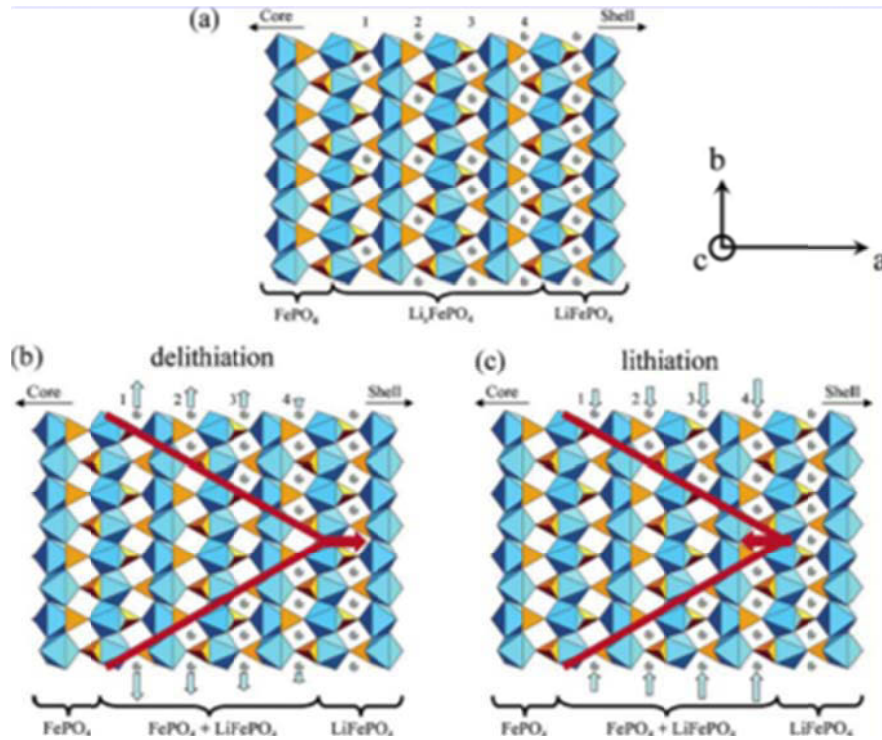


Figure 35: Schematic views of the interfacial region between  $\text{LiFePO}_4$  and  $\text{FePO}_4$  phases, (a) hypothesis of a disordered  $\text{Li}_x\text{FePO}_4$  phase with a gradient of Li content between  $\text{FePO}_4$  and  $\text{LiFePO}_4$ , (b) front phase evolution during delithiation, (c) front phase during lithiation [6].



According to the results from acoustic emission monitoring and considering the models for lithiation and delithiation [6, 10], AE technique could offer a possibility to evaluate more accurately this phenomena.

Table 8 shows the overall AE energy increase during the first charge and discharge. Again, it can be seen that the intercalation of lithium ion is more energetic then the deintercalation (Figure 34).

*Table 8: Energy gap corresponding to the lithium insertion/deinsertion for Li/LiFePO<sub>4</sub> cell.*

Cell N°	$\Delta AE$ (aJ) charge	$\Delta AE$ (aJ) discharge
NKLH_4	53	86
NKLH_16	12	30
NKLH_13	6	13
NKLH_11	5	26
NKLH_10	2	16

#### III.5.4. Formation MCMB/ LiFePO<sub>4</sub> cells

The AE study the formation of “complete” MCMB/LiFePO<sub>4</sub> energy storage system was carried out on two types of cells with different [Ah] ratios between the positive and negative active materials. Typically the negative active material is in  $\approx 10\%$  excess in order to avoid lithium plating in the end of the charge [50]. This case was implemented in the type II cells, where the ration  $C_{PAM} / C_{NAM}$  is equal to 0.7. The case of enormous graphite excess in the cell was implemented in the type I cells where the [Ah] ratio  $C_{PAM} / C_{NAM}$  is equal to 0.2.

##### **III.5.4.1. Formation MCMB/ LiFePO<sub>4</sub> type I**

The freshly prepared MCMB//Electrolyte//LiFePO<sub>4</sub> cells with capacity balance of 0.2 were formed using a charge/discharge cycling at constant current C/20h at 50°C. The cells specifications and test conditions are presented in Table 9.

Table 9: Characteristic of the MCMB/LiFePO<sub>4</sub> type I cells and formation conditions.

N° cells	Nominal Capacity LiFePO <sub>4</sub> [mAh]	Nominal Capacity MCMB [mAh]	Specific Capacity [mAh/cm <sup>2</sup> ]	Formation conditions	Acoustic conditions	Irreversible Capacity loss [%]
NKMLC_1	4.33	25.90	Specific Capacity LiFePO <sub>4</sub> 2.7	CC/CV I <sub>ch/dsch</sub> =C/20h	Threshold = 25 dB Band Pass Filters from 100kHz to 1Mhz Preamplifiers gain 60dB	40
NKMLC_2	4.47	25.39		36		
NKMLC_3	4.37	24.41		39		
NKMLC_4	4.47	25.73		32		
NKMLC_5	4.52	25.49		28		
NKMLC_6	4.29	25.68	Specific Capacity MCMB 12.6	Discharge termination U < 2V vs. Li <sup>+</sup> /Li		37
NKMLC_7	4.52	25.52				32
NKMLC_8	4.49	26.01				43

Figure 36 presents the AE activity in terms of cumulated hits (CH) from both sensors, sensor 1 attached to the LiFePO<sub>4</sub> terminal and sensor 2 attached to the MCMB terminal during the battery formation with constant current.

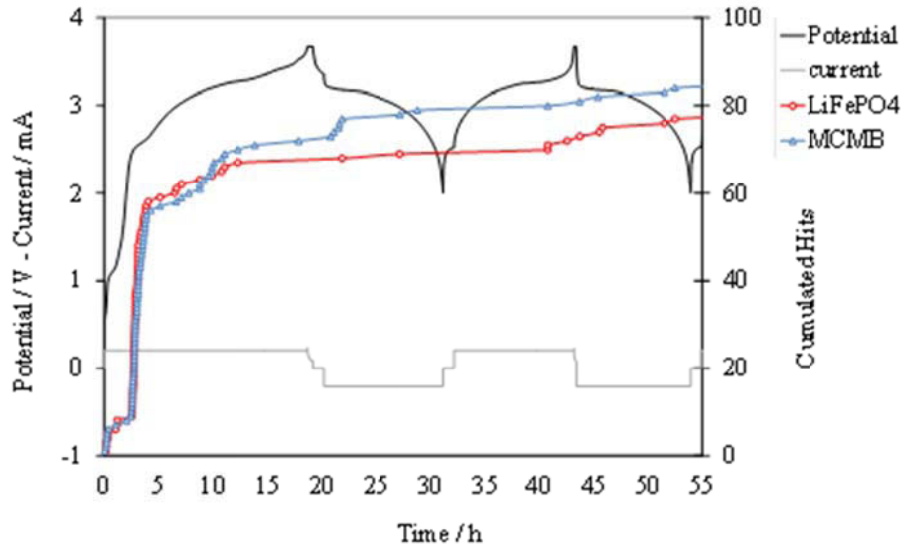


Figure 36: Evolution of the cumulative hits and the cell voltage plotted versus time for MCMB/LiFePO<sub>4</sub> type I cell.

The acoustic activity detected by the sensor attached to the positive electrode terminal (LiFePO<sub>4</sub>) is close to the one detected from sensor on the negative electrode terminal (MCMB). The AE signal is mainly observed during the first charge in the period when the passivation film is formed on the graphite electrode in a way similar to the one observed at the Li/MCMB cells (Figure 36).

In order to compare the acoustic data collected for complete cells with those obtained on Li/MCMB and on Li/LiFePO<sub>4</sub>, the insertion rate ( $x$ ) of lithium was calculated by taking into account the initial capacity of each electrode:

$$\text{Equation 3:} \quad x(t) = \frac{\int_{t=0}^t I dt}{m_e \cdot C_{th}}$$

where  $I$  is the current (mA),  $m_e$  is the active mass of the electrode (g) and  $C_{th}$  is the specific capacity (mAh/g) obtained by the formula:

$$\text{Equation 4:} \quad C_{th} = \frac{zF}{3.6 M}$$

Where  $F$  is the Faraday constant = 96500C,  $z$  is the number of participating in the electrochemical reaction electron and  $M$  is the molar mass of the electrode material (g/mol).

The electrochemical reactions at the positive electrode and the negative electrode during charge and specific capacity values are listed in Table 10.

*Table 10: Electrochemical reactions and specific capacity of the electrode materials in MCMB/LiFePO<sub>4</sub> cells.*

<b>LiFePO<sub>4</sub></b>	<b>Graphite</b>
$\text{LiFePO}_4 \rightarrow \text{FePO}_4 + \text{Li}^+ + \text{e}^-$	$6\text{C} + \text{Li}^+ + \text{e}^- \rightarrow \text{LiC}_6$
$C_{th} = 170 \text{ mAh/g}$	$C_{th} = 372 \text{ mAh/g}$
90 weight %	91 weight %
$C_{PAM} = 154 \text{ mAh/g}$	$C_{NAM} = 340 \text{ mAh/g}$

In our case we have a capacity balance ( $C_{PAM}/C_{NAM}$ ) equal to 0.2. Before formation, the balance is strongly moved towards the negative electrode. During the first charge the insertion ratio  $x$  is equal to 1: the extraction of lithium ions from LiFePO<sub>4</sub> is close to 99%, but only about 60 % of lithium is recovered ( $x \approx 0.60$ ) in the following discharge (Figure 37). This corresponds to irreversible loss of about 40 % of the cell capacity. This phenomenon is due to the low positive to negative active material ratio and the huge surface area of the passivated graphite electrode.

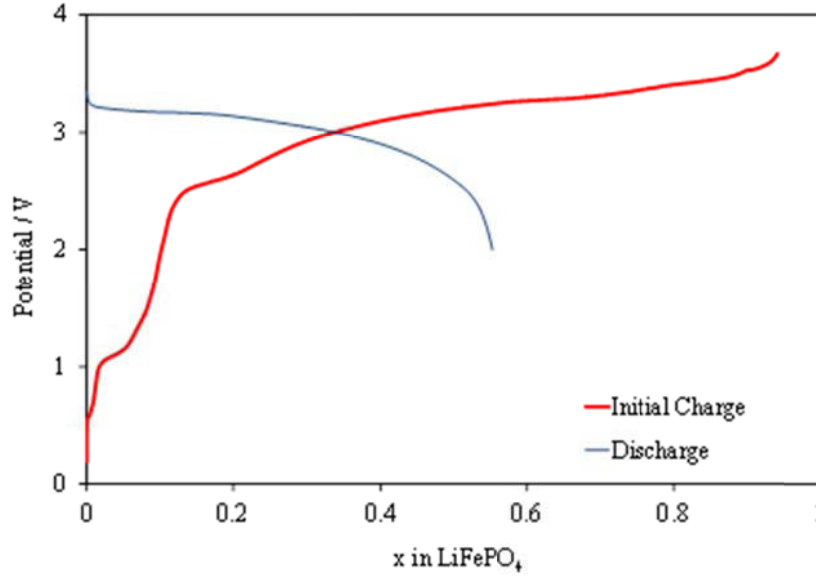


Figure 37: Charge/discharge profile of the cell voltage versus the insertion ratio  $x$  in  $\text{LiFePO}_4$  for the first cycle of MCMB/ $\text{LiFePO}_4$  fresh cells (at  $I = C/20h$ ).

The results obtained for MCMB/ $\text{LiFePO}_4$  cells were compared with the data for Li/MCMB cells using the parameter “State of Formation” SOF presented in Equation 5:

Equation 5: 
$$\text{SOF} = \frac{Q(t)}{C_{\text{th}}} \cdot 100$$

The state of formation is the ratio between the ongoing amount of electricity and total theoretical electrode capacity. For Li/MCMB cell the potential from which the film formation begins is 0.8 V vs.  $\text{Li}^{+}/\text{Li}$ . In the case of a battery it is difficult to determine exactly this potential because the plateau of potential is less well defined. Figure 38 presents the potential transient of the lithium insertion in the graphite in the case of formation of cell Li/MCMB (represented in the black color in the graph). The red line corresponds to the beginning of the formation of a complete battery MCMB/ $\text{LiFePO}_4$ . The comparison of the curves indicates that the film formation in the complete cell starts around 1.25V [51]. The beginning of film formation is denoted by dotted grey line (Figure 38).

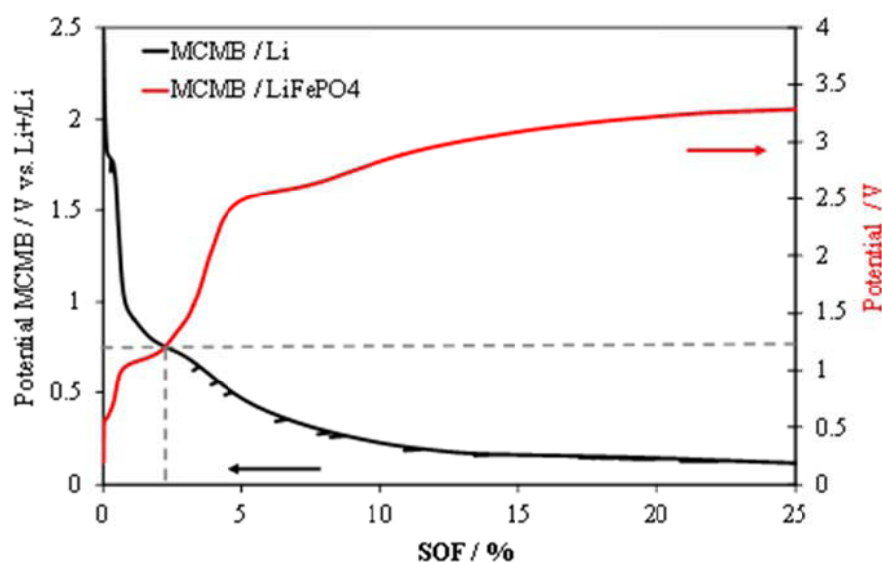
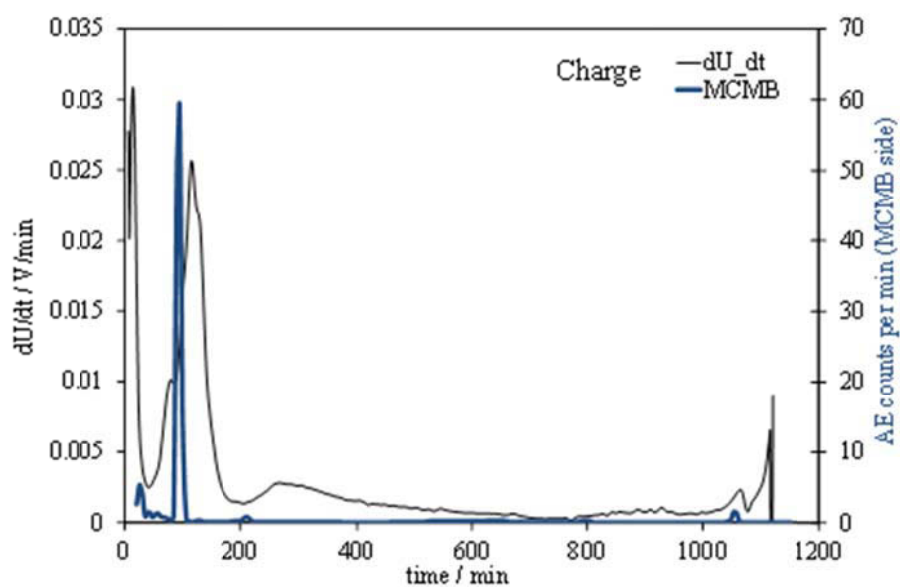
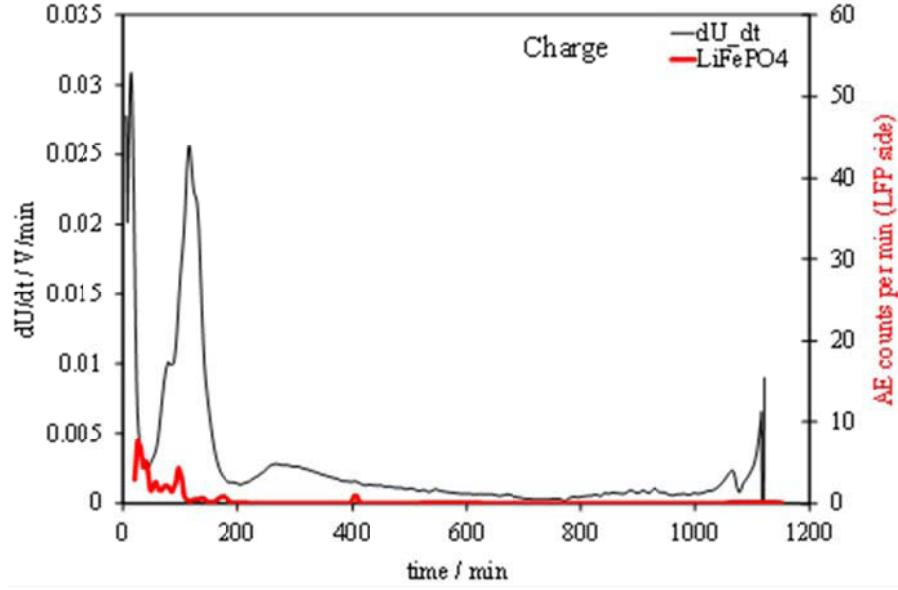


Figure 38 : Potential and cell voltage vs. State of Formation curves for Li/MCMB and for cell MCMB/LiFePO<sub>4</sub> cells.

Figure 39 presents the rate of the acoustic activity expressed in number of counts per minute and the derivative of the cell voltage in V/min versus time.



(a)



(b)

Figure 39: Time derivatives of the potential and the AE counts: recorded by the sensor connected to MCMB terminal (a), and to LiFePO<sub>4</sub> terminal (b).

It is obvious that the acoustic events rate coming from the negative electrode during the first charge is stronger than this obtained from positive electrode. Based on the comparison between the calculated SOF and the acoustic events rates, we can conclude that the acoustic events detected around 1.25V are correlated with the film formation (SEI) and those beyond 1.25V can be related to the lithium intercalation in the graphite.

#### III.5.4.2. Formation MCMB/ LiFePO<sub>4</sub> type II

Several fresh cells was prepared with MCMB/LiFePO<sub>4</sub> electrodes having a capacity balance ( $C_{\text{PAM}}/C_{\text{NAM}}$ ) of 0.7 and formed at 50°C under different conditions indicated in Table 11.

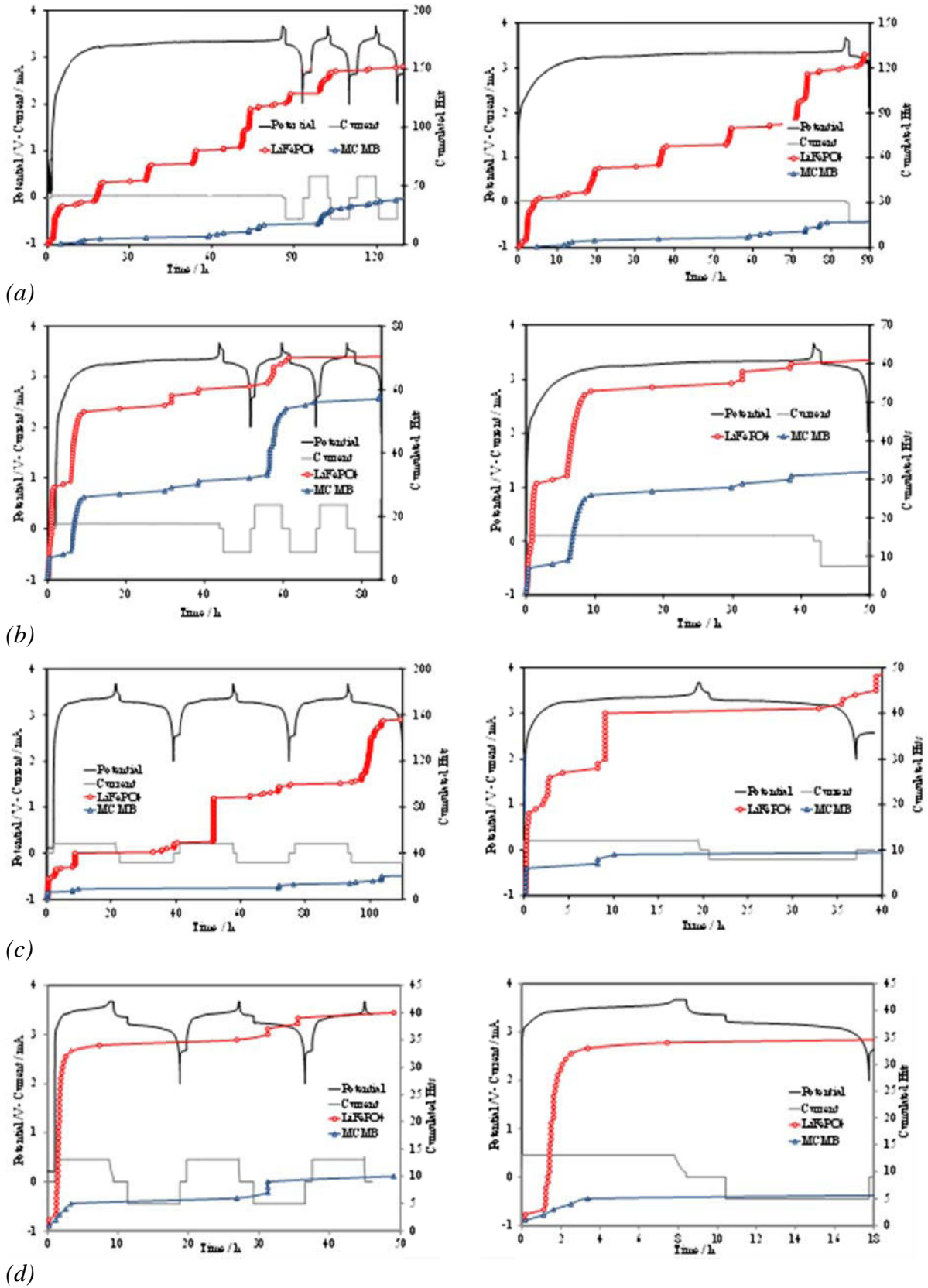
The first charge was carried out with different values at the current: C/100h (NKMLC\_9), C/50h (NKMLC\_11), C/20h (NKMLC\_13), C/10h (NKMLC\_12) and C/5h (NKMLC\_15). The next discharge and the two subsequent cycles were realized at  $I = C/10h$  and at room temperature. The potential limits were 2V for discharge and 3.7V for charge.

Table 11: Characteristics of the MCMB/LiFePO<sub>4</sub> - type II cells and formation conditions.

N° cells	Nominal Capacity LiFePO <sub>4</sub> [mAh]	Nominal Capacity MCMB [mAh]	Specific Capacity [mAh/cm <sup>2</sup> ]	Formation conditions	Acoustic conditions	Irreversible Capacity loss [%]
NKMLC_9	3.69	8.97	Specific Capacity LiFePO <sub>4</sub> 2.8 Specific Capacity MCMB 3.7	CC/CV I <sub>ch</sub> = C/100h U = 3.7V until I <sub>ch</sub> < C/50h T = 50°C	Threshold 25 dB Band Pass Filters 100kHz -1Mhz Preamplifiers gain 60dB Sensor R15	19.03
NKMLC_11	3.88	7.82		CC/CV I <sub>ch</sub> = C/50h 3.7V U = 3.7V until I <sub>ch</sub> < C/50h T = 50°C		20.44
NKMLC_13	4.06	6.91		CC/CV I <sub>ch</sub> = C/20h U = 3.7V until I <sub>ch</sub> < C/50h T = 50°C		18.33
NKMLC_12	3.78	6.80		CC/CV I <sub>ch/dsch</sub> = C/10h U = 3.7V until I <sub>ch</sub> < C/50h T = 50°C		15.45
NKMLC_15	4.06	6.30		CC/CV I <sub>ch/dsch</sub> = C/5h U = 3.7V until I <sub>ch</sub> < C/50h T = 50°C		13.82

The acoustic emission activity was monitored using the same protocols applied during the experiments on Li/Graphite and Li/LiFePO<sub>4</sub> cells. The aim of this study is to associate the acoustic activity and the current rate as well as the connection between SEI electric properties formed at different currents and the calendar aging process.

Figure 40 presents the AE activity in terms of cumulated hits (CH) from both sensor (sensor 1 attached to the LiFePO<sub>4</sub> terminal and sensor 2 to the MCMB side) during the battery formation with constant current.





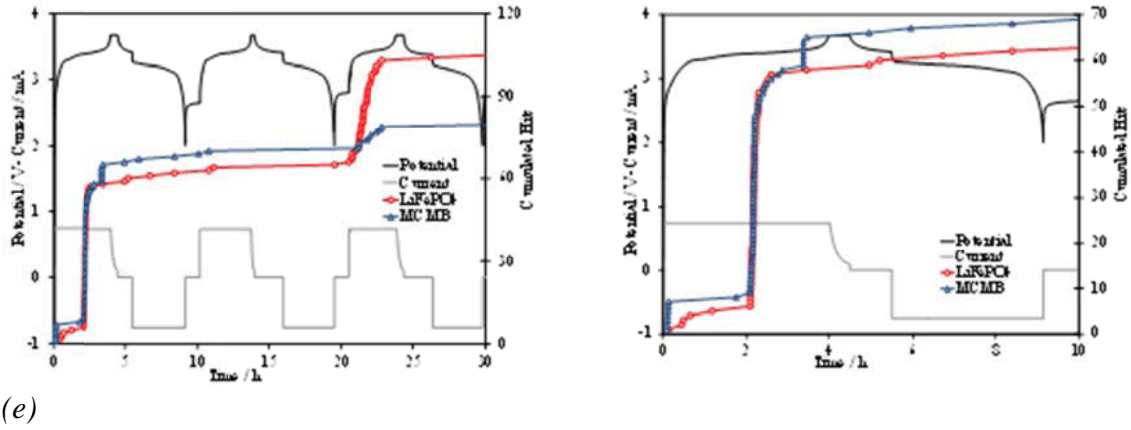


Figure 40: Cumulated hits, cell voltage and current plotted versus time for different cases of the formation current: C/100h (a), C/50h (b), C/20h (c), C/10h (d) and C/5h (e).

Conversely what was previously observed in the cells type I, the AE is less defined and its profile changes from one cell to the other one. It is interesting to note that the acoustic activity obtained from sensor attached to LiFePO<sub>4</sub> electrode is higher than activity detected from sensor attached to MCMB electrode. These differences could be attributed to the mass of the negative electrode materials used on the cells type II (22 mg Graphite in type II against 70 mg in type I).

By observing the voltage profile and the cumulated hits of the acoustic events during the formation with different current rates plotted in Figure 40, it should be noted that the acoustic events during the first charge for the sensor connected to positive terminal (LiFePO<sub>4</sub>) looks like steps. If we summarize the information obtained from the acoustic events during all five different formation current rates, we can conclude that two main domains of acoustic events appear:

- First one at 1.25V,
- Second one between 2V and 3V.

According to that we have shown in paragraph §III.5.4.1, the jump of the acoustic activity at 1.25V corresponds to SEI film formation on MCMB. The acoustic activity between 2V and 3V are more complex to be correlated with electrochemical phenomena inside the cell, being not observed systematically for all the cells. We assume that their origins are still related the MCMB electrode, because such events were not detected during the experiments performed on Li/LiFePO<sub>4</sub> cells. It could be linked to default breach of graphite structure.

Figure 41 presents the comparison between several acoustic emission parameters as amplitude, counts, energy extracted from the acoustic emission experiment during the formation with different current rates. It is interesting to note that the acoustic emission parameters are maximal for the cell formed with current rate C/10h. In contrary, they are minimal for the cells formed with current rates C/50h and C/100h. The process of SEI formation can be considered similar to the processes of electrochemical polymerization. During the latter the application of low current density leads to the deposition of dense layers with low porosity [52]. Thus we can suggest that too high current (C/5h) results in too porous SEI which cannot cover well the graphite surface.

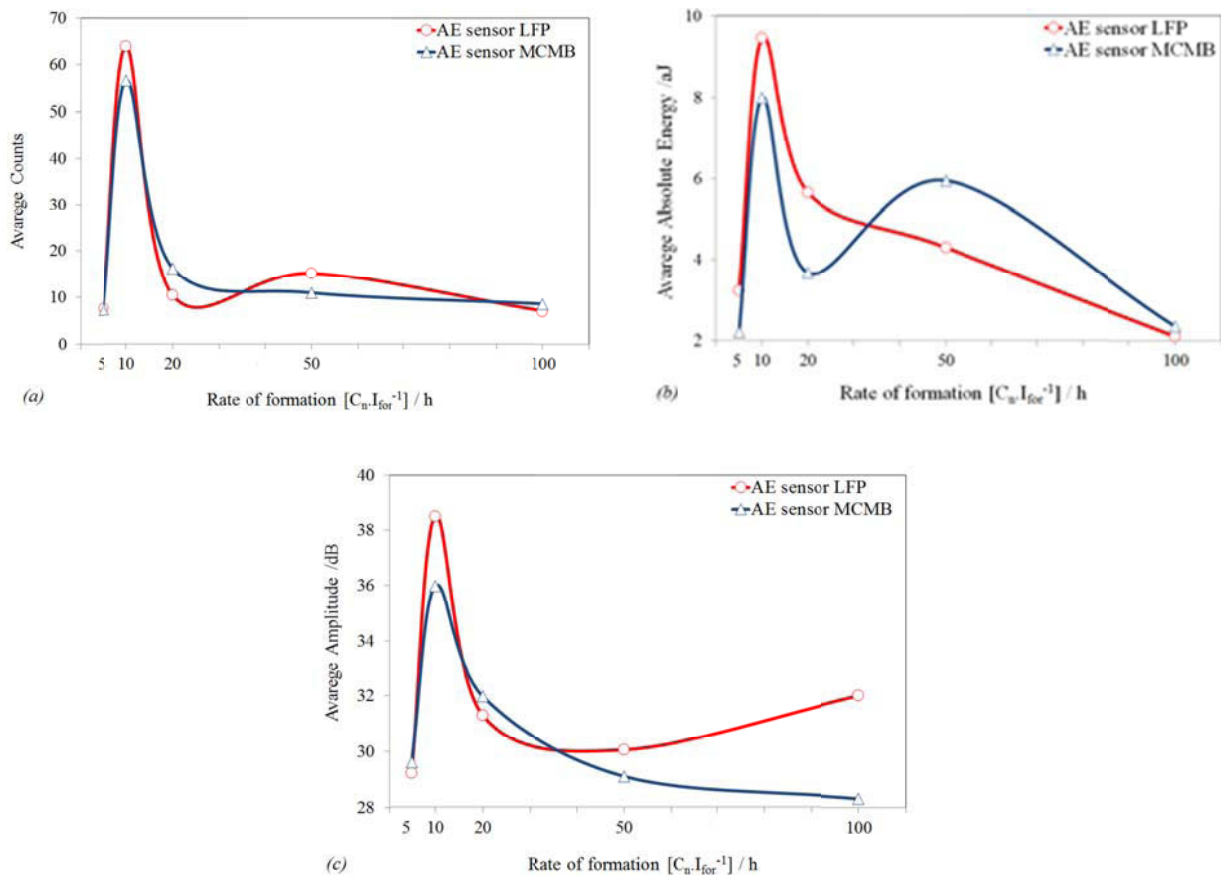


Figure 41: Evolution of the average AE parameters counts (a), energy (b), amplitude (c) vs. rate of formation.

#### III.5.4.3. Spectral analysis of the Acoustic Emission data

The spectral analysis of the AE signals has been done by using Noesis software. AE data obtained during formation of: Li/MCMB, Li/LiFePO<sub>4</sub>, and completed cells type I and II were analyzed. The corresponding AE spectra of the peak frequency parameter are plotted in

Figure 42, for the case of formation with the current equal to C/20h. Two main classes of events can be recognized:

- Class 1: between 100 kHz and 250 kHz,
- Class 2: between 250 kHz and 400 kHz.

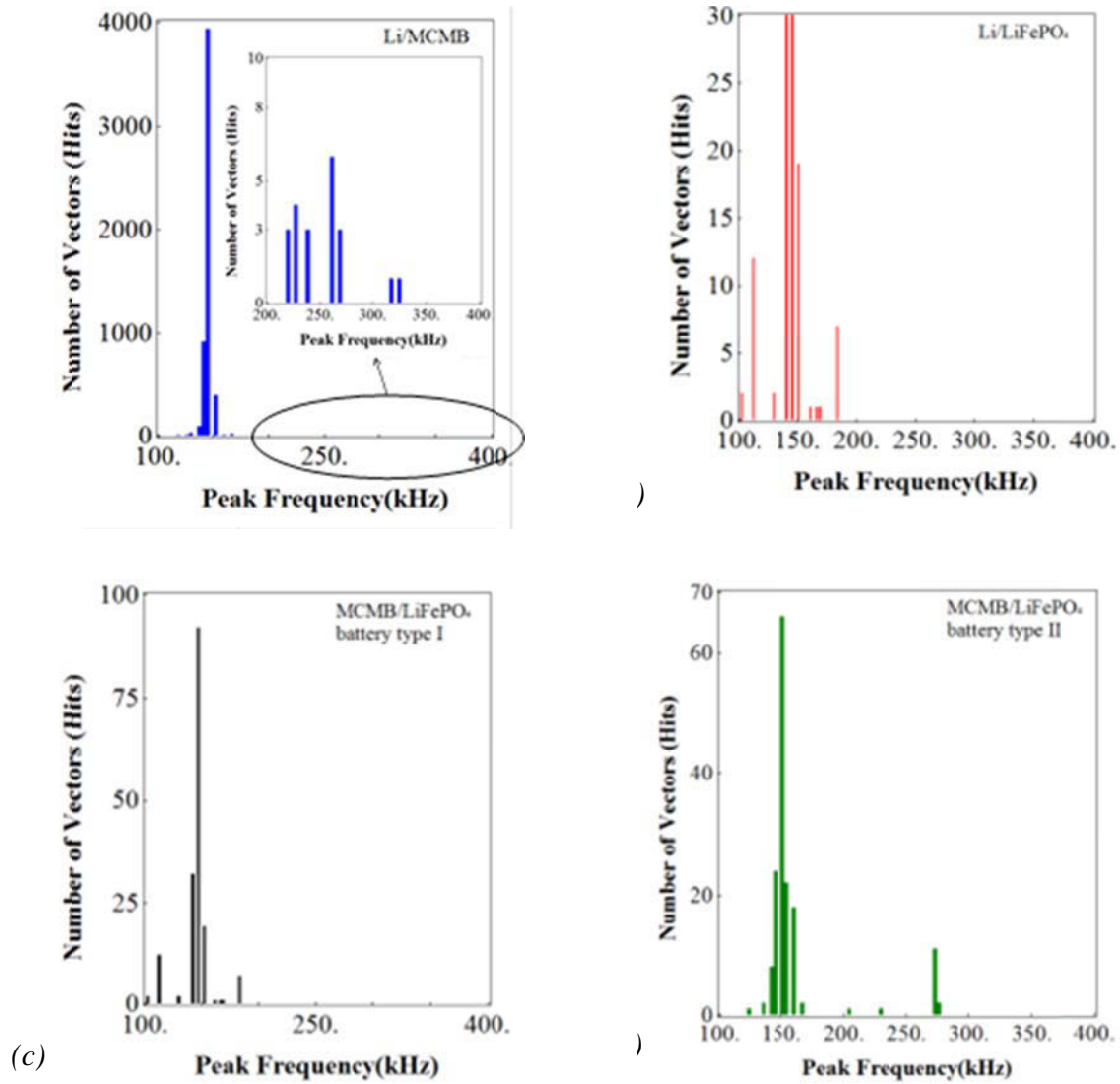


Figure 42: Peak Frequency spectra of the AE signals detected during the formation of cells: (a) Li/MCMB, (b) Li/LiFePO<sub>4</sub>, (c) MCMB/ LiFePO<sub>4</sub> –type I and (d) MCMB/ LiFePO<sub>4</sub> –type II with current equal to C/20h.

The first class of events represents characteristic frequencies between 100 and 250 kHz, large duration, rise time and high energy with maximum of the number of events at 150 kHz. These types of signals are associated with the formation of gas bubbles due to the degradation

of the electrolyte [53]. The fact that they are observed for all four types of cells leads to the suggestion that the electrolyte degradation is related :

- to the gases produced during the SEI formation in the case of graphite/Li
- to gassing phenomena of unidentified origin in the case of Li/LiFePO<sub>4</sub>. If we consider that each acoustic activity event appears in the frequency domain around 150 kHz, the latter could systematically be attributed to gassing phenomena. Such gassing phenomena can be related to impurities in the electrolyte or in the material.

The second class of events is characterized by short duration and rise time and with a main peak frequency of 290 kHz. The frequency domain between 250 kHz to 400 kHz is related to mechanical cracking phenomena [54, 55]. The absence of such events in this frequency domain for Li/LiFePO<sub>4</sub> cell (Figure 42b) can be related to the almost zero change of the FePO<sub>4</sub> lattice during the charge / discharge cycling. For the cells type II the AE events corresponding to mechanical cracking appear in the AE spectra (Figure 42d). However when the Ah-ratio LFP/MCMB is 0.2 (type I) these AE events are absent (Figure 42c). This can be explained with the fact that only a small portion of the graphite is lithiated hence the specific volume of the electrode material changes very slightly during the charge / discharge cycling. This small volume change is not sufficient to induce enough mechanical stress which can cause a cracking.

The Table 12 summaries the main values like duration, rise time, energy, peak frequency, average frequency and amplitude for both classes of events during the formation process of the different cells.

Table 12: Main characteristic parameters recorded for AE population of cells subjected to formation.

N° battery	AE parameters (value for the first formation cycle)	Class1	Class 2
<i>Li/MCMB</i>	Duration ( $\mu$ s)	570	319
	Rise Time ( $\mu$ s)	304	48
	Energy (aJ)	50	18
	Average Frequency (kHz)	400	222
	Peak Frequency (kHz)	139	327
	Amplitude (dB)	47	41
<i>Li/ LiFePO<sub>4</sub></i>	Duration ( $\mu$ s)	790	-
	Rise Time ( $\mu$ s)	202	
	Energy (aJ)	30	
	Average Frequency (kHz)	800	
	Peak Frequency (kHz)	170	
	Amplitude (dB)	52	
<i>MCMB/ LiFePO<sub>4</sub> –type I</i>	Duration ( $\mu$ s)	720	-
	Rise Time ( $\mu$ s)	221	
	Energy (aJ)	94	
	Average Frequency (kHz)	467	
	Peak Frequency (kHz)	185	
	Amplitude (dB)	52	
<i>MCMB/ LiFePO<sub>4</sub> –type II</i>	Duration ( $\mu$ s)	489	156
	Rise Time ( $\mu$ s)	296	30
	Energy (aJ)	20	1
	Average Frequency (kHz)	810	400
	Peak Frequency (kHz)	160	290
	Amplitude (dB)	45	26

### III.6. Calendar aging of the MCMB/LiFePO<sub>4</sub> –type II

After their formation, the cells were stored in thermostatic chamber at temperature 40°C for calendar aging. Periodic check-ups of the battery performance were carried out each two weeks. The check-up test includes CC/CV cycling at current rate  $I = C_n/10h$  for 5 cycles and impedance spectroscopy measurements from 65 kHz to 10mHz with amplitude of 5mV measured at open circuit after completed charge (SOC = 100%) and after completed discharge (SOC = 0%).

Figure 43 represents the evolution of the capacity (measured at the fifth discharge) as a function of the calendar time for the five cells formed at different current rates.

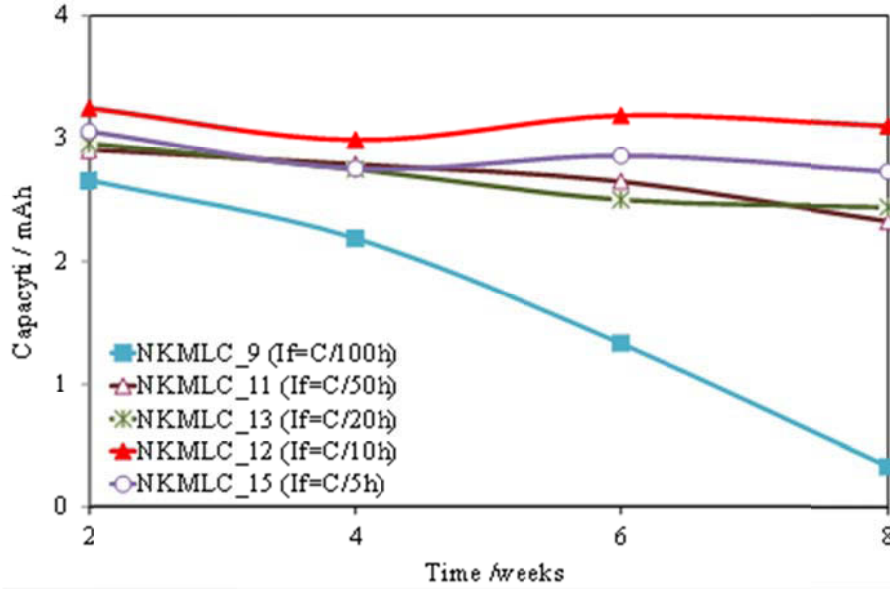


Figure 43: Capacity evolution during the calendar aging at 40°C and SOC=100% for the cells MCMB/LiFePO<sub>4</sub> formed at various current rates.

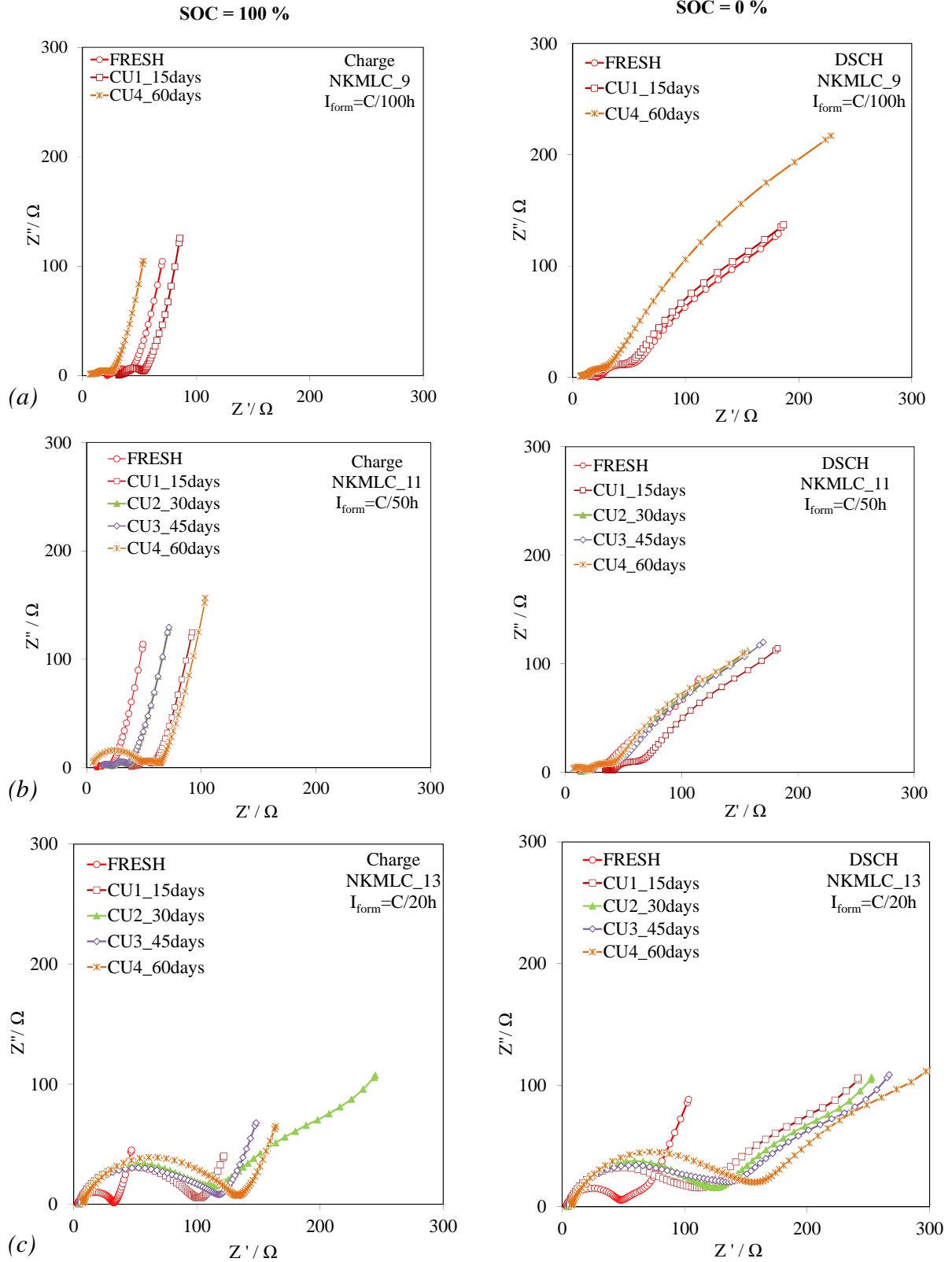
There is a tendency of rapid capacity decay of the cell formed at C/100h current rate. The capacity of the cell formed at C/50h decreases slowly. The cells formed at C/20h and C/5h show the slowest ageing rate, while the capacity of the cell formed at C/10h seems to remain unchanged after 6 weeks of storage.

We can rank the formation current rate from the best to the worst:

$$C/10h \sim C/5h > C/20h > C/50h > C/100h$$

The results obtained from the calendar ageing can be compared with AE events recorded during the formation (Figure 43 and Figure 41). The data show that the cell formed at C/10h exhibits the most intensive AE activity during the formation process. The C/5h formation seems to be suitable to deliver a good calendar aging behavior, while its associated AE activity was not significantly different from those observed at C/20h, C/50h and C/100h current rates.

Figure 44 shows the evolution of the impedance spectra of the cells subjected to calendar ageing in completely charge and completely discharge state.



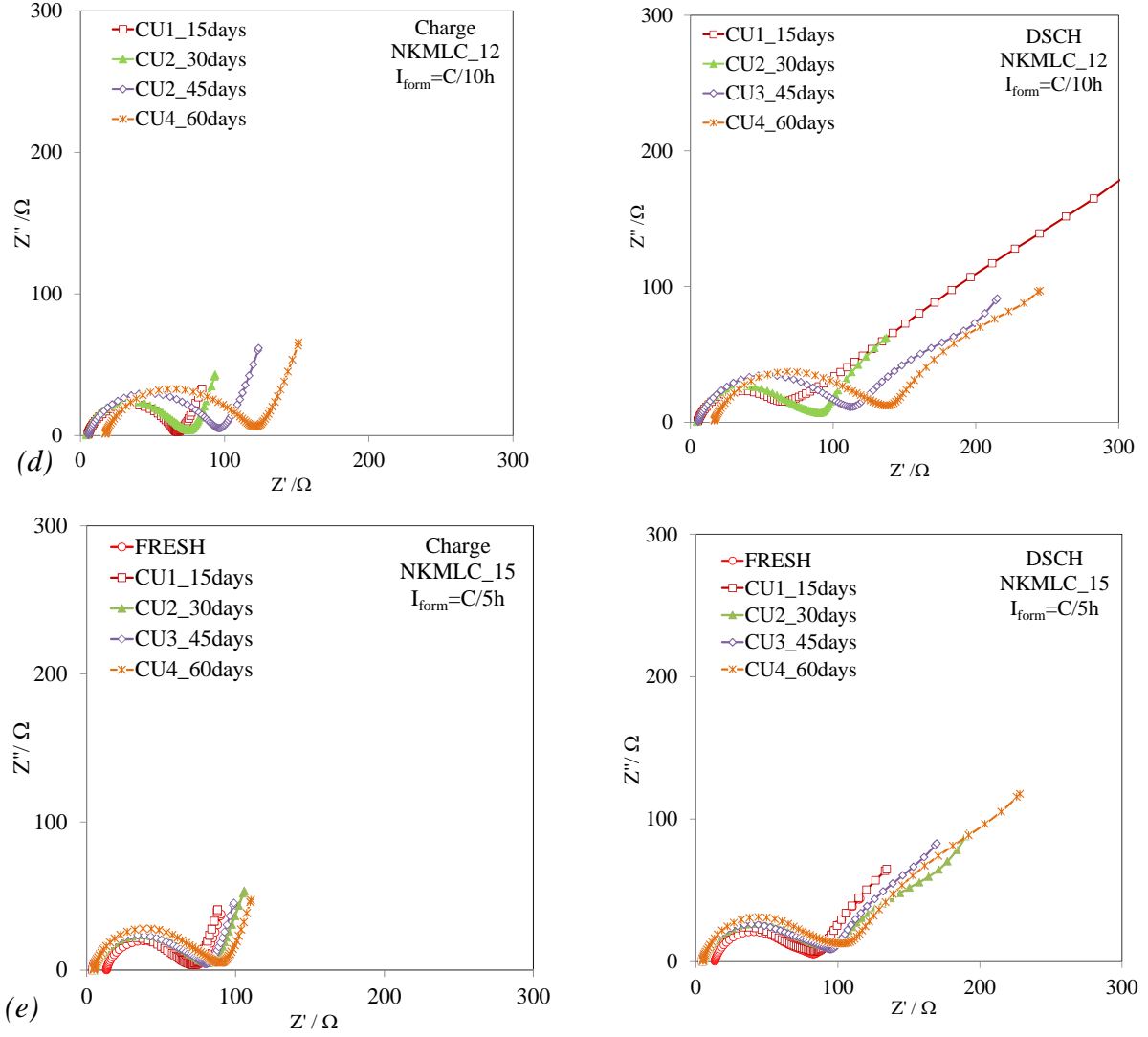


Figure 44: Evolution of the Impedance spectra during the calendar aging test at 100% SOC and 0% SOC: (a) NKMLC\_9, (b) NKMLC\_11, (c) NKMLC\_13, (d) NKMLC\_12, (e) NKMLC\_15.

The shape of Nyquist spectra resembles to the typical data for Li-ion Batteries [56, 57]. According to Barsoukov (Figure 45) the high frequency part of the spectrum contains the internal resistance of the cell (separator, electrolyte, electrode and wires), one or several semi-circuits correspond to the interface and charge transfer resistance, and at low frequencies the straight line typical is related to diffusion phenomena [57]. The model schema of the Li-ion electrode and corresponding equivalent circuit representation are shown in Figure 45. This model is related only to one electrode and electrolyte/electrolyte interface. In the case of complete cell, the both electrodes and their interfaces contribute to the impedance of the cell.



However, to just estimate roughly the resistance part of the cell, we have decided to use the simple model of equivalent circuit.

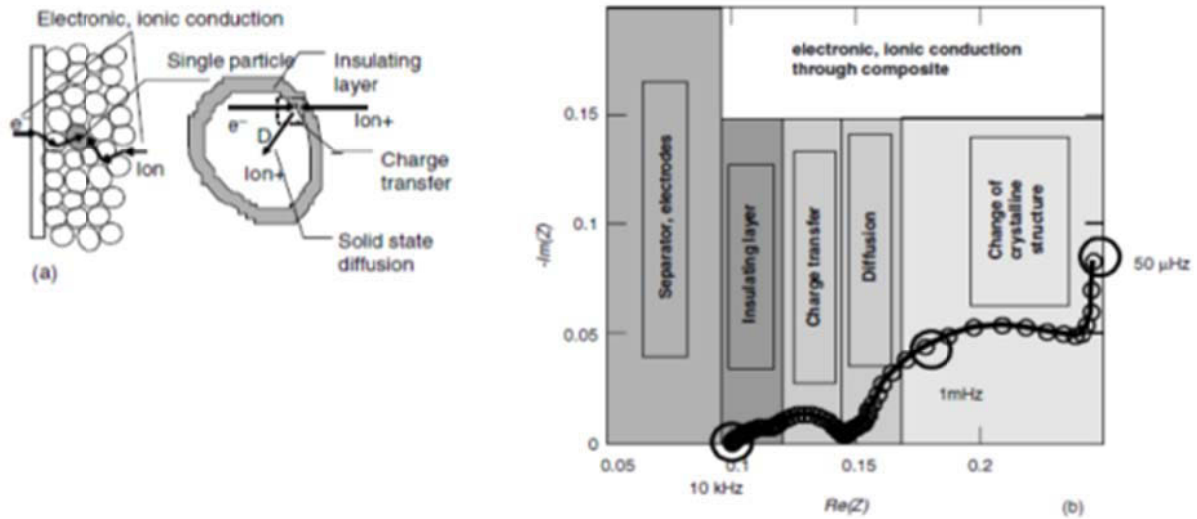
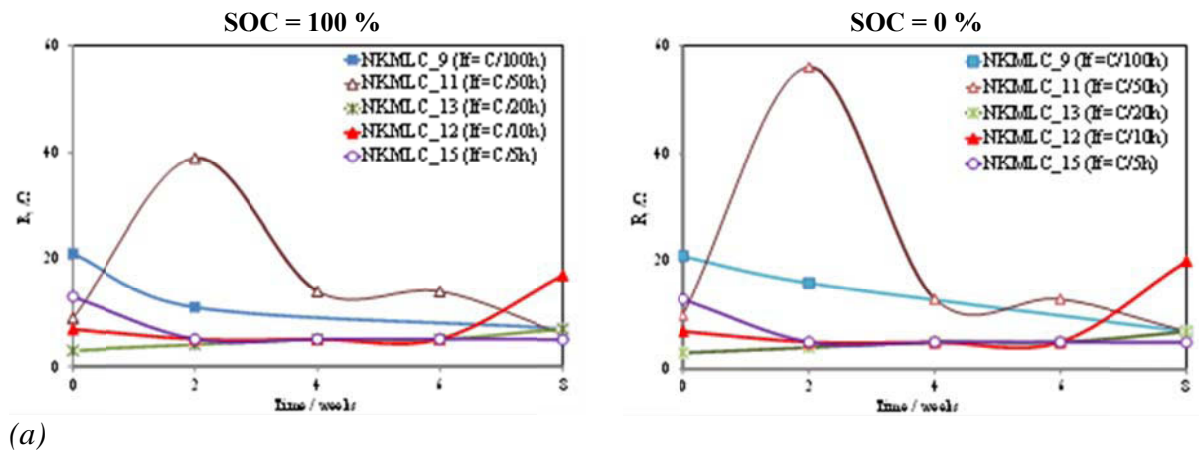
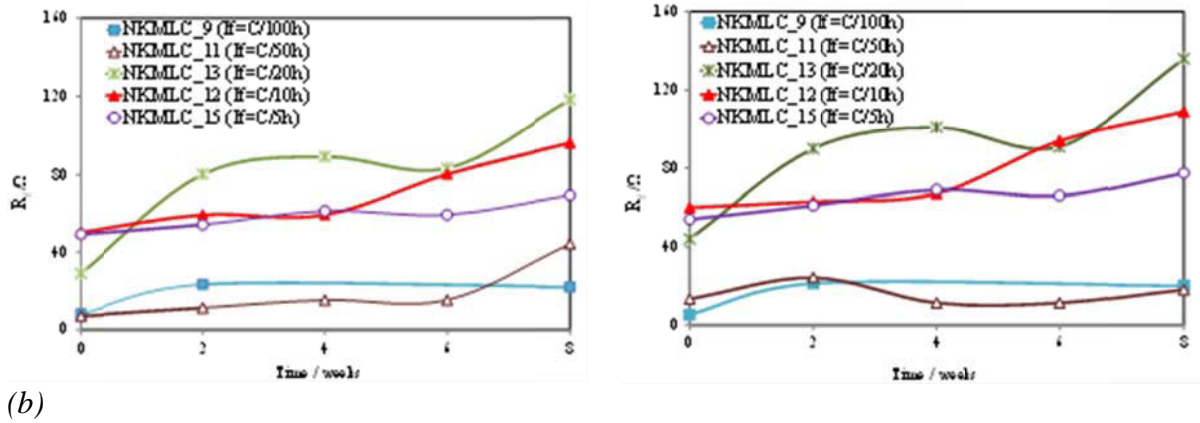


Figure 45: Schema of Li-ion electrode with its principle kinetics steps (a) and corresponding impedance spectrum (b) [56].

The evolution of internal resistance and SEI resistance during the calendar ageing is presented in Figure 46 and its data in Table 13. The SEI resistance remained almost the same for the cells formed with low current rates (C/100h and C/50h). The low film resistance is accompanied with rapid capacity fade. This combination of facts leads to the conclusion, that the passivation film formed onto graphite surface is not formed correctly [18]. The capacity fading can be attributed to the exfoliation of the graphite particles, due to the insufficient thickness of SEI indicated by its low resistance. The latter doesn't protect well the negative active material.



(a)



(b)

Figure 46: Evolution of the internal resistance (a) and SEI resistance (b) measured in 100 % SOC and 0 % SOC during the calendar aging.

The SEI resistance of the batteries formed with current C/20h, C/10h and C/5h is higher and increases with the progress of the calendar ageing. However the capacity doesn't decrease substantially.

Table 13: Comparison between internal resistance and passivation film resistance (SEI).

N° battery Current formation	Time [Weeks]	Ri [Ω] (SOC 100%)	Ri [Ω] (SOC 0%)	Rf [Ω] (SOC 100%)	Rf [Ω] (SOC 0%)
NKMLC_9 $I_{\text{form}}=C/100h$	0	21	21	8	5
	2	11	16	23	21
	4	-	-	-	-
	6	-	-	-	-
	8	7	7	22	20
NKMLC_11 $I_{\text{form}}=C/50h$	0	9	10	7	13
	2	39	56	11	24
	4	14	13	15	11
	6	14	13	15	11
	8	6	7	44	18
NKMLC_13 $I_{\text{form}}=C/20h$	0	3	3	29	44
	2	4	4	80	90
	4	5	5	89	101
	6	5	5	83	91
	8	7	7	118	136
NKMLC_12 $I_{\text{form}}=C/10h$	0	7	7	50	60
	2	5	5	59	63
	4	5	5	59	67
	6	5	5	80	94
	8	17	20	96	109
NKMLC_15 $I_{\text{form}}=C/5h$	0	13	13	49	54
	2	5	5	54	61
	4	5	5	61	69
	6	5	5	59	66
	8	5	5	69	78

### III.7. Experimental study on the MCMB/ LiFePO<sub>4</sub> under abusive conditions

Several MCMB/LiFePO<sub>4</sub> cells type II have been tested under abuse conditions: overcharge, overdischarge and external short circuit. All the experiments were coupled with acoustic emission monitoring with R15 sensors connected on the positive and negative electrode sides of the cell. Acoustic emission activity has been recorded continuously. The tested MCMB/LFP coin-cells are limited by the capacity of the positive electrode. The lattes will be the first to be overdischarged or overcharged. The schema presented in Figure 47 gives the possible reactions occurring during overcharge or overdischarge of the cell.

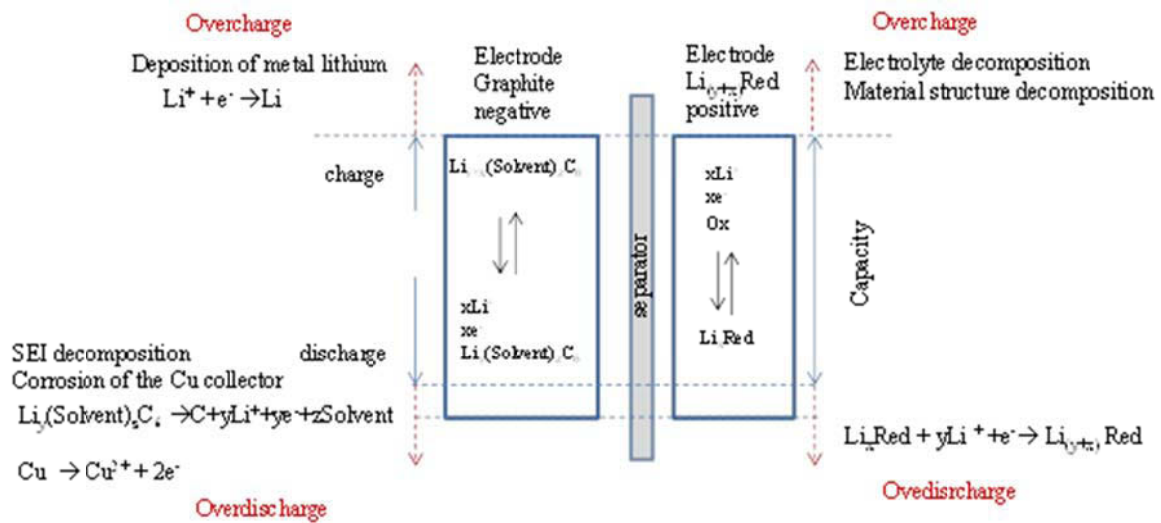


Figure 47: Possible reactions appearing in the positive and the negative electrodes during abusive tests.

During the overcharge the possible reactions inside the cell (where negative electrode is in surplus) are the collapsing of the structure of the positive electrode due to a complete lithium deinsertion, and degradation of the electrolyte, due to its electrochemical oxidation. The overlithiation of MCMB allowing starting a dendrite growth of Li-metal can occur much later. During the overdischarge, overlithiation of LFP occurs firstly. SEI decomposition and corrosion of the negative electrode collector can start later.

### III.7.1. Overcharge Tests

The evolution of the cell voltage, current and AE counts during the overcharge test are presented in Figure 48. The test was performed at ambient temperature from 3.3V up to 5V. The voltage is increased progressively by step of 0.1V. The voltage is maintained until the current drops below C/20h.

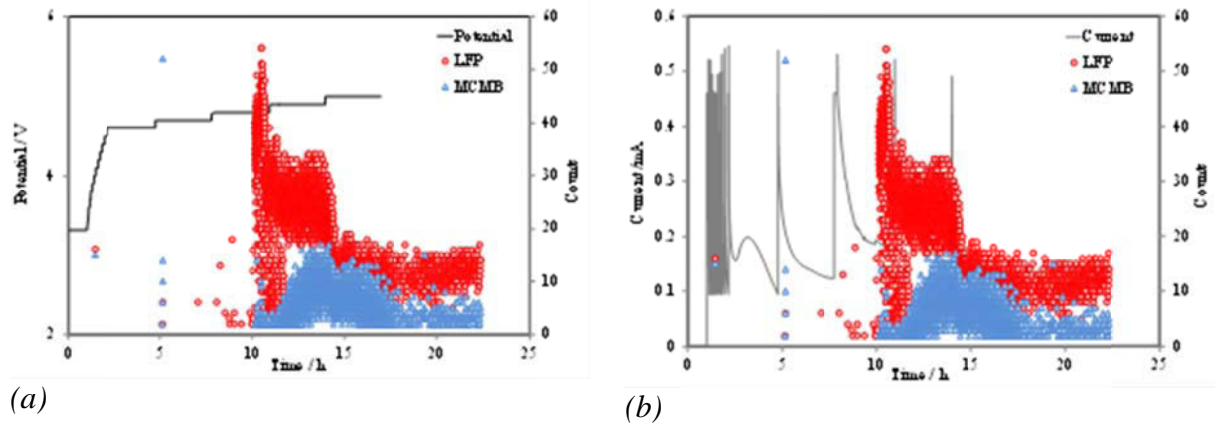


Figure 48: Overcharge process, presented in (a) evolution of counts and cell voltage and (b) evolution of counts and current rate.

The acoustic activity detected by the sensor attached to the positive electrode can be attributed to the electrolyte oxidation process taking place with gas emission [58]. The gas emission is confirmed by the frequency analysis of the acoustic data (by using Noesis). The AE spectra of the parameters peak frequency obtained for the cases of overdischarge and classical charge are presented in Figure 49. It can be seen that only one class of events is obtained. This class is located in the frequency domain between 100 and 250 kHz associated with gas bubbles formation due to the degradation of the electrolyte [53, 54]. It should be noted that during the overcharge the intensity of the events in many magnitudes higher showing that AE is capable to distinguish the start of the overcharge.

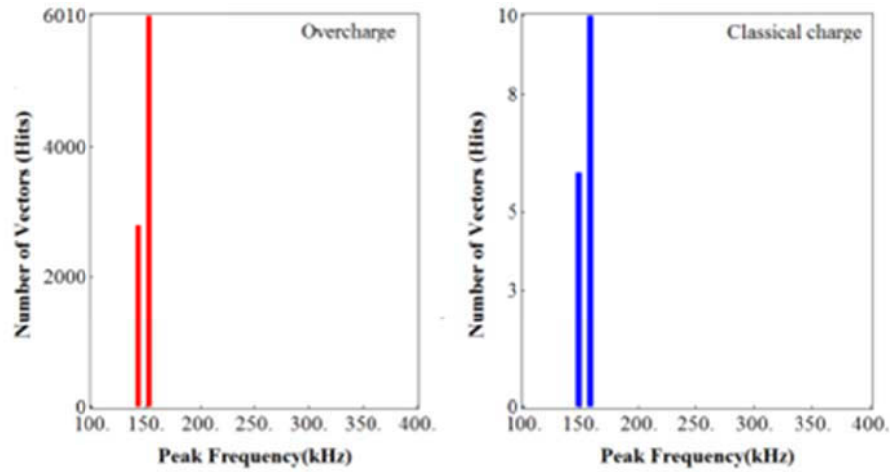


Figure 49: Peak Frequency histogram of the AE signals detected during overcharge test.

### III.7.2. Overdischarge and External short-circuit tests

The overdischarge tests were performed at ambient temperature applying a constant current equal to C/20h from 3.7V down to 0V.

The short-circuit test was performed applying potentiostatically a voltage equal to 1V. This voltage is much lower than the usual discharge cut-off voltage (2V) and the cell reacts by delivering its limiting discharge current. Such experiment is possible due to the small capacity of the cell. This procedure is slightly different than the typical short-circuit test where the cell is externally short circuited externally by a shunt with very low resistance [59].

During both overdischarge and external short-circuit tests any acoustic activity were detected.

### III.8. Conclusions

This chapter has shown that the acoustic emission technique is suitable to characterize the first discharge of graphite//electrolyte//lithium cells, SEI formation and the reaction happening during abusive conditions. It was demonstrated that the acoustic emission activity can be correlated with the electrochemical phenomena like formation of the Solid Electrolyte Interface, process of lithium intercalation and deintercalation in the structure of the positive  $\text{LiFePO}_4$  electrode and negative graphite electrode. The acoustic activity can be attributed to mechanical phenomena as a gas formation and cracking of the active materials.

Even if the recorded “number of hits” or “absolute energy” ranks are not identical between the various cells, their evolution follows the same trend and the each phenomena can be detected. One can obtain information on the quality of the passivation film, the electrode and the electrolyte degradation considering their type.

The results from the overcharge tests demonstrate that the acoustic activity can be attributed to the electrolyte oxidation process taking place with gas evolution. The latter was confirmed by the frequency spectral analysis of the acoustic data.

## References

1. Padhi A.K., Nonjundaswamy K.S., Masquelier C., “*Journal of Electrochem. Soc.*”, Vol.144, N°5, (1997), 1609-1613.
2. Padhi A.K., Nonjundaswamy K.S., Goodenough J.B., “*Journal of Electrochem. Soc.*”, Vol.144, N°4, (1997), 1188-1194.
3. Molenda J., Molenda M., in “*Metal, Ceramic and Polymeric Composites for Various Uses*”, (Cuppoletti J., Eds.), Chapter N°30, INTECH open access publisher, (2011), 621-636.
4. Delmans C., Maccario M., Croguennec, “*Nature Materials*”, Vol.7, (2008), 665-671.
5. Ramana C.V., Mauger A., “*Journal of Power Sources*”, 187, (2009), 555-564.
6. Laffont L., Delacourt C., Gibot P., “*Chem. Mater.*”, 18, (2006), 5520-5529.
7. Chen G., Song X., “*Electroch. Solid-State Let.*”, Vol.9, N°6, (2006), A295 – A298.
8. Yamada A., Koizumi H., “*Electroch. Solid-State Let.*”, Vol.8, N°8, (2005), A409 – A413.
9. Ellis B.L., Lee K.T., Nazar L., “*Chemistry of Materials Review*”, 22, (2010), 691-714.
10. Shrinivasan V., Newman J., “*Journal of Electrochem. Soc.*”, Vol.151, N°10, (2004), A1517-1529.
11. Andersson A.S., Thomas J.O., “*Journal of Power Sources*”, 97, (2001), 498-502.
12. Sides C., Croce F., “*Electroch. Solid-State Let.*”, Vol.8, N°9, (2005), A484 – A487.
13. Gao M., Lin Y., “*Electrochimica Acta*”, 55, (2010), 8043-8050.
14. Chen Z., Dahn J.R., “*Journal of Electrochem. Soc.*”, Vol.149, N°9, (2002), A1184-1189.
15. <http://www.pulead.com.cn> manufacturer
16. Aurbach D., Markovsky B., “*Electrochimica Acta*”, 45, (1999), 67 – 86.
17. Aurbach D. in “*Advance in Lithium-Ion Batteries*”, (Schalkwijk W.A., Scrosati B. Eds.), Chapter 1, KLUMER ACADEMIC PUBLISHERS, (2002), 6-77.
18. Aurbach D., Zinigrad E., Cohen Y., “*Solid State Ionics*”, 148, (2002), 405-416.
19. Vetter J., Novak P., Wagner M.R., “*Journal of Power Sources*”, 147, (2005), 269-281.
20. Besenhard M.W., Spahr E., Novak P., “*Advance material*”, Vol.10, N°10, (1998), 725-763.
21. Winter M., Moeller K.-C., Besenhard in “*Lithium Batteries Science and Technology*”, (Nazri G.-A., Pistoia G. Eds.), Chapter 5, Springer, (2009), 143-194.
22. Funabiki A., Inaba M., Abe T., Ogumi Z. “*Electrochimica Acta*”, 45, (1999), 865 –871.
23. Funabiki A., Inaba M., Abe T., Ogumi Z. “*Carbon*”, 37, (1999), 1591 –1598.
24. Dahn J.R., “*Physics. Rev. B*”, 44, (1991), 9170.
25. Inaba M., Yoshida H., Ogumi Z., “*Journal of Electroch. Soc.*”, 142, (1995), 20-26.

26. Peled E., Golodnisky D., in “*Lithium ion batteries Solid-Electrolytes Interphase*”, (Balbuena P., Wang Y., Eds.), Chapter 1, Imperial College Press, (2004), 1-59.
27. Aurbach D., “*Journal of Power Sources*”, 89, (2000), 206-218.
28. Ein-Eli Y., Thomas R., Aurbach D., Markovsky B., “*Journal of Electrochem.Soc.*”, 143, (1996), L273-L277.
29. Ein-Eli Y., Stephen F., “*Journal of Electrochem.Soc.*”, Vol.145, N°1, (1998), L1-L3.
30. Aurbach D., Ein-Eli Y., Markovsky B., “*Journal of Electrochem. Soc.*”, Vol.142, N°9, (1995), 2882-2890.
31. Yan J., Su Y.-C., Xia B.-J., “*Electrochimica Acta*”, 54, (2009), 3538 – 3542.
32. Aurbach D., Cohen Y., in “*Lithium ion batteries Solid-Electrolytes Interphase*”, (Balbuena P., Wang Y., Eds.), Chapter 2, Imperial College Press, (2004), 70-139.
33. Nazri M., Yebka B., Nazri G.-A., in “*Lithium Batteries Science and Technology*”, (Nazri G.-A., Pistoia G., Eds.), Chapter 6, Springer, (2009), 195-218.
34. Funabiki A., Yuasa S.-I., “*Journal of Electrochem. Soc.*”, Vol.145, N°1, (1998), 172-178.
35. Piao T., Park S.-M., “*Journal of Electrochem. Soc.*”, Vol.146, N°8, (1999), 2794-2798.
36. Naji A., Ghanbaja J., Willmann P., “*Journal of Power Sources*”, 81 – 82, (1999), 207 -211.
37. Dollé M., Grugeon S., Beaudoin B., “*Journal of Power Sources*”, 97-98, (2001), 104-106.
38. Groot J., “*PhD.Thesis*”, from “Chalmers University of Technology”, (2012), 5-18.
39. Andersson A.M., Edstrom K., “*Journal of Power Sources*”, 81-82, (1999), 8-12.
40. Richard M.N., Dahn J.R., “*Journal of Electrochemical Society*”, 146, N°6, (1999), 2068-2077.
41. Broussely M., Biensan Ph., “*Journal of Power Sources*”, 146, (2005), 90-96.
42. Whittingham M.S., “*Chemical Reviews*”, Vol.104, N°10, (2004), 4271-4301.
43. Verama P., Maire P., Novak P., “*Electrochimica Acta*”, 55, (2010), 6332-6341.
44. Zhong C., Bin-Feng W., Ke-Min W., “*Sensors and Actuators B*”, 50, (1998), 27-37.
45. Holzapfel M., Martinier A., “*Journal of Electroanal. Chem.*”, 546, (2003), 41-50.
46. Aurbach D., Levi M.D., “*Journal Phis. Chem. B*”, 101, (1997), 4641-4647.
47. Xu K., “*Chem. Rev.*”, 104, (2004), 4303-4417.
48. Imanishi N., Takeda Y., in “*Lithium Ion Batteries: Fundamentals and Performance*”, (Wakihara M., Yamamoto O.,Eds.), Chapter 5,Kodasha Ltd., Tokyo, (1998), 98-126.
49. Sawai K., Tomura H., Ohzuku T., “*Denki Kogako*”, Vol.66, N°3, (1998), 301-307.
50. Zhang S.S., Xu K., Jow T.R., “*Journal of Power Sources*”, 160, (2006), 1349-1354.
51. Xu M., Zhou L., “*Journal of Electrochemical Society*”, 158, N°11, (2011), A1202-A1206.



52. Gospodinova N., Terlemezyan L., "*Progres Polymer Science*", 23, (1998), 1443-1484.
53. Etiemble A., Idrissi H., "*Proceeding of the EWGAE 2012*"
54. Didier-Laurent S., Idrissi H., "*Journal of Power Sources*", 179, (2008), 412-416.
55. Etiemble A., Idrissi H., "*Proceeding of the EWGAE 2010*"
56. Barsoukov E. in "*Impedance Spectroscopy Theory, Experiment, and Applications*", (Barsoukov E., Macdonald J.R., Eds.), Chapter 4, WILEY-INTERSCIENCE, (2005), 444-457.
57. Aurbach D., Markovsky B., Levi M.D., "*Journal of Power Sources*", 81-82, (1999), 95-111.
58. Tobishima S., Yamaki J., "*Journal of Power Sources*", 81-82, (1999), 882-886.
59. Spotnitz R., Franklin J., "*Journal of Power Sources*", 113, (2003), 81-100.

## **Chapter IV**

**Evaluation of Acoustic Emission as a suitable tool for ageing  
characterization of LiAl/MnO<sub>2</sub> cell.**

<b>Chapter IV</b>	145
Evaluation of Acoustic Emission as a suitable tool for ageing characterization of LiAl/MnO <sub>2</sub> cell.	145
<b>Résumé</b>	147
<b>Summary</b>	147
<b>IV.1. Introduction</b>	148
<b>IV.2. Electrochemical reactions</b>	148
IV.2.1. Lithium alloys as negative electrode in Li-ion batteries	148
IV.2.2. Manganese oxides as positive electrode in Li-ion batteries	153
IV.2.3. Degradation phenomena	155
IV.2.3.1. Degradation phenomena in lithium alloys used as negative electrodes	155
IV.2.3.2. Degradation phenomena in manganese oxide as positive electrode	156
<b>IV.3. Acoustic emission dedicated to the study of these types of materials</b>	156
IV.3.1. Study of the lithium intercalation in different metal alloys by Acoustic Emission monitoring	156
IV.3.2. Acoustic Emission monitoring during the lithium intercalation in manganese oxides	157
<b>IV.4. Evaluation of the Acoustic Emission Technique as a suitable tool for ageing characterization of commercial LiAl/MnO<sub>2</sub></b>	158
IV.4.1. Details about cell construction	159
IV.4.2. Experimental set-up	160
IV.4.3. Initial characterization	162
IV.4.4. Cycling voltammetry	163
IV.4.5. Ageing tests	167
<b>IV.5. Study under abusive conditions.</b>	177
IV.5.1. Overcharge Process	177
IV.5.2. Overdischarge Process	179
<b>IV.6. Conclusions</b>	182
<b>References</b>	183

## Résumé

*Dans ce chapitre, les mécanismes d'insertion des ions lithium dans l'alliage LiAl et dans LiMnO<sub>2</sub>, tous deux présents en tant qu'électrode négative et électrode positive dans un type d'éléments commerciaux, ont été étudiés, et cela en combinant une variété de techniques électrochimiques, la technique d'émission acoustique (EA) et des analyses structurales post-mortem par DRX. Le but de cette étude était d'étudier la faisabilité des mesures EA pour la caractérisation du vieillissement des cellules Li-ion. Nous avons ainsi pu détecter et caractériser le processus électrochimique prédominant et qui concerne l'électrode négative lithium-aluminium associé à une transformation de phase intermétallique et une forte expansion volumique. En particulier, pendant le cyclage, nous avons observé que l'activité acoustique était concentrée lors du processus de décharge. Nous l'avons attribuée majoritairement à la transformation de phase  $\alpha$ -LiAl à  $\beta$ -LiAl et dans une moindre mesure à l'intercalation du lithium de MnO<sub>2</sub> à LiMnO<sub>2</sub>. L'émission acoustique a été ainsi utilisée comme procédé non destructif pour le suivi des processus se produisant à l'intérieur de la cellule.*

## Summary

*In this chapter the mechanism of lithium ion insertion in LiAl alloys used as negative electrode and LiMnO<sub>2</sub> oxide into LiAl/MnO<sub>2</sub> cell has been studied by combining electrochemical method, acoustic emission technique, XRD analyses and SEM observation. The aim of this study was to consider the feasibility of the AE analysis for ageing characterization of Li-ion cells, as well as to detect and characterize the electrochemical and structural processes which appear rather into the negative electrode ( $\alpha/\beta$  intermetallic phase transformation). The acoustic emission was used as a nondestructive method for monitoring of the processes occurring inside the cell. During cycling, the acoustic events were concentrated along the discharge process. The latter was attributed to the phase transformation of  $\alpha$ -LiAl to  $\beta$ -LiAl and the intercalation of lithium in the MnO<sub>2</sub> to form LiMnO<sub>2</sub>.*

## IV.1. Introduction

The objective of this chapter is to show the capability of AE to be used as a method for characterization of the ageing of lithium batteries. Commercial LiAl/MnO<sub>2</sub> coin cell were selected for this study. The study was focused on the negative electrode material LiAl, but MnO<sub>2</sub> positive electrode was also characterized.

As discussed in the first chapter, lithium alloys could be suitable Li-ion negative electrode candidates thanks to their high specific energy. Unfortunately they are lacking cycle life (due to the detrimental effect of the large volume expansion–contraction accompanying electrochemical alloy formation) and specific power density (due to low diffusion coefficient of lithium inside the alloy structure). The cycle life could be improved by limiting the depth of discharge (DOD) and the current density of the cycling [1, 2]. The extent of volume change is not reduced by reducing the size of metal but does render the phase transitions that accompany alloy formation more easy, and reduces cracking within the electrode.

Concerning the positive electrode, MnO<sub>2</sub> materials exist in several crystalline structures, with different electrochemical activity. They are interesting for battery application due to their low cost, low toxicity and stability at overcharge.

Three characterization techniques were used to study the electrode materials before and after the ageing: AE, XRD and SEM analyses. That combination of methods has been already used in several studies [3, 4 and 5]. The purpose of the combination of these three methods is to identify and to correlate the sources of the acoustic emission with the electrochemical phenomena in the battery. The final aim is to use of AE techniques as a possible indicator for battery ageing diagnostics.

## IV.2. Electrochemical reactions

### IV.2.1. Lithium alloys as negative electrode in Li-ion batteries

The use of the alloy of LiAl as a negative electrode is based on the reversible insertion of lithium into the host material according to the following reaction:



The binary alloy phase diagram shown in Figure 1, suggests that aluminum can form three alloys with Li : LiAl, Li<sub>1,5</sub>Al (= Li<sub>3</sub>Al<sub>2</sub>) and Li<sub>2,25</sub>Al (=Li<sub>9</sub>Al<sub>4</sub>) [6, 7, 8].

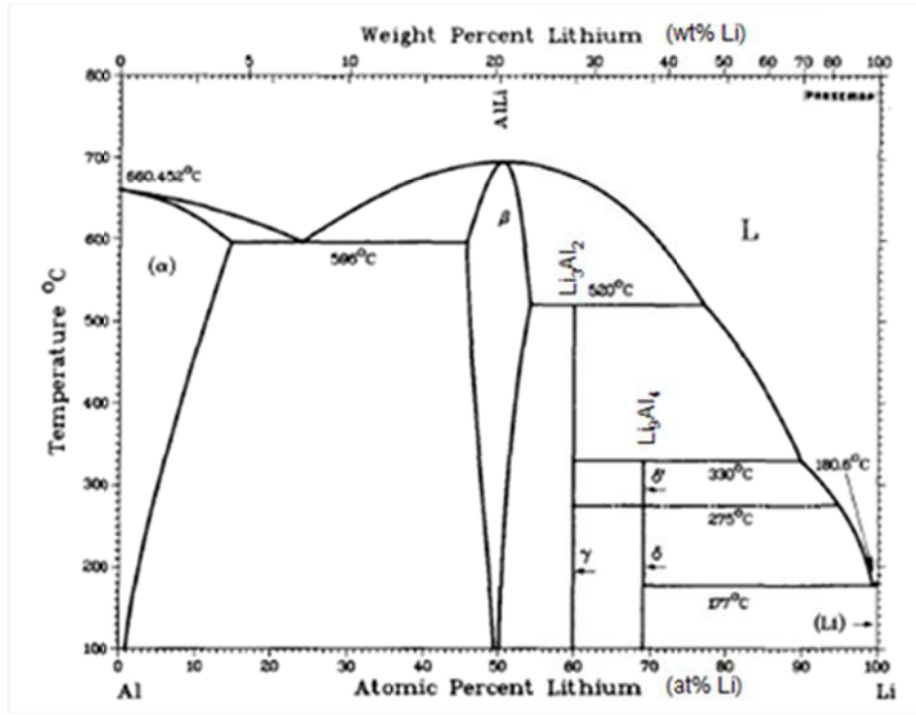


Figure 1: Phase diagram of the system lithium-aluminum [8].

As indicated in Table 1 the theoretical specific capacity of LiAl phase is 993 mAh/g, which is much higher than that of the graphite (372 mAh/g). For the richest lithium-aluminium alloy ( $\text{Li}_9\text{Al}_4$ ), the maximum theoretical mass capacity is 2235 mAh/g (with 2.25 Li incorporated for each Al atom) [7]. The richest composition can be obtained only in particular media as molten salt [9].

Table 1: Summary of Al-Li binary phases and their theoretical mass capacity [7].

Phase	Calculation $C_{th} = zF/nM$ $F = 96485 \text{ C/mol} = 26.8 \text{ Ah/mol} = 26800 \text{ mAh/mol}$ $M(\text{Al}) = 26.98 \text{ g/mol}$	Theoretical mass capacity $C_{th} \text{ (mAh/g)}$
LiAl	$= 1 \times 26800 / (26.98)$	993
$\text{Li}_{1.5}\text{Al}$ ( $\text{Li}_3\text{Al}_2$ )	$= 3 \times 26800 / (26.98 \times 2)$	1490
$\text{Li}_{2.25}\text{Al}$ ( $\text{Li}_9\text{Al}_4$ )	$= 9 \times 26800 / (26.98 \times 4)$	2235

The Figure 2 presents a typical cyclic voltammogram and galvanostatic voltage transient of lithium insertion/deinsertion in aluminum thin film cycled in  $\text{LiPF}_6$  in 2:1 EC: DMC electrolyte [11]. The nominal voltage of LiAl is around 0.3V versus  $\text{Li}^+/\text{Li}$ . Comparing this value to the one of the graphite electrode (0.01V vs.  $\text{Li}^+/\text{Li}$ ), the interest of the alloys as a negative electrode is obvious. The potential region I (between 2 V/Li and 0.26V/Li) is

attributed to the presence of an oxidized layer detected by XPS spectroscopy and confirmed by the fact that no change is observed in the XRD patterns (bulk). The large plateau at 0.26V/Li is assigned to the formation of LiAl alloy. The region III does not lead to the formation of the richest lithium alloy ( $\text{Li}_{2.25}\text{Al}$ ) according to the number of ampere-hour measured during the discharge step. As mentioned previously, the quantity of accommodated lithium is strongly dependent to the morphology of aluminum and the applied current and temperature.

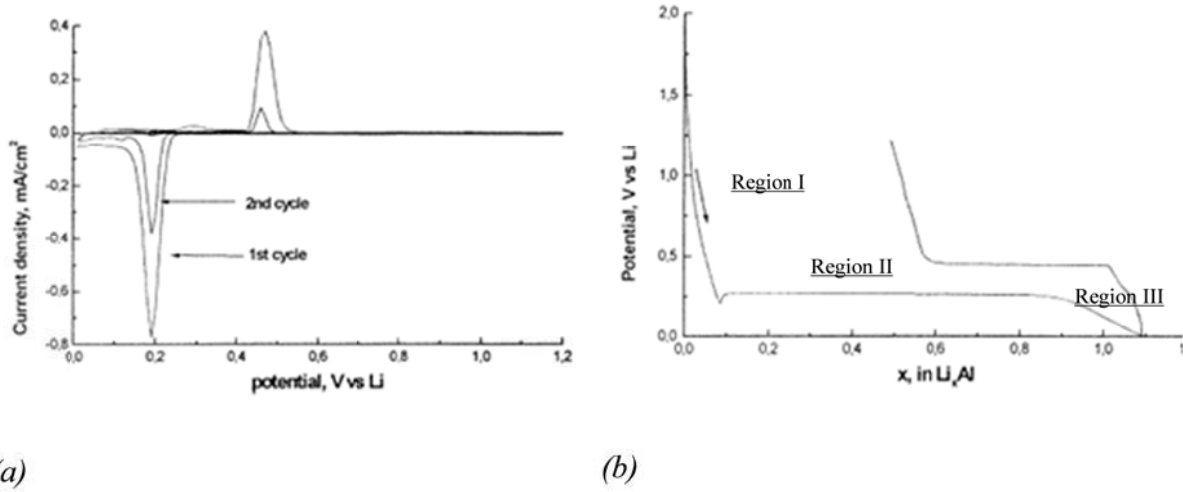


Figure 2: (a) Typical cyclic voltamogram (0.08mV/s, 1.2 -0,01V) (b) Typical galvanostatic curve (C/4 rate, 1.2 -0,01V) of an aluminum thin film electrode in  $\text{Li}^+$  electrode (0.3 $\mu\text{m}$ ) [11].

The alloy formation process can be divided into three regions: electrochemical incorporation, diffusion of the incorporated element in the growing layer of the intermetallic compound and chemical affinity between metals. The diffusion of lithium in the alloyed lattice is generally the process which determines the rate capability for lithium insertion. This process largely studied by chronopotentiometry is described by the Cottrell equation [12]:

$$\text{Equation 2} \quad i = zF(C_{\text{Li}}^* - C_{\text{Li}})\sqrt{\frac{D}{\pi t}}$$

With  $i$ : Current density ( $\text{A}/\text{cm}^2$ ),

$F$  = Faraday constant (96485 C/mol),

$C_{\text{Li}}^*$ : Concentration of lithium in the intermetallic compound ( $\text{mol}/\text{cm}^3$ ),

$C_{Li}$  : Concentration of lithium in the alloy at the starting state (mol/cm<sup>3</sup>),

$z$  : Number of electrons (to reduce/oxidize one molecule of active mass),

$D$ : Diffusion coefficient of lithium (cm<sup>2</sup>/s),

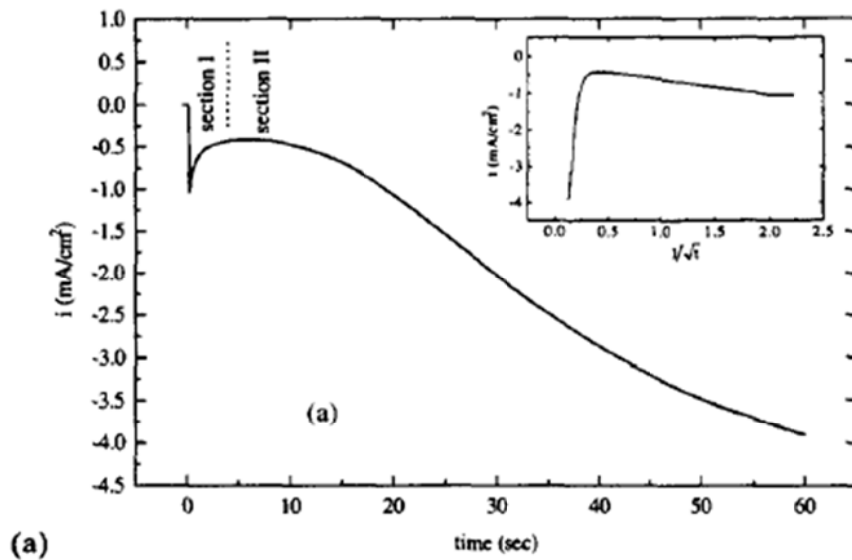
$t$ : time (s).

The diffusion coefficient corresponding to the lithium intercalation in aluminum alloys first was reported by Machill and Rahner [12]. The experiment was carried out in a three-electrode cell with working electrode which is a small cylinder of aluminum placed in a Teflon holder (surface area: 0.196 cm<sup>2</sup>), and counter and reference electrodes lithium pellets. According to the Cottrell equation, the diffusion coefficient can be determined by plotted  $i = f(\frac{1}{\sqrt{t}})$  and by calculating the slope (Equation 3), the straight section obtained from Figure 3.

Equation 3 :

$$m = zF(C_{Li}^{\circ} - C_{Li})\sqrt{\frac{D}{\pi}}$$

As shown in Figure 3, the slope ( $m$ ) is different according to the lithium content in alloy. The diffusion coefficient of lithium is lower when lithium diffuses within (a) aluminum free lithium than (b) aluminum charged with lithium [12, 13].





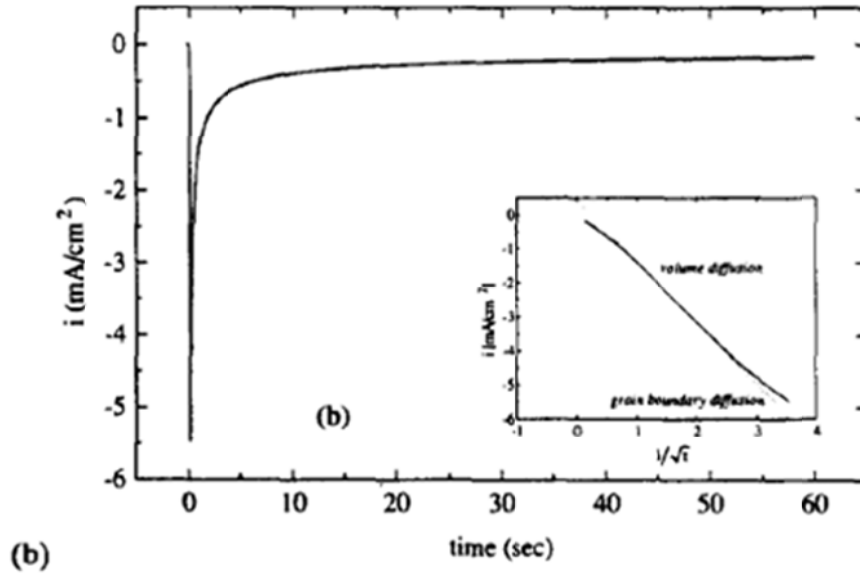


Figure 3: (a) Potentiostatic transient and Cottrell linearization for free lithium aluminum (potential shift from rest potential to  $E=0V$  vs. Li; 1M LiClO<sub>4</sub>/PC), (b) Potentiostatic transient and Cottrell linearization for aluminum charged with 3.6C/cm<sup>2</sup> of lithium (potential shift from rest potential to  $E=0V$  vs. Li; 1M LiClO<sub>4</sub>/PC) [12, 13].

The authors described that during the discharge, the first step is an acceptance of the lithium ions on the top of the metal surface until reaching the limiting concentration of 2.6 at.% (Li<sub>0.03</sub>Al) and thus  $\alpha$ -LiAl phase has been formed. It is known that the rate of lithium diffusion inside the  $\alpha$ -LiAl phase is very slow ( $D \approx 10^{-12}$  cm<sup>2</sup>/s). During this first period, metallic lithium can be plated on the electrode surface if the diffusion rate inside the host is lower than the deposition rate. With increasing lithium content a new phase is growing:  $\beta$ -LiAl with 50 at. % Li (LiAl). The rate of diffusion velocity inside the  $\beta$ -LiAl phase is higher ( $D \approx 10^{-10}$  cm<sup>2</sup>/s) than in  $\alpha$ -LiAl. The nucleation of  $\alpha$ -LiAl and growth of  $\beta$ -LiAl have been described with 3-D model of nucleation by Abyaneh and Fleischmann [14, 15]. In this model, the 3-D formation of new phase is represented as right circular cones, with their basis lying on the substrate.

To complete this explanation and to understand better the electrochemical properties of LiAl, it is important to mention the structural difference in crystal structure of  $\alpha$ -LiAl and  $\beta$ -LiAl. Aluminum and  $\alpha$ -LiAl have a cubic face centered phase crystal structure (FCC) and while the  $\beta$ -LiAl phase is cubic body centered phase (BCC) as presented in Figure 4.

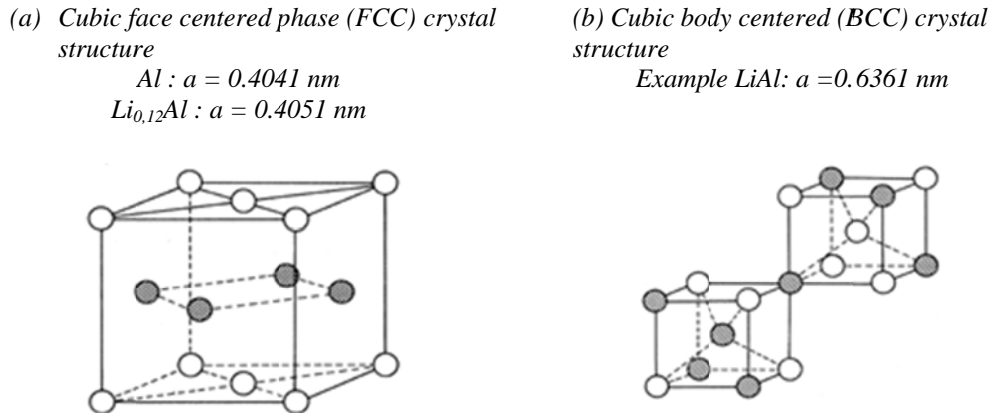


Figure 4: Crystal structure of LiAl alloys: (a) cubic face centered phase (FCC)  $\alpha$ -LiAl phase structure and (b) cubic body centered phase (BCC)  $\beta$ -LiAl phase [16].

The crystal structure change leads to an increase and decrease of the materials volume during the lithium insertion/desinsertion.

Figure 5 presents schematic illustration of lithiation of the crystalline Al caused by phase transition of Al in  $\beta$ -LiAl and  $\alpha$ -LiAl. The  $\beta$ -LiAl and  $\alpha$ -LiAl exist together [13, 17, 19].

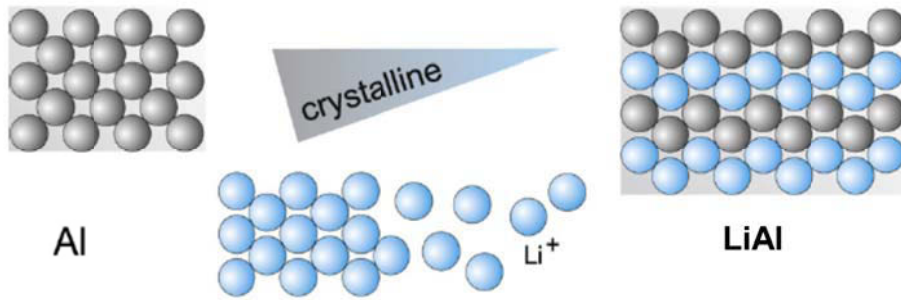


Figure 5: Schematic illustration of the volume change in crystalline Al caused by phase transition of Al in LiAl alloys [18].

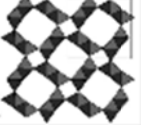


The crystal volume expansion is around 100%, explaining the poor cycle life of the lithium-aluminum alloy if deeply inserted/deinserted. This volume expansion creates an accumulation of mechanical stress in the electrode. During the deinsertion the volume decreases leading to mechanical strains. The structural modifications contribute to the disintegration in active material.

#### IV.2.2. Manganese oxides as positive electrode in Li-ion batteries

Manganese dioxide has been exploited for many years as battery electrode materials: in Leclanché cell in 1867, in alkaline battery ( $\text{MnO}_2/\text{Zn}$ ) as well as in lithium-ion cells. Manganese dioxide exists in various crystalline phases:  $\alpha$ - $\text{MnO}_2$ ,  $\beta$ - $\text{MnO}_2$ ,  $\gamma$ - $\text{MnO}_2$ ,  $\delta$ - $\text{MnO}_2$ ,

$\lambda$ - $\text{MnO}_2$  with electrochemical behaviors very diverse as indicated in Table 2 [13, 20, 21]. The variance in the structure between the different manganese oxides is due to the way of connecting the basic octahedral unit  $[\text{MnO}_6]$ . As an example, the  $\alpha$ - $\text{MnO}_2$  type is constructed from double chain of  $[\text{MnO}_6]$  octahedral forming 2x2 tunnels [23, 24].

Table 2: Crystal structures of  $\text{MnO}_2$ .

Type modification $\text{MnO}_2$	Crystal structure	Electrochemical behavior in non-aqueous lithium cell
$\alpha$ $\text{MnO}_2$ 	Hollandite, Psilomelane (2x2) tunnel structure	Voltage range from 2V to 3.8V vs. $\text{Li}^+/\text{Li}$ $C = 210 \text{ mAh/g}$ (the structure of $\alpha$ $\text{MnO}_2$ accommodate 0.7 $\text{Li/Mn}$ )
$\beta$ $\text{MnO}_2$ 	Pyrolusite/Rutile-type, Ramsdellite (1x1) tunnel structure	Voltage range from 2V to 3.8V vs. $\text{Li}^+/\text{Li}$ $C_{\text{init}} = 210 \text{ mAh/g}$
$\gamma$ $\text{MnO}_2$ 	Nsutit = Pyrolusite and Ramsdellite Domains with (1x1) and (2x2) tunnel structure	Voltage range from 2V to 3.8V vs. $\text{Li}^+/\text{Li}$ $C_{\text{init}} = 250 \text{ mAh/g}$
$\delta$ $\text{MnO}_2$	Layer – type Layers with $\text{MnO}_6$ – octahedrons cubic closet packing of oxygen	Voltage range from 2V to 4 V vs. $\text{Li}^+/\text{Li}$ $C_{\text{init}} = 200 \text{ mAh/g}$
$\lambda$ $\text{MnO}_2$	Spinel – type Atoms with manganese atoms in octahedral sites	Voltage range from 2V to 3.8V vs. $\text{Li}^+/\text{Li}$ $C_{\text{init}} = 200 \text{ mAh/g}$

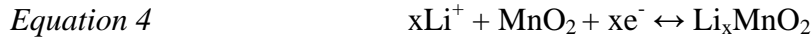
The electrochemical properties of the manganese oxides with different crystal structure depend on parameters as powder morphology, crystalline structure or bulk density [22]. Regarding their electrochemical performance, the most used oxide for industrial purpose is  $\gamma$   $\text{MnO}_2$  [13, 20, 21]. Its interest is it can provide voltage up to 3.8V vs.  $\text{Li}^+/\text{Li}$ . The voltage of the LMO electrode depends not only on the formal valence state of the manganese ions, but also on the relative position of the lithium in the structure. That impacts the voltage profile characterizing each structure potentially used as active material for Li-ion cells. This is linked with the difficulty to remove a lithium ion from a particular site during charge and the vice versa: during insertion process, the sites with the deepest energy wells will be occupied first. The latter, means that higher voltages have to be applied to remove lithium from particular sites within the crystalline structure. Most  $\text{MnO}_2$  structures can, in maximum, accommodate one lithium per formula until the  $\text{LiMnO}_2$  stoichiometry is reached. The complete reaction

involves the complete reduction of  $\text{Mn}^{(+IV)}$  to  $\text{Mn}^{(+III)}$  and delivers the theoretical electrode capacity of 308 mAh/g as calculated in Table 3 [25].

*Table 3: Theoretical mass capacity of  $\text{LiMnO}_2$ .*

Phase	Calculation	Theoretical mass capacity $C_{th}$ (mAh/g)
	$C_{th} = zF/M.3.6$ $F = 96485\text{C/mol} = 26,8\text{Ah/mol} = 26800\text{mAh/mol}$ $M(\text{Mn}) = 54.9\text{g/mol}$ $M(\text{O}) = 16\text{g/mol}$	
$\text{LiMnO}_2$	$= 1 \times 26800 / (54.9 + 16 \times 2)$	308

The reversibility of the lithium intercalation into  $\text{MnO}_2$  depends on the degree of discharge ( $x < 1$  in Equation 4).



This consideration limits consequently the mass capacity to a practical value of about 260 mAh/g, or less, depending of the crystalline structure, the structural stability at low lithium insertion rate and the electrode conception. It is important to note that other forms of manganese oxide compounds exist as  $\text{LiMn}_2\text{O}_4$  (spinel structure) which are able to intercalate lithium with a theoretical capacity of about 154 mAh/g [27, 28, 29].

#### IV.2.3. Degradation phenomena

Ageing of the electrode materials can be defined as their modification of the properties, which is related to various degradation phenomena of the current collector, change of the crystal structure of the positive or the negative electrode material, or degradation of the electrolyte. This paragraph will present a brief discussion of the ageing phenomena in the  $\text{LiAl}$  and  $\text{LiMnO}_2$  electrodes in order to explain further the obtained experimental results for the selected battery technology.

##### **IV.2.3.1. Degradation phenomena in lithium alloys used as negative electrodes**

The capacity decay observed during the cycling of various Li alloys is connected with the mechanical degradation of the electrode due to the huge volume change during insertion /removal of Li into the electrode host matrix [30, 31]. Those variations lead to a fast disintegration and cracking of the alloys. For example [31], Figure 6 shows SEM images of  $\text{LiAl}$  electrodes before and after cycling. The SEM images correspond to  $\text{LiAl}$  electrode

cycled in coin cell with following construction:  $\text{LiAl}/\text{LiPF}_6$  (EC, DMC)/ $\text{LiFePO}_4$  under C/10h regime.

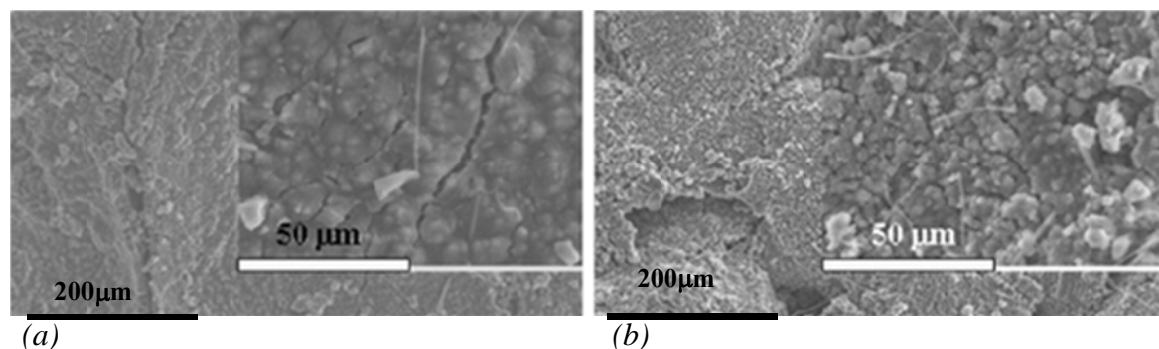


Figure 6: SEM image of LiAl negative electrode after cycling in rocking-chair cell with  $\text{LiFePO}_4$  positive electrode (a) after 5 cycles and (b) after 20 cycles [31].

The surface morphology of the cycled LiAl electrodes after 5 cycles (Figure 6a), and after 20 cycles (Figure 6b) is different, showing cracking and powdering of the active material. The mechanical degradation of the material leads to loss of electrical contact between particles [18].

In general, the decomposition of species from the electrolyte is less pronounced on Li alloys due to their more positive operating potential [32].

#### IV.2.3.2. Degradation phenomena in manganese oxide as positive electrode

The increase lithium insertion into  $\text{MnO}_2$  during the ageing could lead to an irreversible modification of the host structure and cause damaged the electrode. The factors responsible for such structural modifications are: instability of hexagonal-close-packed structure as well as, displacement of manganese ions into interstitial position in host structure, lattice distortion due to the Jahn-Teller effects (transformation of the crystal structure from cubic into tetragonal) [25].

### IV.3. Acoustic emission dedicated to the study of these types of materials

#### IV.3.1. Study of the lithium intercalation in different metal alloys by Acoustic Emission monitoring

Very few studies concerning acoustic emission monitoring of Li intercalation in metals and alloys have been found. Staikov *et al.* studied the formation of the  $\beta$ -LiAl phase during electrochemical incorporation of lithium into aluminum from molten  $\text{LiCl} - \text{KCl}$ , by

chronoamperometric and acoustic emission technique [34]. It was concluded that the acoustic emission events detected during the formation of the  $\beta$ -LiAl can be related to the release of the stress generated the electrochemical lithium incorporation in the aluminum.

Several recent works evaluate the lithium insertion inside silicon by acoustic emission monitoring [4, 5, 35, 36]. These studies were focused on the acoustic emission monitoring during the cycling of silicon electrodes in standard coin cell with lithium foil as counter and reference electrode. The extracted parameters from the acoustic emission wave forms like amplitude, duration, frequency and energy, were used for: a) identification of the film formation on the surface of the silicon electrode [35] and b) correlation with the state of charge of the cell [4, 5, 36].

Study of Villevielle summarized the results obtained from AE monitoring of morphological changes during cycling in Li/NiSb<sub>2</sub> cell [3]. The NiSb<sub>2</sub> compound was cycled in a Swagelok cell versus Li foil while monitoring AE over a period of three cycles. The cumulated absolute energy was monitored and compared with cell potential. Sudden jumps of the energy were observed at voltage plateaus corresponding to the SEI formation and active material conversion [3].

#### IV.3.2. Acoustic Emission monitoring during the lithium intercalation in manganese oxides

The first series of papers dealing with AE during battery operation are published by Ohzuku *et al.* in the end of nineties [37, 38]. They examined the Li/MnO<sub>2</sub> cells: the positive electrode was heat treated electrolytic manganese dioxide (HEMD); the negative electrode was lithium foil. Intensive acoustic emission events were observed during the discharge. No events were detected in the beginning of the charge, but continuous acoustic emission activity was observed during the subsequent open circuit period (Figure 7).

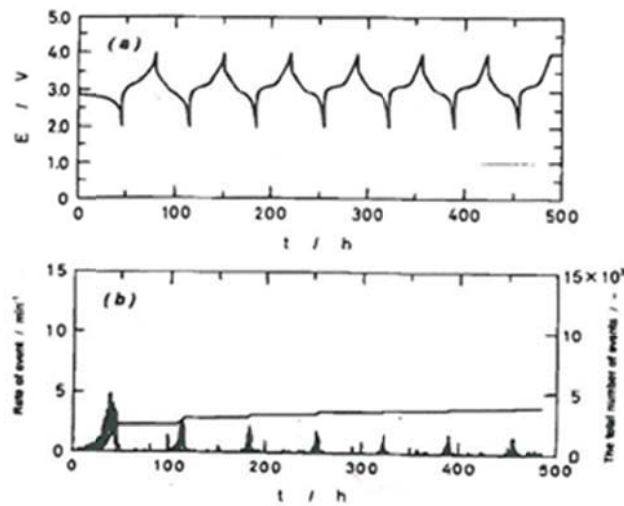


Figure 7: Charge and discharge curves (a) for extended cycles of Li/MnO<sub>2</sub> cell with monitoring of acoustic events (b) [37].

During the cycling the number of events decreases gradually (Figure 7). The authors connected the decrease of the intensity of the acoustic events with the fade of the capacity due to a powdering of the active material. They separated the acoustic emission signal using the frequency in two classes:

- The high frequency signals were attributed to cracking sound of materials including crystalline and noncrystalline solids. These events appear during the discharge and are correlated to the particle fracture during the lithium insertion in the solid host matrix.
- The low frequency signals were attributed to sharp cracking sound of gas bubbles formed in the electrolyte. These events appear during the open circuit voltage and are correlated to gas evolution phenomena.

The authors suggest that these results can be a base for prevention or prediction of failures inside the cell.

#### IV.4. Evaluation of the Acoustic Emission Technique as a suitable tool for ageing characterization of commercial LiAl/MnO<sub>2</sub>

The aim of this paragraph is to evaluate the capability of AE technique to be used as a method for characterization of the ageing phenomena of commercial LiAl/MnO<sub>2</sub> batteries. The electrochemical reactions at the electrodes during the charge-discharge cycling are given in (Figure 8).

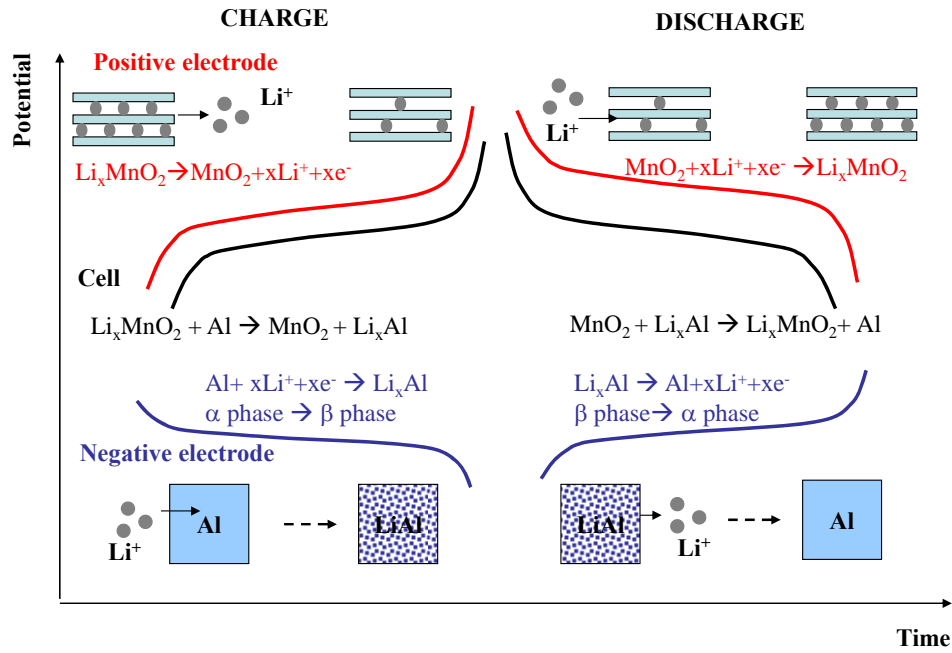


Figure 8: Electrochemical reactions and schematic model of lithium insertion and extraction in the positive and the negative active materials during the charge/discharge cycling. The volume change of the lithium-aluminium alloy is also represented on the bottom of the schema.

The insertion/extraction of lithium inside the LiAl alloy comes along with a modification of the crystal lattice, from  $\alpha$ -phase for low Li concentration compounds to  $\beta$ -phase for Li rich alloys [12, 19]. In order to understand better the relation between the material strain, fracture and cell performance, LiAl/MnO<sub>2</sub> cell were characterized during the cycling by acoustic emission (AE) technique and by *post mortem* analyses –XRD and SEM techniques.

#### IV.4.1. Details about cell construction

LiAl/MnO<sub>2</sub> rechargeable coin cell type CR2032 produced by Maxell were used in this study [39]. The tear-down analyses show that the positive electrode material is pasted on Al mesh and the negative electrode material is welded directly onto the cell casing internal surface. The tests have been started shortly after their delivery. Cells have a nominal voltage of 3.3 V and a nominal capacity of 65mAh (325h autonomy). The dimension of the cells is a diameter of 20 mm and a height of 3.2 mm, and their weight is 3g (Figure 9).



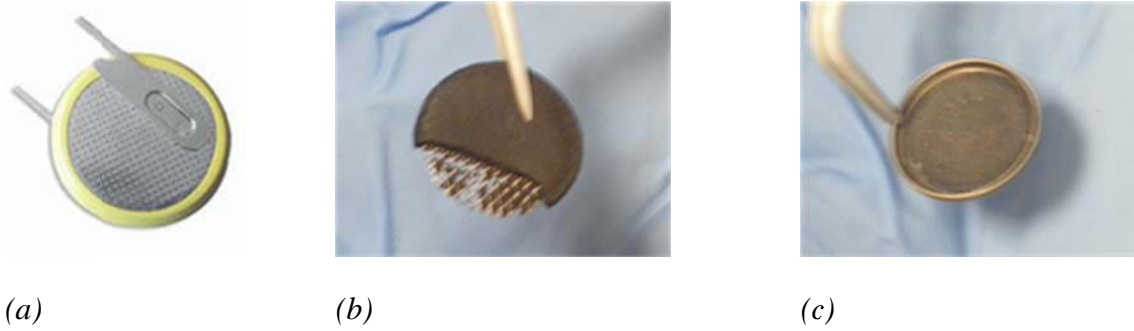


Figure 9: Cell construction: a) coin cell, b) positive electrode  $\text{MnO}_2$ , c) negative electrode  $\text{LiAl}$ .

These coin cells are able to achieve 1.000 cycles at 10% depth of discharge (DOD), but this performance is drastically reduced by the increase of the depth of discharge to only 60 cycles at DOD = 50% and 20 cycles at DOD = 100%. By adapting the depth of discharge level, an accelerated aging of the cell could be achieved in short time.

#### IV.4.2. Experimental set-up

The initial characterizations of  $\text{LiAl/MnO}_2$  cell have been done at different discharge rates, in order to determine the experimental capacity dependence on the discharge current (Peukert approach).

Other cells were examined by cyclic voltammetry. In the case of the commercial cells ( $\text{LiAl/MnO}_2$ ), the potential regions were explored from 2V to 3.25V at scanning rate 0.015 mV/s applying four consecutive cycles. By tear-down extraction, positive and negative electrodes were assembled in new coin cell using the Li foil. These cells were tested by cyclic voltammogram (CVA) under the following conditions: potential scan from 2V up to 3.25V vs.  $\text{Li}^+/\text{Li}$  for  $\text{Li/MnO}_2$  cells, and from 0.01V to 0.5V for cells  $\text{Li/LiAl}$  with a scan rate same as in the case of complete cells 0.015 mV/s.

Finally cell aging tests were performed. The aging procedure for the  $\text{LiAl/MnO}_2$  cells consists of complete charge/discharge cycles (DOD = 100%) under C/20h constant current between 2V and 3.3V at room temperature (25°C). Table 4 gives an overview of the design of the experiments.

Table 4: Overview of the design of experiments

Number of cells tested	Experiment type
4	<u>Peukert capacities:</u> C/100h, C/50, C/20, C/5
4	<u>Cyclic voltammetry cells LiAl/MnO<sub>2</sub>:</u> 2V to 3.25V at scanning rate 0.015 mV/s, 4 cycles
2	<u>Cyclic voltammetry cells Li/MnO<sub>2</sub>:</u> 2V to 3.25V at scanning rate 0.015 mV/s, 2 cycles
2	<u>Cyclic voltammetry cells Li/LiAl:</u> 0.01V to 0.5V at scanning rate 0.015 mV/s, 2 cycles
4	<u>Aging procedure - Galvanostatic cycling:</u> C/20h rate (30 cycles)

The electrochemical experiments were performed by using a computer controlled potentiostat /galvanostat SOLARTRON MULTISTAT 1470.

All the experiments were coupled with acoustic emission monitoring with two R15 sensors connected on the both sides of the cell: the sensor 1 is coupled to the positive electrode and sensor 2 to the negative electrode. The AE events detected by the sensors at the corresponding electrode (side of the coin cell) should be more intensive than the signal detected by the other sensor on the opposite side due to the different interfaces to be crossed by the elastic waves. A preamp gain of 40dB and a sample rate of 5MSPS were applied. Acoustic emission activity was registered as a hit by the system when the signal exceeded a threshold of 28dB.

Several XRD analyses were performed on the negative active material in a completely charged and discharged state of fresh and aged cells. The material was extracted from the electrode in glove box and placed onto lamella. Before analysis the sample is protected with a thin film of Kapton. The XRD analyses were done on a BRÜKER D8 Advance diffractometer (Bragg Brentano geometry) equipped with a Cu anticathode (Cu K<sub>α</sub> radiation).

SEM observations were done using an electronic microscope Philips XL'30 connected with EDX analyzer (INCA, Oxford instrument).

#### IV.4.3. Initial characterization

The performances of the LiAl/MnO<sub>2</sub> cells have been several at various discharge rates:  $C_{nom}/100h$ ,  $C_{nom}/50h$ ,  $C_{nom}/20h$  and  $C_{nom}/5h$  in order to find a good compromise between the time of the study and the optimal operating conditions for this cell. A comparison between measured data and the capacity values from the datasheet is presented in Figure 10. The relationship between the discharge current and discharge capacity can be expressed using the Peukert's equation:

Equation 5: 
$$C_p = I^k \cdot t$$

Where (I) is the galvanostatic discharge current, t is the discharge time, and (k) and ( $C_p$ ) are empiric constants which can be calculated from (log I) vs. (log t) plot shown Figure 10.

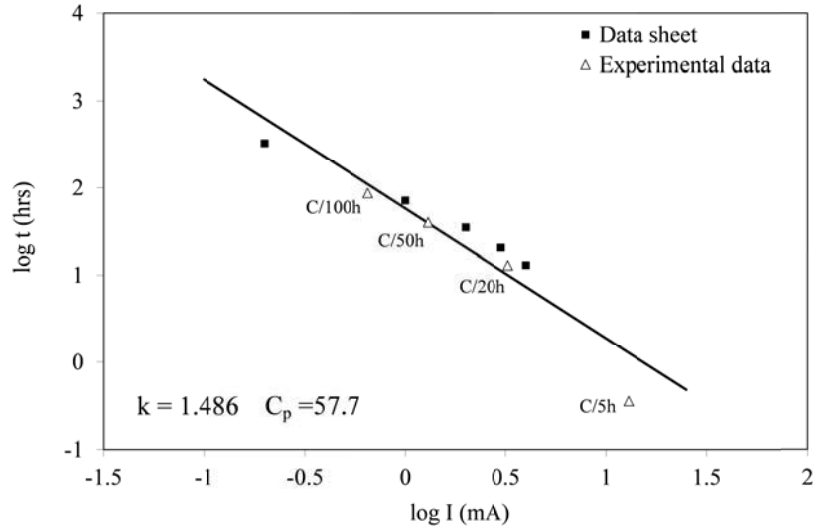


Figure 10: Peukert's equation applied to experimental data obtained for LiAl/MnO<sub>2</sub> cells

In this equation the constant (k) depends on the active materials nature, on the temperature, on the concentration of the electrolyte as well as on the design of the cell [40, 42]. The obtained data shows that the Peukert's equation is applicable in the current range between 0.2 mA and 4 mA. Taking into account the experimental and the manufacturer values, the Peukert's coefficient k is 1.486 and the Peukert's capacity  $C_p$  is 57.7 mAh. The value of the Peukert's coefficient is representative of cells used in low current applications where k is usually close to 1.5 [41, 42].

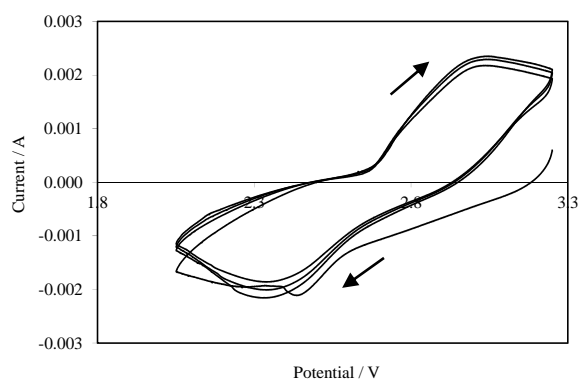
The choice of current equal to  $C_{nom}/20h$  is a good compromise for the ageing experiments corresponding roughly to 50% of the nominal capacity observed typically at  $C_{nom}/100h$ .

#### IV.4.4. Cycling voltammetry

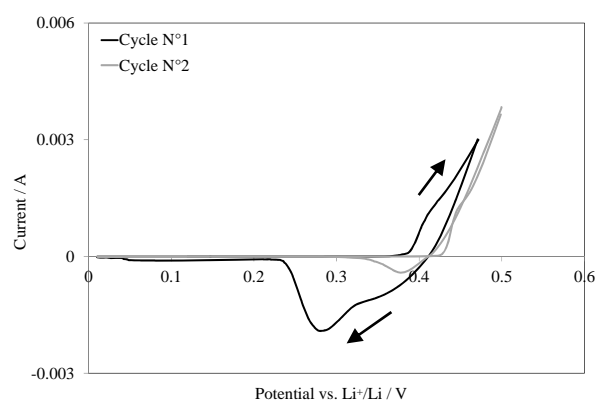
The cycling voltammograms obtained from tested LiAl/MnO<sub>2</sub>, Li/LiAl and Li/MnO<sub>2</sub> cells are shown in Figure 11.

The results of the complete cell (Figure 11a) show that during the cathodic sweep a large reduction peak appears at  $\approx 2.3\text{V}$  where the lithium de-inserted from  $\beta\text{-LiAl}$  phase is inserted inside MnO<sub>2</sub> [43]. The lithium insertion into MnO<sub>2</sub> materials induces modification into the host structure with generally a volume expansion especially for higher insertion rates [44, 45]. Accumulation of stress and strain within the active material leads to micro-cracks [4, 45] and irreversible damages. This reduction peak is correlated with the large oxidation peak at 3.0V where the opposite reactions occur [11, 46]. The cyclic voltammetry of the complete cell can also be used to reveal reactions occurring during the electrochemical processes but the oxidation and reduction peaks are not well defined. This is the reason why the electrodes have been characterized individually. The (Figure 11b) represents the cycling voltammogram of Li/LiAl cell. It can be seen a reduction shoulder at 0.35V vs. Li<sup>+</sup>/Li and a peak at 0.27V vs. Li<sup>+</sup>/Li during the cathodic potential sweep. The peak at 0.27V vs. Li<sup>+</sup>/Li disappears at the second cycle. During the oxidation process (the anodic potential sweep), a shoulder at 0.43V vs. Li<sup>+</sup>/Li is visible. The reduction and the oxidation peaks at 0.27-0.35V and 0.43V respectively could be attributed to the insertion/extraction of Li<sup>+</sup> from the low lithium concentrated alloy ( $\alpha\text{-LiAl}$  phase) to the rich lithium concentrated alloy  $\beta\text{-LiAl}$  phase [11].

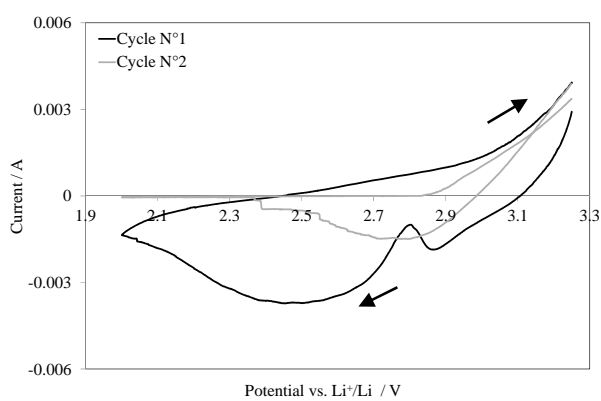
The cyclic voltammetry of Li/MnO<sub>2</sub> (Figure 11c) showed a reduction peak at about 2.7V vs. Li<sup>+</sup>/Li and an oxidation shoulder at 3.2V vs. Li<sup>+</sup>/Li which can be attributed to the insertion/deinsertion of Li from the MnO<sub>2</sub> matrix [46, 47, 48].



(a)



(b)



(c)

Figure 11 : Cyclic voltammetry of (a)  $\text{LiAl/MnO}_2$ , (b)  $\text{Li/LiAl}$  and (c)  $\text{Li/MnO}_2$  at scanning rate  $0.015 \text{ mV/s}$ .

The acoustic emission activity has been monitored simultaneously with the carried out cyclic voltammetry. The evolution of the potential, current and AE amplitude during this experiment is presented in Figure 13.

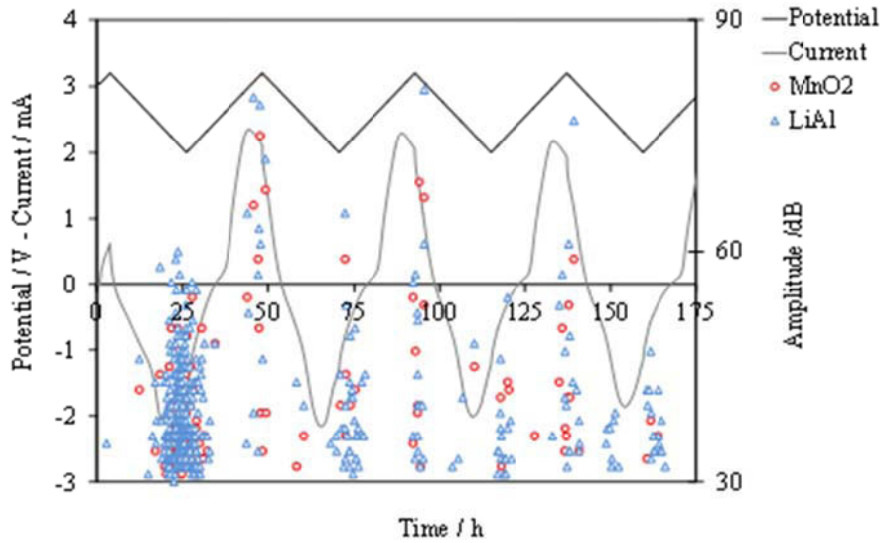


Figure 12: Acoustic emission activity recorded during the cyclic voltammetry for LiAl/MnO<sub>2</sub>.

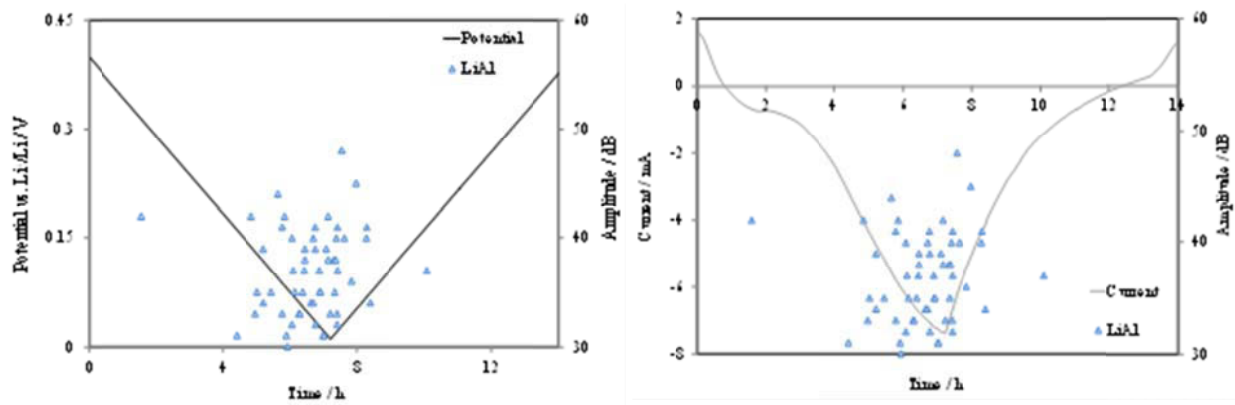
The acoustic emission activity is notable at the end of the reduction sweep beginning at approximately 2.7V. That voltage region corresponds to the end of the delithiation of LiAl alloy and the complete lithiation of MnO<sub>2</sub>, assuming that the limiting electrode is the positive one. The possible acoustic emission sources can be attributed to the  $\beta/\alpha$  phase transition at the negative electrode [12, 49] as well as the particle fractures during the lithium ion insertion into MnO<sub>2</sub> matrix at positive electrode [37, 38]. AE activity is detected too in the beginning of the next oxidation sweep, but in less intensive extent until approximately 2.3V. Another weak AE activity appears in the end of that oxidation sweep. During that oxidation sweep, delithiation of MnO<sub>2</sub> and lithiation of LiAl are accomplished but EA sources are not still clearly attributed. This will be discussed in more details in the next section.

A decrease of the number of acoustic emission events is observed with the increase of the number of cycles. Table 5 gives a summary of the discharge capacity corresponding to the reduction sweep and the acoustic emission activity for each cycle for LiAl/MnO<sub>2</sub> cell. The decrease of the discharge capacity is followed by a decrease of acoustic emission activity.

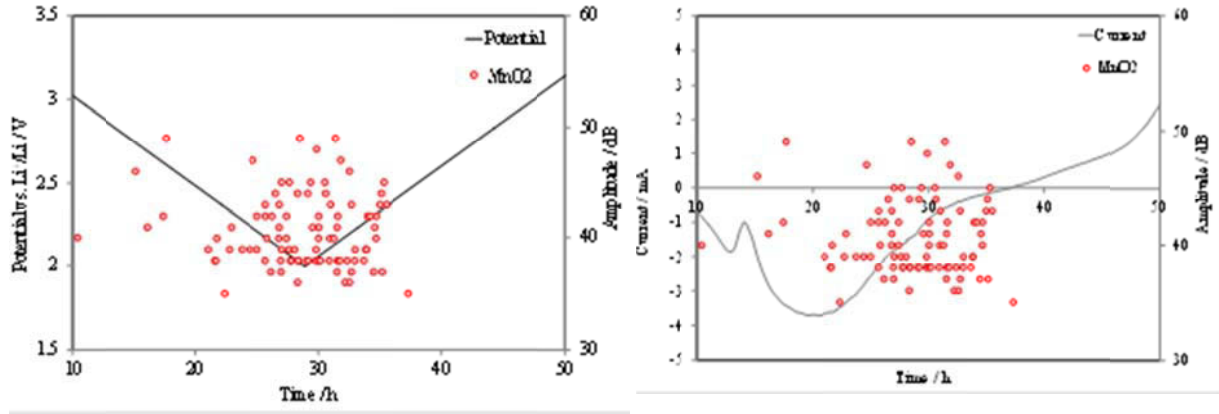
*Table 5: Comparison between the capacity of the LiAl/MnO<sub>2</sub> cell, and acoustic emission activity during the cycling voltammetry experiment.*

CV cycle	Cycle N°1	Cycle N°2	Cycle N°3	Cycle N°4
Capacity [mAh]	32	28	24	24
Hits (LiAl)	140	50	34	13
Hits (MnO <sub>2</sub> )	91	18	11	8

Figure 13 presents the evolution of the current, potential and AE activity of the cells assembled with Li-foil and tear-down extracted LiAl and LiMnO<sub>2</sub> electrodes during the cyclic voltammetry characterization. The acoustic activity is stronger in the end of the reduction sweep for both electrodes (during the lithiation reaction). In the electrochemical cell Li/LiAl the acoustic activity begins at 0.2V and continues until 0V vs. Li<sup>+</sup>/Li. It is possible to assume that the electrochemical reaction at the interface LiAl//electrolyte related to the diffusion phenomena of lithium inside the alloy ( $\alpha$ -LiAl to  $\beta$ -LiAl transition within the whole active material) produce a mechanical stress (cracking related to this phase transition and swelling of the alloy with the increase of lithium content). Consequently acoustic activity is detected during the reduction sweep of the cyclic voltammetry of Li/LiAl (Figure 13a) [19]. This phenomenon is illustrated in Figure 12 for the complete cell in the end of the oxidation ramp. In the electrochemical cell Li/MnO<sub>2</sub>, the acoustic activity during the reduction sweep around 2.3V is correlated with the stress inside the structure of the positive material due to the lithiation (Figure 13b). As reported in [37, 38], when the stress exceed an elastic limit a particle fracture occurs. This phenomenon is illustrated in Figure 12 for the complete cell in the end of the reduction ramp.



(a)

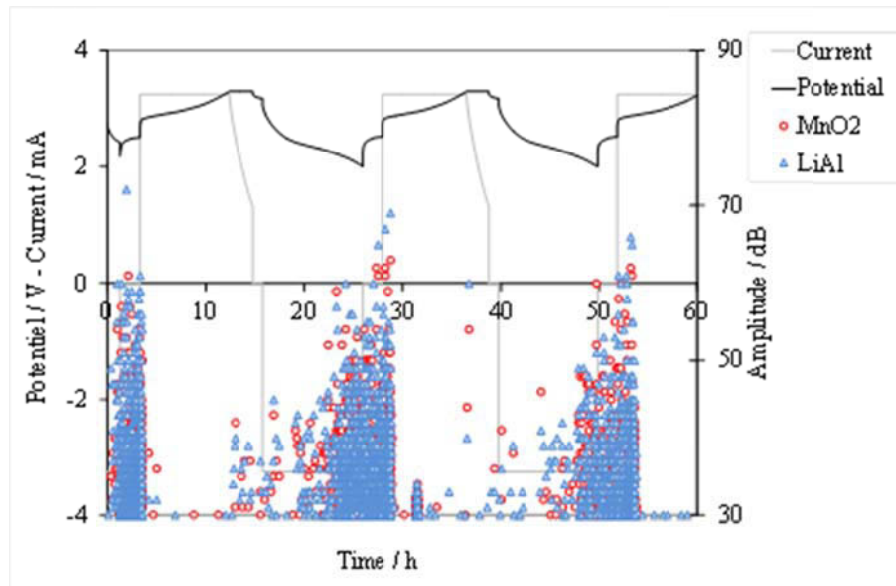


(b)

Figure 13: Acoustic activity (on the right axis) recorded simultaneously to the attainment of the cyclic voltammetry for a) Li/LiAl and b) Li/MnO<sub>2</sub>. The potential scan is represented on the left axis of the curve.

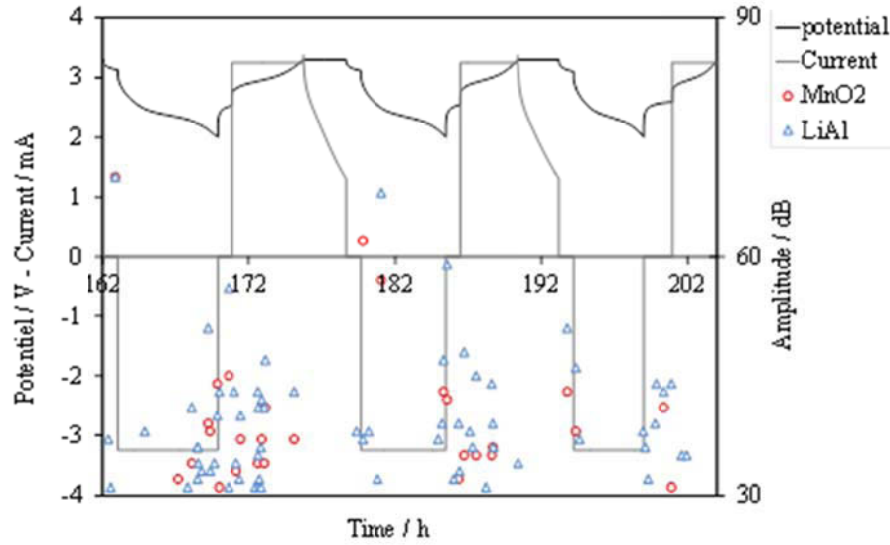
#### IV.4.5. Ageing tests

The cycling ageing tests were carried out at room T (25°C) with a current equal to C/20h and limiting cell voltage between 2V and 3.3V. The acoustic emission activity has been recorded continuously during the whole cycling test (Figure 14).



(a)





(b)

Figure 14 : Voltage profile of the charge/discharge cycling and the corresponding AE activity in terms of counts (C) versus time recorded by the both sensors for (a) first three cycles and for (b) the last three cycles (from 28 cycles realized according to the cycling results presented above).

The acoustic emission activity is very intensive during the discharge and especially at its end (below 2.4V). This result corresponds to the same electrochemical phenomena producing AE signal during the reduction sweep of the CVA tests discussed previously. It is interesting to note that intensive acoustic activity is also detected during the open circuit period after the discharge (Figure 14a). When the charge process is started immediately after the discharge, as observed in Figure 15, the acoustic activity disappears sharply when the sign (direction) of the current is inversed.

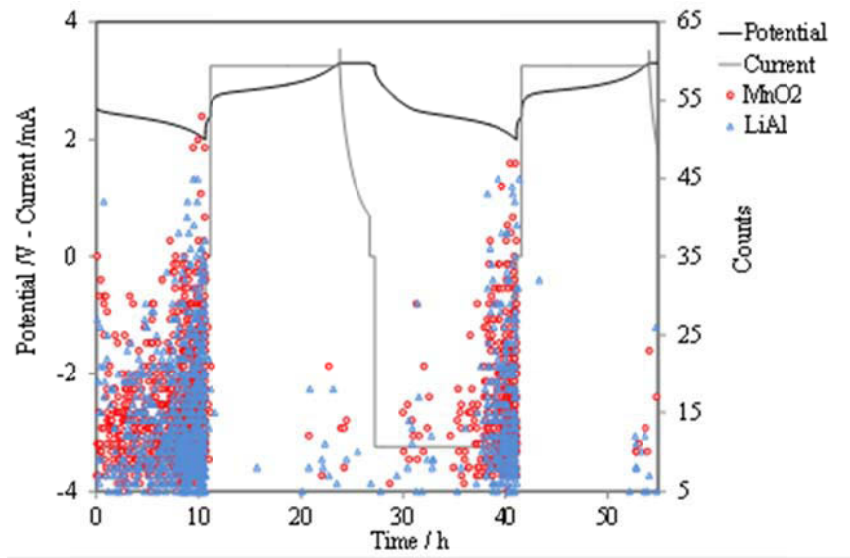
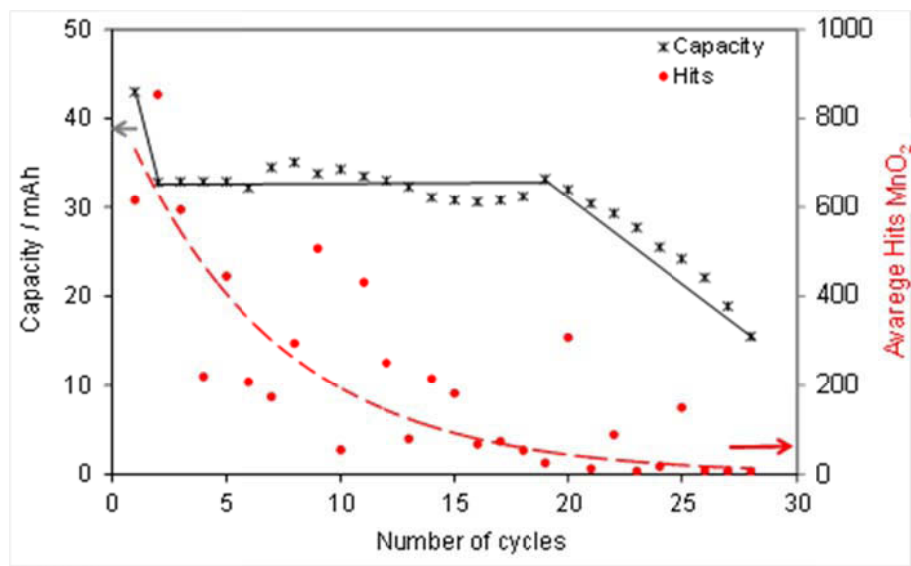
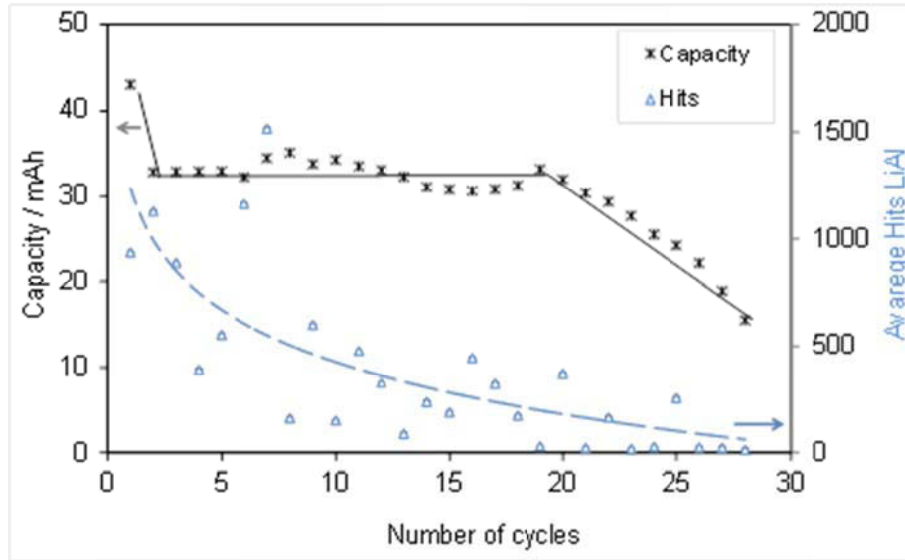


Figure 15: Voltage profile on cycling and AE activity in terms of counts versus time recorded by the both sensors.

A possible explanation of that AE activity is that the lithium concentration inside  $\alpha$ -LiAl is homogenizing slowly due to the low lithium ion diffusion coefficient inside the alloy structure [50]. On cycling, the acoustic emission activity decrease gradually as shown in (Figure 14b). This decrease could be connected with the degradation of the active materials which do not participate completely in the electrochemical reactions. As shown in a Figure 16, a capacity loss of 20% is obtained after 20 cycles at DOD = 100%. The average number of hits per cycle is also plotted versus time confirming the decrease of the acoustic activity with the aging of the cell.



(a)



(b)

Figure 16: Evolution of the capacity during cycling (at  $C_{nom}/20$ ) and correlation with the acoustic activity, detected by the positive (a) and the negative (b) side sensor (the plotted AE parameter is average number of hit per cycle).

The correlation between the acoustic activity and the capacity of the cell is more notable in Figure 17. Beyond about 50 hits per cycle a sharp fading of the capacity is observed.

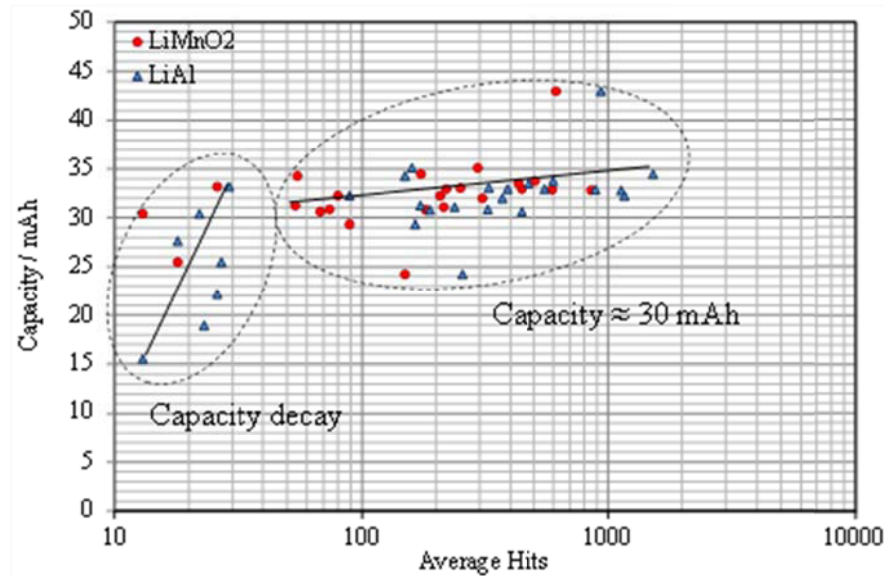


Figure 17: Correlation between the discharge capacity of LiAl/MnO<sub>2</sub> and the average number of hits per cycle.

Each acoustic emission event is characterized by different parameters like frequency, duration, energy etc... [37]. Thus it is possible to separate and classify the different events

(phenomena) by comparing their characteristic frequency. Formation of the gas bubbles due to electrolyte degradation is known to be observed in the peak frequency between 80 kHz to 250 kHz. The mechanical cracking is observed at higher frequency, from 250 kHz to 400 kHz [51]. The characteristic frequencies are available from spectral analysis of the acoustic signal. The spectral analysis of the AE events taking place in the cell is plotted in Figure 18 for the first and the last three cycles.

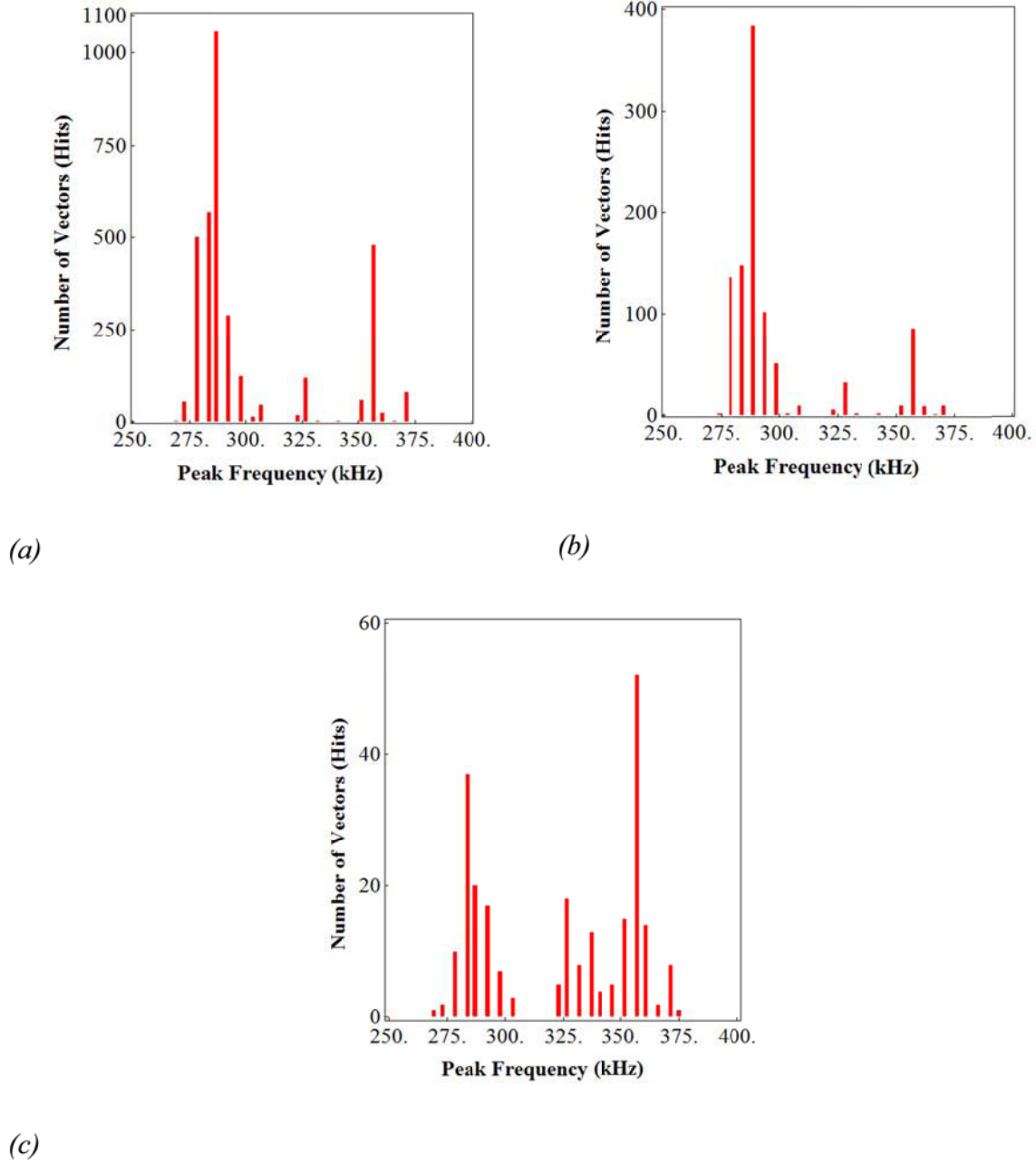


Figure 18: Spectral analysis of acoustic activity during the aging of  $\text{LiAl/MnO}_2$  (a) for the first three cycles and (b) for the middle cycles, (c) for the last three cycles (the scale of x-axis is limited to the domain where acoustic activity is detected).

The results show that the phenomena stay in the same frequency domain between 260 to 380 kHz. With the fresh cell, the number of hits is numerous and the peak frequency is comprised between 260 to 300 kHz, with a maximum number of events at  $\approx 280$  kHz. With the aged one, the hits are less abundant and the frequency distribution is bimodal with events between 260kHz and 300 kHz and between 325 kHz and 380 kHz, with a maximum number of events at  $\approx 360$  kHz. According to Etienne [51] and Ohzuku [37] these frequencies correspond to particle cracking mechanisms. We assume in this case the aging could be related to two different mechanical mechanisms on negative or positive electrode or on the both, but this assumption needs further analyses.

In order to understand more precisely the degradation mechanism and the recorded acoustic activity, samples of the active materials were analyzed with X-ray Diffraction analyses (XRD) and Scanning Electronic Microscopy (SEM).

The XRD analyses of the negative active material (Figure 18) shows the presence of two different phases of LiAl depending on the state of charge and the aging (fresh or aged):  $\beta$ -LiAl (face-centered cubic) contains high quantity of lithium and  $\alpha$ -LiAl (face-centered cubic) containing low quantity of lithium. It is well known in the literature [52] that during cycling according to the degradation of LiAl alloy, the phase  $\beta$ -LiAl becomes more predominant over the phase  $\alpha$ -LiAl.

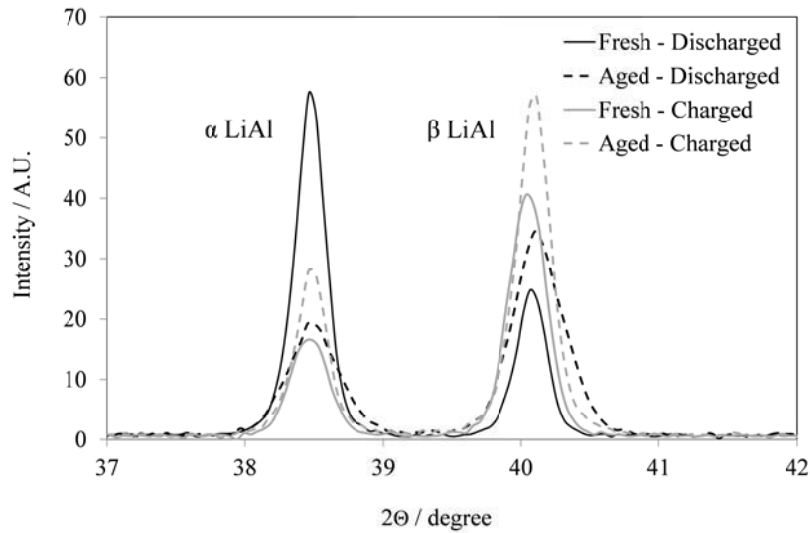


Figure 18: X-ray Diffraction patterns.

The ratio between the peak heights was used to evaluate the phase composition of the negative electrodes Table 6. For the fresh cell, in charged state,  $\beta$ -LiAl is the predominant

phase and the ratio  $\alpha/\beta \approx 1/3$ . In discharged state for the fresh cell  $\alpha$  phase becomes higher than  $\beta$ , with a ratio  $\alpha/\beta \approx 2$ .

*Table 6: Relative quantity of  $\alpha$ LiAl and  $\beta$ LiAl phases at discharged and charged states for fresh and aged cells.*

% mass	$\alpha$ LiAl	$\beta$ LiAl
LiAl charged (fresh)	23 %	77 %
LiAl discharged (fresh)	64 %	36 %
LiAl charged (aged)	25 %	75 %
LiAl discharged (aged)	29 %	71 %

For the aged cell in charged state the ratio  $\alpha/\beta$  is approximately the same as for the fresh one ( $\approx 1/3$ ).

However, in discharged state, conversely to the fresh one, this ratio does not change ( $\alpha/\beta \approx 1/3$ ) indicating that the lithium cannot be extracted from the alloys.

For the positive electrode due to its amorphous nature, the XRD analysis does not give exploitable information.

Figure 19 presented SEM micrographs of fresh and aged LiAl electrode. The fresh negative active material consists of compact particles with a size of 60-70 $\mu$ m. After the aging the negative active material is converted into a porous mass constituted by particles with much smaller size in the range of 10 $\mu$ m.

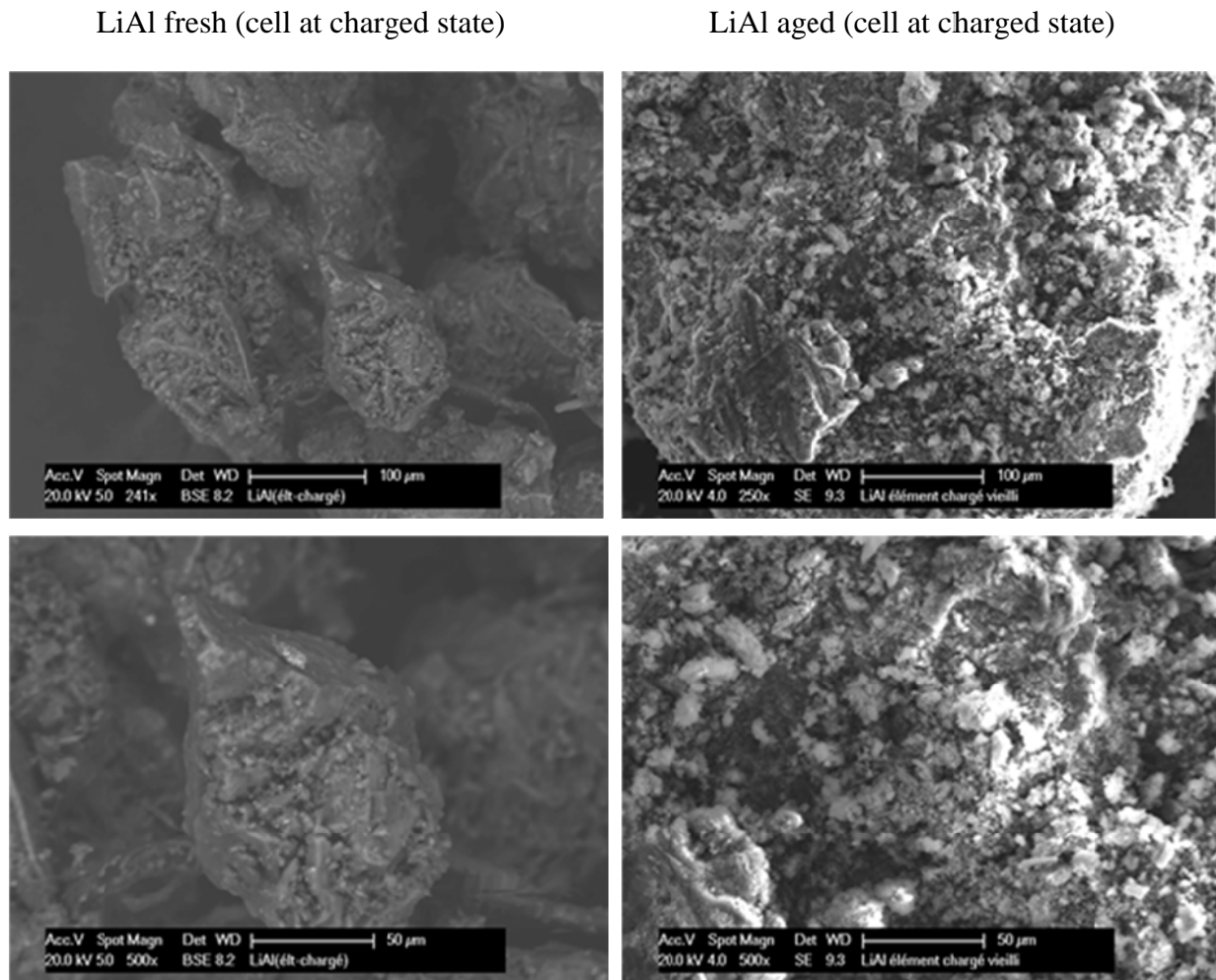


*Figure 19: Scanning electronic micrograph of fresh and aged LiAl electrode*

The Figure 20 shows the SEM micrographs of fresh and aged  $\text{MnO}_2$  electrode in discharge state (fully lithiated material). The SEM micrographs show a decrease of the particle size indicating a fracturing with the ageing. The fracturing could explain the capacity loss during the cycling, due to a loss of electrical integrity of the electrode.

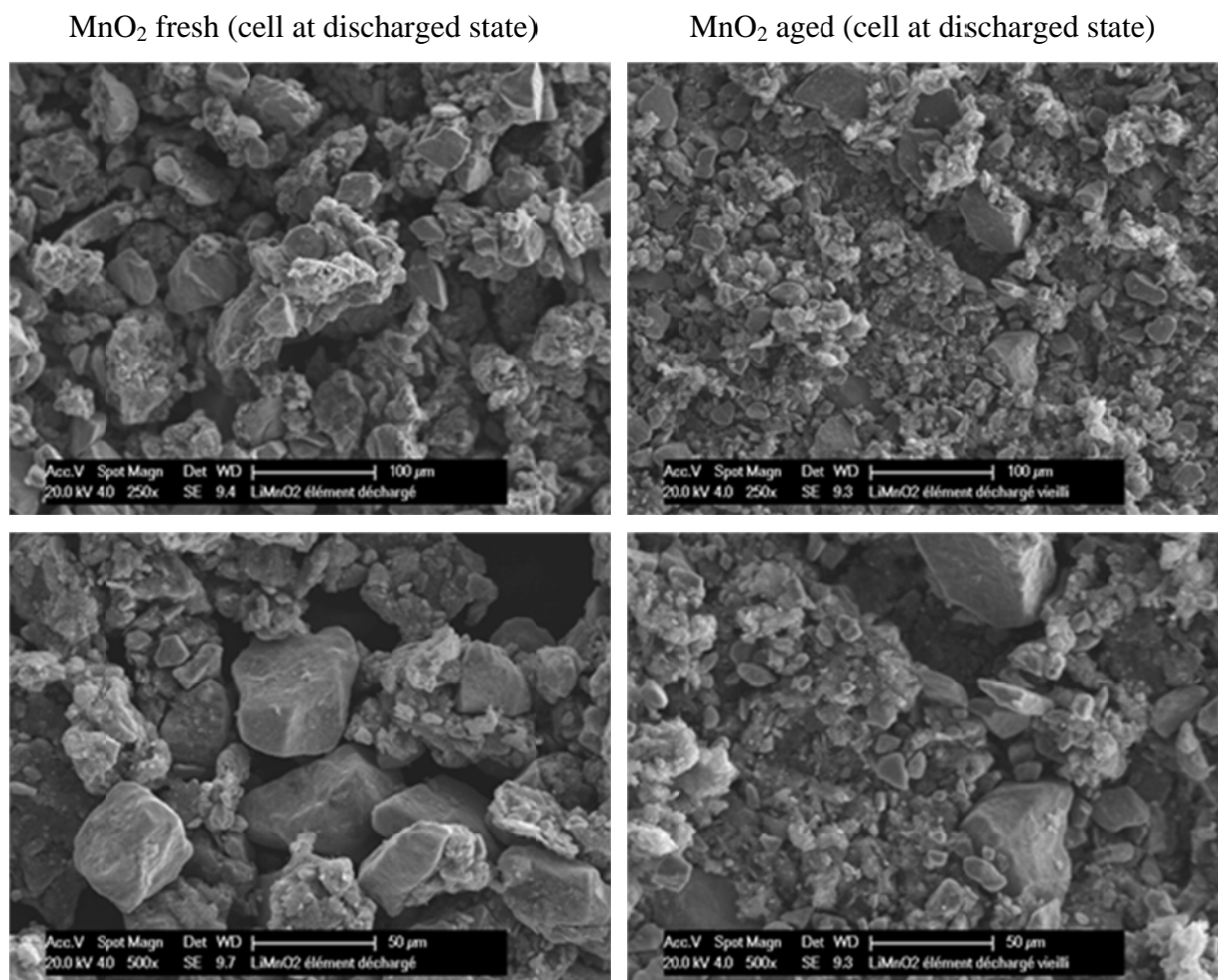


Figure 20: Scanning electronic micrograph of fresh and aged MnO<sub>2</sub> electrode

Thus the acoustic emission activity can be correlated with the overall mechanical phenomena within the cell like:

- cracks and particle fragmentation of MnO<sub>2</sub>,
- cracking due to the crystalline phase transition and swelling of the LiAl alloy.

In order to check the correlation between the acoustic emission activity and the capacity fade, we carried out a cycling test in CCCV regime with  $I = C_{20h}/20h$ . The depth of discharge was limited down to 2.75V during 320 shallow cycles (Figure 21). This voltage limit has been chosen because no AE is observed between 3.3V and 2.7V as mentioned previously.



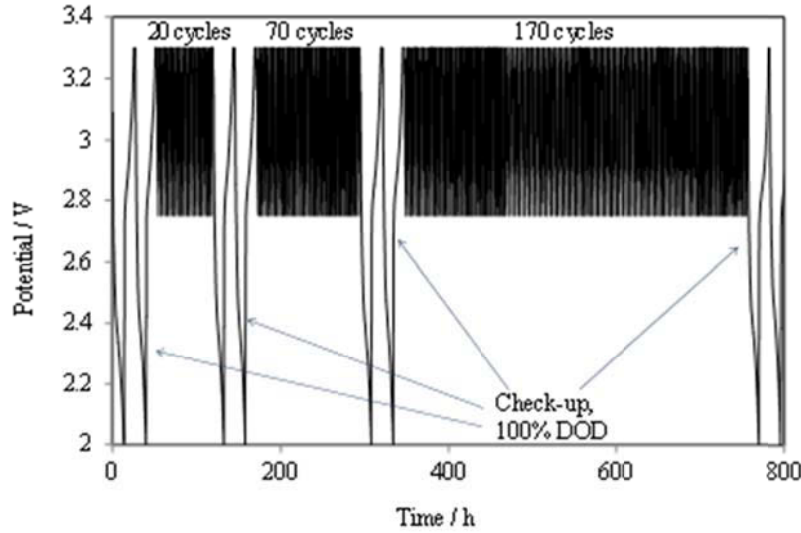


Figure 21 : Voltage of the cell during the shallow cycling.

The value of the capacity  $C_{20h}$  was calculated from the Peukert tests described previously in the paragraph §IV.4.3 (Figure 10) to be about 38mAh. This value was used to normalize the cumulative discharge capacity in order to obtain the number of the equivalent cycles. Roughly, 12-13 shallow (micro) cycles correspond to one equivalent cycle as it is shown in Figure 22. The applied cut-off voltage of 2.75V corresponds to about 3mAh of discharged electricity, hence the cell is cycled from SOC = 100% to SOC  $\approx$  92%.

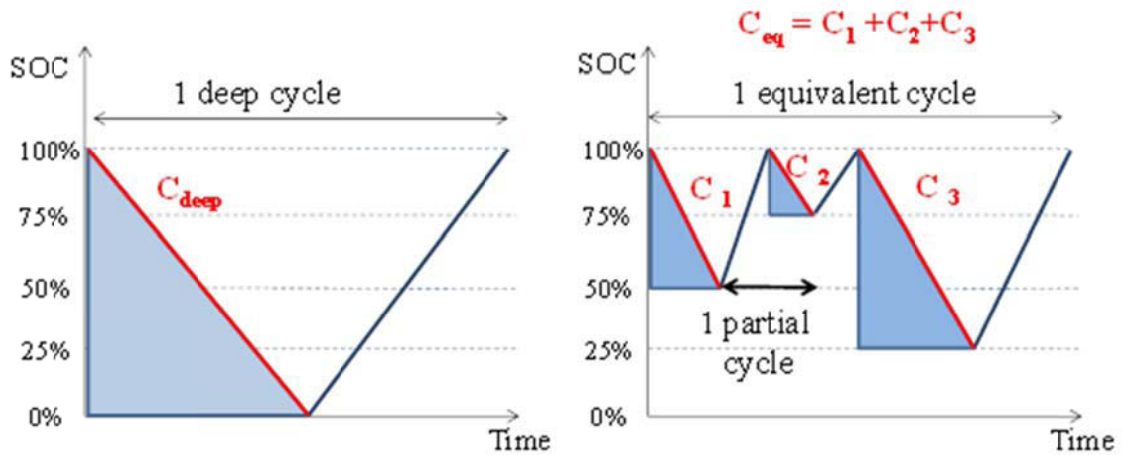


Figure 22: Scheme of representation of deep cycling and micro cycling.

Four check-up tests were done during the shallow cycling - after 20, 70, 170 and 320 micro-cycles (shallow) cycles, or respectively 1.6, 5.6, 13.6 and 25.6 equivalent cycles. Each check-up includes two cycles with depth of discharge equal to 100%. The comparison between the deep cycling and the shallow cycling presented in Figure 23, shows that during the shallow cycling no capacity loss is observed.

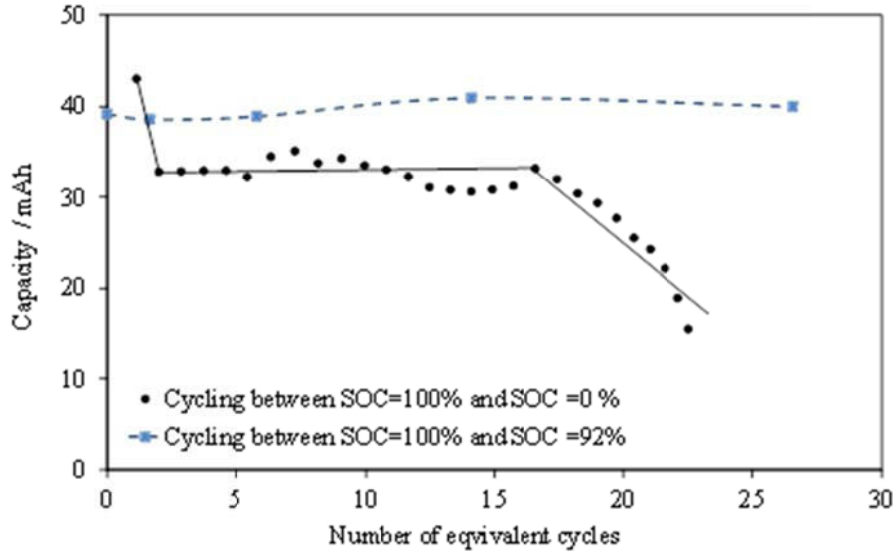


Figure 23: Comparison of the cycling performance at deep and shallow cycling.

Thus it can be supposed that the AE activity is related to the presence of degradation phenomena and vice versa, the absence of such activity is an indication for cycling with low ageing rate. When the cell is aged, the intensity of these phenomena is reduced leading to a decrease of the acoustic activity. Moreover on cycling, when the depth of discharge is limited at a voltage threshold around 2.75V, well above the appearance of acoustic activity, any sustained capacity fade was observed after 320 shallow cycles.

#### IV.5. Study under abusive conditions.

The LiAl/MnO<sub>2</sub> cells have been tested under abusive conditions: overcharge from fully charged state up to 5V and overdischarge from 3.3V to 0V with a C/20h constant current condition.

All the experiments were coupled with acoustic emission monitoring using one R15 sensor connected to the positive electrode side of the cell. Acoustic emission activity has been recorded continuously within the whole overcharge and overdischarge process.

##### IV.5.1. Overcharge Process

The result from the overcharge test is present in Figure 24. The test is performed at ambient temperature, from 3.3V potential up to 5V, at the CC regime with current rate C/20h, after classical CCCV cycling.

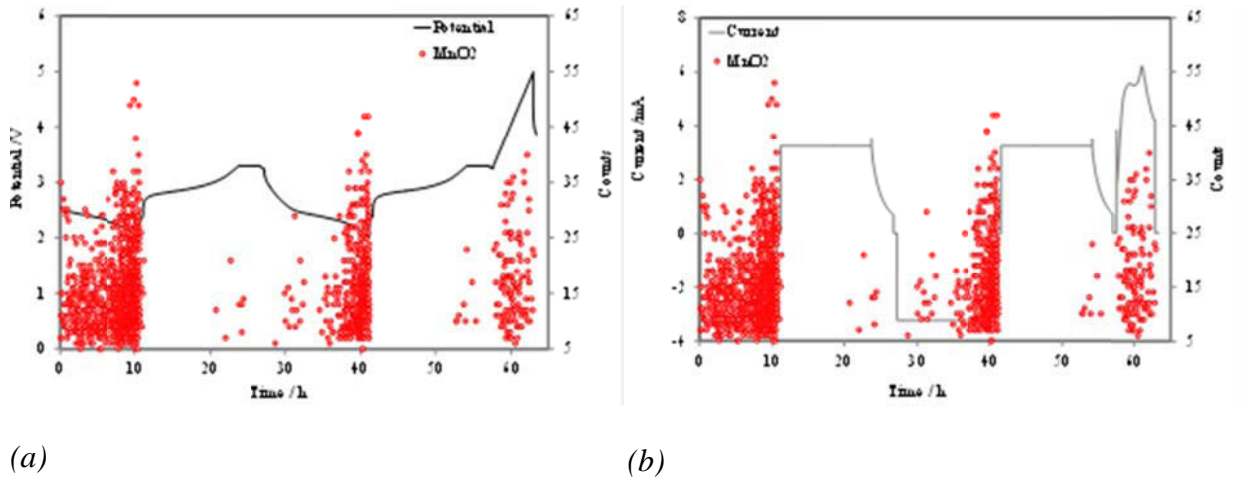


Figure 24: Overcharge process: (a) potential and acoustic activity counts plotted versus time (b) current evolution during and acoustic counts.

As observed previously, the acoustic emission response during the charge from 2V up to 3.3V is very weak. When the cell voltage exceeds the maximum charge threshold voltage authorized by the manufacturer (up to 3.3V), the acoustic events appears. As we already mentioned in §I.10 the possible reactions inside the Li- ion cell during the overcharge are:

if the capacity of the positive electrode limits the capacity of the cell :

- collapsing of the structure of the positive electrode due to the fully lithium deinsertion, and oxidative decomposition of the electrolyte;

if the capacity of the negative electrode limits the capacity of the cell [55, 56]:

- dendrite formation due to the deposition of  $\text{Li}^+$  on the surface of the alloys.

In all the cases, the degradation of the electrolyte takes place with a gas evolution [57].

The detected acoustic emission signal can be related to one or of these phenomena.

The acoustic emission data was subjected to a frequency analysis with Noesis software. The acoustic emission data recorded during the classical cycling and during the overcharge was analyzed separately. The results from this analysis are presented in Figure 25. Both spectra contain two classes of events with peaks centered at similar frequency values.

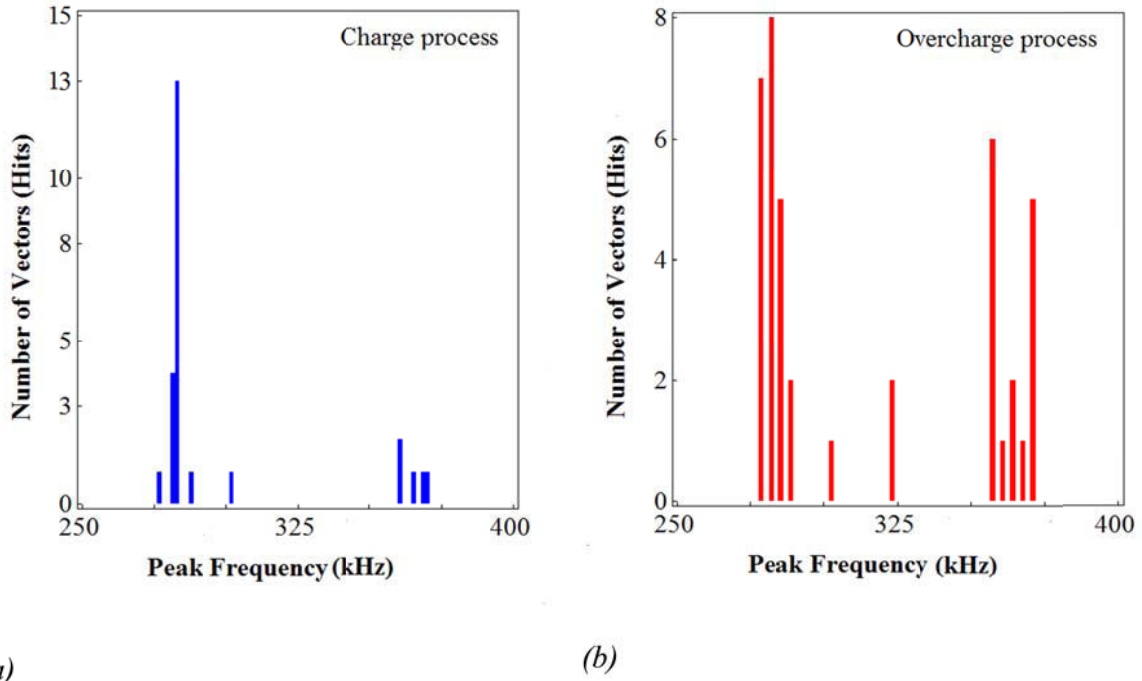


Figure 25: Peak frequency histogram of AE signals detected during (a) normal charge and (b) overcharge test (the scale of x-axis is limited to the domain where acoustic activity is detected).

Two main conclusions can be proposed:

- Concerning the frequency: the classes have the characteristic frequency between 250 kHz and 400 kHz. These types of signals are associated with practical cracking mechanisms [53, 54, 55]. No new acoustic activity appears during overcharge. Therefore we can assume that no gas emission occurs indicating that electrolyte seems stable in this voltage range (3.3V – 5V).
- Concerning the number of events, the intensity of the AE events is lower during the overcharge.

#### IV.5.2. Overdischarge Process

The results from overdischarge test are presented in Figure 26. The test was performed at ambient temperature, from 3.3V down to 0V, initially at galvanostatic conditions with current equal to C/20h down to 2V and further potentiodynamically with a voltage ramp of 0.09mV/s.

According to results obtained during the “regular” phase of the discharge (3.3V- 2V), the acoustic emission is very intensive due to the crystal phase transformation in negative

electrode. During the subsequent over-discharge phase ( $U < 2V$ ) the acoustic emission events continued but with lesser intensity.

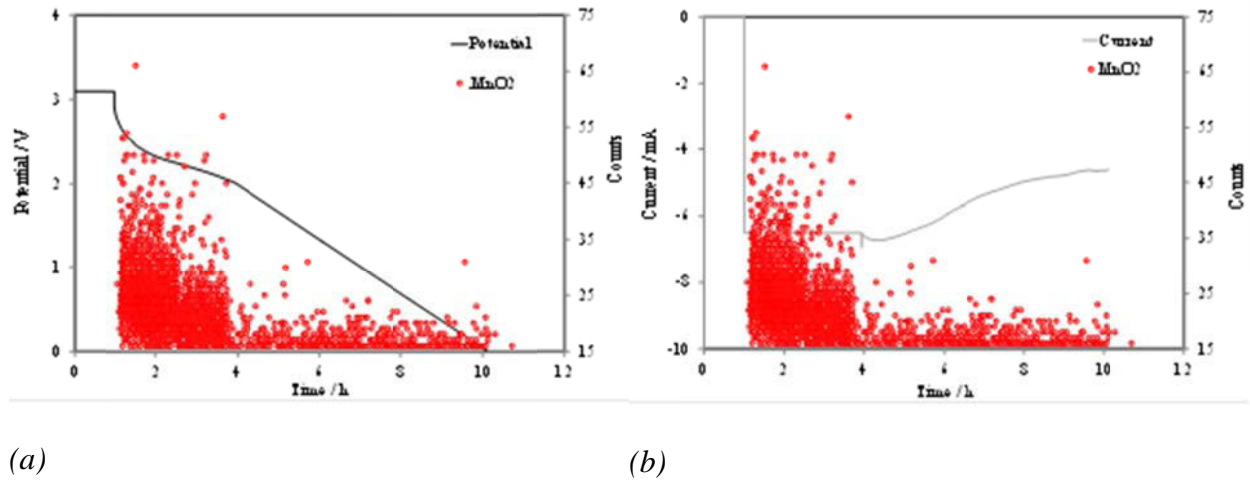


Figure 26: Electrochemical and AE data during the overdischarge process: (a) acoustic emission presented in terms of counts plotted versus potential and (b) plotted versus current.

The following electrochemical processes can take place and generate AE events during overdischarge:

If the negative electrode limits the capacity of the cell, there can be:

- depletion of lithium of the negative electrodes,
- oxidation of current collector [58].

If the positive electrode limits, the capacity of the cell:

- Overlithiation of positive electrode.

The frequency spectral analyses of the events during this experiment are presented in Figure 27. Two classes of events have been defined depending on voltage range: between 3.3V and 2V the classical discharge and between 2V and 0V the overdischarge. In all cases the frequency domain is identical corresponding to the cracking phenomena [53, 51, 55]. During the overdischarge fewer events are observed.

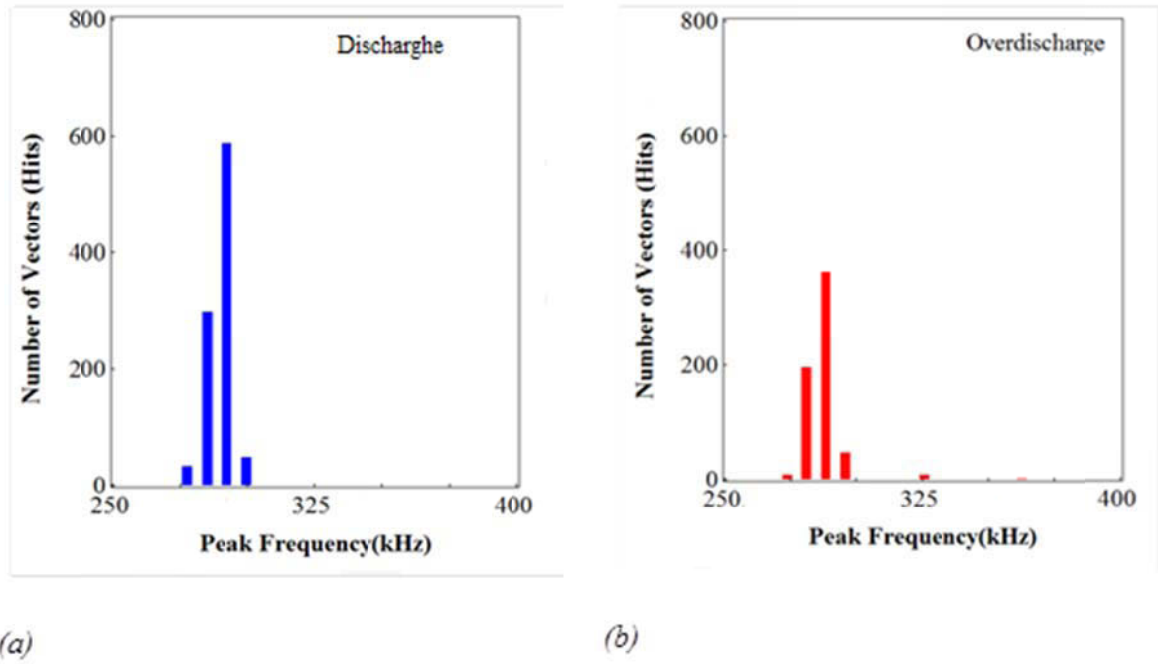


Figure 27: Peak frequency histogram of AE signals detected during (a) regular discharge and (b) overdischarge test (the scale of x-axis is limited to the domain where acoustic activity is detected).

## IV.6. Conclusions

The aim of this part of the thesis was to study the aging mechanisms in LiAl/MnO<sub>2</sub> cells by *in-situ* AE monitoring and *post-mortem* analyses (XRD and SEM).

It was demonstrated that acoustic emission technique is able to detect cracking in LiAl/MnO<sub>2</sub> cells. The main capacity fade phenomena are particle fracturing concerning the positive electrode MnO<sub>2</sub> and irreversible  $\alpha/\beta$  LiAl alloy phase transition which appears at the negative electrode. The capacity fading (state of health) correlates well with the fading of the Acoustic Emission activity suggesting that the latter can be used as a battery state of health (SOH) indicator. A specific signal treatment like spectral analysis can be used further as a component of the battery management system.

During the normal operation all acoustic activity events are characterized only in the frequency domain between 250 kHz and 400 kHz corresponding to the mechanical stress through aging mechanism in both active materials.

Under abuse conditions (overcharge/overdischarge) acoustic events remain with the same characteristic frequencies observed during normal cycling and related to the formation of fracture in the active materials. Any additional phenomena like gas formation or electrolyte degradation were detected.

The acoustic emission signal detected during the discharge can be used to diagnose weak cells in the pack. If three or more sensors are installed in the pack, these weak cells can be identified precisely using triangulation of the signals.

## References

1. Huggins R. A., “*Journal of Power Sources*”, 81–82 (1999), 13–19.
2. Besenhard J.O., Yang J., Winter M., *Journal of Power Sources*, 68, (1997), 87-90.
3. Villevielle C., Boinet M., Monconduit L., “*Electrochem. Comm.*”, 12 (2010), 1336.
4. Rhodes K., Dudney N., “*Journal of Electrochemical Society*”, 157, (2010), A1354–A1360.
5. Rhodes K., Kirkham M., “*Rev. Sci. Instruments*”, 82, (2011), 075107-1-8.
6. McAlister A.J., “*Bull. Alloy Phase diagrams*”, 3, (1982), 177.
7. Lindsay M.J., Wang G.X., Liu H.K., “*Journal of Power Sources*”, 119-121 (2003), 84-87.
8. Callister W.D., “*Fundamentals of Materials Science and Engineering*”, 10S, (2005), 1-16.
9. Jonn Wen C., Boukmamp B.A., Weppner W., *J. Electrochem. Soc.*, 126, (1979), 2258–2266.
10. Puhakainen K., Bostrom M., T., “*Journal of Solid State Chemistry*”, 183, (2010), 2528-2533.
11. Hamon Y., Brousse T., Jousse F., “*Journal of Power Sources*”, 97-98 (2001), 185-187
12. Machill S., Rahner D., “*Journal of Power Sources*”, 54 (1995), 428-432.
13. Rahner D., Machill S. in “*New promising Electrochemical Systems for Rechargeable Batteries*” Ed. Barsukov V., and Beck F. NATO ASI Series, (1995), 32-52.
14. Geronov Y., Zlatilova P., “*Electrochimica Acta*”, Vol.29 N°4 (1984), 551-555.
15. Abyaneh M.Y., Fleischman M., “*Electrochimica Acta*”, Vol.27 (1982), 1513.
16. Guo X.-Q., Podloucky R., “*Physical Review B*”, Vol.40, N°5 (1989), 2793-2800.
17. Baranski A.S., Fawcett W.R., “*J. Electrochem. Soc.*”, Vol.129 (5), (1982), 901-907.
18. Thoss F., Giebel L., Oswald S., “*Electrochimica Acta*”, 60 (2012), 85-94.
19. Rahner D., Machill S., “*Solid State Ionics*”, 86-88, (1996), 891-896.
20. Portehault D., Cassaignon S., “*Journal of Material Science*”, 19 (2009), 2407-2416.
21. Rahner D., Machill S., “*Journal Solid State Electrochem.*”, 2, (1998), 78-84.
22. Jia Z., Yiping D., “*Journal of Crystal Growth*”, 312, (2010), 2788-2794.
23. Banov B. in “*New trends in Intercalation Compounds for Energy Storage*”, (Julien C., Pereira-Ramos J.P., Momchilov A. Eds.), Vol.61, NATO Science Series, (2002), 393-403.
24. Wang X., Li Y., “*Chem. Commun.*”, (2002), 764-765.
25. Thackeray M.M., “*Prog. Solid St. Chem.*”, Vol.25 (1997), 1-71.
26. Goodenough J.B., Kim Youngsik, “*Chemistry of Materials*”, 22 (2010), 587 – 603.
27. Koksang R., Barker J., “*Solid State Ionics*”, 84 (1996), 1 – 2.
28. Manev V., Banov B., Momchilov A., “*Journal of Power Sources*”, 57 (1995), 99 – 103.



29. Tarascon J.M., Wang E., “*Journal of Electrochemical Society*”, Vol.138, N° 10 (1991), 2859 – 2864.
30. Fauteux D., Koksang R., “*Journal of Applied Electrochem.*”, 23 (1993), 1 – 10.
31. Morales J., Trocoli R., “*Electrochimica Acta*”, 55, (2010), 3075 – 3082.
32. Broussely M., Herreyre S., “*Journal of Power Sources*”, 97 – 98, (2001), 13 – 21.
33. Patil A., Patil V., Shin D.W., “*Material Research Bulletin*”, 43, (2008), 1913 – 1942.
34. Staikov G., Yankulov P.D., “*Electrochimica Acta*”, Vol.29 N°5, (1984), 661 – 665.
35. Alias M., “*PhD.Thesis*”, from “Universite de Nantes”, (2008), 28-52.
36. Kalnaus S., Rhodes K., “*Journal of Power Sources*”, 196, (2011), 8116-8124.
37. Ohzuku T., Tomura H., Sawai K., “*J. Electrochem. Soc.*”, 144 (10), (1997), 3496.
38. Sawai K., Tomura H., Ohzuku T., “*Denki Kagaku*”, Vol. 66 N°3, (1998), 301 – 307.
39. Data sheet Maxell at [http:// www.maxel.co.jp](http://www.maxel.co.jp)
40. Peukert W., “*Elektrotech. Z*”, 18, (1897), 287.
41. Pavlov D. in “*Power Source for Electrical Vehicles*”, (B.D. McNicol, D.A.J.Rand Eds.), Chapter N°5, Elsevier Amsterdam, (1984), 111.
42. Doerffel D., Abu Sharkh S., “*Journal of Power Sources*”, 155, (2006), 395.
43. Fung Y. S., “*Journal of Applied Electrochemistry*”, 22, (1992), 255.
44. Zhang X., Sasty A.M., “*Journal of Electrochem. Soc.*”, 155, (2008), A542-A552.
45. Christensen J., Newman J., “*Journal of Electrochem. Soc.*”, 153, (2008), A1019-A1030.
46. Ceder G., Mishra S.K., “*Electroch. Solid-State Letters.*”, 2 (11), (1999), 550.
47. Yoshio M., Nakamura H., “*Electrochimica Acta*”, 45, (1999), 273-283.
48. Wu S., Yu M., “*Journal of Power Sources*”, 165, (2007), 660-665.
49. Kumagai K., Kikuchi Y., “*Journal of Applied Electrochemistry*”, 22, (1992), 728-732.
50. Benedek R., Thackeray M.M., “*Journal of Power Sources*”, 110, (2002), 406.
51. Etienneble A., Idrissi H., Roué L., “*221st ESC Meeting*”, Abstract N°546, (2012).
52. Melendres C.A., Sy C.C., “*Journal Electrochem. Soc.*”, 125, N°5, (1978), 727.
53. Etienneble A., Idrissi H., “*Proceeding of the EWGAE*”, (2010).
54. Etienneble A., Idrissi H., “*Proceeding of the EWGAE*”, (2012).
55. Arora A., Harris J., “*International Stationary Battery Conference - Battcon*”, (2011), 17-1
56. Leising R.A., Palazzo M.J., “*Journal of Power Sources*”, 97-98 (2001), 681-683.
57. Belov D., Yang M.-H., “*Solid State Ionics*”, 179, (2008), 1816-1821
58. Mikolajczak C., Kahn M. in “*Lithium-Ion Batteries hazard and Use Assement*”, The Fire Protection Research Foundation, Chapter N°4, (2011), 46-71.

---

---

<b>General Conclusion</b>
---------------------------

## General Conclusion

The objective of this thesis was to bring prove(s) that the acoustic emission technique is a suitable to improve the knowledge about the electrochemical processes occurring inside the Li-ion cell under normal or abuse operating and, for a second part, to evaluate its capability to deliver new types of state of charge and state of health indicators.

Considering the results presented in the chapters III and IV, we have given some proves which demonstrate that this is really possible.

In the beginning of chapter III, the formation process of Graphite/LiFePO<sub>4</sub> cells has been studied in details. It has been established, by separately characterization of each electrode that the acoustic emission during this first formation charge is principally generated by the graphite electrode. The acoustic activity is produced by the electrochemical reactions involved in the formation of the passivation film (gas emission, cracking of the edges of the graphite planes) and by the successive lithium insertion stages (opening of the graphene planes, sudden break of defects inside the structure with the increase of the insertion rate). The formation step, considered as crucial to guarantee the best performances of the cell in time regarding the self-discharge and the capacity fading, could be managed more precisely by adapting for example the profile of the current. We have observed that a film formed with currents higher than C/20h leads to better performances in comparison with cells formed with C/50h or C/100h. We proposed also a method to define the origin of the waves and to localize them within the cell thanks to the presence of the two acoustic sensors. Abuse tests have been also performed indicating that the acoustic emission can prevent dangerous events like overcharge and consequently it could contribute to secure the technology.

In the chapter IV, we have studied the cycling behavior of commercial LiAl/MnO<sub>2</sub> cells. We have observed that the acoustic activity is stronger at the end of the discharge when the insertion of lithium from MnO<sub>2</sub> and the decrease of the concentration of lithium of the alloy occur. The capacity loss can be correlated with a decrease of the acoustic activity. XRD analyses on fresh and aged LiAl materials showed that the  $\beta$ -phase becomes predominant over the  $\alpha$ -phase during cycling. It appears that the most lithiated zones within the alloy are not

---

able to be delithiated certainly because of the volume expansion leading to disconnections within the electrode active material.

The acoustic activity monitoring allowed the access to new types of parameters (hits, frequency, absolute energy...) which can lead to a innovate approach to identify and characterize the electrochemical mechanisms within the lithium-ion cells. The reported results opened new perspectives for management of the formation process especially for the cells integrating graphite negative electrodes. In parallel, we have demonstrated that the aging of cells with lithium alloy electrodes can be evaluated by AE and the analysis the evolution of the acoustic activity provide a new type of state of health indication.

In perspective, it would be interesting to continue this study more deeply in the several following directions:

- Exploring other types of battery technologies like  $\text{LiCoO}_2$ , NMC, LTO, Zebra, lead-acid,
  - Testing of batteries with higher capacity, and different designs (spirally-wound, prismatic) and packaging (aluminum casing, soft pouch) as well as complete packs including multiple cells in series and parallel,
  - Further evaluation of the safety aspects in order to prevent thermal runaway, explosion, etc...,
  - To use advanced methods to identify the origin and the location of the different sources of events,
  - To study further the AE evolution during the formation of bigger cells of various Li-ion technologies in order to implement this method in the industrial manufacturing of the Li-ion batteries.
-

## Glossary

AE	Acoustic Emission
$\Delta AE$	Absolute Energy [aJ]
AET	Acoustic Emission Technique
AFM	Atomic Force Spectroscopy
ARC	Accelerated Rate Calorimetry
BMS	Battery Management System
CC	Constant Current
CC/CV	Constant Current/ Constant Voltage
CVA	Cyclic Voltammetry
CE	Counter Electrode
$C_f$	Full Discharge capacity [mAh]
$C_{nom}$	Nominal capacity [mAh]
$C_{res}$	Residual discharge capacity [mAh]
$C_{th}$	Theoretical capacity [mAh]
$C_{PAM}$	Specific Capacity of Positive Active Material [mAh/g]
$C_{NAM}$	Specific Capacity of Negative Active Material [mAh/g]
$C_{Li}^*$	Concentration of lithium in the intercalation compound [mol/cm <sup>3</sup> ]
$C_{Li}$	Concentration of lithium in the alloy at the starting state [mol/cm <sup>3</sup> ]
$C_D$	Capacitance
CMC	Carboxy Methyl Cellulose
$CPE_f$	Constant Phase Element of Passivation film capacitance
$CPE_{dl}$	Constant Phase Element of Electric double layer capacitance
D	Diffusion coefficient of lithium [cm <sup>2</sup> /s]
DOD	Depth of Discharge
DSC	Differential Scanning Calorimetry
DMC	Dimethyl carbonate
EV	Electrical Vehicle
EMF	Electromotive force
EC	Ethylene Carbonate

---

EQCM	Electrochemical Quartz Crystal Microscopy
EIS	Electrochemical Impedance Spectroscopy
$E_{th}$	Electrochemical thermodynamic potential of electrode
$\eta$	Electrode overpotential
$f_{max/min}$	Frequency range
FFT	Fast Fourier Transformation
FTIR	Fourier Transformation Infra-Red Spectroscopy
F	Faraday constant (96485 C/mol)
GIC	Graphite Intercalation compounds
HEV	Hybrid Electrical Vehicle
HDT	Hit Definition Time
HLT	Hit Lockout Time
NDT	Non Destructive Technique
NBR	Nitrile Butadiene Rubber
NMR	1-methyl 2-pyrrolidone
PHEV	Plugin Hybrid Electrical Vehicle
PDT	Peak Definition Time
PC	Propylene Carbonate
PVDF	Polyvinylidene fluoride
$Q_{ch}$	Injected charge [mAh]
Q	Ongoing amount of electricity [mAh]
$R_f$	Resistance of the passivation film
$R_{ct}$	Charge transfer resistance
SOC	State of Charge
SOH	State of Health
SOS	State of Security
SOF	State of Formation
SEM	Scanning electron Microscopy
SEI	Solid Electrolyte Interface
SHE	Standard Hydrogen Electrode

---

TEM	Transmission Electron Microscopy
TGA	Thermo Gravimetric Analysis
XRD	X-ray Diffraction
XPS	X-ray Photoelectron Spectroscopy
$z$	Number of electrons
WE	Working electrode

---



## Appendix 1: Valorization of results from the thesis

### Publications

1. N. Kircheva, P-X.Thivel, S.Genies, D. Brun –Buisson and Y. Bultel, “*ESC Trans.*”, 35 (14), (2011), 19-26.
2. N. Kircheva, P-X.Thivel, S.Genies, D.Brun –Buisson, “*Journal Electrochem. Soc.*”, Vol. 159, (2012), A18-A25.
3. N. Kircheva, S.Tant, B. Legros, S. Genies, S. Rosisni, P-X.Thivel “*EWGAE-ICAE proceeding*”, (2012).
4. N. Kircheva, S.Genies, C. Chabrol, P-X.Thivel, “*Electrochimica Acta*”, in press (2012).

### Patent applications

1. S. Genies, D. Brun-Buisson, N. Kircheva, P.-X. Thivel, “*Procède de Surveillance d’une batterie Li-ion et dispositif de surveillance pour mise en ouvertures*”, N° E.N.11 53663 (29/04/2011).
2. S. Genies, N. Kircheva, P.-X. Thivel, S. Hing , “*Utilisation des signaux d’émission acoustique comme indicateur d’état de santé et de sécurité*”, N° DD13766ST (01/07/2012).

### Presentation of the results

1. N.Kircheva, P-X.Thivel, S.Genies, D.Brun –Buisson and Y.Bultel, “*Study of SEI formation in Li-Ion batteries by Acoustic Emission technique*”, lecture by N.Kircheva on the 219th ESC Meeting, Montréal May 1 – 6, 2011
  2. N.Kircheva, P-X.Thivel, S.Genies, “*Contribution of the Acoustic Emission to study behavior of the MCMB / LiFePO4 batteries*”, lecture by N.Kircheva on the GEFCI Meeting, Balaruc les Bains Mars 12 – 15, 2012.
  3. P-X.Thivel, N.Kircheva, S.Tant, B. Legros, S. Genies, S. Rosisni, “*Acoustic Methods as a Tool for Management of Electrochemical Process of Energy*”, lecture by P.-X. Thivel on the EWGAE-ICAE Meeting, Granada 12 – 15 September, 2012.
-

---

---